Faculty of Engineering and Science

An Experimental and Numerical Study of Axially Loaded Lightweight Concrete Wall Panels

Timothy Ting Zhi Hong

This thesis is presented for the Degree of
Doctor of Philosophy
of
Curtin University

June 2019

Declaration

To the best of my knowledge and belief this thesis contains no material previously published by any other person except where due acknowledgment has been made.

This thesis contains no material which has been accepted for the award of any other degree or diploma in any university.

Signature: Timothy

Date : 26/6/2019

Publications

1. Timothy Z.H. Ting, Muhammad E. Rahman, Hieng H. Lau, Matthew Z.Y. Ting, Vikram Pakrashi. 2019. Oil Palm Kernel Shell – A Potential Sustainable Construction Material. Reference Module in Materials Science and Materials Engineering. Elsevier. ISBN 9780128035818, https://doi.org/10.1016/B978-0-12-803581-8.11541-3.

2. T.Z.H. Ting, M.E. Rahman, H.H. Lau, M.Z.Y. Ting. 2019. Recent development and perspective of lightweight aggregates based self-compacting concrete. Construction and Building Materials Volume 201 Pages 763-777. ISSN 0950-0618. https://doi.org/10.1016/j.conbuildmat.2018.12.128.

3. T.Z.H. Ting, M.E. Rahman and H.H. Lau. 2019. Lightweight Self-compacting Concrete Incorporating Oil Palm Shell. IOP Conference Series: Materials Science and Engineering. 95 012096

4. T.Z.H. Ting, M.E. Rahman and H.H. Lau. 2019. Compressive Strength of OPS based Self-compacting Concrete Incorporated with Fly Ash under Elevated Temperature. IOP Conference Series: Materials Science and Engineering. 95 012086

Abstract

Precast concrete wall panel has gained popularity in building construction in the past decades especially in the latest trend to embrace Modern Methods of Construction (MMC). The advantages of precast components are fast erection, cost effectiveness and anticipated structural performance. However, the local concrete construction industry is looking further for innovative construction methods that are less labour intensive since the production of precast concrete components still requires a fairly large number of skilled workers. Thus, a more innovative concrete, which is lightweight self-compacting concrete (LWSCC), has been introduced as alternative materials to the conventional concrete, and also to promote automation processes. At the present moment, the wall design equations provided in the design standards such as ACI 318, AS 3600, BS 8110 and Eurocode do not consider the material properties of lightweight concrete. In addition, limited study has been carried out on the axially loaded lightweight concrete wall. Thus, this research is aimed to investigate the axial behaviour of lightweight concrete wall through experimental and numerical studies, and subsequently develop design equations to predict ultimate axial capacity of the wall.

LWSCC mix design incorporating Oil Palm Shell (OPS) as full replacement of coarse aggregates and fly ash as partial replacement of cement in the range of 30% to 50% has been developed using particle packing theorem. Three aspects of fresh concrete properties including passing ability, filling ability and segregation resistance of the mixtures have been assessed in accordance with the European Federation of National Associations Representing for Concrete (EFNARC) guidelines. Afterwards, the developed mix design was used as the material for constructing the wall specimens. In this research, the experimental studies of the walls involved material properties tests and load bearing tests. A total of 24 wall specimens with different aspect ratios and slenderness ratios were tested with pin-end conditions. Subsequently, the axial capacities of wall specimens were compared with those calculated from the design equations. As for the numerical simulation studies, lightweight concrete wall was modelled using finite element analysis (FEA) software, ABAQUS. In this regard, a constitutive material model based on the combination of damage mechanics and plasticity, concrete damaged plasticity (CDP), was employed for the lightweight concrete. FEA results were validated against the experimental results and

benchmarked with the results from the published literatures. Thereupon, a series of parametric study was carried out using the validated models on the effect of eccentricity, slenderness ratio, aspect ratio, compressive strength, elastic modulus and tensile strength. Based on the experimental and FEA results, two design equations were consequently derived for predicting axial capacity lightweight concrete wall.

The developed LWSCC mix designs fulfil the fresh concrete properties requirements of the EFNARC guidelines. The experimental studies show that LWSCC, with the use of OPS as full replacement to normal weight aggregates (NWA), and fly ash as partial replacement of cement, is potentially a sustainable alternative construction material. With respect to the main finding, both the experimental and FEA results have manifested that the axial strength is significantly affected by slenderness ratio and eccentricity while aspect ratio has insignificant effect. Furthermore, the FEA results have also indicated that the axial capacity of wall increases non-linearly as compressive strength increases. This study has revealed that the axial capacity of concrete wall is not only affected by eccentricity, slenderness ratio and compressive strength but also its elastic modulus. The use of lightweight aggregate in concrete reduces its elastic modulus at a given compressive strength which results in reduced axial strength to resist buckling. The existing design equations, from all the design standards and previous researches, are conservative and only limited to predicting the axial strength of normal weight concrete wall. Elastic stiffness of concrete, which is a crucial factor responsible for wall buckling, is not taken into account in these equations. To prevail over the shortcomings, two design equations are developed which can be used to predict the axial capacities of lightweight, normal weight and high strength concrete walls.

Acknowledgment

First of all, I would like to express my sincere gratitude to Assoc. Prof. Dr. Muhammad Ekhlasur Rahman, my main supervisor for his relentless encouragement, constructive guidance and words of motivation throughout the duration of this research study and moreover for the inspiration he provided to ensure the completion of this work.

Special thanks must also go to Prof. Dr. Lau Hieng Ho, my associate supervisor, for his unselfish guidance and words of encouragement.

I must also thank the technicians Mr Anthony Njok Balan, Ms Sharinna, Mr Mohd Hidayat, and Mr Kelvin Wong Kin Yin for tirelessly assisting in the laboratory works.

To my friends, Mr Kevin Chang Wei Kiat, Mr Talal Mohammad Ali, Mr Alvin Kung Teck Zing, Mr Kong Sang Haw, Mr Elvis Huong Zhuang Yew, Mr Boon Soon Guan and Mr Ting Yuk Shyh who assisted me in setting up for experimental tests, I would like to show my heartfelt gratefulness.

With great appreciation, I would like to acknowledge the research grant from Curtin Malaysia Research Institute (CMRI) for providing funding for my research work.

Most importantly, I must express my very profound gratitude to my family especially my father and brother for providing me with unfailing support and continuous encouragement throughout the course of study.

Table of Contents

Declaration ii
Publications iii
Abstract iv
Acknowledgment vi
Table of Contents vii
List of Figures xii
List of Tables xviii
Nomenclature xx
1.0 Introduction 1
1.1. Background 1
1.1.1. Concrete Load Bearing Wall 1
1.1.2. Lightweight Self-compacting Concrete 3
1.2. Aim and Objectives 9
1.3. Scope of Work 9
1.4. Research Significance and Contribution 10
1.5. Report Outlines 12
2. Literature Review 13
2.1. Introduction 13
2.2. Lightweight Self-compacting Concrete 13
2.2.1. Supplementary Cementitious Materials 13
2.2.2. Characteristic of Lightweight Aggregates in SCC 16
2.2.3. Mix Design Methods 19
2.2.4. Fresh Properties of LWSCC 29
2.2.5. Hardened Properties of LWSCC 35
2.2.6. Oil Palm Shell Concrete 40
2.2.7. Summary 44
2.3. Load Bearing Wall Design Equation in Design Standards 44
2.3.1. Introduction 44
2.3.2. ACI Design Equation 45
2.3.3. Australian Standard Design Equation 46
2.3.4. British Standard Design Equation 47
2.3.5. Eurocode 2 Design Equation 48
2.3.6. Comparison of Design Equation 48

2.3.7. Remark 49
2.4. Research on Load Bearing Wall and Design Equation 50
2.4.1. Seddon (1956) 50
2.4.2. Leabu (1959) 51
2.4.3. Oberlender (1975) 51
2.4.4. Pillai and Parthasarathy (1977) 52
2.4.5. Kripanarayanan (1977) 52
2.4.6. Zielinski et al. (1983) 53
2.4.7. Saheb and Desayi (1989) 53
2.4.8. Fragomeni and Mendis (1996) 54
2.4.9. Sanjayan (2000) 55
2.4.10. Doh and Fragomeni (2005) 56
2.4.11. Ganesan et al. (2012) 57
2.4.12. Ganesan et al. (2013) 58
2.4.13. Robinson et al. (2013) 58
2.4.14. Huang et al. (2014) 59
2.4.15. Remark 59
2.5. Finite element analysis 61
2.5.1. Concrete Modelling 62
2.5.2. Steel Reinforcement Modelling 67
2.6. Concluding Remark 68
3. Mix Design Development 70
3.1. Introduction 70
3.2. Materials and Experimental Programme 70
3.2.1. Materials 70
3.2.2. Mixing Method 72
3.2.3. Test on Fresh Properties 72
3.2.4. Test on Hardened Properties 76
3.3. LWSCC Mix Design 78
3.3.1. Particle Packing Method 78
3.3.2. Mix Design Algorithm 78
3.3.3. LWSCC Mix Proportion and Discussion 82
3.4. Fresh Properties 84
3.4.1. EFNARC Requirement 84
3.4.2. Experimental Test Results 85

3.4.3. Filling Ability 85
3.4.4. Passing Ability 89
3.4.5. Segregation Resistance 91
3.5. Hardened Properties under Room Temperature 93
3.5.1. Density 93
3.5.2. Compressive Strength at Room Temperature 94
3.5.3. Tensile Splitting Strength 96
3.5.4. SEM Analysis 100
3.5.5. Water Absorption 103
3.6. Hardened Properties under Elevated Temperature 104
3.6.1. Compressive Strength at Elevated Temperature 104
3.6.2. Mass Loss 106
3.7. Concluding Remark 107
4. Experimental Investigation on Wall Panels 109
4.1. Introduction 109
4.2. Experimental Programme 109
4.2.1. Specimen 109
4.2.2. Material Properties 113
4.2.3. Casting of Specimens 114
4.2.4. Measurement of Specimen 115
4.2.5. Test Setup and Procedure 115
4.3. Test Results and Observation 117
4.3.1. Crack Patterns and Failure Mode 117
4.3.2. Load versus Deflection Behaviour 119
4.3.3. Failure Loads 123
4.3.4. Evaluation of Current Design Equations 126
4.4. Summary 132
5. Numerical Modelling and Analysis 133
5.1. Introduction 133
5.2. Concrete Damaged Plasticity 133
5.2.1. Strain Rate 133
5.2.2. Effective Stress and Evolution of the Scalar Damage Factor 134
5.2.3. Hardening Variable 136
5.2.4. Yield Function 137
5.2.5. Non-associated Potential Flow 139

5.2.6. Viscoplastic Regularization 140
5.3. Finite Element Modelling 141
5.3.1. Model Geometry 141
5.3.2. Material Property 142
5.3.3. CDP Input Parameters 150
5.3.4. Contact 154
5.3.5. Element Type 155
5.3.6. Boundary Conditions 156
5.3.7. Time Step Configuration 157
5.3.8. FEA Simulation Procedures 158
5.4. Model Verification 160
5.4.1. Quasi-static Analysis Verification 160
5.4.2. Mesh Convergence Study 160
5.4.3. Experimental Results 162
5.4.4. Comparative Study 171
5.5. Parametric Studies 174
5.5.1. Effect of Slenderness Ratio 174
5.5.2. Effect of Eccentricity 177
5.5.3. Effect of Aspect Ratio 178
5.5.4. Effect of Concrete Strength 180
5.5.5. Effect of Elastic Modulus 183
5.5.6. Effect of Tensile Strength 186
5.6. Concluding Remark 189
6. Rational Design Method 191
6.1. Introduction 191
6.2. Proposed Design Equation 191
6.3. Proposed Equation by using RSM 197
6.3.1. Prediction Model 197
6.3.2. ANOVA and Model Fitness 198
6.4. Evaluation of Proposed Equation 200
6.4.1. Experimental Results 200
6.4.2. Published Results 203
6.5. Concluding Remark 209
7. Conclusions and Future Recommendation 210
7.1. Introduction 210

7.2. Conclusions 210
7.2.1. Conclusions from Objective 1 210
7.2.2. Conclusions from Objective 2 212
7.2.3. Conclusions from Objective 3 212
7.2.4. Conclusions from Objective 4 213
7.3. Recommendations & Future Works 214
References 215
Appendices 231
A. Mix Design Calculations 232
B. Trial Mix 234
C. Design Calculations 236
C.1. Design Parameters 236
C.2. Design Standard 236
C.3. Previous researches 238
D. Results of Parametric Studies 243
E. RSM Data 263
F. Details of Published Concrete Wall Test Results 264

List of Figures

Figure 1.1: Behaviour of wall panels: (a) One-way action (b) Two-way action 3
Figure 1.2: Oil pam shell aggregates 7
Figure 2.1: Excess Paste Theory (Abdizadeh et al., 2009) 21
Figure 2.2: DMDA method (Hwang & Hung, 2005) 22
Figure 2.3: Packing density and porosity of concrete mix (Hwang & Hung, 2005) .. 22
Figure 2.4: Total voids versus Vw/Vcm (Kaffetzakis & Papanicolaou, 2012) 23
Figure 2.5: Semi-automated LWSCC mix design procedure (Kaffetzakis & Papanicolaou, 2016a) 24
Figure 2.6: PP Test Illustration (Kanadasan & Razak, 2014) 25
Figure 2.7: (a) Partial filling of cement mortar in pore (b) Uniform filling of mortar with mineral admixture in pore (Alengaram et al., 2011) 43
Figure 2.8: Comparison of Design Equation 49
Figure 2.9: Comparison of Finite Element Results with experimental results (Claeson & Gylltoft, 1998) 62
Figure 2.10: Comparison of finite element results and experimental results (Huang et al., 2014) 63
Figure 2.11: Comparison of experimental and FEA model failure mode (Lechner & Fischer, 2015) 63
Figure 2.12: Failure mode of FEA model (Mohamad et al., 2017) 65
Figure 2.13: Load versus lateral deflection (Mohamad et al., 2017) 65
Figure 2.14: Failure mode of FEA model (Ho & Doh, 2018) 66
Figure 3.1: OPS particle size distribution 71
Figure 3.2: Slump flow apparatus 73
Figure 3.3: V-funnel apparatus 74
Figure 3.4: J-ring apparatus 75
Figure 3.5: PP Test Illustration (Kanadasan & Razak, 2014) 78
Figure 3.6: Flowchart for achieving LWSCC mix design 81
Figure 3.7: Influence of coarse to fine aggregate ratio on bulk density and void ratio 82
Figure 3.8: Comparison of maximum slump spread 86
Figure 3.9: Comparison of slump flow time 88
Figure 3.10: V-funnel time comparison 88

Figure 3.11: Viscosity class variation with T500 and V-funnel flow time 89
Figure 3.12: T 500 and max spread comparison 90
Figure 3.13: Comparison of j-ring block step height 90
Figure 3.14: Comparison of segregation ratio 91
Figure 3.15: Comparison of VSI index 92
Figure 3.16: Typical slump flow appearance 92
Figure 3.17: Comparison of mixes density 94
Figure 3.18: LWSCC compressive strength development with time 96
Figure 3.19: LWSCC splitting tensile strength development with time 98
Figure 3.20: Correlation of LWSCC compressive strength to splitting tensile strength 99
Figure 3.21: Correlation of compressive strength to ratio of splitting tensile to compressive strength 99
Figure 3.22: Relationship between 28-days compressive strength and calculated splitting tensile strength 100
Figure 3.23: SEM image of ITZ of M0 at 28-day 101
Figure 3.24: SEM image of ITZ of M0 at 90-day 101
Figure 3.25: SEM image of ITZ of M50 at 28-day 102
Figure 3.26: SEM image of aggregate part at ITZ of M50 at 90-day 102
Figure 3.27: Water absorption of OPS based LWSCC 104
Figure 3.28. Compressive strength versus temperature 106
Figure 3.29. Weight loss 107
Figure 4.1: T60-AR5.3SR23 specimen layout 110
Figure 4.2: T25-AR1.8SR12 specimen layout 111
Figure 4.3: T25-AR1.8SR17 specimen layout 111
Figure 4.4: T25-AR1.8SR23 specimen layout 112
Figure 4.5: T25-AR3.1SR23 specimen layout 112
Figure 4.6: T25-AR5.3SR23 specimen layout 113
Figure 4.7: Freshly casted concrete wall specimen 114
Figure 4.8: Detail of support condition 116
Figure 4.9: Experimental test setup for (a) T60 series, (b) T25 series 116
Figure 4.10: Failure mode of specimen (a) T25-AR1.8SR12, (b) T25-AR1.8SR17, (c) T25-AR1.8SR23 (d) T25-AR3.1SR23 118

Figure 4.11: Failure mode of specimen: (a) T60-AR5.3SR23, (b) T25-AR5.3SR23 119
Figure 4.12: Load versus lateral deflection at top quarter of specimen T60-AR5.3SR23 120
Figure 4.13: Load versus lateral deflection at mid height of specimen T60-AR5.3SR23 120
Figure 4.14: Load versus lateral deflection at bottom quarter of specimen T60-AR5.3SR23 121
Figure 4.15: Load versus lateral deflection at mid height of specimen T25-AR1.8SR12 121
Figure 4.16: Load versus lateral deflection at mid height of specimen T25-AR1.8SR17 122
Figure 4.17: Load versus lateral deflection at mid height of specimen T25-AR1.8SR23 122
Figure 4.18: Load versus lateral deflection at mid height of specimen T25-AR3.1SR23 123
Figure 4.19: Load versus lateral deflection at mid height of specimen T25-AR5.3SR23 123
Figure 4.20: Axial strength ratio versus slenderness ratio 125
Figure 4.21: Axial strength ratio versus aspect ratio 126
Figure 4.22: Experimental versus calculated results from standard equations 128
Figure 4.23: Experimental versus calculated results from previous researches 129
Figure 5.1: Reponses of concrete under uniaxial loading in tension 135
Figure 5.2: Reponses of concrete under uniaxial loading in compression 135
Figure 5.3: Yield surface in plane stress state 137
Figure 5.4: Yield surfaces in deviatoric plane, corresponding to different values of K_c 138
Figure 5.5: Hyperbolic Drucker-Prager flow potential function 140
Figure 5.6: Model geometry 141
Figure 5.7: Comparison of stress-strain curve of normal and light-weight concrete (Lim & Ozbakkaloglu, 2014) 142
Figure 5.8: Stress-strain model of unconfined concrete in compression proposed by Yang et al. (2014) 143
Figure 5.9: Experimental stress-strain curve vs empirical model 145

Figure 5.10: Tension stiffening model proposed by Nayal and Rasheed (2006)..... 147
Figure 5.11: Modified tension stiffening model by Wahalathantri et al. (2011) for ABAQUS 148
Figure 5.12: Tensile stress-strain curve of lightweight concrete based on Wahalathantri et al. (2011)..... 148
Figure 5.13: Stress-strain curve of steel reinforcement 149
Figure 5.14: Dilation angle sensitivity study 151
Figure 5.15: Eccentricity sensitivity study..... 151
Figure 5.16: Biaxial to uniaxial ratio sensitivity study 152
Figure 5.17: K_c sensitivity study 153
Figure 5.18: Viscosity parameter sensitivity study..... 153
Figure 5.19: Embedment of steel reinforcement into concrete..... 155
Figure 5.20: 8 nodes brick element..... 156
Figure 5.21: Boundary and loading condition used in wall model 157
Figure 5.22: Finite Element Analysis Procedure 159
Figure 5.23: Comparison of energy at different loading stage for specimen T60-AR5.3SR23 160
Figure 5.24: Mesh convergence study for specimen T60-AR5.3SR23 (Failure load) 161
Figure 5.25: Mesh convergence study for specimen T60-AR5.3SR23 (Mid lateral displacement) 161
Figure 5.26: Experimental versus FEA failure mode of wall T60-AR5.3SR23 163
Figure 5.27: Experimental versus FEA failure mode of wall T25-AR1.8SR12 163
Figure 5.28: Experimental versus FEA failure mode of wall T25-AR1.8SR17 164
Figure 5.29: Experimental versus FEA failure mode of wall T25-AR1.8SR23 164
Figure 5.30: Experimental versus FEA failure mode of wall T25-AR3.1SR23 165
Figure 5.31: Experimental versus FEA failure mode of wall T25-AR5.3SR23 165
Figure 5.32: Experimental and FEA load versus top quarter deflection curves (T60-AR5.3SR23)..... 166
Figure 5.33: Experimental and FEA load versus mid height deflection curves (T60-AR5.3SR23)..... 167
Figure 5.34: Experimental and FEA load versus bottom quarter deflection curves (T60-AR5.3SR23)..... 167

Figure 5.35: Experimental and FEA load versus mid height deflection curves (T25-AR1.8SR12) 168
Figure 5.36: Experimental and FEA load versus mid height deflection curves (T25-AR1.8SR17) 168
Figure 5.37: Experimental and FEA load versus mid height deflection curves (T25-AR1.8SR23) 169
Figure 5.38: Experimental and FEA load versus mid height deflection curves (T25-AR3.1SR23) 169
Figure 5.39: Experimental and FEA load versus mid height deflection curves (T25-AR5.3SR23) 170
Figure 5.40: Comparison of FEA and experimental failure load 171
Figure 5.41: Comparison of FEA and published experimental failure load 173
Figure 5.42: Published experimental versus FEA failure mode 173
Figure 5.43: Axial strength ratio versus slenderness ratio (AR = 0.5, 1, 5.3, e = t/600, f'_c = 13.7MPa, ρ = 1800kg/m^3, f_t/ f'_c=0.08) 176
Figure 5.44: Axial strength ratio versus slenderness ratio (AR = 0.5, 1, 5.3, e = t/12, f'_c = 13.7MPa, ρ = 1800kg/m^3, f_t/ f'_c=0.08) 176
Figure 5.45: Axial strength ratio versus slenderness ratio (AR = 0.5, 1, 5.3, e = t/6, f'_c = 13.7MPa, ρ = 1800kg/m^3, f_t/ f'_c=0.08) 177
Figure 5.46: Axial strength ratio versus slenderness ratio (AR = 5.3, e = t/600, t/20, t/12, t/6, f'_c = 13.7MPa, ρ = 1800kg/m^3, f_t/ f'_c=0.08) 178
Figure 5.47: Axial strength ratio versus aspect ratio (AR = 0.5, 0.75, 1, 2, 3, 4, 5.3, e = t/12, f'_c = 13.7MPa, ρ = 1800kg/m^3, f_t/ f'_c=0.08) 179
Figure 5.48: Axial strength ratio versus aspect ratio (AR = 0.5, 0.75, 1, 2, 3, 4, 5.3, e = t/6, f'_c = 13.7MPa, ρ = 1800kg/m^3, f_t/ f'_c=0.08) 179
Figure 5.49: Axial strength ratio versus slenderness ratio (AR = 5.3, e = t/20, f'_c = 13.7, 25, 40, 60, 80MPa, ρ = 1800kg/m^3, f_t/ f'_c=0.08) 182
Figure 5.50: Axial strength ratio versus slenderness ratio (AR = 5.3, e = t/12, f'_c = 13.7, 25, 40, 60, 80MPa, ρ = 1800kg/m^3, f_t/ f'_c=0.08) 183
Figure 5.51: Axial strength ratio versus slenderness ratio (AR = 5.3, e = t/6, f'_c = 13.7, 25, 40, 60, 80MPa, ρ = 1800kg/m^3, f_t/ f'_c=0.08) 183
Figure 5.52: Axial strength ratio versus slenderness ratio (AR = 5.3, e = t/20, f'_c = 13.7MPa, ρ = 1600, 1800, 2000, 2200, 2400kg/m^3, f_t/ f'_c=0.08) 185

Figure 5.53: Axial strength ratio versus slenderness ratio (AR = 5.3, e = t/12, f'_c = 13.7MPa, ρ = 1600, 1800, 2000, 2200, 2400kg/m^3, f_t/ f'_c=0.08) 186
Figure 5.54: Axial strength ratio versus slenderness ratio (AR = 5.3, e = t/6, f'_c = 13.7MPa, ρ = 1600, 1800, 2000, 2200, 2400kg/m^3, f_t/ f'_c=0.08) 186
Figure 5.55: Axial strength ratio versus slenderness ratio (AR = 5.3, e = t/12, f'_c = 13.7MPa, ρ = 1800kg/m^3, f_t/ f'_c= 0.05, 0.08, 0.15) 188
Figure 5.56: Axial strength ratio versus slenderness ratio (AR = 5.3, e = t/6, f'_c = 13.7MPa, ρ = 1800kg/m^3, f_t/ f'_c= 0.05, 0.08, 0.15) 189
Figure 6.1: Concrete stress block 192
Figure 6.2: Regression analysis for λ at, (a) e = t/20; (b) e= t/12; (c) e = t/6 194
Figure 6.3: Regression analysis for parameter e 195
Figure 6.4: Regression analysis for f'c 195
Figure 6.5: Regression analysis for parameter E 196
Figure 6.6: Predicted versus actual values of axial strength ratio 199
Figure 6.7: Calculated (Eq. 6-5) versus experimental results 201
Figure 6.8: Calculated (Eq. 6-8) versus experimental results 201
Figure 6.9: Calculated (Eq. 6-5) versus published results 204
Figure 6.10: Calculated (Eq. 6-8) versus published results 204

List of Tables

Table 2.1: Comparison of mix design method 29
Table 2.2: SCC workability criteria of EFNARC (2002) guidelines 30
Table 2.3: Physical properties of OPS 41
Table 2.4: k value for end support 45
Table 2.5: Minimum reinforcement of concrete wall in ACI 318-14 45
Table 2.6: Limitations of design equations 60
Table 2.7: CDP material parameters of (Mohamad et al., 2017) 65
Table 2.8:CDP material parameters of (Ho & Doh, 2018) 66
Table 3.1: Chemical properties of cement and fly ash 71
Table 3.2: Physical properties of aggregates 72
Table 3.3: VSI criteria 76
Table 3.4: Summary of mix design 84
Table 3.5: EFNARC requirement 85
Table 3.6: Summary of fresh properties 85
Table 3.7: Concrete density 93
Table 3.8: Concrete compressive strength at different age 95
Table 3.9: Concrete splitting tensile strength at different age 96
Table 3.10: Splitting tensile strength equations from various researchers 98
Table 3.11: Water absorption value of OPS based LWSCC 104
Table 3.12. Compressive strength of concrete specimen at elevated temperature 105
Table 3.13. Relative strength ratio at elevated temperature 105
Table 3.14. Mass loss for LWSCC 106
Table 4.1: Specimen specification 110
Table 4.2: LWSCC mix design used for wall specimen 113
Table 4.3: Actual measurement, eccentricity and material properties 115
Table 4.4: Experimental results for concrete load bearing wall test 124
Table 4.5: Comparison of experiment results and calculated results using various standard design equation 127
Table 4.6: Comparison of experimental results with calculated results using design equation from previous research 131
Table 5.1: Wall geometric properties 141
Table 5.2: Comparison of elastic modulus 144

Table 5.3: Input values for compressive behaviour in Concrete Damaged plasticity 146
Table 5.4: Input values for tensile behaviour in Concrete Damaged plasticity 149
Table 5.5: Stress-strain curve of steel reinforcement 150
Table 5.6: Material parameters for CDP model 154
Table 5.7: Summary of mesh convergence study 162
Table 5.8: Comparison of experimental and FEA results 170
Table 5.9: Comparison of published experimental result and FEA result 172
Table 5.10: Range of parametric studies 174
Table 5.11: Effect of compressive strength 181
Table 5.12: Comparison of axial strength ratio 182
Table 5.13: Effect of elastic modulus (f'c=13.7MPa) 185
Table 5.14: Effect of tensile strength 188
Table 6.1: Parameter ranges for RSM 197
Table 6.2: ANOVA of RSM 199
Table 6.3: Calculated ultimate load 202
Table 6.4: Comparison of normalized failure load 202
Table 6.5: Calculated and published results 205
Table 6.6: Comparison of normalized calculated and published results 207

Nomenclature

The followings are alphabet notations used throughout the thesis:

A_g	Gross sectional area of concrete
A_s	Steel reinforcement area
$AR_{f/c\ agg}$	Ratio of coarse/fine aggregate to total aggregates
C	Compressive strength parameter
D_0^{el}	Initial elastic stiffness
d	Damage parameter
d_c	Compressive damage parameter
d_{max}	Maximum spread value
d_{perp}	spread value perpendicular to d_{max}
d_t	Tensile damage parameter
d_v	Viscous stiffness degradation variable
E	Elastic modulus parameter
E_c	Elastic modulus of concrete
E_o	Initial undamaged elastic stiffness
E_s	Elastic modulus of steel
e, e_o	Load eccentricity
e_i	Eccentricity from geometrical imperfections
e_L	Eccentricity parameter
e_r	Eccentricity ratio
e_{tot}	Total eccentricity
e_v	Void ratio
$e_{x,1}$, $e_{x,2}$	Resultant eccentricity
f'_c	Cylinder compressive strength
f_{cf}	Flexural strength of concrete
$f_{ct.sp}$	Experimental tensile splitting stress
f'_{cu}	Cube compressive strength
f_i	Pre-defined field variables
f_{sy}	Yield stress of steel
f_t	Splitting tensile strength
G	Flow function

H	Height of wall
H_e , H_{we}	Effective height
h_1	Height of LWSCC inside J-ring
h_2	Height of LWSCC outside J-ring
K_c	K_c parameter
k	Effective length factor
L, W	Length of wall
M_{cr}	Cracking moment
m	Ratio of concrete compressive strength to steel yield stress
n_w	Ultimate axial capacity per unit length
O_m	Oven-dry density
P_{cal}	Calculated failure load
P_E	Euler buckling load
P_{exp}	Experimental failure load
P_{FEA}	FEA failure load
P_u	Ultimate axial capacity
PP	Particle packing value
$\bar{p}$	Effective hydrostatic pressure
$\bar{q}$	Von Mises equivalent effective stress
S	Slump flow value
S_H	Block step value
$\bar{S}$	Deviatoric effective stress
$SG_{f/c\ agg}$	Specific gravity of coarse/fine aggregate
s_t, s_c	Stress state function
T_{10s}	V-funnel time after 10 sec stand still
T_{5min}	V-funnel time after 5min stand still
T_{500}	Time for LWSCC to flow 500mm diameter
$T_{500\ (J-Ring)}$	Time for LWSCC to flow 500mm diameter in J-ring
t, t_w	Thickness of wall
W_c	Weight of LWSCC
W_p	Weight of balance
W_{ps}	Weight of sieved portion
w_t, w_c	Weight parameter

Greek Symbols

α	Eccentricity parameter
α_2, γ	Equivalent stress block parameters
β	Effective length factor
β_1	Parameter for ascending and descending branch of stress strain curve
ε_0	Concrete strain correspond to ultimate compressive stress
ε_c	Concrete strain
$\varepsilon_{c.t}$	Total compressive strain
ε_{eng}	Engineering strain
ε_i	Inelastic compressive strain
$\varepsilon_{t.cr}$	Critical tensile strain
ε_t^{ck}	Inelastic tensile strain
$\varepsilon_{plastic}^{pl}$	Plastic strain
$\dot{\varepsilon}$	Total strain rate
$\dot{\varepsilon}^e$	Elastic strain rate
$\dot{\varepsilon}_v^{pl}$	Viscoplastic strain rate tensor
$\dot{\varepsilon}^{pl}$	Plastic strain rate
$\tilde{\varepsilon}_c^{pl}$	Equivalent plastic strain in compression
$\tilde{\varepsilon}_t^{pl}$	Equivalent plastic strain in tension
$\dot{\tilde{\varepsilon}}_c^{pl}$	Effective plastic strain rates in compression
$\dot{\tilde{\varepsilon}}_t^{pl}$	Effective plastic strain rates in tension
θ	Temperature
λ	Slenderness ratio
$\dot{\lambda}$	Non-negative scalar hardening parameter
μ	Viscosity parameter
ξ	Constant parameter
Π	Sieved portion
ρ	Concrete density
ρ_s , ρ_m	Steel reinforcement ratio
σ	Stress
σ_{b0}	Biaxial compressive yield stress

σ_{c0}	Uniaxial compressive yield stress
$\bar{\sigma}_c$, $\bar{\sigma}_t$	Effective stress
σ_{ct}	Uniaxial tensile stress
σ_{max}	Ultimate compressive stress
$\hat{\bar{\sigma}}_{max}$	Maximum eigenvalue
σ_{true}	True stress
φ	Angle of dilation

1.0 Introduction

1.1. Background

1.1.1. Concrete Load Bearing Wall

Concrete wall panel is becoming increasingly popular as a load bearing structural member to transfer load from roof to foundation. Previously, concrete wall panel was mostly viewed as a partition member to isolate the internal building interspace as well as to provide protection against external environment (Popescu et al., 2015). Due to the extremely conservative design approach provided in the early version of concrete design standards, concrete wall panel was mostly designed with little consideration of structural capacity to sustain load.

With better understanding of the behaviour of concrete wall panel as load carrying structural member due to substantial research, design guidelines have been gradually developed and improved. More reliable data has proven that the early version of concrete design standard underestimated the capability of concrete wall panel to be used as structural member (Doh & Fragomeni, 2005; S Fragomeni & Mendis, 1999; Saheb & Desayi, 1989). Nevertheless, all the current standards allow concrete wall panel to be designed as structural member.

Reinforced concrete wall panels are now considered as important load transferring structural members in building structures. The function of concrete wall panel is determined by the chosen structural system as well as the corresponding type of loading. For wall subjected to wind and seismic loadings, it behaves as a shear wall to resist lateral loading. Concrete wall panel can be designed as load bearing wall if it resists vertical loading only, without being subjected to bending.

Lately, Modern Methods of Construction (MMC) have been promoted in building industry all over the world with the aim to improve material and human resource efficiency in addition to environmental sustainability (Nadim, 2012). For this reason, precast concrete components are gaining popularity in construction industry. As for precast concrete components, they can be manufactured either in factory or on-site, transported, handled and assembled at the construction sites. In this regard, greater speed and ease in completing buildings have promoted precast wall as a popular building component.

With the increasing demand of light weight material application in construction industry, lightweight concrete is gaining popularity in order to reduce the self-weight of concrete structures (Liew et al., 2017). Significant cost reduction can be incurred from lighter and reduced size of structural components. The application of lightweight concrete in fabricating precast concrete wall panel has increasingly gained popularity. However, the production of precast concrete components still requires a large number of skilled workers. In this connection, local concrete industry is looking for innovative design method that requires less labour during fabrication without scarifying the load carrying capacity. Thus, lightweight self-compacting concrete (LWSCC) has been introduced as an alternative material to substitute the conventional concrete, and also to promote automation processes.

At the present moment, the standards such as American Concrete Institute (ACI 318) standard, Australian Standard (AS 3600) and Eurocode provide simplified equations to determine the load bearing capacity of concrete wall panel. According to several researchers, the design equation provided by ACI standard is conservative. Due to its over simplicity, such equation is not able to account for the material and geometric nonlinearity in the buckling failure of slender concrete wall panel (Robinson et al., 2013). In ACI standard, a further reduction factor is used to account for the effect of lightweight concrete application. This reduction factor yields even more conservative load bearing capacity of lightweight concrete wall panel. This could further underestimate the capability of lightweight concrete to be designed as a load bearing wall.

Against this backdrop, this research focuses on the behaviour of axially loaded lightweight concrete wall panel with and without eccentricity. The concrete wall panel under axial loading in idealized condition generally behaves as one-way action with hinged condition at both the top and bottom and with free vertical edges. It can develop a uniaxial curvature in the direction of loading. However, the wall panels are likely to behave as two-way action whereby biaxial curvature can occur in both directions, which are parallel and perpendicular to loading when both edges of the wall are restrained, as illustrated in Figure 1.1. Since the thickness of concrete wall panel is smaller compared to the other dimensions, slenderness effect is introduced. Slenderness ratio is defined as the ratio of wall height to thickness. The behaviour of wall panels under axial loading can vary substantially from short and wide to deep and

narrow slender members (Saheb & Desayi, 1989). Similar to column, the failure mode of wall panel under axial loading is highly dependent on the slenderness ratio in which a small slenderness ratio can cause crushing failure while larger slenderness ratio leads to buckling failure. The ultimate load bearing capacity of wall panel is greatly affected by the slenderness ratio.

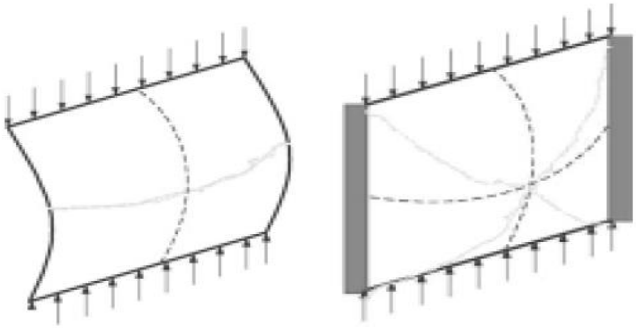

Figure 1.1: Behaviour of wall panels: (a) One-way action (b) Two-way action

From the extensive literature review undertaken, popular researches tend to focus on normal and high strength concrete wall panels rather than lightweight concrete wall panel. In this aspect, the reduced elastic stiffness of lightweight concrete is crucial in determining the load bearing capacity of slender wall panel under eccentric loading. More research in lightweight concrete wall is important in order to have better insight into the subject. As such, this research is aimed to study the structural behaviour of axially loaded lightweight concrete wall. Thereupon, rational design methodology in the form of equations is developed for the walls.

1.1.2. Lightweight Self-compacting Concrete

1.1.2.1. Concrete Sustainability Problem

Concrete is a very common construction material which has been widely used as it is highly versatile, easily available and economical (Rodriguez de Sensale et al., 2015). According to Samson et al. (2016), concrete is considered as the most utilized construction materials in the world due to its relatively low and competitive cost. More recent statistics show that there is more than 26.8 billion tonnes of normal concrete being produced globally per year (Senaratne et al., 2016). This huge production has caused the construction sector to face the issue of gradual exhaustion of natural resources as well as the difficulty in accessing them. In the aspect of the environmental impact of the concrete production, study shows that this impact can be reduced through

the use of alternative materials (Mehta, 2001). The more common practice is partial replacement of cement and to use alternative materials as aggregates.

Also for the reason of the high demand of concrete in construction industry, a large amount of normal weight aggregates (NWA) is consumed which has resulted in gradual depletion of natural gravel and crushed rock. The situation warrants the urgency to intensify the research and development of more sustainable construction materials. As such, great opportunity exists by incorporating construction and demolition wastes into concrete mix as aggregates in order to improve its resource productivity (Mehta, 2001).

Research has been carried out for utilizing recycled aggregate from demolition waste (Duan & Poon, 2014; Etxeberria et al., 2007; Xiao et al., 2005). The recycle process involves stock piling, crushing, pre-sizing, sorting, screening and contaminant elimination. However, processing of recycled aggregates requires large amount of energy and causes high carbon dioxide emission. Alternatively, other materials such as lightweight aggregates (LWA), either arises naturally or being generated as by-product from industrial processing, can be used to replace NWA in the concrete production. This leads to the production of lightweight concrete (LWC). LWC is commonly produced by replacing the normal weight aggregates with LWA. In this connection, extensive research has been carried out to utilize the waste generated in the industries as alternative construction materials in concrete due to growing of sustainability consciousness (Alengaram et al., 2013; Aslam et al., 2016).

1.1.2.2. Development of lightweight self-compacting concrete

With the advancement of concrete technology, attempts have been made in developing new high performance materials that possess the benefits and characteristics of SCC and LWC in the past decades. An innovative concrete, lightweight self-compacting concrete (LWSCC), which possesses the properties of both LWC and SCC has been developed. LWSCC is produced by replacement of NWA with LWA in SCC. According to ACI 213 (2014), the density of structural lightweight concrete falls within the range of 1120 $kg/m^3$to 1920 kg/m^3. Aggregates contribute to the most of the weight of concrete and commonly constitute about 60% by volume of SCC (Topçu & Uygunoğlu, 2010). As such, due to porous structure of LWA, it is able to reduce the density as well as the thermal conductivity of concrete. The use of LWSCC brings

about several benefits such as reduced self-weight, shorter construction period, lower construction cost and elimination of noise emitted from vibration machines as well as better heat and sound insulation due to the voids in LWA (Grabois et al., 2016; Papanicolaou & Kaffetzakis, 2010; Vakhshouri & Nejadi, 2016). Since the present construction industry is experiencing the shortage of skilled workers as well as the difficulty in hiring new generation of skilled workers (Kim et al., 2010), LWSCC, which is less labour intensive, can be a timely solution to these shortcomings. In addition, LWSCC, which is very suitable for manufacturing precast units, can be used to promote mechanisation or even automation processes in construction industry. The assembly of precast building component units on site makes the construction methods more straightforward and thus more efficient.

1.1.2.3. Application of lightweight self-compacting concrete

LWSCC has been employed as an alternative construction material in structural construction such as cable stayed bridge construction since 1992 in Japan (Ohno et al., 1993). Dymond (2007) had designed and constructed a 20m pre-stressed beam by using LWSCC while Lahkega and Stenah (2011) studied the possibility of utilizing LWSCC in a full scale wall. Also, Shi and Yang (2005) had utilized LWSCC in the application of thin precast C-shaped wall. Meanwhile, Hubertova and Hela (2007) made use of LWSCC in the construction of stadium walkway structural elements. Lately, the use of LWSCC has gradually gained popularity not only in construction but also in research field.

1.1.2.4. Problems in lightweight self-compacting concrete

There are several common issues in developing mix design of LWSCC. As LWA is porous material and generally irregular in shape, its workability is poor and compressive strength is relatively low when compared to gravel. As such, a large amount of cement paste is required for LWSCC to achieve desired workability and targeted compressive strength. Due to the porous structure of LWA, it has high water absorption capacity which tends to absorb water during batching, resulting in poor workability. The high water absorption of LWA makes it difficult to estimate the required water volume for batching. The common practice to overcome this issue is to allow LWA to achieve saturated surface dry (SSD) condition before batching (Domagała, 2015). However, care must be taken since different types of LWA have

different water absorption rates. Excessive water can increase the risk of bleeding and segregation (Illidge, 2010; Juradin et al., 2012). Moreover, the densities of lightweight aggregates are generally lower than those of the mortar matrix and natural aggregates in concrete (Topçu & Uygunoğlu, 2010). Therefore, the difference in density between LWA and normal weight sand can alter the fresh properties of LWSCC mixture. The resulting poor self-compaction and segregation of aggregates can severely affect the durability and structural performance of concrete in hardened state (Juradin et al., 2012; Kwasny et al., 2012). Thus, the use of LWA in SCC is still regarded as new development in concrete technology and thus, further investigation and study are required. In addition, no guideline has been published for developing mix design of LWSCC.

1.1.2.5. Types of lightweight aggregates

Lightweight aggregates can generally be categorized into natural and artificial types. The common natural LWA are pumice, diatomite, volcanic cinders, scoria and tuff (ACI-213, 2003; A. Neville, 2008). As for the artificial LWA, it can be further categorized into industrial wastes and processed natural materials (Aslam et al., 2016). Sintered slate, sintered pulverized fuel ash, expanded or foamed blast furnace slag and colliery wastes are more common industrial wastes used as LWAs. In addition, there are also processed natural materials such as shale, expanded clay, slate, vermiculite and perlite which can be used as LWAs in manufacturing concrete (H. Mahmud, 2010). Numerous researches have been concentrated on utilizing artificial LWA in developing LWSCC. It is even more beneficial to utilize the waste as alternative material for aggregates in concrete as it can mitigate the environmental impacts arising from waste disposal such as pollution as well as extra energy consumption.

1.1.2.6. Oil Palm Shell – An Agricultural Waste as Renewable Material

Oil palm shell (OPS) is one of the waste products generated after the extraction of oil from oil palm tree (Okafor, 1988; Okpala, 1990). Two types of oil can be extracted from palm nut. They are palm oil and kernel oil which are extracted from outer and inner cores of the nut respectively. After oil extraction, the inner core of the nut, known as palm kernel, has the potential to be used as concrete coarse aggregate. Covered by a hard endocarp, palm kernel shell is also known as oil palm shell (Pantzaris & Mohd Jaaffar, 2002).

Malaysia is abundantly cultivated with palm oil trees. According to Tripathi et al. (2015), Malaysia produces more than 52% of the total palm oil in the world. Palm oil tree coverage in Malaysia is about 3.8 million hectares and is expected to increase to 5 million hectares by the year 2020 (Alengaram et al., 2013; Gungat et al., 2013). OPS is produced in large quantities by oil palm mill. Over 4 million tonnes of solid wastes are produced annually (Alengaram et al., 2013; Aslam et al., 2016; Nagaratnam et al., 2016). Since the demand for palm oil is increasing, the production of solid wastes by oil palm industry is expected to increase too. These agriculture waste materials, a component of which is OPS, are traditionally disposed of either through incineration by conventional process or in landfill (Rahman Sobuz et al., 2014). Typical OPS aggregate is shown in Figure 1.2. These disposal methods are not only expensive but also have created many environmental issues. To minimize the environmental impact of handling and disposing these agricultural wastes, many researchers have been studying the potential of using OPS as replacement material in construction industry. Teo et al. (2007) claimed that OPS possesses the potential to be used as alternative coarse aggregates in concrete.

Figure 1.2: Oil pam shell aggregates

For the past 32 years, extensive research has been carried out on using OPS as alternative aggregates for the production of lightweight concrete in South East Asia (Alengaram et al., 2013). OPS is generally a porous material with porosity of 37% (Okpala, 1990). The porous structure of OPS greatly reduces the density and thermal conductivity. As a result, cellular structure of OPS reduces the weight of concrete and provides better thermal insulation. The reduction in density of OPS concrete is about 20 to 25% when compared to normal concrete (Shafigh et al., 2010).

At earlier years, poor workability (with low slump value) of concrete using OPS was reported by several researchers (Mannan & Ganapathy, 2001; Okafor, 1988; Okpala, 1990) even though high water to cement ratio was used. This is due to the irregular flaky shaped shape of OPS which makes cement difficult to lubricate aggregates to achieve workability. However, desirable workability was observed with the incorporation of small amount superplasticizer (A. M. Neville, 1995). Thus, superplasticizer is used in developing OPS concrete by subsequent researchers (Mo et al., 2016; Serri et al., 2015; Shafigh et al., 2012). Also, several researchers demonstrated that proper proportioned OPS concrete can achieve compressive strength above 30MPa (Farahani et al., 2017; Shafigh et al., 2011; Shafigh et al., 2012). However, in all cases, relatively large amount of cement or binder content was used to produce higher strength OPS concrete.

To date, none of the researchers has successfully developed SCC by using OPS. In the meantime, as mentioned by Mo et al. (2016), the use of OPS in concrete requires relatively high amount of cement content and superplasticizer dosage in order to achieve anticipated workability and compression strength. Since SCC also requires a large amount of cement content to achieve self-compacting ability, it would make economic sense to incorporate OPS concrete into SCC. The extra cement material cost can be compensated by the elimination of cost for concrete vibration. The use of OPS and fly ash in producing concrete has brought about many benefits and encouraged further interest in research and development. Accordingly, investigation is also carried out to develop and evaluate the fresh and hardened concrete properties of LWSCC utilizing OPS as coarse aggregates.

1.2. Aim and Objectives

The aim of this research is to investigate the compression behaviour of lightweight self-compacting concrete wall and to propose wall design equations. The objectives of this research are as below:

1. To develop lightweight self-compacting concrete mix design, incorporating fly ash as partial replacement of cement and oil palm shell (OPS) as replacement of coarse aggregates.
2. To assess experimentally the behaviour of axially loaded lightweight concrete wall panel.
3. To model the lightweight concrete wall panel by using Finite Element Analysis (FEA) software, ABAQUS and to carry out parametric studies so as to examine the effects of slenderness ratio, eccentricity, compressive strength, tensile strength and elastic modulus on the strength of concrete wall panel.
4. To develop a rational design methodology in the form of design equation to evaluate the axial load bearing capacity of concrete wall panel, inclusive of that manufactured from lightweight concrete.

1.3. Scope of Work

The scope of this research project comprises of designing and assessing the fresh and hardened properties of concrete, assessing the behaviour of wall panel under axial loading experimentally and numerically, and finally to carry out parametric studies by using FEA model. The following presents the overview of work in order to achieve the aim of this research.

In achieving objective one, the mix proportion of lightweight self-compacting incorporating oil palm shell (OPS) as full coarse aggregates replacement was developed based on close particle packing theorem. Three levels of fly ash replacement (30%, 40%, and 50%) were made to the control mixes. A total of four LWSCC mixes were obtained successfully. The resulting fresh properties including filling ability, passing ability and segregation resistance were evaluated in accordance to the procedures and requirements of EFNARC (2002). Nonetheless, the hardened properties of LWSCC including compressive strength and splitting tensile strength

were evaluated at the ages of 7, 28 and 90 days. In addition, microstructural analysis of concrete samples using SEM and EDX techniques were carried out to study the interfacial transition zone (ITZ) between binders and aggregates.

As for objective two, experimental studies were carried out on the axial behaviour of lightweight concrete wall panels cast by using the mix proportion successfully developed from the previous works as stated in objective one. The wall panels were designed to suit the specification of laboratory equipment. Wall panels of three different values of slenderness ratio were chosen in order to study the effect of slenderness ratio on walls. Four specimens were prepared for each type of wall. All these wall specimens were tested and subsequently the test results were used to validate the FEA model constructed, as illustrated in the next objective.

In order to achieve objective three, ABAQUS was used for finite element modelling. Concrete damaged plasticity (CDP) was chosen to model the lightweight concrete material properties of wall. The constructed models were validated by using experimental results obtained from the works done in objective two. In addition, the constructed models were also benchmarked with experimental results of normal concrete wall panel obtained from the published literatures. Then, parametric studies were carried out to study the effects of slenderness ratio, eccentricity, compressive strength, tensile strength and elastic modulus on the strength of concrete wall panel.

Finally, as objective four, together with all the experimental and numerical modelling results obtained, two design equations have been derived. These equations were then compared with most of the existing equations available in the published literature. Calculated results of the proposed equations were also compared with the results obtained in this research in order to demonstrate their validity and applicability.

1.4. Research Significance and Contribution

This research provides contribution to the growing field of knowledge as shown below:

1. The research makes use of oil palm shell (OPS) as an alternative lightweight construction material in construction industry. To date, there is limited research on the use of OPS in SCC. This research has demonstrated that OPS based SCC can be proportioned by using close-particle packing method. The proposed LWSCC

can effectively reuse biomass waste, reduces self-weight and evades the requirement of mechanical vibration of fresh concrete so as to promote environmental sustainability and hence is a more innovative construction material.

2. Most of the researchers concentrated on studying the behaviour of normal and high strength concrete walls. However, there is limited research conducted on the lightweight concrete wall. This research can contribute more insights into the structural performance of lightweight structural wall panel under axial loading. This research has also demonstrated that LWSCC can be used as material in precast concrete wall panel production. It could promote mechanisation or even automation processes in construction industry since the assembly of precast building components units on site will make the construction methods simpler, more straightforward, faster and hence more cost effective.
3. By using finite element analysis to model lightweight concrete wall panel, a realistic model can be developed to provide greater insight into the axial behaviour of concrete wall panel. Instead of carrying out full scale tests which require comprehensive as well as expensive laboratory works and equipment, finite element model can be alternatively used to predict the load carrying capacity. This study also demonstrates that finite element is suitable and capable to be used for parametric study for concrete wall panel. Through FEA model, the effect of several parameters can be studied and more data can be generated for deriving wall capacity equation.
4. Many of the researchers have stated that the simplified design equations available in standards are conservative. The existing design equations, from all the design standards and previous researches, are conservative and only limited to predicting the axial strength of normal weight concrete wall. Elastic stiffness of concrete, which is a crucial factor responsible for wall buckling, is not taken into account in these equations. To prevail over the shortcomings, the works in this research have led to the derivation of more accurate design equations which are based on experimental and numerical results which can take into account more material properties.

1.5. Report Outlines

The followings are the outlines of the chapters for this report.

Chapter 2 reviews the relevant literature related to lightweight self-compacting concrete (LWSCC) and concrete load bearing wall. The development of lightweight self-compacting concrete mix design and empirical design equation of concrete load bearing wall are reviewed.

Chapter 3 depicts the methodology for developing LWSCC mix design and the material property study of the developed LWSCC mix design.

Chapter 4 elaborates experimental studies of concrete load bearing wall. All the test results and observations are discussed.

Chapter 5 presents the finite element modelling methodology on lightweight and normal weight concrete wall panels. The validation of models by using experimental results and benchmarking are presented. The results and observation of parametric studies are also discussed.

Chapter 6 details the proposed design equation. The applicability of proposed equation is discussed.

Chapter 7 concludes the findings of this research. This chapter also provides recommendations for further studies.

2. Literature Review

2.1. Introduction

Chapter Two gives a detailed description of literature review of previous research works related to this project. The main subjects of the literature review include the lightweight self-compacting concrete (LWSCC), design approaches and experimental investigation of concrete load bearing wall, and related finite element studies. The existing methods and limitations for developing mix design of LWSCC are evaluated. Moreover, literatures related to concrete load bearing wall either in one-way or two-way and associated limitation are explored. More specifically, the factors that affect the ultimate load bearing capacity of load bearing wall are being looked into. In addition, finite element modelling of axially loaded structural concrete wall is reviewed.

2.2. Lightweight Self-compacting Concrete

Similar to SCC, LWSCC must attain the desired fresh properties of filling ability, passing ability and segregation resistance in order to achieve the self-compacting ability (Shi et al., 2015). Filling ability, which is also known as flow ability, is the ability to flow and fill the formwork completely under its own weight while passing ability is the ability to flow through the confined spaces between congested steel reinforcement area without tendency to segregate or block the space within formworks. Segregation resistance is the ability to remain homogeneous during the process of transporting, placing and after placing without tendency to bleed and induce separation of aggregates from mortar.

2.2.1. Supplementary Cementitious Materials

Concrete is generally made up of sand, water, coarse and fine aggregates with Portland cement as cementitious material for binder. Self-compacting concrete requires a large amount of cementitious material to achieve self-compacting characteristics. The practice of adding supplementary cementitious materials into concrete is gaining popularity due to their economic and environmental benefits. Supplementary cementitious materials are commonly generated from industrial waste, agro-waste or processing by-product (Samad & Shah, 2017). Common supplementary cementitious

materials used in concrete are fly ash (FA), silica fume, palm oil fuel ash, ground granulated blast furnace slag, rice husk ash, metakaolin, and a few others (Juenger et al., 2019). These materials can either be used independently or mixed with portland cement with different combination of up to three types supplementary cementitious materials to produce concrete (Lothenbach et al., 2011). Implementation of these materials in concrete can improve strength, workability and durability.

Among the numerous types of supplementary cementitious materials, fly ash (FA) is the most common supplementary cementitious material that can be incorporated in the concrete in order to reduce the material cost as well as to improve both the fresh and hardened state properties. When compared to other supplementary cementitious materials, fly ash is easily available. Fly ash, a type of pozzolanic material, is an industrial waste produced by furnaces of electrical power plant. As fly ash is generated from burning of pulverized coal, it can exhibit high pozzolanic activity. The main constituents of fly ash are silica, alumina, iron, and calcium which can react with calcium hydroxide to form calcium silicate hydrate and calcium aluminate hydrate. Fly ash is made up of fine grained particles with grain size less than 1 μm to over 100μm (Owaid et al., 2012). The density of fly ash ranges from 540 to 860kg/m^3. The bulk density is reported to range from 1120 to 1500kg/m^3. The colour can vary from tan to dark grey depending on the chemical composition. The same class of fly ash from different sources, although produced at the same electrical plant but with different coal sources, burning techniques, and environmental technologies, can alter the properties of fly ash significantly (Aïtcin, 2016). According to ASTM C 618 , fly ash is classified into Class C and Class F category. Class F materials are generally low-calcium (less than 10% CaO) fly ashes with carbon contents usually less than 5%. Class C materials are often high-calcium (10% to 30% CaO) fly ashes with carbon contents less than 2%. Class C ashes can rapidly hydrate and harden within 45 minutes when exposed to water. The common replacement levels for Class F fly ash are at 15% to 25% by mass of cementitious material while for Class C fly ash, they are at the levels of 15% to 40%. The replacement level depends on the reactivity of fly ash and the desired performance of concrete (Helmuth, 1987).

In supplementary cementitious material (SCM), hydraulic activity, pozzolanic activity or both take place which contribute to the properties of concrete. As in Portland cement, hydraulic activity occurs in phases when the SCM chemically reacts with water,

forming cementitious hydration products. In contrast, pozzolanic activity is the reaction between siliceous or aluminosiliceous material in the SCM with calcium hydroxide, forming calcium silicate hydrate and other cementitious compounds. Since calcium silicate hydrate is a better hydration product, the pozzolanic reaction contributes higher strength to the hardened concrete on long term.

The partial replacement of cement with fly ash is gaining popularity due to its ability to improve the fresh concrete properties. Bouzoubaa and Lachemi (2001) reported that the use of superplasticizer tended to decrease when higher level of class F fly ash replacement was made. According to Malhotra (2002), for normally vibrated concrete, the water demand decreased up to 20% with the use of fly ash. Also, the author stated that Class C fly ash requires lesser superplasticizer than class F fly ash to achieve the same workability. A few researchers demonstrated that high volume fly ash replacement up to 70% in SCC can result in significant enhancement of workability (Bouzoubaa & Lachemi, 2001; Dinakar et al., 2008). In the study of Khatib (2008), the workability improved with the increment of fly ash replacement up to 80% by keeping constant both w/b ratio and superplasticizer content. The author showed the slump flow of SCC without fly ash was found to be 635mm while addition of fly ash from 20% to 80% lead to spread value greater than 700mm. It has been reported by Ramanathan et al. (2013) that partial replacement of cement by fly ash can result in higher volume of paste due to its lower density and this increases the paste volume which in turn reduces the friction at the fine aggregate-paste interface. These can improve the cohesiveness and plasticity of concrete, resulting in improved workability. Similar trend was also reported by Jalal et al. (2015).

The hardened properties of concrete containing fly ash is highly dependent on the level of fly ash replacement and the class of fly ash. Generally, fly ash concrete attained lower compressive strength than cement concrete at early stage. This has been demonstrated by numerous researchers (Bouzoubaa & Lachemi, 2001; Khatib, 2008; Ramanathan et al., 2013). This is attributed to the slower pozzolanic reaction of fly ash with calcium hydroxide in hydrated cement. As lime from cement hydration reacts with fly ash, fly ash containing concrete is gaining strength over time. The higher the replacement level of fly ash in concrete, the higher reduction in the hardened properties is expected since there is not enough cement hydration products react with fly ash. Khatib (2008) also studied compressive strength of SCC with fly ash replacement up

to 80%. The author stated that strength reduction can be observed whenever concrete is replaced with fly ash compared with concrete that contained cement only. However, the author only investigated the concrete strength up to 56 days. None of the concrete with fly ash replacement achieved comparable strength to cement concrete in the research work of Khatib (2008). Fly ash concrete may require longer time to gain its strength. M. Liu (2010) also studied fly ash replacement up to 80% in SCC. The study was carried out up to 180days. 20% fly ash replacement was found to be the optimum in their studies as the strength was close to control concrete at the age of 90 days. Significant strength development was observed for high level fly ash replacement (above 60%) in the study. Atiş (2003) also reported that 50% fly ash replacement in SCC can result in comparable strength of control concrete. Therefore, it can be concluded that the optimum fly ash replacement in SCC is able to improve the strength of hardened concrete.

In short, partial replacement of fly ash in SCC improves both their fresh and hardened state properties. In consideration of this as well as its easy availability, fly ash is chosen as supplementary cementitious material in the developing mix design of LWSCC in this research.

2.2.2. Characteristic of Lightweight Aggregates in SCC

Extensive study has been carried out by many researchers in utilizing lightweight aggregates (LWA) in SCC. Hwang and Hung (2005) utilized reservoir fine sediment as coarse aggregates in SCC while Bogas et al. (2012) and Hubertová and Hela (2013) studied the possibility of expanded clay as coarse aggregates. Pumice has been used as lightweight coarse aggregates and studied by several researchers under different temperature and mix proportioning (Andiç-Çakır & Hızal, 2012; Kaffetzakis & Papanicolaou, 2012; Papanicolaou & Kaffetzakis, 2010; Uygunoğlu & Topçu, 2009). Also, Shi and Wu (2005) and Lo et al. (2007) have utilized expanded shale as LWA for SCC. Moreover, Kanadasan and Razak (2014) used agriculture waste, palm oil clinker, as aggregates in SCC. In all these studies, it is noted that the fresh and hardened state properties of LWSCC are highly dependent on the physical properties of LWA used.

2.2.2.1. Specific Gravity

Specific gravity is defined as the ratio of the material mass to the mass of an equal volume of water at the temperature of 23°C. Generally, lightweight aggregates (LWA) have different values of specific gravity which are not more than those of normal weight aggregates. The specific gravity for pumice aggregates is within the range of 0.69 to 1.84. Andiç-Çakır and Hızal (2012) reported the lowest specific gravity of pumice aggregates is 0.69 while Topçu and Uygunoğlu (2010) reported the highest specific gravity of 1.84. For expanded shale aggregates, the specific gravity values are in the range of 1.33 to 1.35, which are considerably consistent. Expanded clay aggregates have the specific gravities of 0.42 to 1.78. Gopi et al. (2015) found the lowest specific gravity of 0.42 for expended clay aggregates while Shanker (2016) found the highest of 1.75. This inconsistency of specific gravity may be due to the situation whereby the aggregates are supplied from different sources as well as the different ways they are processed in the industry. By comparing the LWA and NWA, the specific gravity of LWA is 10% to 80% lower than that of NWA. Aggregate specific gravity is important in the calculation of weight-to-volume relationships and to compute various volume-related quantities such as voids present in aggregate, and that the voids that must be filled by cementitious materials. It affects the resulting workability and final density of the designed LWSCC.

2.2.2.2. Size Distribution of LWA

Lightweight aggregates (LWA) generally occur in different particle shape and size. Sieve analysis or gradation test is a common method for determining the particle size distribution. The particle size distribution of LWA is crucial in engineering application as it can be used to verify the compliance of design requirement, production control and specifications. The use of well graded aggregates in SCC will minimize the voids which leads to optimum workability and strength. As such, selection of appropriate size distribution of aggregates is important in designing LWSCC mix.

2.2.2.3. Shape Thickness and Texture

According to Tviksta (2000), the performance of SCC is very sensitive to the characteristics of aggregates. These characteristics include shape, texture, maximum size, grading and morphology. The shape and size of coarse aggregates have

significant influence on the particle packing and aggregate interlocking within the matrix. They are the factors in determining the amount of paste volume to cover all the particles. LWAs commonly exist in angular and flaky shape. Khaleel et al. (2011) had studied the effect of maximum aggregate size on flowability of SCC. The authors found that the flowability of SCC decreased with the increase of coarse aggregate size. The authors also recommended the use of coarse aggregates with the maximum 10mm size as it can produce higher strength SCC than that produced by using coarse aggregates of the maximum 20mm size. From the review of LWA of several researchers (Floyd et al., 2015; Grabois et al., 2016; Kaffetzakis & Papanicolaou, 2016a; Kurt et al., 2016; Rajamanickam & Vaiyapuri, 2016), most of the maximum size of coarse LWA used in LWSCC is either 12.5mm or 16mm. This is to promote a good interlocking effect between them to enhance the packing characteristics and flowability of SCC which will guarantee the strength of concrete (Kanadasan & Razak, 2014).

2.2.2.4. Water Absorption

LWA are generally porous materials which tend to absorb water. LWA will absorb and hold more moisture than normal weight aggregates. As a result, pre-wetting of LWA is required before batching and this practice has been used in manufacturing lightweight concrete (LWC). Depending on the cellular structure of LWA, it may also take longer time to achieve saturated surface dry (SSD) condition (Peters, 1999). The 24-hour water absorption of these three aggregates is in the range of 5 to 80%. LWSCC is sensitive to the water content of LWA as it can alter the resulting workability and compressive strength of concrete. The water to binder ratio of concrete can also be affected by the water absorption of LWA (X. Liu et al., 2011). The water absorption capacity of LWA must be specified in order to maintain the consistency of LWSCC. According to Shafigh et al. (2012), concrete with porous aggregates is less sensitive to poor curing as the strength may vary only 6 to 11%. This is due to the fact that the water present in aggregate pores is capable of providing internal curing. The sensitivity can be reduced when lower water to binder ratio is used. The water present in aggregates can reduce plastic shrinkage due to unfavourable drying condition and provide internal curing which leads to more complete hydration of cement (Pierce, 2007).

2.2.2.5. Remark

The mix proportion of LWSCC and its corresponding performance in terms of both fresh and hardened states are greatly dependent on the physical properties of LWA incorporated. Concerning the characteristics of LWA such as specific gravity, size gradation, shape, texture, and water absorption capacity, they can significantly alter the amount of material used in mix design. Specific gravity of LWA used can affect the resulting concrete density. From the review above, it is noted that the specific gravity of LWA of less than 2.0 is used to produce lightweight concrete in order to produce concrete of density below 1920kg/m^3. Aggregate size, gradation and texture can greatly influence the amount of cement paste used to lubricate aggregates in order to achieve self-compacting ability as well as to fill in the voids between them. Since LWA is generally present as angular and flaky shape, most of the researchers have limited the maximum coarse aggregates size up to 12.5 or 16mm. This can reduce the surface-to-volume ratio which minimizes cement used and improves workability, resulting in lower cost. Moreover, the water absorption of LWA can greatly affect both the fresh and hardened properties. High water absorption LWA can cause workability loss when it is used as dry condition during batching. Saturated LWA can greatly alter the water to cementitious material ratio used which will result in poor compressive strength of concrete. In the light of considerable influence of water absorption of LWA, LWA must be pre-wetted and allowed to achieve saturated surface dry (SDD) condition in order to prevent either water loss or high water content before batching.

2.2.3. Mix Design Methods

The mix proportions of LWSCC are crucial in its application as the selected proportions can affect the required properties in fresh and hardened states. Similar to SCC, LWSCC must attain the desired fresh properties such as filling ability, passing ability and segregation resistance so as to fulfil the self-compacting requirement. Filling ability, which is also known as flow ability, is the capability of concrete to flow and fill the formwork completely under its own weight. Meanwhile, passing ability refers to the capability to flow past the confined spaces between steel reinforcement congested area without segregating and clogging within the space of formworks. Segregation resistance is the capability to stay homogeneous during the process of

transporting, placing and after placing without tendency to bleed and separation of aggregates from mortar. Similar to any other type of concrete, strength, volume stability and durability of the hardened LWSCC are important in structural applications (Sethy et al., 2016). The performance of LWSCC is greatly influenced by the constituents of raw materials, the dosage of chemical and mineral admixtures, types of aggregate used, packing density, water to cement ratio (W/C) and design procedures.

At the present moment, standardized method for obtaining mix design of SCC does not exist. Many researchers have developed and proposed several design methods for SCC based on scientific theories and empirical expressions. In the context of SCC, the design methods can be classified into five categories based on their design principles, which are empirical design method, compressive strength method, close aggregate packing method, statistical factorial method and rheology of paste model (Shi et al., 2015). However, there are limited mix design methods which have been developed for LWSCC. The majority of the available LWSCC mix design methods in literatures are mainly based on close aggregate packing method. Many researchers prefer to develop the mix design of LWSCC by trial and error method as most of the proposed methods are not suitable to be used once the requirement of application is changed. This is commonly done by varying the binder content, binder to water ratio, admixture dosage, fine and coarse aggregate ratio. The review of LWSCC mix design method will be presented in the following section.

2.2.3.1. Shi and Wu Method

The combination of least void volume for binary aggregate mixture, excess paste theory and ACI 211 has been adopted by Shi and Wu (2005) in proportioning the mix design of LWSCC. The relationship between void volume or density of combined aggregates and coarse to fine aggregates volume ratio is determined by using particle packing concept in accordance with ASTM C29/ C29M. The least void volume of combined aggregates was found to be 0.5 in their study. However, the authors recommended to use coarse to fine aggregates ratio of 0.6 as it does not increase much void but decreases the density significantly. Excess paste theory is then used to determine the minimum quantity of paste required to fill in the void among the aggregates, to allow SCC to flow with minimum frictions between aggregates as well as to balance the mixture by the quantity of water retained by the aggregates as

illustrated in Figure 2.1. The required volume of excess paste is highly dependent on the characteristics of LWA, such as gradation, shape and surface texture, which can be determined through laboratory tests. The cement content and water to cement ratio are then determined from ACI 211 based on the designed compressive strength. The cement content is fixed at the determined value while excess paste is produced from powders including fly ash and glass powder. The workability is then adjusted by varying the SP dosage. The authors successfully design LWSCC with satisfactory flowability and segregation resistance by using the proposed method. However, the proposed method requires intensive laboratory work to obtain the necessary information to proportion mix design.

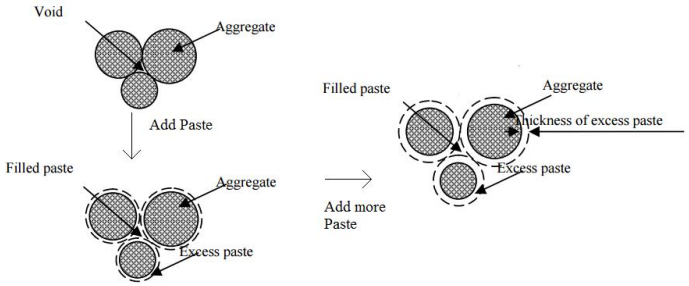

Figure 2.1: Excess Paste Theory (Abdizadeh et al., 2009)

2.2.3.2. Hwang and Hung Method

For DMDA, Hwang and Hung (2005) developed this method based on ACI 318 and the fact that high physical density can produce optimum physical properties. In DMDA method, the mixture proportion algorithm is classified into aggregate phase and paste phase. Aggregate phase comprises lightweight aggregate, normal weight fine aggregate and fly ash while cement, slag, water and superplasticizer constitute paste phase. Finer particles fill the voids of the coarse aggregates to minimize the porosity in order to form the major skeleton of aggregates phase as shown in Figure 2.2. This in turn increases the density of solid materials and reduces the content of cement paste as illustrated in Figure 2.3. Paste phase is mainly used for lubricating aggregates in order to achieve concrete workability. This method is suitable for mix proportion design aimed to reduce water and cement content by using the physical packing density of aggregate which results in lower permeability of LWSCC. Though, this method does not take into account the optimum weight of concrete as long as the optimum properties are obtained. This may result in high density concrete. The authors

recommended to use high water to binder (w/b) ratio of more than 0.42 to prevent autogenous shrinkage of the cement paste due to cement hydration and pozzolanic reaction. In fact, it is not necessary to use high w/b ratio when LWA is pre-soaked and has achieved saturated surface dry condition (SSD) before casting. The water from internal pores is able to prevent the autogenous shrinkage. Moreover, in this method, the aggregates packing density can be enhanced by adding fly ash which fills the voids in LWA. Fly ash should not be considered as the part of aggregate phase as it is supplementary cementitious material.

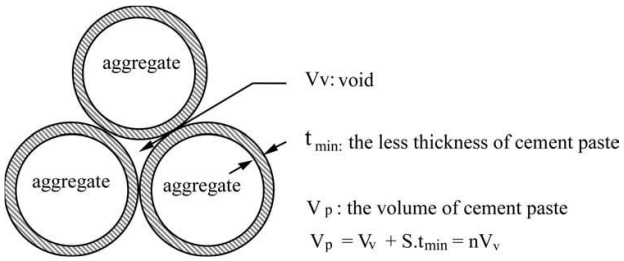

Figure 2.2: DMDA method (Hwang & Hung, 2005)

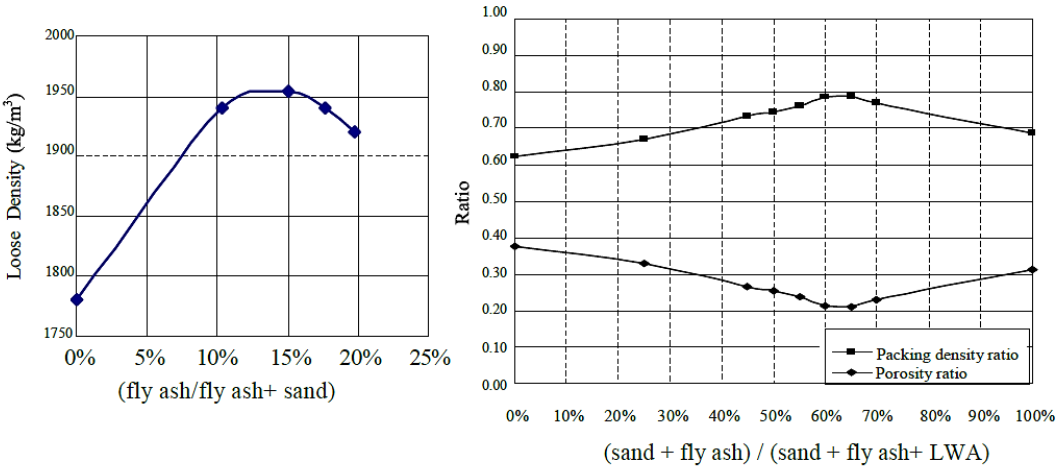

Figure 2.3: Packing density and porosity of concrete mix (Hwang & Hung, 2005)

2.2.3.3. Kaffetzekis and Papanicolaou Method

Kaffetzakis and Papanicolaou (2012) proposed another LWSCC mix design method based on optimum packing point (OPP) concept and workability criteria. This method involves the investigation of paste, mortar and concrete phase of material. Cement

paste and mortar are assessed through wet packing method, which is used to determine the packing density of cement paste and mortar. This concept involves the determination of total voids and air voids, as well as the solid concentration factor of a given water to cementitious materials volumetric ratio (V_w/V_{cm}). High V_w/V_{cm} ratio is used as trial initially. The ratio is then decreased until solid concentration factor is about to decrease. Void ratio versus V_w/V_{cm}curve will be plotted based on the trials as shown in Figure 2.4 . Optimum packing and void ratio can be determined from the curve. The derived mortars from OPP concept must be assessed for self-compactness through slump-flow and V-funnel tests. This method assumes that the least void volume of mixture corresponds to the optimum flowability in both paste and mortar. For concrete phase, the aggregate packing index is first determined from aggregate apparent density and particle density. LWSCC is then proportioned by modifying the mortar to aggregate void volumetric ratio based on the equation derived by Jacobsen and Arntsen (2008). The workability must be assessed using SCC fresh concrete test. The authors argue that maximizing packing density should be solely used to determine the mix proportion of LWSCC, which contradicts with the method proposed by Hwang and Hung (2005).

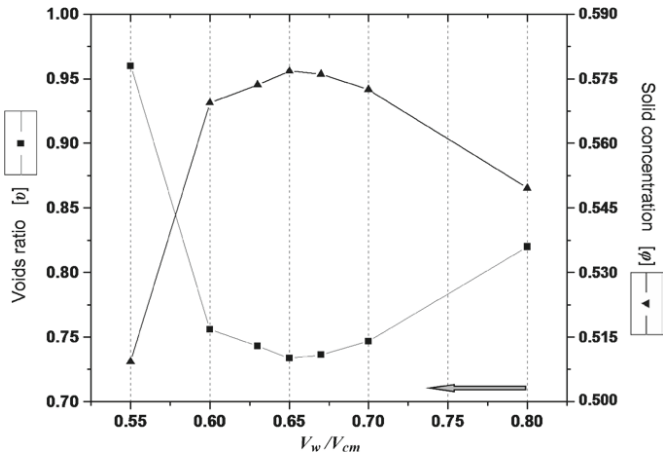

Figure 2.4: Total voids versus V_w/V_{cm} (Kaffetzakis & Papanicolaou, 2012)

Kaffetzakis and Papanicolaou (2016b) proposed a semi-automated mix design methodology which was based on the concept of optimum packing point (OPP) from their previous research and incorporated with statistical analysis. The authors derived a series of procedures from statistical analysis and previous research works to proportion the LWSCC mix design based on the target performance. Three performance parameters, which are 28-day compressive strength ($f_{lcm.cube}$), oven-dry

density (ρ) and slump flow (S-F), can be pre-set in the equations from the statistical analysis in order to determine the required mix proportion. Design parameters including volumetric ratio of LWA (V_{la}), water to cementitious material ratio (W_{ef}/CM) and cementitious material content (CM) can be calculated based on the design performances and equations proposed by Kaffetzakis and Papanicolaou (2016a). These procedures involve specifying the desired performance, calculation of design parameters and implementation of OPP procedures as illustrated in Figure 2.5. The authors have validated the design procedure by carrying out two LWSCC mix designs and the resulting performance correlates well with the proposed target. However, this method is only limited to the use of certain materials such as cement, limestone fillers, silica fume and pumice aggregates. Further laboratory investigation as stated in previous research (Kaffetzakis & Papanicolaou, 2012) has to be carried out if other materials are used in producing LWSCC.

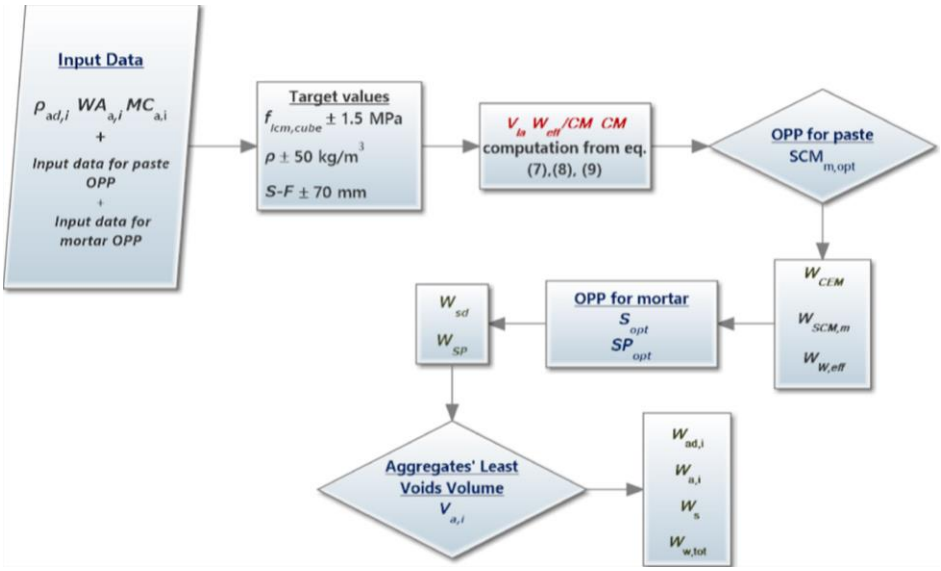

Figure 2.5: Semi-automated LWSCC mix design procedure (Kaffetzakis & Papanicolaou, 2016a)

2.2.3.4. Kanadasan and Razak Method

Kanadasan and Razak (2014) modified the particle packing method of SCC which was originally proposed by Choi et al. (2006) to allow for the substitution of palm oil clinker (POC) aggregates in SCC. The substitution can be made on either fine or coarse aggregates at the level of 0% to 100%. It is based on the concept of minimizing the void of concrete by using appropriate size and gradation of aggregate with the use of

minimum volume of paste as shown in Figure 2.6. The authors introduced an additional correction lubrication factor (LCF) to particle packing factor (PP) to allow for the characteristics of LWA aggregates when aggregates substitution is made in LWSCC mix design. The authors highlighted that the voids produced by flaky and porous structure of POC aggregates could be filled and lubricated by the binder paste. The proposed method fixed the fine aggregate ratios at 0.5 and 0.6 to allow wider range of ratios for SCC. The authors studied the cement contents which varied from 380 to 420kg/m^3 and recommended that 420kg/m^3 could produce the optimum performance SCC. However, the authors also mentioned that trial has to be carried out to ensure the required performance. The authors also demonstrated experimentally that the proposed method is able to produce LWSCC when 100% substitution of LWA is incorporated. PP theory is able to produce LWSCC mix design with minimum void volume relative to coarse aggregate, minimum water to binder ratio, maximum cementitious materials density as well as the optimum fresh concrete properties. This theory provides good understanding of the consumption of aggregate and paste volume for a given unit volume of concrete. The proposed method is also applicable for a variety of combination of other aggregates. However, the PP factor and CLF have to be determined in laboratory if other types of aggregates and their combinations are used. Besides, the actual performances of the designed mix must be checked in laboratory.

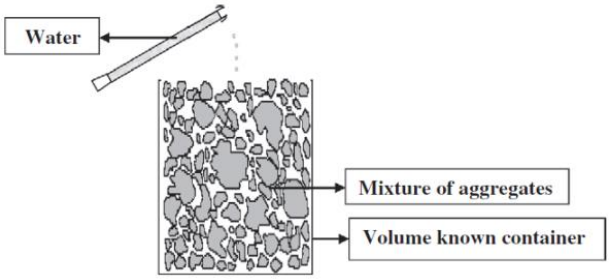

Figure 2.6: PP Test Illustration (Kanadasan & Razak, 2014)

2.2.3.5. Li et al. Method

Li et al. (2017) proposed another LWSCC mix design method based on the packing and mortar film thickness theory. This method determines the sufficient amount of paste to fill the voids between aggregates and form a thin layer to overcome the frictions between aggregates which is similar to the DMDA proposed by Hwang and Hung (2005). The methodology involves two stages, which are the optimization of

granular skeleton of aggregates and cementitious material composition. Stage one involves the characterization of coarse and fine aggregates in terms of bulk density and void volume percentage. The authors adopted the method proposed by Shi and Wu (2005) to obtain the optimum balance point between bulk density or porosity of aggregates and coarse aggregates to total aggregates ratio (V_g/V_{Total}). The authors recommended to use coarse to total aggregates ratio of 0.6. The value higher than 0.6 could result in more consumption of paste to fill the void in LWA which could lead to more production cost. A value less than 0.6 will result in higher density which contradicts the definition of lightweight concrete. These values are then used to determine the optimum coarse to fine aggregates volume ratio with the consideration of mortar film thickness (MFT). MFT is defined as half the average distance between the particle surfaces of coarse aggregate. It reflects the dosage and physical properties of coarse aggregates including aggregate grading and stacking porosity. Stage two involves the optimization of minimum water content required for binder by using the method proposed by Laboratory Central des Ponts et Chausses (LCPC). Cement, mineral admixtures water and filler dosage are then determined based on the minimum water and the respective material density. The amount of SP dosage needs to be determined through the rheology study of mortar in laboratory. Trial batch must be carried out to ensure the mix design can achieve the required performance. The authors highlighted that the mixing time should not be more than 3 minutes to avoid segregation. The authors suggested an equation to estimate the dry density of LWSCC mixture from the proposed design as Eq. 2-1.

$$\rho_{dry} = m_s + m_g + 1.2m_{cm} \qquad \text{Eq. 2-1}$$

where m_s is the mass of sand; m_g is the mass of coarse aggregates; and m_{cm} is the mass of cementitious materials. From the results of validation tests, the authors stated that interfacial transition zone (ITZ) between aggregates and paste can be improved and made more compacted due to the increase of MFT. The authors have successfully developed the LWSCC mix design with adequate fresh properties and compressive strength up to 54MPa by using the proposed methodology. In short, the proposed method is based on simple design principles and is applicable to other type of LWA. However, the proposed method is not able to proportion the LWSCC mix design based on specified workability and compressive strength criteria.

2.2.3.6. Nepomuceno et al. Method

Nepomuceno et al. (2018) modified a normal weight SCC mix design method which was originally proposed by their previous research (Nepomuceno et al., 2012; Nepomuceno et al., 2016; Nepomuceno et al., 2014) to develop LWSCC mix design. The proposed methodology is based on the rheological study of mortar phase and combination of it with coarse aggregates in concrete phase. This methodology involves the characterization of constituent materials, determination of volumetric ratio of both fine aggregates and coarse aggregates from reference grading curve which was originally proposed by Nepomuceno et al. (2014), and powder material to total volume of respective content. Volume ratio of water to power content and mass ratio of superplasticizer to powder content are then determined experimentally in mortar phase through iterative process until flow capacity and fluidity complied to the required rheology. The volume of LWA is then determined by quantifying the ratio between the volume of mortar and coarse aggregates and finally the volume of void is defined based on the porosity of LWA. In this method, the effect of low density of LWA was considered by adding extra criteria in mortar rheological study stage. The flow properties in mortar phase must be able to prevent the dynamic and static segregation of LWA. The authors stated that the dynamic segregation resistance can be evaluated during workability test while static segregation is evaluated by visual observation of axially cut cylinders after 24 hours of batching. The authors noticed that the reference grading curve of NWA is applicable to LWA since the LWA used in their research has more round and spherical shape compared to NWA. However, the reference grading curve must be determined in laboratory by using the method proposed by Nepomuceno et al. (2014) and Nepomuceno et al. (2016) if LWA of different shape index is used. LWSCC can be proportioned based on the required fresh and hardened properties such passing ability, density and compressive strength. The passing ability of designed LWSCC can also be quantified by V_m/V_g ratio by using the statistical equation proposed by Nepomuceno et al. (2014) and Nepomuceno et al. (2016). The density of the designed mix is highly dependent on V_m/V_g ratio and can be considered in the equation of this proposed method. The designed compressive strength of LWSCC can be quantified by varying W/C ratio and V_m/V_g ratio through statistical equation or design chart provided. The authors have successfully developed the LWSCC mix design with adequate fresh properties and compressive strength in the range of 35 to

59MPa by using the proposed methodology. In short, compared to the methodology proposed by other researchers, this method is able to proportion the LWSCC mix design based on the selected passing ability, density and compressive strength requirements.

2.2.3.7. Remark

Although Mazaheripour et al. (2011) recommended to apply high performance concrete mix design method for LWSCC to avoid segregation and maintain the strength, the method cannot produce optimum LWSCC mix proportion in terms of fresh and hardened properties. The resulting density is not within the upper limit of lightweight concrete specified in ASTM. It is clear from the research reviewed above that most of the proposed methodologies for proportioning LWSCC mix design are based on close aggregate packing principle. Aggregates packing principle is used to determine the least void among the aggregates in order to minimize the void produced by LWA as well as to determine the optimum coarse to fine aggregates ratio to produce the lowest density LWSCC. From the literatures above, it is noticed that the coarse to fine aggregates ratio used is generally in the range of 0.5 to 0.6 and the ratio of 0.6 is recommended by most of the researchers as it is the most cost effective. The paste is then applied to fill the voids to become LWSCC which can be determined through either excess paste theory or rheological study of cement paste or mortar. For comparison purpose, all the reviewed LWSCC mix design methods are summarized in Table 2.1. Among the several methods, particle packing (PP) methods of Kanadasan and Razak (2014) is chosen for mix proportioning in this research. It is because this method provides good understanding of the amount of paste consumption required in order to lubricate aggregates to facilitate self-compacting ability for a given unit volume of concrete.

Table 2.1: Comparison of mix design method

Researchers	Advantage	Disadvantage
Shi and Wu (2005)	○ Minimum amount of cement paste is required to facilitate self-compacting ability can be determined.	○ It has limited application with other types of aggregates and SCM.
Hwang and Hung (2005)	○ It considers the durability performance of mix design in proportioning stage.	○ High w/b ratio is fixed in the procedures, which compromises its resulting compressive strength.
Kaffetzakis and Papanicolaou (2012)	○ Mix design can be proportioned based on required performance including fresh properties.	○ It has limited application with other types of aggregates and SCM.
Kanadasan and Razak (2014)	○ It provides good understanding of the amount of paste consumption required in to achieve self-compacting ability. ○ It can be used for variety of aggregates combination	○ It is not able to proportion the LWSCC mix design based on specified workability and compressive strength criteria.
Li et al. (2017)	○ Mix design can be proportioned based on required density. ○ The fresh properties of mix design can be controlled through MFT.	○ It is not able to proportion the LWSCC mix design based on specified workability and compressive strength criteria. ○ Comprehensive material characterization tests are required.
Nepomuceno et al. (2018)	○ Mix design can be proportioned based on required performance including density, fresh and hardened properties.	○ Aggregate reference curves are not suitable for all type of lightweight aggregates. Comprehensive material characterization tests have to be carried out.

2.2.4. Fresh Properties of LWSCC

2.2.4.1. LWSCC Workability Criteria

LWSCC must be assessed for filling ability, passing ability and segregation resistance and they are used to measure the workability of LWSCC. There are several methods for assessing each of these properties. Several publications such as EFNARC (2002) and ACI-237 (2007) provide the guidelines to carry out workability test for SCC. The

methods to assess the filling ability are slump flow, T_{500}, Kajama box, v-funnel, o-funnel and orimet. Assessing the filling ability is the most fundamental test for any type of SCC as it can be used to assess the consistency of SCC to meet the guideline requirements. The test for assessing passing ability are L-box, U-box, J-ring and Kajama box. These tests adopt the concepts of allowing SCC to pass through a pre-set spacing. This spacing is the smallest gap whereby SCC can flow continuously to fill the formwork. Also, segregation resistance can be assessed through penetration, sieve segregation, settlement column and visual segregation. SCC is mostly prone to segregation during and after placing. Segregation is a crucial problem in the casting of vertically tall structural element as it can lead to the uneven distribution of aggregates and mortar in LWSCC. The workability performance requirements of EFNARC (2002) for SCC are shown in Table 2.2. According to EFNARC (2002), these criteria are developed based on the current knowledge and research. SCC with fresh properties outside these criteria may be acceptable if it is able to perform properly under the required conditions. Future developments will likely produce different requirements for these criteria. For example, these criteria may be relaxed if the formwork design is very simple or the spacing between the reinforcement is large.

Table 2.2: SCC workability criteria of EFNARC (2002) guidelines

Workability	Test	Class	Criteria
Filling ability	Slump Flow (mm)	SF1	550-650
		SF2	660-750
		SF3	760-850
	T500 (s)	VS1/VF1	≤ 2 V − Funnel ≤ 8
		VS2/VF2	≥ 2 time(s) 9 − 25
Passing ability	Step height in J-ring (mm)	PA1	Sj ≤ 15 (59 mm bar spacing)
		PA2	Sj ≤ 15 (40 mm bar spacing)
	L-Box		0.8 - 0.1
	U-Box		0 - 30
Segregation Resistance	Sieve segregation (%)	SR1	≤ 20
		SR2	≤ 15

2.2.4.2. Review of Previous Research

In the past decade, substantial study has been done on the fresh and hardened properties of LWSCC. Lotfy et al. (2015a) studied LWSCC with different type of LWA including furnace slag, expanded clay and expanded shale. The authors found that LWSCC with expanded shale as LWA achieved the best workability with respect to filling ability, passing ability and segregation resistance among the three aggregates. Lotfy et al. (2015a) explained that the fine portion of expanded shale aggregates is finer than the other two LWA which results in better packing density and less void between the aggregates particle, allowing the excess paste in LWSCC to achieve better flowability and segregation resistance. The excess paste required for improving workability highly depends on the gradation, shape and surface texture of aggregates. They agreed with the research outcome of Shi and Wu (2005). In short, the workability of LWSCC is highly dependent on the aggregates packing density and void volume.

Lotfy et al. (2015b) performed a series of experimental investigation on the parameters affecting the workability of LWSCC. They studied the effect of water to binder ratio (w/b), superplasticizer dosage and total binder content on the workability of LWSCC. Expanded shale was used as aggregates in LWSCC. From their research outcome, the filling ability and passing ability of LWSCC were found to be improved significantly with the increasing of w/b ratio and superplasticizer dosage respectively as well as the combination of these two parameters. The improved parameters were indicated by the increased spread of slump flow, reduction of v-funnel flow time and increased of L-box ratio. However, with the fixed amount of superplasticizer, there was a limit to the improvement of the filling ability of LWSCC by increasing the content of binder. The increase in binder content resulted in higher demand of superplasticizer so as to maintain similar filling ability. Similarly, the increase in water and superplasticizer dosage was found to be able to improve the passing ability. However, the increase in binder content would affect the passing ability negatively. In contrast, segregation resistance was found to be improved with the increase of binder content as it can enhance the packing density of LWSCC mixture. Nonetheless, poor segregation resistance was resulted as water and superplasticizer dosage increased. They agreed with the research findings of Sonebi et al. (2007) that the fresh properties of SCC are significantly affected by water and superplasticizer dosage. LWSCC exhibits similar behaviour to the normal SCC when influenced by water and superplasticizer dosage.

In general, the performance of LWSCC workability with respect to filling ability, passing ability and segregation resistance is greatly influenced by water to binder ratio, superplasticizer dosage and total binder content.

Grabois et al. (2016) investigated the effect of steel fibers on fresh and hardened properties of LWSCC. Expanded clay was used as aggregates in their research. The addition of steel fibers in LWSCC was able to slightly increase the slump flow spread. It is because steel fibers, which have comparatively higher density, provide more self-weight for SCC to flow under gravity. However, the V-funnel flow time decreased with the addition of steel fibers due to the blockage of steel fibers inside the V-funnel restricted area. They demonstrated that the LWSCC with poor flow time were able to be used for casting the "U"-shape thin wall panel. The aggregates and fibers were found to be homogenously distributed along the panel length. The findings in their study have provided a new understanding that LWSCC is able to fill the narrow formwork even with the flow time outside the SCC workability requirement as stated in Table 2.2.

On the other hand, Mohammadi et al. (2015) examined the effect of silica fume with 0% to 15% of binder replacement on the properties of LWSCC workability with expanded clay and perlite as aggregates. The flowability and segregation resistance of LWSCC were found to be improved with the replacement as well as the increased dosage of silica fume. They also concluded that LWSCC with expanded clay as aggregates achieved better workability compared to LWSCC with perlite as aggregates.

Corinaldesi and Moriconi (2015) studied the effect of the addition of synthetic fibers in LWSCC with expanded clay as aggregates and recycled concrete aggregate as partial replacement. It was noticed that the incorporation of fibers was able to improve the filling ability while it had negative effect on the passing ability. Silica fume was also studied. They observed that addition of small amount of silica fume resulted in higher viscosity. Poor flowability and passing ability were observed but the segregation resistance was improved. Similar observation was obtained with addition of silica fume in LWSCC with synthetic fibers. However, the findings of Corinaldesi and Moriconi (2015) had contradicted the findings obtained by Mohammadi et al. (2015).

A comprehensive study of LWSCC was done by Floyd et al. (2015) on the effect of cementitious material and aggregate type on the workability of LWSCC. Two types of aggregates, which were expanded clay and expanded shale, were studied by them. They found that better visual stability of LWSCC was achieved by increasing the cement content. Similar to the findings of other researchers, the increase in superplasticizer dosage resulted in improved filling and flowing ability. With the constant amount of SP dosage and w/b ratio, the increase of volumetric sand to total aggregate ratio was found to be able to produce better fresh properties with the optimum ratio of 0.51. Also, no significant improvement in fresh properties was noted by incorporation of silica fume at 5% and 10% in LWSCC with lower cement content. For LWSCC with high cement content, the fresh properties tend to be improved with only 5% or 10% incorporation. Poorer fresh properties were achieved by LWSCC with Type I cement compared to Type III cement. The fresh properties of LWSCC with Type III cement can be improved by partially replacing binder with fly ash as shown in their study. Floyd et al. (2015) stated that LWSCC with expanded shale exhibited better fresh properties compared to expanded clay with the same amount of other mixture content which agreed with the findings of Lotfy et al. (2015a). Also, the authors changed the coarse aggregates distribution in their study by limiting the maximum aggregate size to 12.5mm. This resulted in better fresh properties. In short, the fresh properties of LWSCC are highly dependent on binder content, SP dosage, type of aggregates used and volumetric sand to total aggregate ratio.

Kurt et al. (2015) investigated the effects of fly ash, different water to binder ratios and replacement of pumice aggregates with natural aggregates on LWSCC. The filling ability was found to be improved with the increase of water to binder ratio as well as fly ash replacement. Due to the low pozzolanic activities of fly ash, its increase could retard the bonding of water to mixture and hence the loss of workability. However, segregation was observed in their research when water to binder ratio exceeded the optimum value. Also, the spreading capability of slump flow was found to be increased with the density increase of LWSCC as the spread and placement properties of LWSCC were highly dependent on its own weight. With the increase of pumice aggregates in LWSCC, the time required to spread 500mm diameter increased and also the V-funnel flow time. This can be explained by the loss of weight with the replacement of LWA in LWSCC which resulted in self-weight to be less than threshold

stress. Since the self-weight was below the threshold stress, the authors implied that it could increase the tendency of static segregation.

Bozkurta and Taşkin (2017) studied the effect of the use of barite, fly ash and pumice as powder on the LWSCC fresh properties. The authors observed that LWSCC with barite powder was the best among three types of powder in improving the fresh properties in terms of flowability and filling ability. However, the authors reported that the use of barite as powder content in LWSCC could cause bleeding due to its poor adhesiveness and viscosity resistance. As such, the ratio of low adhesive powder content is crucial in developing LWSCC to prevent bleeding.

Ardalan et al. (2017) investigated the effect of fly ash, pumice and slag as binder partial replacement in LWSCC on retention workability after 50minutes. The authors stated that pumice blend required more superplasticizer dosage to achieve target slump flow among the three types of supplementary cementitious materials. Conversely, fly ash blend required lesser dosage of SP in order to achieve the target slump flow. It can be explained that the spherical geometry of fly ash particles is able to reduce the fraction resistance of cement particles and thus enhance the mixture fluidity. Among the three types of blend mixture, fly ash blended LWSCC showed significant slump flow loss after 50minutes while pumice blended LWSCC showed the best retention capacity.

Law et al. (2018) studied the LWSCC incorporated with perlite, scoria and polystyrene (BTS) as lightweight aggregates. LWSCC with BTS are highly prone to segregation due to their ultra-lightweight characteristics. This could be overcome by using higher binder content which could provide sufficient plastic viscosity to suspend the aggregates in concrete. The passing ability of LWSCC with scoria aggregates decreased with the increase of scoria aggregates replacement. The authors recommended to improve the passing ability by increasing the binder content. The author concluded that the use of lightweight aggregates at high level replacement to produce LWSCC could result in adverse effect on workability. Meanwhile, Aslani et al. (2018) studied the effect of partial replacement of scoria and recycled aggregates in LWSCC. Their mix designs were similar to that of Law et al. (2018). The authors reported that although recycled aggregates contributed negative influence on workability of LWSCC, the combination of recycled aggregates and scoria aggregates was still able to produce LWSCC that fulfilled the criteria of EFNARC (2002).

2.2.4.3. Remark

The studies presented so far provide evidence that the workability of LWSCC is highly dependent on the aggregates packing density and void volume. In general, similar to normal SCC, the performance of LWSCC workability with respect to filling ability, passing ability and segregation resistance is greatly influenced by water to binder ratio, superplasticizer dosage and total binder content. The inclusion of different types of supplementary materials has different effects on LWSCC workability. When silica fume is used, and with increasing replacement level, the segregation resistance of LWSCC is found to be improved while it has negative effect on filling and passing ability. The inclusion of fly ash as binary or ternary blend can not only improve all the three fresh properties but also reduce the amount of SP required. In addition, the incorporation of fibers such as steel and synthetic fibers is able to improve the filling ability but causes negative effect on passing ability.

2.2.5. Hardened Properties of LWSCC

2.2.5.1. Compressive Strength

The most important required property of any innovative material is its compressive strength. The compressive strength of concrete has great influence on its structural performance. As mentioned previously, the compressive strength of LWSCC is significantly affected by the composition of raw materials, the dosage of chemical and mineral admixtures, types of aggregate used, packing density and water to binder ratio (W/B).

Substantial research has been done on the compressive strength of LWSCC with different parameters. Corinaldesi and Moriconi (2015) studied the effect of addition of synthetic fibers in LWSCC with expanded clay as aggregates and recycled concrete aggregate as partial replacement. In their research, low density LWSCC (1250kg/m^3) with concrete strength of grade 40 at 28-day age could be achieved by the addition of silica fume which could enhance the concrete strength development. According to the authors, the addition of macrofibers did not compromise the degree of concrete compaction, but could result in more viscous concrete. However, the compression strength was found to be 10% higher than LWSCC without fibers. Similar trends of LWSCC compression strength were obtained by using steel fibers or synthetic fibers

at high dosage. Thus, addition of fibres such as steel, synthetic and macro fibers increases the compressive strength of LWSCC.

Lotfy et al. (2015a) conducted a series of study on the hardened properties of LWSCC by using different types of LWA such as furnace slag, expanded clay and expanded shale. The volume ratios of coarse to fine aggregate of all the mixtures were determined by particle packing procedures in accordance with ASTM C29/C29M. They had found that LWSCC with expanded shale as LWA achieved the highest strength and expanded clay attained the lowest among the three types of LWA. The authors explained that these were attributed to the lower volume of coarse LWA for LWSCC with expanded shale. Expanded shale aggregates achieved superior packing density which reduced the coarse portion required and enabled more fine particles to fill up the voids in the concrete matrix. Lotfy et al. (2015a) suggested that higher strength LWSCC could be proportioned with relatively low dry density, high aggregate packing density and low coarse to total aggregates volume ratio. The authors also noticed that aggregates are the weak point of the concrete matrix in LWSCC as all the failed samples exhibited aggregate fracture. It is also proven by the studies of Nepomuceno et al. (2018). The authors reported that LWSCC attained lower compressive strength when compared to normal SCC with the same mix proportion. LWSCC achieved compressive strengths between 35 and 57MPa while SCC achieved the range 53 to 87MPa. As pointed out by these researchers, under compression, LWSCC fails with the rapture of LWA as it forms the weak link in the concrete matrix.

Lotfy et al. (2015b) performed a series of experimental investigation on the parameters that affected the hardened properties of LWSCC. The w/b ratio and total binder content were found to be the main parameters affecting the LWSCC compressive strength. The LWSCC strength increased with the decrease of w/b ratio. The 28-day compressive strength also increased with the increase of total binder content. The amount of superplasticizer dosage was found to have no effect on the LWSCC strength. These findings conformed to the basic knowledge of concrete property.

Grabois et al. (2016) observed that their LWSCC mix design was able to achieve 70% of the 28-day strength in a day. Their mix design is suitable for high early strength application. Also, the incorporation of steel fibers in LWSCC could result in lower compressive strength. For failure mode, they noticed that the rupture occurred through

the LWA and yet the interfacial transition zone was still intact. The authors explained that the mortar was stronger than LWA in lightweight concrete which was in conformity with the findings of Lotfy et al. (2015a). The use of expanded clay aggregates could result in better paste-porous LWA bonding.

Mohammadi et al. (2015) studied the effect of silica fume on LWSCC containing perlite and expanded clay as LWA. They observed that the LWSCC containing expanded clay as LWA achieved higher compressive strength than perlite as LWA. However, the difference in compressive strength decreased with the increase of silica fume replacement. The replacement of silica fume in LWSCC could increase its compressive strength. Nevertheless, Mohammadi et al. (2015) only studied the silica fume replacement up to 20% of total binder. The result is yet to be known if the silica fume replacement is more than 20%. The optimum replacement percentage is also not known.

Kurt et al. (2015) conducted a series of experimental test to investigate the effect of fly ash, different water to binder ratio and replacement of pumice aggregates with natural aggregates on LWSCC. With the increasing percentage of pumice aggregates replacement, the compressive strength of LWSCC decreased significantly. This concurred with the findings of Floyd et al. (2015) and Grabois et al. (2016) that the LWA is generally weaker than mortar even though both authors used different types of LWA. Also, Kurt et al. (2015) found the compressive strength decreased with higher water content which is generally true. LWSCC with fly ash replacement gains strength at the slower rate than that without fly ash replacement at the early stage (e.g. 7 days). Nevertheless, they achieve almost similar strength at later age (e.g. 90 days). The authors attributed the findings to low pozzolanic activity of fly ash at the early stage when fly ash content was increased. The replacement of fly ash in LWSCC could significantly improve the fresh concrete properties but requires longer time to gain strength.

A comprehensive study was done by Floyd et al. (2015) to investigate the effect of cementitious material and aggregates type on the properties of LWSCC. The LWSCC with expanded clay was found to fail around the aggregate particle while LWSCC with expanded shale failed with the fracture of individual particles. The authors explained that the smooth surface of expanded shale aggregates had caused poor bonding

between the aggregates and cement mortar. From the failure mode of LWSCC with expanded clay, Floyd et al. (2015) concluded that the compressive strength of LWSCC is greatly influenced by the strength of LWA. The authors also found that water to binder ratio had less significant effect on compressive strength of LWSCC designed with high cement content in their particular research. The authors also observed that it was difficult to estimate the moisture content of wet LWA before concrete casting. The moisture content can cause significant variation in compressive strength of LWSCC with the given amount of cement content and w/b ratio.

Ardalan et al. (2017) studied the compressive strength of LWSCC with different types of supplementary cementitious material including fly ash, slag, pumice and silica fume in binary and ternary blend. The authors stated that the use of fly ash and pumice at high level replacement could result in significant strength reduction. However, slag with high level replacement showed comparable strength to control mix. Ternary blend of cement, pumice and silica fume resulted in increased compressive strength compared to control mix. The author also noticed that increasing of silica fume content could significantly improve the compressive strength after 28 days.

Law et al. (2018) studied the compressive strength of LWSCC incorporated with perlite, scoria and polystyrene (BTS) as lightweight aggregates. Increase in LWA content in LWSCC could result in decrease in compressive strength. Among the three types of LWA, scoria based LWSCC showed less significantly strength reduction when the LWA content was increased. The authors reported that the use of BTS in LWSCC could result in weak bond between the binder paste and the aggregates, thereby creating a weak interfacial transition zone and hence reduction in compressive strength. Perlite based LWSCC showed most significant strength loss when the LWA content was increased. The authors explained that the excess pore water in the perlite was released due to crushing during mixing, causing weaker concrete strength.

2.2.5.2. Tensile Strength

Concrete is generally weak under tension action. The tensile strength of concrete is commonly used to estimate the load that will cause the development of cracking in the member under flexural loading. Once the concrete cracks, the concrete behaviour will be affected (Malárics & Müller, 2010). In the research done by Corinaldesi and Moriconi (2015), the LWSCC tensile strength did not improve with the addition of

synthetic fibers. By referring to the works done by Lotfy et al. (2015a), similar trends were found in tensile splitting strength, as in compressive strength. LWSCC with expanded shale as LWA achieved the highest strength and expanded clay attained the lowest. The authors developed the mathematical correlation expression of LWSCC tensile splitting strength to compressive strength. This is shown as Eq. 2-2. They compared the accuracy of their equation for estimating tensile splitting strength with the equations from FIB model and ACI 318. They noticed that the FIB equation extremely underestimated the tensile splitting strength of lightweight concrete.

$$f_t = 0.0177 f_c'^{1.33} \qquad \text{Eq. 2-2}$$

In the study conducted by Grabois et al. (2016), the tensile strength of LWSCC was determined under direct tensile loading. Tensile strength of LWSCC was found to be improved for about 30% with the addition of steel fibers. They stated that addition of small amount of steel fibers in LWSCC could improve the tensile strength up to the first crack under direct tensile loading. Nevertheless, more study concerning the tensile strength of LWSCC is essential for it to fully replace conventional concrete in any structure.

2.2.5.3. Remark

In contrary to normal SCC, the compressive strength of LWSCC is mainly governed by the homogeneity of the batched concrete. The uniformity and homogeneity of LWSCC are governed by mixing time and procedure. As highlighted by Li et al. (2017), mixing time should not be longer than 3 minutes in order to avoid segregation. Longer mixing time can cause LWA to segregate and float at the top of concrete. Consequently, the hardened concrete has unbalanced aggregates distribution with more aggregates at the top and more cement mortar at the bottom which can result in poor compressive strength. Well distribution of aggregates throughout the matrix of concrete can maximize its compressive strength. It can be said that the strength variability of LWSCC can be related to its aggregates distribution and hence is the function of segregation resistance.

Since the mortar of LWSCC is normally stronger than LWA, the compressive strength of LWSCC is also dependent on the strength and proportion of LWA. The compressive strength of LWSCC is sensitive to changes in mix component properties and their

proportions such as water to binder ratio, binder content and the incorporation of supplementary cementitious materials. These factors must be considered properly in mix design in order to achieve anticipated workability in fresh state and compressive strength in hardened state. The optimum implementation of supplementary materials such as fly ash, slag and silica fume can improve compressive strength. In addition, the incorporation of fibres such as steel, synthetic and macro fibers will increase compressive strength of LWSCC.

2.2.6. Oil Palm Shell Concrete

2.2.6.1. Characteristic of OPS

In general, the mechanical properties of OPS concrete are greatly dependent on the physical properties of OPS itself. The specific gravity of OPS reported by several researchers is in the range of 1.17 to 1.62. The specific gravity of OPS is obviously lower than that of normal weight aggregates. Typical particle size distribution of OPS reported by researcher is shown in Table 2.3. It is noticed that the particle size distribution of OPS is in the range of 3mm to 14mm. The loose bulk density of OPS is the range of 500 to 600 kg/m^3 while compacted bulk density is in the range of 600 to 740kg/m^3. The bulk density of OPS is generally influenced by its shape and size.

As for the shape of OPS aggregate, it could take the form of irregular flaky shape, angular, circular or polygonal, depending on the extraction method. The surface texture of OPS remains fairly smooth on both sides. Rough and spiky attire can be observed at the broken part. The thickness of OPS varies from 0.15mm to 8mm.

OPS aggregate is composed of porous structure and hence it tends to have high water absorption. Depending on the oil palm tree species and OPS maturity age, the 24-hour water absorption rate can vary from 14% to 33%. Table 2.3 shows the water absorption of OPS reported by several researchers.

Since OPS has lower specific gravity and bulk density, the density of OPS concrete commonly falls in the range of 1600 to 1900 kg/m^3. However, smooth texture and irregular shape of OPS can cause poor bonding between aggregates and cement paste. The water absorption of normal weight aggregate is commonly reported as 0.5 to 1%, which is extremely low when compared to OPS. As such, when developing mix design of SCC using OPS aggregates, conventional SCC mix design method cannot be

applied to obtain the mix design for OPS based SCC. The aforementioned LWSCC mix design method which considers the effect of shape, size distribution and water absorbability will be appropriate to develop LWSCC using OPS aggregate.

Table 2.3: Physical properties of OPS

Researcher	Specific Gravity	Loose bulk density (kg/m^3)	Compacted bulk density (kg/m^3)	Water absorption (%)
Okpala (1990)	1.37	512	589	27.3
Jumaat et al. (2009)	1.37	566	620	23.8
Shafigh et al. (2016)	1.21	-	-	20
Gibigaye et al. (2017)	1.31	530	-	19.93
Farahani et al. (2017)	1.19	-	674	20.6

2.2.6.2. Workability of OPS Concrete

Several researchers (Mannan & Ganapathy, 2001; Okafor, 1988; Okpala, 1990) reported poor workability (low slump value) of OPS concrete even though high water to cement ratio was used at the earlier age. The irregular flaky shaped shape and high water absorption of OPS caused poor workability. By incorporating small amount of superplasticizer, reasonable workability can be achieved (A. M. Neville, 1995). As such, superplasticizer is used in developing OPS concrete by subsequence researchers (Mo et al., 2016; Serri et al., 2015; Shafigh et al., 2012). Similar to normal concrete, the workability of normally vibrated OPS concrete improves with increasing of water to cement ratio. However, several researchers stated low slump value not necessary can assure high compressive strength. Yew et al. (2014) studied OPS concrete with different age of OPS ranging from 3 to 15 years and the effect of OPS size on workability. The authors observed the workability of OPS improved when older OPS was used. However, the workability was degraded when the maximum aggregates size decreased from 12.5mm to 9.5mm. The authors explained that crushing process increases the irregularity shapes of OPS which can prevent the concrete to achieve full compaction. In addition, Farahani et al. (2017) reported that the inclusion of supplementary cementitious material (SCM) such as fly ash and silica fume can improve the workability of OPS concrete significantly.

From the literature review above, it can be seen that none of the researchers developed LWSCC mix design by using OPS aggregate. As mentioned above, the selection of

appropriate shape and right size gradation of OPS is crucial in obtaining workable OPS concrete. These criteria are also crucial in developing LWSCC mix design since LWSCC is greatly dependent on these characteristics.

2.2.6.3. Compressive Strength of OPS Concrete

Considerable research has been conducted on using waste (OPS) as alternative aggregates for the production of lightweight concrete in South East Asia (Alengaram et al., 2013). Much effort has been made by researchers in order to improve compressive strength of OPS concrete. Compressive strength of OPS concrete can vary with the mix proportion and curing condition. At earlier years, Abdullah (1984) designed OPS concrete with w/c ratio of 0.4 in accordance to ACI. The designated OPS concrete achieved cube compressive strength of 20MPa. Okafor (1988) concluded that concrete with compressive strength above 30MPa could not be produced by using OPS as aggregates.

Several researchers studied the method to improve the compressive strength such as chemical treatment of OPS (Chai et al., 2014; Mannan et al., 2006) and curing condition (Mannan et al., 2002; Shafigh et al., 2012). Mannan et al. (2006) carried out pre-treatment to OPS aggregates by using concentrated borate, sodium dichromate, ferrous sulphate, cupric sulphate pentahydrate, acetic acid, slaked lime and polyvinyl alcohol (PVA) solutions. The authors noticed that the concrete with OPS pre-treated with PVA solution was able to improve the compressive strength by almost 40%, which was from 23.6MPa to 32.84MPa. The authors explained that OPS pre-treated with PVA solution was able to improve the adhesion bond between OPS and cement paste. However, it will not be economical to carry out pre-treatment to OPS aggregates for industrial use. Shafigh et al. (2012) studied the effect of curing condition including continuous dry and moist skin conditions curing, no curing regime and initial water curing regimes of 2, 4 and 6 days on compressive strength. It was noticed that by reducing the w/c ratio of OPS concrete, the sensitivity in poor curing can be minimized. The authors explained that the water content in the pore of OPS could provide internal curing which resulted in enhanced hydration process, improved strength development, reduced autogenous shrinkage, reduced permeability and hence reduced sensitivity to curing.

Also, several researchers demonstrated that proper proportioned OPS concrete can achieve compressive strength above 30MPa. Shafigh et al. (2011) successfully produced high strength OPS concrete with 28-day compressive strength of 42 to 48MPa. Shafigh et al. (2012) also reported the compressive strength of 34 to 53MPa in their studies. A more recent research by Farahani et al. (2017) showed that OPS concrete with compressive strength 28 to 40MPa can be produced with binary and ternary blended cement.

Okpala (1990) stated that the compressive strength of OPS concrete is greatly dependent on the interface bonding aggregates and cement paste. Mannan and Ganapathy (2004) reported that the individual characteristics of OPS aggregate including strength, thickness and density are lower than those of granite aggregate. The authors stated that the non-uniform configuration of OPKS is one of the factors affecting its compressive strength. The authors also claimed that the compressive strength is determined by both the aggregate strength and the strength of hardened paste, and is ultimately depends on either one of them which fails first. Alengaram et al. (2011) observed that compressive strengths of OPS concrete specimens that contained mineral admixtures were higher than those without mineral admixtures. The authors stated that the infilling of pores by the mineral admixtures in general enhances the bond between the PKS and the matrix in the interfacial transition zone (ITZ). The image in Figure 2.7 shows the SEM image of mortar filling in the empty pore. It can be concluded that the compressive strength of OPS concrete is highly dependent on the bonding between (ITZ) of binder and aggregates phase.

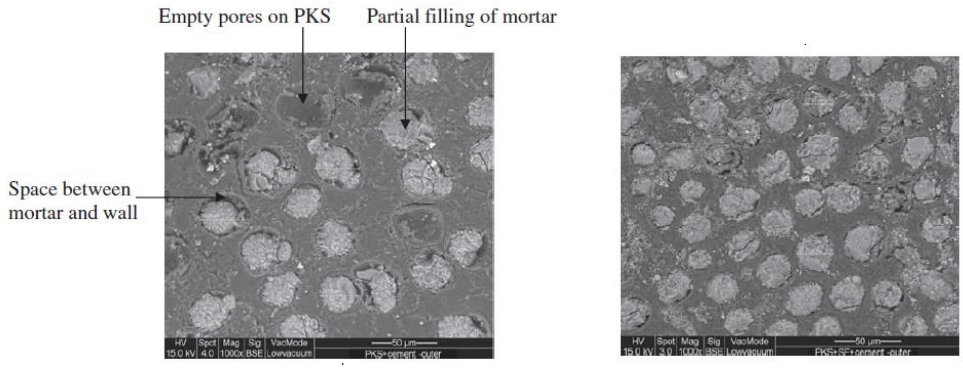

Figure 2.7: (a) Partial filling of cement mortar in pore (b) Uniform filling of mortar with mineral admixture in pore (Alengaram et al., 2011)

It is noticed that the compressive strength of concrete made of OPS aggregates are generally low. Although pre-treatment of OPS aggregates can improve compressive strength significantly, it is not economical and practical for industrial use yet. Instead of enhancing strength of OPS concrete through treatment and curing condition, the improvement of ITZ between binder and aggregates can be another option. OPS concrete is generally less sensitive to poor curing since the water present in the aggregate pore could provide internal curing. As such, only traditional curing method will be chosen for the curing of LWSCC in this research. Since the bonding of ITZ between binder and aggregates is a crucial factor for its compressive strength, SCM will be incorporated to enhance the bonding of ITZ.

2.2.7. Summary

From the review of lightweight material as coarse aggregates above, it is noted that no research work has been done for utilizing oil palm shell (OPS) as LWA in SCC. Also, very limited research has been done on the method for developing mix design of organic based LWA in LWSCC. OPS has been used as LWAC in normally vibrated concrete by many researchers but not in SCC. It is the intention of this research to develop the LWSCC mix proportion by using OPS as it (OPS) is a renewable material from agriculture waste. Close particle packing method will be used to develop the LWSCC mix design. It can provide good understanding of the amount of paste consumption required for lubricating aggregates to facilitate self-compacting ability for a given unit volume of concrete.

2.3. Load Bearing Wall Design Equation in Design Standards

2.3.1. Introduction

In this section, the current equations for designing concrete load bearing walls from the standards ACI 318, AS 3600, BS 8110 and Eurocode 2 are reviewed. These design standards provide empirical design equations to determine the load bearing capacity of axially loaded concrete wall panel. The features, as well as the associated limitations, of the equations are discussed.

2.3.2. ACI Design Equation

ACI 318-14 provides two methods for concrete wall design. The ultimate load bearing capacity of concrete wall can be determined by using either column design interaction chart in accordance to Chapter 10 of ACI 318-14 or simplified equation in Chapter 11 of the standards. ACI 318-14 provides an empirical equation to determine axial load capacity of concrete wall in Chapter 11. The simplified equation is shown as Eq. 2-3:

$$P_u = \varphi 0.55 f'_c A_c \left[1 - \left(\frac{kH}{32t}\right)^2\right] \quad \text{Eq. 2-3}$$

where k is the effective length factor for end condition support as shown in Table 2.4. Proper reduction factor can be used for compression member in accordance with Clause 21.2.1.

Table 2.4: k value for end support

k	Support condition
0.8	Wall braced against lateral translation at both ends and restrained against rotation at one or both end
1.0	Wall braced against lateral translation at both ends only
2.0	Wall not braced

In this equation, it is assumed eccentric loading is applied at the eccentricity of t/6. This equation is only applicable when minimum reinforcement ratio has been provided for the structural members and H/t or L/t must be less than or equal to 25. The reinforcement requirements are shown in Table 2.5.

Table 2.5: Minimum reinforcement of concrete wall in ACI 318-14

Bar size (mm)	f_y (MPa)	Minimum longitudinal reinforcement	Minimum transverse reinforcement
≤16	≥ 420	0.0012	0.0020
	<420	0.0015	0.0025
>16	any	0.0015	0.0025

For unreinforced concrete wall, the design load bearing capacity can be determined by using Eq. 2-4.

$$P_u = \varphi 0.45 f'_c A_c \left[1 - \left(\frac{H}{32t}\right)^2\right] \quad \text{Eq. 2-4}$$

Several limitations of the empirical design equation of ACI 318-14 are identified as follow:

i. The design equation is limited to concrete wall with planar and solid rectangular section which is used for load bearing only.
ii. The design equation is only applicable to wall which is simply supported at both the top and bottom.
iii. The design load bearing capacity can only be determined for wall with slenderness ratio up to 25. Negative capacity is resulted if the slenderness ratio is more than 25.
iv. The load is assumed to be applied at t/6 from centre of thickness. It will be conservative for load eccentricity less than t/6 and less conservative for load eccentricity greater than t/6.
v. The effect of aspect ratio is not considered in the equation. Several researchers (Ganesan et al., 2013; Saheb & Desayi, 1989) proved that aspect ratio can affect the load bearing capacity of concrete wall.
vi. The effect of elastic modulus is not considered in the equation. The elastic modulus of lightweight concrete is generally lesser than that of normal concrete due to different types of aggregate are used. Elastic modulus of concrete can greatly affect the buckling capacity of concrete load bearing wall.

2.3.3. Australian Standard Design Equation

Similar to ACI 318-14, AS 3600 also provides two approaches for the determination of concrete wall load bearing capacity. The axial load capacity can either be determined from simplified equation or by using column design interaction chart method. The equation is shown as Eq. 2-5.

$$\varphi N_u = \varphi(t_w - 1.2e - 2e_a)0.6f'_c \quad \text{Eq. 2-5}$$

where $e_a = H_{we}^2/2500t_w$

Some limitations of the AS3600 empirical design equation are identified as below:

i. The design equation is only applicable to wall which is simply supported at both the top and bottom.
ii. The design equation is only applicable for wall with slenderness ratio up to 30. Similar to ACI equation, negative capacity is resulted if the slenderness ratio is more than 30.
iii. Minimum eccentricity (e) of 0.05t must be considered. It will be conservative for load eccentricity less than 0.05t.
iv. The concrete strength (f'_c) must not exceed 65MPa.
v. Similar to ACI equation, the effect of aspect ratio is not considered in the equation.
vi. The effect of reinforcement is ignored in the equation.
vii. The effect of elastic modulus is not considered in the equation.

2.3.4. British Standard Design Equation

In BS 8110-97, different equations are provided for the determination of ultimate axial load capacity. For stocky reinforced wall, the equation is as Eq. 2-6.

$$n_w \leq 0.35 f_{cu} A_c + 0.7 f_y A_{sc} \quad \text{Eq. 2-6}$$

where n_w is the ultimate axial load per unit length of wall and f_{cu} is the characteristic compressive cube strength in MPa.

For plain concrete braced slender wall,

$$n_w = 0.3(t_w - 1.2e - 2e_a) f'_{cu} \quad \text{Eq. 2-7}$$

where $e_a = H_{we}^2 / 2500 t_w$

For, plain concrete unbraced wall,

$$n_w \leq 0.3\left(h - 2e_{x,1}\right) f_{cu} \quad \text{Eq. 2-8}$$

$$n_w \leq 0.3\left\{h - 2\left(e_{x,2} + e_a\right)\right\} f_{cu} \quad \text{Eq. 2-9}$$

where $e_{x,1}$ and $e_{x,2}$ are the resultant eccentricities at the top and bottom respectively.

The simplified equation of braced slender wall provided in BS standard is similar to that of AS 3600. The only difference is that it has lower factor value of 0.3 instead of 0.6. The simplified equation of AS 3600 is modified based on BS standard equation.

As such, BS standard equation has similar limitation to that of AS 3600. Generally, it has limitation as below:

i. The length of wall must be 4 times of its thickness
ii. Higher minimum reinforcement ratio is required for crack control
iii. A minimum eccentricity (*e*) of 0.05t or 20mm, whichever is greater, must be considered.

2.3.5. Eurocode 2 Design Equation

Eurocode 2 also provides simplified design equation to determine the load bearing capacity of concrete wall, which is shown as Eq. 2-10.

$$N_{rd} = \varphi(f'_c bh) \qquad \text{Eq. 2-10}$$

where

$$\varphi = 1.14\left(\frac{1-2e_{tot}}{h}\right) - 0.02\left(\frac{l_o}{h}\right) \leq \left(\frac{1-2e_{tot}}{h}\right)$$

where $e_{tot} = e_o + e_i$,

e_o is the first order eccentricity including any eccentricity from above floor,

e_i is additional eccentricity which consider the effect of geometrical imperfections.

The simplified design equation provided by Eurocode 2 is different from other standards. The effect of eccentricity, second order effect and creep effect are considered in a single factor, which is φ. The limitations of the Eurocode empirical design equation are identified as below:

i. The design equation is limited to concrete wall with planar and solid rectangular section which is used for load bearing only.
ii. The design equation does not take into consideration of the effects of non-linear increment of compressive strength.

2.3.6. Comparison of Design Equation

The ultimate failure load envelops of simplified design equations from standards are compared in this section. All the design equations from these standards have been expressed as design axial strength ratio for comparison as shown in Figure 2.8. It is assumed that the eccentricity is to be taken as t/6 for this comparison.

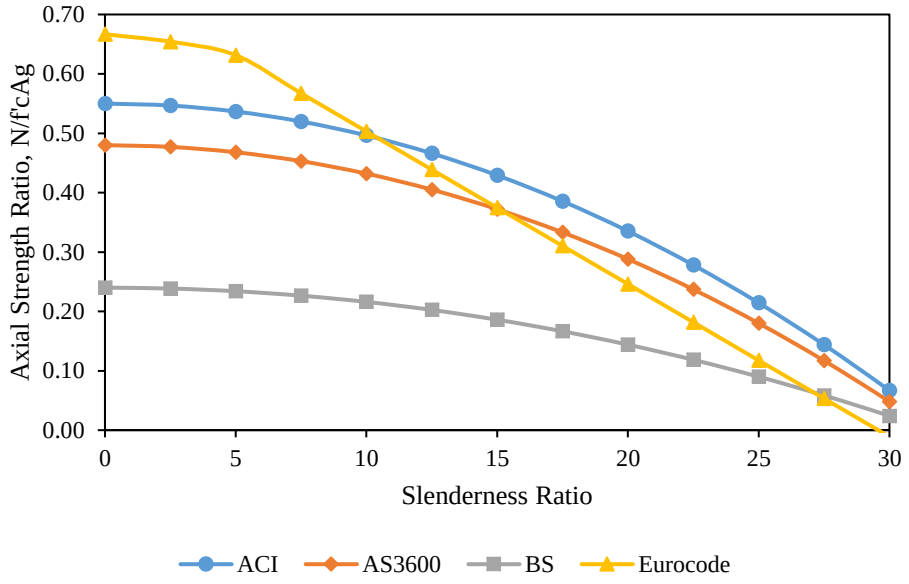

Figure 2.8: Comparison of Design Equation

It can be seen from Figure 2.8 that all the simplified design equations from standards can only calculate the ultimate load bearing capacity of concrete wall up to slenderness ratio of 30. Beyond this value, negative value is yielded since these equations are not calibrated with available data for slenderness ratio more than 30. The design equation of Eurocode 2 has higher design value envelope for slenderness ratio less than 10. Among the four design equations, ACI 318 provides the highest value for slenderness ratio of more than 10. The design equations of ACI 318 and AS 3600 have almost similar design envelopes. Among the four equations, it can be observed that British standard has the lowest design envelope since it has lower factor compared to AS 3600.

2.3.7. Remark

In summary, all the design standards provide similar guidelines for minimum reinforcement which is used for temperature and shrinkage control. The contribution of reinforcement is not considered in these equations. The design equations of ACI 318, AS 3600 and Eurocode 2 have the similar design envelopes while the design equations of British standard have the lowest and most conservative design envelope. Several researchers have argued that the ACI 318 design equation is conservative. Since ACI 318 design equation has the highest design envelope for slenderness ratio more than 10, it can be implied that all the design equations provided by the standards are conservative. All the design equations can only allow for slenderness ratio up to 30. In addition, the effects of material non-linearity including non-linear increment of

compressive strength and elastic modulus which are responsible for buckling are not considered in these equation. In this connection, all the design equations in the four standards require revision and improvement.

2.4. Research on Load Bearing Wall and Design Equation

In this section, design equations for concrete load bearing walls from the published literatures are reviewed. The experimental features from previous researchers, derived design equations as well as the associated limitations are also discussed. These semi-empirical equations are generally derived by correlating the experimental data with the equations based on scientific theory.

2.4.1. Seddon (1956)

Seddon (1956) studied the behaviour of concrete wall under concentric and eccentric loadings in one-way action. In the study, the slenderness ratio of concrete wall panels was varied from 18 to 54 and the cube strength was in the range of 13 to 35MPa. The author noticed that the concrete grade in the range of 13 to 35MPa had little effect on concrete wall panel strength. Concrete wall panel failed by crushing for slenderness ratio less than 20 while buckling failure was noticed for slenderness ratio more than 20. No significant strength reduction was observed for buckling to occur instead of crushing. When the slenderness ratio was increased from 30 to 50, no significant strength reduction was observed. The author also found that aspect ratio less than 1.5 affected the wall strength significantly for wall with slenderness ratio less than 30. The concrete wall panel could achieve compressive strength as high as cube strength when the aspect ratio was 0.75 and subjected to concentric loading. The contribution of single layer reinforcement was negligible while two layers of reinforcement, which could improve the tension failure, were more effective in increasing the wall panel strength for small eccentricity loading. The test outcome of Seddon (1956) provided the comprehensive understanding on how concrete material characteristics and geometrical factors affected the load bearing strength of concrete wall panel. These findings had been used as a framework to derive the wall design equation of British Standard in which the effect of eccentricity and additional eccentricity due to slenderness ratio were allowed for.

2.4.2. Leabu (1959)

Meanwhile, Leabu (1959) conducted theoretical study based on allowable compressive stress concept to derive an equation for concrete wall panel under concentric loading. The equation is presented as Eq. 2-11.

$$P_u = 0.2\mathrm{f'_c}\left[1 - \left(\frac{\mathrm{H}}{40\mathrm{t}}\right)^3\right] \qquad \text{Eq. 2-11}$$

This equation only takes the effect of slenderness ratio into account without considering other factors. It is noticed that the factor of this equation is extremely low which will yield very conservative result. This equation is quite similar to the early version of ACI 318 (1963) empirical equation with the exception that a higher factor of 0.225 is being used in ACI 318 (1963) equation.

2.4.3. Oberlender (1975)

Oberlender (1975) conducted a comprehensive study on 54 wall panels with slenderness ratio varied from 8 to 28 and aspect ratio from 1 to 3.5. The compressive cylinder strength of wall panels also varied from 28 to 42MPa. Minimum reinforcement ratios of 0.0033 and 0.0047 were provided for vertical and horizontal direction respectively. The wall panels were tested while hinged at both the top and bottom. They were subjected to uniformly distributed concentric loading and eccentric loading at 1/6th of wall thickness. For the wall loaded under concentric loading, the authors noticed crushing failure for wall panel with slenderness ratio less than 20 while buckling failure was observed for slenderness ratio at 28. Combinations of crushing and slight buckling were observed for slenderness ratios of 20 and 24. It was noticed that buckling failure was observed for slenderness ratio of greater than 20 when the wall panel loaded eccentrically. The authors proposed an empirical equation based on their research findings as Eq. 2-12.

$$P_u = \varphi 0.6 f'_u A_c \left[1 - \left(\frac{H}{30t}\right)^2\right] \qquad \text{Eq. 2-12}$$

2.4.4. Pillai and Parthasarathy (1977)

Pillai and Parthasarathy (1977) focused on testing of reinforced concrete wall panel with one layer of mesh embedded in its mid thickness. A total of 18 panels with slenderness ratios which ranged from 5 to 30, aspect ratios from 0.57 to 3.0 and wall thickness values of 40 to 80mm had been tested. The tests were carried out while hinged at both the top and bottom and under eccentric loading at t/6. The proposed studies were to verify the accuracy of theoretical calculation of extended column concept and empirical equation from ACI 318 (1971). The author noticed that the ultimate strength of wall panels estimated from column theory method with moment magnification as well as empirical equation were very conservative. The authors further recommended an empirical equation derived from their research results, shown as Eq. 2-13. The only difference of this proposed equation from that of ACI 318 (1971) was that the slenderness ratio term was modified to 50 instead of 40. It still has all the limitations of the later.

$$P_u = \varphi 0.57 f'_c A_c \left[1 - \left(\frac{H}{50t}\right)^2\right] \quad \text{Eq. 2-13}$$

2.4.5. Kripanarayanan (1977)

Meanwhile, Kripanarayanan (1977) conducted a theoretical analysis of reinforced concrete walls which were 200, 250 and 300mm in thickness while the reinforcement ratio was varied from 0.0015 to 0.01. The panels were load at the eccentricity of t/6. The authors proposed an empirical equation, Eq. 2-14, which consists of two functions, F_1 and F_2.

$$P_u = F_1 f'_c A_g F_2 \quad \text{Eq. 2-14}$$

where F_1=0.55 and $F_2 = \left[1 - \left(\frac{H}{32t}\right)^2\right]$.

The authors stated that substantial increase of wall capacity was observed when reinforcement ratio was increased from 0.0075 to 0.01. However, the wall axial capacity did not increase significantly with minimum reinforcement (0.0025) and therefore the contribution by reinforcement was neglected in the equation. Since the proposed F_2 did not yield realistic capacity estimation for wall with pin-ended supports, the authors recommended to include k factor in F_2 and it was modified to $F_2 =$

$\left[1-\left(\frac{kH}{40t}\right)^2\right]$. The proposed equation has been accepted by ACI in the form where the denominator of F_2 term is 32. It is incorporated in the current ACI 318 standard. The limitations of this equation were discussed in section 2.3.2.

2.4.6. Zielinski et al. (1983)

Zielinski et al. (1983) carried out an experimental study on five full scale ribbed walls under both concentric loading and eccentric loading of t/6. These wall panels were reinforced with two layers of mesh and had the geometry of 13.5 as slenderness ratio and 2.25 as aspect ratio. The authors compared the results of un-ribbed and ribbed wall and concluded that the inclusion of ribs can improve the stiffness and rigidity of wall panels. The authors proposed a design equation based on their research findings as Eq. 2-15.

$$P_u = \varphi 0.55 f'_c A_c \left[1-\left(\frac{H}{40t}\right)^2\right][1+\rho_m(m-1)] \qquad \text{Eq. 2-15}$$

The proposed equation is only applicable to the wall with slenderness ratio up to 40 and the applied load must be at eccentricity less than t/6. One of the features of the proposed equation is that the effect of reinforcement ratio is included.

2.4.7. Saheb and Desayi (1989)

Saheb and Desayi (1989) conducted a number of investigations into the effects of aspect ratio, slenderness ratio, vertical and horizontal reinforcement ratio on load bearing capacity of reinforced concrete wall under one-way action. A total of 24 samples of concrete grade 20 were studied. The slenderness ratio was varied from 9 to 27 while aspect ratio varied from 0.67 to 2. The vertical reinforcement ratio was varied from 0.0017 to 0.0085 while horizontal reinforcement varied from 0.002 to 0.005. Similar to other researchers, the wall panels were loaded at $1/6^{th}$ of wall thickness with hinges at both the top and bottom. From their research outcome, the authors concluded that the ultimate strength of wall panel decreased with increasing of aspect ratio from 0.67 to 2.0. Also, the ultimate strength of wall panel decreased non-linearly with increasing of slenderness ration from 9 to 27. The authors also found that the ultimate strength of wall panel increased linearly with vertical reinforcement ratio but the increase of horizontal reinforcement ratio had negligible effect. The authors introduced

aspect ratio effect and modified the design equations from ACI equation and Zielinski et al. (1983). The new equations are divided into two parts and are shown as Eq. 2-16 and Eq. 2-17 respectively.

$$P_u = \varphi 0.55\left[f'_c A_c + \left(f_y - f'_c\right)A_s\right]\left[1 - \left(\frac{kH}{32t}\right)^2\right]\left[1.2 - \frac{h}{10L}\right] \text{ for } \frac{H}{L} < 2 \quad \text{Eq. 2-16}$$

$$P_u = \varphi 0.55\left[f'_c A_c + \left(f_y - f'_c\right)A_s\right]\left[1 - \left(\frac{kH}{32t}\right)^2\right] \text{for } \frac{H}{L} \geq 2 \quad \text{Eq. 2-17}$$

It can be seen that reinforcement has been considered in the proposed equation and the term representing slenderness ratio effect is similar to that in ACI equation. The authors demonstrated that the proposed equations could estimate the ultimate strength of reinforced concrete wall panel conservatively by using the test data available in the published literature. However, the proposed equations can only be used for wall with the slenderness ratio up to 32 and are limited to eccentricity of t/6. It is noticed that the equations do not consider the effect of compressive strength which increases non-linearly with ultimate strength. In addition, the equations do not consider the effect of concrete with different types of aggregate which have different values of tensile strength and young modulus.

2.4.8. Fragomeni and Mendis (1996)

Sam Fragomeni and Mendis (1996) performed a series of research to study normal and high strength concrete wall panels. 16 samples were tested as one-way wall while 4 samples were tested as two-way wall at the eccentricity of t/6. The slenderness ratio was varied from 12 to 25 while aspect ratio was varied from 2 to 5. The compressive strength of concrete was in the range of 32.9 to 67.4 MPa. Minimum reinforcement was provided in both vertical and horizontal directions. From the research outcome, the author observed that wall panel of H/t less than 20 failed by crushing while wall panel with H/t equal or greater than 20 failed by buckling. Comparing the normal strength and high strength wall panels of the same dimensions, high strength concrete wall panel exhibited more brittle failure under one-way action. The authors concluded that the failure mode of reinforced concrete wall panel under axial loading is governed by the concrete strength, slenderness ratio, and the amount of reinforcement provided. By comparing the experimental results with those calculated using AS equation, the authors concluded that the implementation of AS 3600 equation was unsafe for high

strength concrete wall panel, especially when only minimum amount of reinforcement was provided. Thus, the equation underestimates the wall capacity.

The authors modified the design equation of AS 3600 by including high strength concrete parameters. The equations are shown in Eq. 2-18 and Eq. 2-19 respectively. They also incorporated an effective height factor from German Code DIN 1045 (1988) into the proposed equations in order to account for the effect of side support.

$$\varphi N_u = \varphi(t_w - 1.2e - 2e_a)0.6f_c' \text{ for} 20 \le f_c' \le 50 \quad \text{Eq. 2-18}$$

$$\varphi N_u = \varphi(t_w - 1.2e - 2e_a)35(1 + (f_c' - 50)/80) \text{ for } 50 \le f_c' \le 80 \quad \text{Eq. 2-19}$$

where

$$H_e = \beta H$$

For 3 side supported,

$$\beta = 1 \Big/ \left[1 + \left(H/_{3L}\right)^2\right] \le 0.3$$

For 4 side supported,

$$\beta = 1 \Big/ \left[1 + \left(H/_{L}\right)^2\right] \quad for\ H \le L$$

$$\beta = L/_{2H} \quad for\ H > L$$

Although the investigation was only limited to compressive strength up to 70MPa, the author stated that the proposed equation was valid for wall panel with compressive strength up to 80MPa due to the conservative approach taken and the use of proper reduction factor. Even though the effect height factor is incorporated, the proposed equation is still not applicable for wall with slenderness ratio greater than 30. Also, the effect of elastic modulus is not considered in the equation.

2.4.9. Sanjayan (2000)

Sanjayan (2000) investigated the influence of reinforcement on reinforced concrete wall panels. Four wall panels of grade 60 concrete, simply supported at the top and bottom, were tested. The loading was applied at the eccentricity of t/2. The first three walls were reinforced with a single layer of steel mesh of different reinforcement ratio while the fourth wall was reinforced with steel fibre. The authors concluded that the

amount of reinforcement provided did not have significant influence on the load capacity of wall panel. Concrete incorporated with fibre reinforcement was found to be less ductile. The authors derived a theoretical equation based on the assumption that the wall was governed by flexural cracking strength and Euler buckling theorem. The equation is indicated as Eq. 2-20.

$$P = \frac{1}{e'}(M_{cr} - M_0) \qquad \text{Eq. 2-20}$$

Where

$$e' = e - \frac{t}{6} + \frac{M_{cr}}{P_E}$$

$$M_{cr} = \frac{bt^2}{6} f_{cf}$$

2.4.10. Doh and Fragomeni (2005)

Doh and Fragomeni (2005) conducted a series of comprehensive research on normal and high strength concrete walls through both experimental and numerical modelling studies. A total of 18 wall panels were tested experimentally with 6 of them tested as one-way wall while 12 of them tested as two-way wall. All the samples were tested at the eccentricity of t/6. The slenderness ratio was varied from 25 to 40 while aspect ratio varied from 1 to 1.6. Minimum reinforcement ratio of 0.0031 was provided in both vertical and horizontal directions.

The authors proposed an empirical design equation by modifying the design equation of AS 3600 and the one proposed by Sam Fragomeni and Mendis (1996). The proposed equation Eq. 2-21 shows that wall strength does not increase proportionally with concrete strength but is represented by $f_c^{0.7}$.

$$\varphi N_u = \varphi 2 f_c'^{0.7}(t_w - 1.2e - 2e_a) \qquad \text{Eq. 2-21}$$

The authors further modified the effective height factor by introducing eccentricity parameter as below:

For wall simply supported at the top and bottom only,

$\beta = 1$ for $H/t < 30$

$$\beta = {18}/{\left({H}/{t}\right)^{0.88}} \text{ for } H/t \geq 30$$

For 4 side supported wall,

$$\beta = {\alpha}/{\left[1 + \left({H}/{L}\right)^{2}\right]} \text{ for } H \leq L$$

$$\beta = {\alpha L}/{2H} \text{ for } H > L$$

Where α is the eccentricity parameter as below,

$$\alpha = {1}/{\left(1 - {e}/{t}\right)} \text{ for } H/t < 30$$

$$\alpha = {18}/{\left[\left(1 - {e}/{t}\right)\left(\left({H}/{t}\right)^{0.88}\right)\right]} \text{ for } H/t \geq 30$$

The equation is applicable for wall with slenderness ratio greater than 30 and it accounts for the effect of side support. It also accounts for the effect of non-linear increase of wall strength with increase of concrete strength. However, the proposed equation still does not consider the effect of lightweight aggregates which give rise to reduced tensile strength and elastic modulus of concrete panels therewith manufactured.

2.4.11. Ganesan et al. (2012)

Ganesan et al. (2012) investigated the behaviour of steel fiber reinforced self-compacting concrete (SFRSCC) and steel fiber reinforced concrete (SFRC) wall panels in one-way action. A total of 16 wall samples were tested. The slenderness ratios of 12 to 30 and aspect ratios of 0.75 to 1.5 were studied. A single layer of reinforcement was provided with reinforcement ratios of 0.0088 and 0.0074 for vertical horizontal directions respectively. Loads were applied at the eccentricity of t/6. All the wall panels were tested while pinned at both the top and bottom. From their research, the authors concluded that the inclusion of steel fibers were able to improve the cracking behaviour and ductility of concrete wall. The effects of slenderness ratio and aspect ratio were similar to normal type of concrete wall. Equation Eq. 2-22 was proposed by the authors to calculate the ultimate axial strength of SFRSCC wall panels based on their experimental investigation. This equation includes the effect of slenderness ratio, aspect ratio and reinforcement ratio.

$$P_u = 0.56\left[f'_c A_g + (f_y - f'_c)A_s\right]\left[1 + \left(\frac{h}{29t}\right) - \left(\frac{H}{26t}\right)^2\right]\left[1 - \left(\frac{h}{11L}\right)\right] \quad \text{Eq. 2-22}$$

2.4.12. Ganesan et al. (2013)

For more recent research, Ganesan et al. (2013) conducted a series of test on 20 samples of reinforced normal concrete and geopolymer concrete wall panels. The slenderness ratio was varied from 12 to 21 while aspect ratio was varied from 1 to 1.875. All the wall panels were tested with pins at both the top and bottom. Loads were applied at the eccentricity of t/6. The author noticed that for the same wall geometry, geopolymer concrete wall panel exhibited more softening behaviour when compared to normal concrete wall panel. Normal concrete wall panel showed steeper slope in load versus lateral deflection when compared to geopolymer concrete wall panel. The authors explained that content of finer particles in the matrix of geopolymer concrete resulted in more ductile behaviour. Attempts were made by the authors to compare the experimental results with those calculated using design equations from the published literature. The authors concluded that these equations are very conservative in predicting the load bearing capacity of geo polymer concrete wall. The authors proposed an equation based on the experimental results to predict the load bearing capacity of both geopolymer and normal concrete wall as Eq. 2-23. Similar assumptions of Saheb were adopted in the derivation of the equation. This equation considered the parameters such as slenderness ratio, aspect ratio and reinforcement ratio. However, the accuracy of this equation is debatable since the equation is derived from only 20 samples. Case study was not conducted to compare the proposed equation with other experimental results to prove the reliability of the equation.

$$P_u = 0.59\left[f'_c A_g + (f_y - f'_c)A_s\right]\left[1 + \left(\frac{h}{40t}\right) - \left(\frac{H}{30t}\right)^2\right]\left[1 - \left(\frac{h}{18L}\right)\right] \quad \text{Eq. 2-23}$$

2.4.13. Robinson et al. (2013)

Robinson et al. (2013) conducted a series of experimental test on axially loaded concrete wall. The authors compared experimental results with calculated results using design methodologies and noticed that the existing design methodologies were very conservative. The authors proposed a new model based on lumped plasticity and it is known as semi-empirical and semi-probabilistic DAT (Design Assisted by Testing). The proposed equation is shown as Eq. 2-24.

$$P_u = \frac{1}{2}\left[\frac{10}{e} - \frac{\lambda}{100e} - 4 \times 10^{-4}\lambda^2\right] f'_c A_g \qquad \text{Eq. 2-24}$$

where e is eccentricity and λ is slenderness ratio.

2.4.14. Huang et al. (2014)

Huang et al. (2014) performed a series of experimental and numerical studies on the load bearing capacity of high strength concrete wall panel. The researchers varied load eccentricity (t/12, t/6, and t/3), slenderness ratio (17, 21, and 27) and vertical reinforcement ratio (0.00164-0.00592). It was found that all high strength concrete wall panels had responded non-linearly because of their geometric and material nonlinearities. The author observed that concrete wall with low reinforcement ratio failed by fracture in the middle height after certain degree of buckling. However, for wall with higher vertical reinforcement ratio i.e. 0.00592, the wall samples failed by buckling in the middle height instead of fracture. This showed that the minimum reinforcement ratio prescribed by both AS 3600 and ACI 318 required further investigation in order to ensure some post peak ductility of high strength concrete wall panel. It was also found that for high strength concrete, there is a limit in increasing the concrete buckling strength by increasing the vertical reinforcement ratio. For general findings, the strength of the high strength concrete wall panel is significantly affected by the load eccentricity and the slenderness ratio. The authors also compared their experimental results with those calculated from column design method and simplified equations from standard. The author concluded that the approaches from design standards were conservative since they do not consider the effect of material non-linearity. Smeared cracking approach and non-linear analysis were adopted by the authors to model and carry out parametric study on high strength concrete wall. However, the authors did not propose any improved design equation to determine the load bearing capacity of concrete wall panel.

2.4.15. Remark

All these studies provide important insights into the development of reinforced concrete load bearing wall and its design equation. The limitations of all the design equations are summarized in Table 2.6. It is noticed that most of the research is concentrated on normal and high strength concrete walls. Hence, there is limited research on axial behaviour of lightweight concrete wall. It is also noted that majority

of the researchers prefer to modify or derive the design equation based on ACI equation. These researchers concentrated on modifying the factors to account for geometric effects, which are slenderness ratio and aspect ratio. However, it is obvious that these simplified equations have not taken into consideration of all the material non-linearity effects. Further improvement of simplified equation can be made through the consideration of factors such as non-linear compressive strength increment, elastic modulus and tensile splitting strength of concrete.

Table 2.6: Limitations of design equations

Researchers	Derivation Approach	Concrete Used for Derivation	Limitations
Leabu (1959)	ACI	Normal concrete	○ Slenderness ratio up to 40 ○ Conservative ○ No consideration of eccentricity, elastic modulus and compressive strength non-linearity
Oberlender (1975)	ACI	Normal concrete	○ Slenderness ratio up to 30 ○ Conservative ○ No consideration of eccentricity, elastic modulus and compressive strength non-linearity
Pillai and Parthasarathy (1977)	ACI	Normal concrete	○ Slenderness ratio up to 50 ○ Conservative ○ No consideration of eccentricity, elastic modulus and compressive strength non-linearity
Kripanarayanan (1977)	ACI	Normal concrete	○ Slenderness ratio up to 32 ○ Conservative ○ No consideration of eccentricity, elastic modulus and compressive strength non-linearity
Zielinski et al. (1983)	ACI	Normal concrete	○ Slenderness ratio up to 40 ○ Conservative ○ No consideration of eccentricity, elastic modulus and compressive strength non-linearity
Saheb and Desayi (1989)	ACI	Normal concrete	○ Slenderness ratio up to 32 ○ Conservative ○ No consideration of eccentricity, elastic modulus and compressive strength non-linearity
Sam Fragomeni and Mendis (1996)	AS	Normal and high strength concrete	○ Slenderness ratio up to 30 ○ Conservative ○ No consideration of elastic modulus and compressive strength non-linearity

(Contd.)

Researchers	Derivation Approach	Concrete Used for Derivation	Limitations
Sanjayan (2000)	Euler buckling theorem	Not specified	○ Equation is not properly calibrated
Doh and Fragomeni (2005)	AS	Normal and high strength concrete	○ No consideration of elastic modulus
Ganesan et al. (2012)	ACI	Steel fiber reinforced concrete	○ Slenderness ratio up to 40 ○ Conservative ○ No consideration of eccentricity, elastic modulus and compressive strength non-linearity
Ganesan et al. (2013)	ACI	Normal and geopolymer concrete	○ Slenderness ratio up to 40 ○ Conservative ○ No consideration of eccentricity, elastic modulus and compressive strength non-linearity
Robinson et al. (2013)	Statistical method	Normal concrete	○ Slenderness ratio up to 40 ○ Equation is not properly calibrated ○ No consideration of elastic modulus and compressive strength non-linearity

2.5. Finite element analysis

Finite element analysis (FEA), being a powerful numerical analysis tool, has been popularly used to study and predict the performance a structure. Once FEA has been validated by using experimental results, it can be effectively used to replace laboratory tests in research field in view of time and cost savings it can bring. There are several attempts (Ho & Doh, 2018; Lechner & Fischer, 2015; Mohamad et al., 2017) to model the axial behaviour of concrete wall by using finite element analysis technique. To date, limited research has been conducted in utilizing lightweight concrete for load bearing wall. Even more limited research has been carried out to model lightweight concrete load bearing wall. In this section, relevant literature related to the finite element modelling of concrete wall under axial load is reviewed. Literature review is carried out based on concrete material modelling, concrete- steel reinforcement interface and the element type.

2.5.1. Concrete Modelling

Researchers usually utilise ABAQUS FEA software in concrete modelling. In ABAQUS FEA software, three types of constitutive modelling techniques are available for modelling concrete structure, which are concrete smeared cracking (CSC), brittle cracking and concrete damaged plasticity (CDP). Similar modelling techniques are also available in other FEA software.

2.5.1.1. Concrete Smeared Cracking Model

Concrete smeared cracking (CSC) model was developed based on the research work of Kupfer et al. (1969), Hillerborg et al. (1976) and Crisfield (1986). This model was primary developed for monotonic straining of concrete structure at low confining pressures. The CSC model is a general model that describes the tensioning stiffening and compressive strain hardening effects of the concrete. There is limited research on using this model to predict the behaviour of axially loaded member.

CSC model has been used by Claeson and Gylltoft (1998) to model the axial behaviour of slender high strength concrete (HSC) column under eccentric loading. The authors demonstrated that CSC model was able to predict the behaviour of HSC column satisfactorily with percentage of error within 10%, as shown in Figure 2.9. However, FEA results tend to predict stiffer behaviour in the initial loading zone.

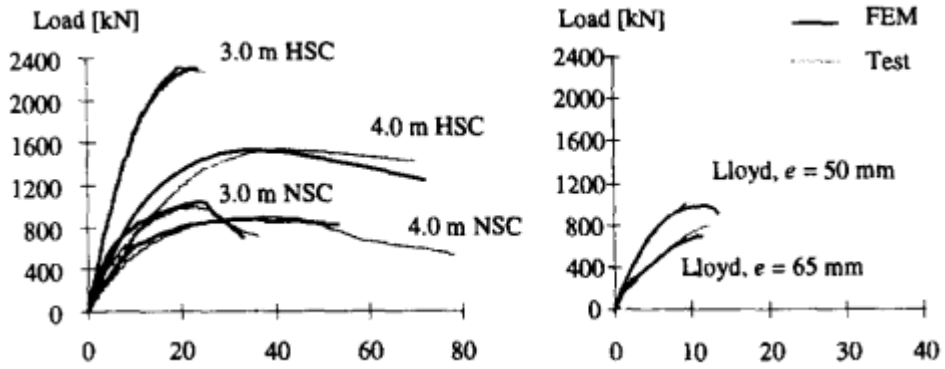

Figure 2.9: Comparison of Finite Element Results with experimental results (Claeson & Gylltoft, 1998)

Huang et al. (2014) applied CSC model in modelling HSC concrete wall panels under axial loading. Arc-length method has been used to determine the buckling point in order to complete nonlinear equilibrium in their analysis. It was observed that the

proposed model is able to predict the behaviour of HSC wall accurately as shown in Figure 2.10. The authors also conducted a series of comparison between their modelling results and experimental results in the literature (Sam Fragomeni & Mendis, 1996; Saheb & Desayi, 1989). The authors demonstrated that the proposed model was able to predict the capacities of concrete wall panels from the published literatures. The mean and standard deviation of normalized FEA to experimental failure load ratios are 0.985 and 0.126 respectively.

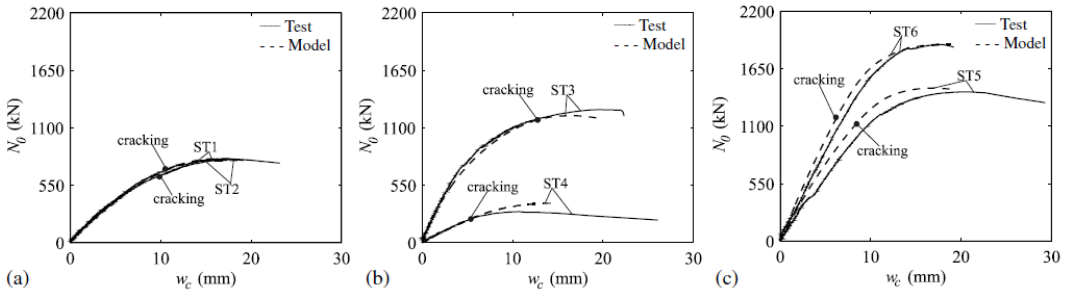

Figure 2.10: Comparison of finite element results and experimental results (Huang et al., 2014)

Lechner and Fischer (2015) adopted CSC, along with implicit solver in modelling the axial behaviour of ultra-high strength concrete (UHSC) wall. The authors demonstrated that CSC model is capable of capturing the cracking and failure of UHSC wall as illustrated in Figure 2.11.

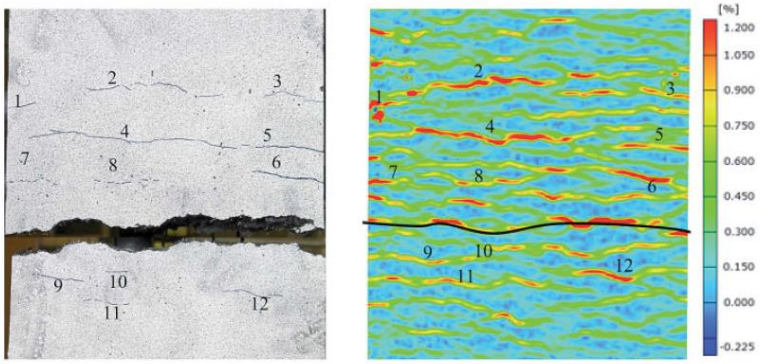

Figure 2.11: Comparison of experimental and FEA model failure mode (Lechner & Fischer, 2015)

2.5.1.2. Brittle Cracking Model

Brittle cracking model is another model available in ABAQUS which is based on the research by Hillerborg et al. (1976). This model is developed for concrete structure whereby its behaviour is dominated by tensile cracking without considering the effect of compressive strain failure. The compression behaviour is assumed to be linear in this model. Thus, this model is not suitable for axially loaded concrete structure in which the compressive failure is the main concern. Axially loaded slender structural member requires a model that can capture both the tensile and compressive failure modes.

2.5.1.3. Concrete Damaged Plasticity

Concrete Damaged Plasticity (CDP) is one of the available options in ABAQUS software which has been widely used by researcher to model the behaviour of concrete structure. CDP implements the concepts of isotropic damaged elasticity which is combined with isotropic tensile and compressive plasticity to depict the inelastic behaviour of concrete. This model is constructed for concrete that will be loaded by monotonic, cyclic, or dynamic loading under low confining pressures.

Mohamad et al. (2017) modelled foam concrete of sandwich wall by using CDP model and explicit solver. The authors adopted the material parameters of CDP model and the values of parameter used are reproduced in Table 2.7. It is clear that the authors did not adopt the default values for CDP model. Viscosity value of 0 can cause convergence issue if implicit solver is used. The authors demonstrated that their model was able to capture the failure mode as illustrated in Figure 2.12. However, the model could not capture well the load-lateral deflection behaviour as shown in Figure 2.13. FEA model tended to exhibit stiffer behaviour at linear elastic region while it showed softer behaviour in plastic region and finally overlapped with experimental results at ultimate load.

Table 2.7: CDP material parameters of (Mohamad et al., 2017)

Parameters	Values
Dilation angle	30°
Eccentricity	1
Initial biaxial/uniaxial ratio, σ_{c0}/σ_{b0}	1.12
K_c	1
Viscosity	0

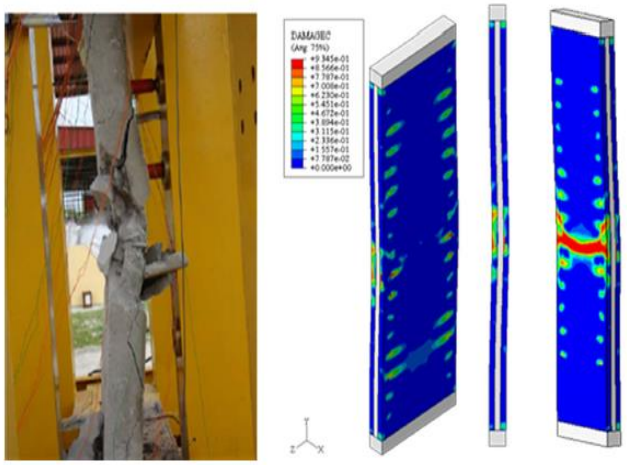

Figure 2.12: Failure mode of FEA model (Mohamad et al., 2017)

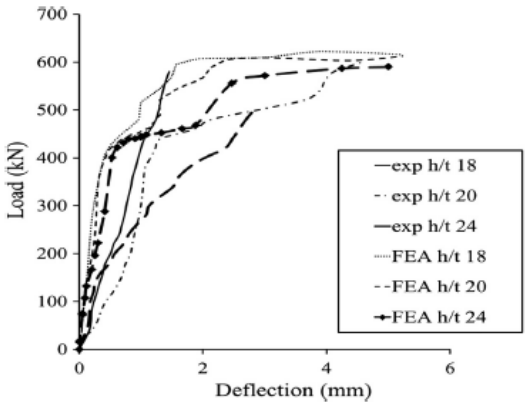

Figure 2.13: Load versus lateral deflection (Mohamad et al., 2017)

Ho and Doh (2018) modelled the behaviour of axially loaded medium strength concrete wall under one-way and two-way actions, with three sides supported. CDP model and modified Riks method were adopted in their model. The default CDP parameters are used as shown in Table 2.8. The authors demonstrated that the proposed model was able to capture the failure mode of concrete wall panel under one-way

action, as shown in Figure 2.14. However, the authors did not present their load-deflection curve.

Table 2.8:CDP material parameters of (Ho & Doh, 2018)

Parameters	Values
Dilation angle	31°
Eccentricity	0.1
Initial biaxial/uniaxial ratio, σ_{c0}/σ_{b0}	1.16
K_c	0.667
Viscosity	0.0001

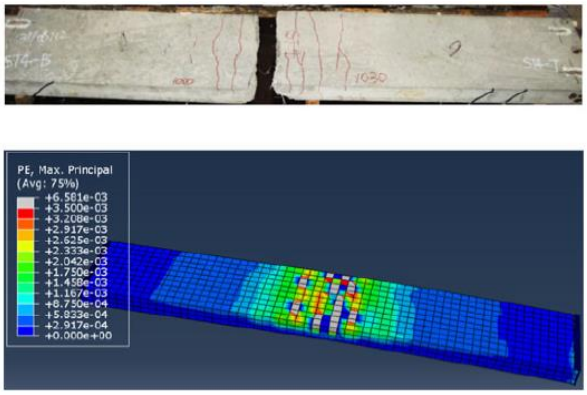

Figure 2.14: Failure mode of FEA model (Ho & Doh, 2018)

2.5.1.4. Remark

Among the three types of model, it is clear that brittle cracking model is not suitable to assess the axial behaviour of concrete structure. Even though some researchers demonstrated that CSC was able to model the axial behaviour of concrete structure, several others (Fanning & Kelly, 2000; Gamino et al., 2010; Liao & Huang, 2018) commented that concrete smeared cracking model works best for flexural concrete structure such as beam under monotonic loading. By comparing CSC and CDP models, CDP is capable to model both monotonic and cyclic loading and also to trace the crack pattern progress through the entire loading history while CSC cannot do so. The literature review above demonstrates that CDP is capable of capturing the axial behaviour of concrete structure. Thus, CDP model is chosen for modelling of axially loaded lightweight concrete wall in this research.

2.5.2. Steel Reinforcement Modelling

The proper definition of interaction between steel reinforcement and concrete material is one of the crucial factors in developing a realistic concrete model. Generally, there are three methods for modelling the bond between steel reinforcement and solid concrete element in three dimensional analyses, which are discrete, embedded and smeared techniques. For discrete method, steel reinforcement can be modelled as truss or beam element and it is connected to concrete mesh nodes as stringers, forming the common nodes between reinforcement and concrete elements. In application, the limitation of the discrete model is that the mesh is restricted by reinforcement location. Full bond between reinforcement and concrete is generally assumed.

As for embedded method, the stiffness of reinforcement elements is determined independent of concrete elements. However, the reinforcement element is embedded into concrete mesh so that its displacements are compatible with surrounding concrete elements. It can create bonds regardless of the establishment of a mesh between elements. This method assumes a perfect bond interaction of the reinforcement with the concrete. Also, the bond slip effect is allowed for in the tension-stiffening model. This method is suitable for concrete structure where its reinforcement is complex whereby the computational time can be reduced.

Smeared method creates a composite layer of steel reinforcement by uniformly distributing reinforcement over the concrete surface. Composite theory is used to construct the properties of material model in the element from individual properties of concrete and reinforcement. For large structural models in which reinforcement details are not essential to capture the overall structure response, this technique is generally applicable.

Among these three methods, embedded method will be chosen for modelling the reinforcement of concrete load bearing wall in this research. This method is generally more computationally efficient by assuming perfect bonding between concrete and steel reinforcement while taking into consideration of its contribution to axial strength. This method has been used by many researchers in modelling concrete structure.

2.6. Concluding Remark

Chapter 2 presents literature review of LWSCC material, design equation of axially loaded concrete load bearing and finite element analysis. Lightweight self-compacting concrete is an innovative material to be used for concrete structural application. Most of the current research done on LWSCC is restricted to a few types of lightweight aggregates only. Furthermore, there is limited research on utilizing oil palm shell as lightweight coarse aggregates for manufacturing LWSCC. Many researches have proven that OPS is a potential alternative material to be used as coarse aggregates in concrete. In the published literature, there are a few established procedures which are based on close aggregate packing method for producing LWSCC. However, the applicability of these procedures on OPS to develop LWSCC mix is still unknown. Thus, there is a need to develop the mix design and study the properties of LWSCC incorporated with OPS.

From the review of the published literatures on axially loaded concrete walls, it is noticed that the research has concentrated on medium strength and high strength concrete. Limited research is being carried out on axially loaded lightweight concrete wall panel. The majority of the researchers have concentrated on modifying the factors to account for geometric effect and high strength concrete. However, none of the researchers has derived design equation for lightweight concrete wall. The existing simplified design equations provided in the design standards ACI 318, AS 3600, Eurocode 2 and British Standard have the similar design envelopes. However, several researchers demonstrated that these design equations are conservative for designing slender concrete walls. It is difficult for such simplified equation to account for the nonlinear behaviour of axially loaded concrete wall panel.

Due to different types of aggregates used in concrete, lightweight concrete generally has different and lower value of elastic modulus for the same compressive strength concrete. Therefore, the material nonlinear characteristics of concrete such as non-linear compressive strength increment and material elastic modulus have to be considered in developing the wall design equation. The study presented herein aims to develop simplified design equations that will consider the aforementioned parameters.

In order to save time and cost, finite element analysis can be widely used as an alternative to laboratory tests in research field. Relevant literature review has been

carried out on the subject as it is used to model the axially loaded concrete wall. To facilitate this research, ABAQUS FEA software is used.

3. Mix Design Development

3.1. Introduction

This Chapter presents a detailed account of the engineering properties of materials used in the study, the test methodology, development and resulting properties of lightweight self-compacting concrete mix design incorporating oil palm shell as full replacement of coarse aggregates. In the research, close particle packing method is adopted as the procedure to obtain the control LWSCC mix design. Subsequently, concrete samples with fly ash replacement levels of 30%, 40% and 50% were casted and then compared to the control mix design. All the tests were carried out in accordance with respective standard procedures. The resulting fresh and hardened concrete properties results were analysed and discussed. Fresh properties including filling ability, passing ability and segregation resistance were assessed against EFNARC (2002) requirements. The hardened properties of concrete such as compressive and tensile strengths were evaluated at 7-day, 28-day and 90-day ages. SEM and EDX analyses were carried out to evaluate the quality of interfacial transition zone. Water absorption and heat resistance were also assessed.

3.2. Materials and Experimental Programme

3.2.1. Materials

3.2.1.1. Ordinary Portland cement (OPC)

Ordinary Portland Cement (OPC) grade 45, conforming to ASTM: C150/C150M-12, is used. The Blaine fineness of cement is 3510cm^3/g. The specific gravity and particle density are 3.14 and 2950kg/m^3 respectively. The material chemical composition is shown in Table 3.1.

3.2.1.2. Fly Ash

The fly ash used in the experiment was obtained from a coal-fired power station in Sejingkat, Kuching and was classified as Class F low calcium fly ash as specified in ASTM C618. The coal was supplied by the coal mine in Merit Pila, Kapit, Sarawak, Malaysia. The material chemical composition is also shown in Table 3.1.

Table 3.1: Chemical properties of cement and fly ash

Chemicals	Cement (%)	Fly Ash (%)
Silicon dioxide (SiO_2)	20.0	57.8
Aluminium oxide (Al_2O_3)	5.2	20.0
Ferric oxide (Fe_2O_3)	3.3	11.7
Calcium oxide (CaO)	63.2	3.28
Magnesium oxide (MgO)	0.8	1.95
Sulfur trioxide (SiO_3)	2.4	0.08
K_2O	-	3.88
TiO_2	-	2.02
Na_2O	-	0.30
Loss on ignition	2.5	0.32

3.2.1.3. Coarse Aggregates

Oil palm shell (OPS) was used as coarse aggregates in this research. OPS was obtained from a palm oil mill in Lambir, Miri-Bintulu, Sarawak, Malaysia. The particle size distribution of OPS and physical properties are shown in Figure 3.1 and Table 3.2 respectively. 60% of OPS size fell within the range of 5mm to 10mm. They were washed and sieved. All the OPS were submerged in water for 24 hours. Subsequently, OPS were allowed to air dry in laboratory in order for them to achieve saturated surface dry (SSD) condition before concrete mixing.

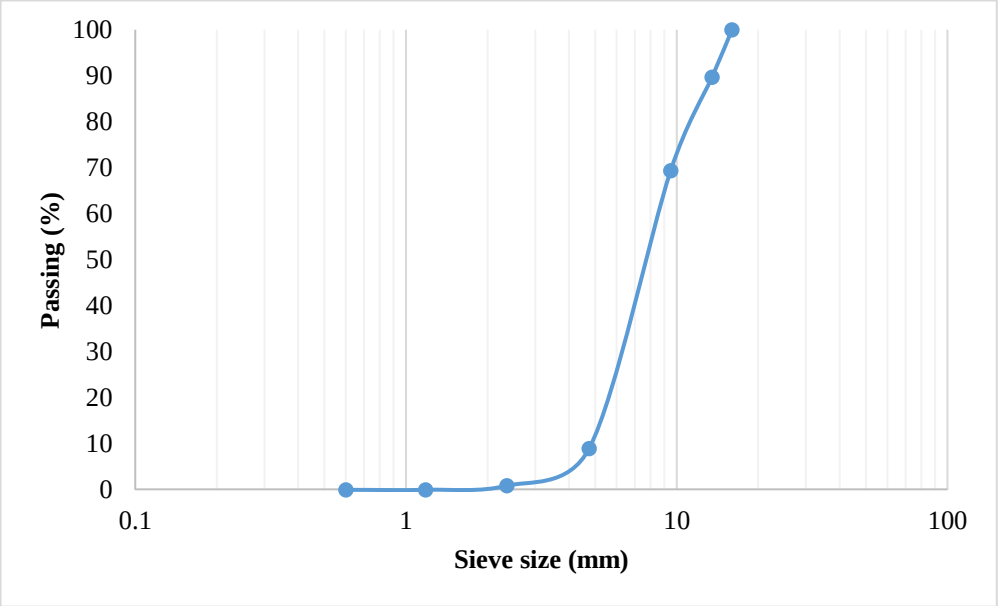

Figure 3.1: OPS particle size distribution

3.2.1.4. Fine Aggregates

Natural river sand and crushed OPS were used as fine aggregates. Crushed OPS used were in the size range of 600μm to 5mm and river sand with nominal size of 600μm. The physical properties of two fine aggregates are shown in Table 3.2.

Table 3.2: Physical properties of aggregates

Physical Property	River Sand	OPS
Specific gravity	2.64	1.19
Fineness modulus	1.32	5.31
Water absorption (24h) (%)	1.1	18.11

3.2.1.5. Superplasticizer

A high range water reducing admixture, Glenium Ace 389, was used in this research. It was supplied by BASF (Malaysia) Sdn. Bhd. According to ASTM C494 and BS En 934-2 European Standard, it is categorized as type F and is capable of reducing the amount of water required for concreting by 12% or more.

3.2.2. Mixing Method

For concrete mixing, forced action cylindrical pan mixer with a vertical axis of rotation was used. LWSCC mix in the amount of about $0.07m^3$ was produced for each batch. An optimum mixing procedure was selected among a number of different mixing procedure. The mixing procedure started by putting all the aggregates into the pan and running the mixer for 1 minute. Then, cement and fly ash were added and the mixing was allowed for another 2 minutes until all the materials were well blended. Next, half of the required amount of water was added slowly to the pan and the mixing continued for another 1 minute. The SP and another half amount of water were then gradually added and mixing continued for further 1 minute.

3.2.3. Test on Fresh Properties

Three fresh concrete properties including filling ability, passing ability and segregation resistance were assessed immediately after the concrete mixing. These tests were carried out in accordance to the standard procedure EFNARC (2002). The proposed tests to evaluate the filling ability in this research were slump flow and V-funnel. The passing ability was assessed by J-ring test while segregation resistance was assessed

through Sieve Segregation Test and Visual Stability Index (VSI). The detailed methodology to carry out all these fresh properties test was depicted in the following section.

3.2.3.1. Slump Flow

Slump flow test was proposed to assess the filling ability. Abram's slump cone with base diameter of 200mm and 300mm in height was used for slump flow test. The testing apparatus is shown in Figure 3.2. Slump flow test was carried out by filling the slump cone and the cone was then lifted vertically to allow concrete to flow freely. The maximum uninterrupted flow diameters in two orthogonal directions were then measured after the flow had stopped. The time for LWSCC to flow 500mm diameter circular spread was also noted as T_{500}. The slump flow diameter was then calculated by using Eq. 3-1.

$$S = (d_{max} + d_{perp})/2 \qquad \text{Eq. 3-1}$$

where S is the slump value (mm), d_{max} is the maximum spread value (mm) and d_{perp} is the spread value perpendicular to the maximum spread.

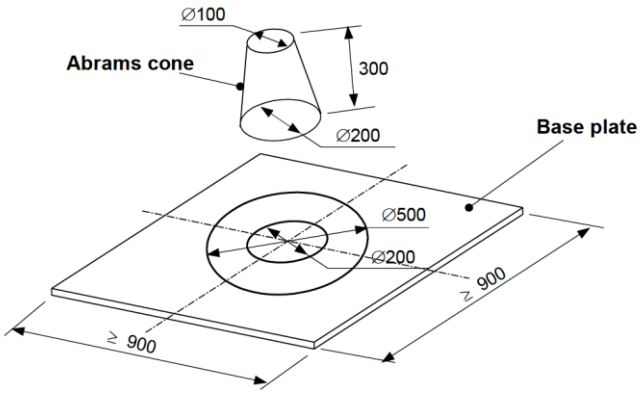

Figure 3.2: Slump flow apparatus

3.2.3.2. V-funnel Test

V-funnel tests were also carried out to evaluate both the viscosity and filling ability of concrete. V-funnel test apparatus is shown in Figure 3.3. The shape of V-funnel restricts the flow of concrete and it requires about 12 litres of concrete to perform the test. The V-funnel was set on steel stand with bracing. Once concrete mixing was completed, the fresh concrete was poured into the V-funnel with trap door closed at

the bottom side. The trap door was opened after 10 seconds of filling the V-funnel. The test was repeated for 5 minutes after filling of V-funnel. The respective values of time required for fresh LWSCC to completely flow through the trap door of V-funnel were recorded as T_{10s} and T_{5min}.

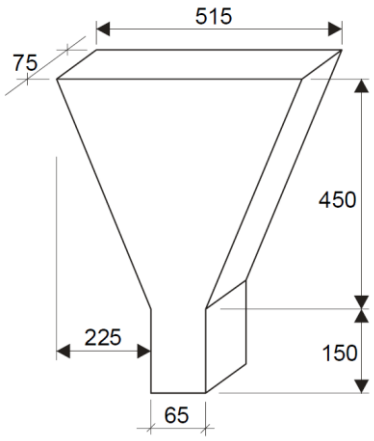

Figure 3.3: V-funnel apparatus

3.2.3.3. J-ring Test

Passing ability was evaluated through J-ring test. J-ring test was proposed to measure the blockage of LWSCC due to the presence of steel reinforcement bars. J-ring test apparatus is illustrated in Figure 3.4. The test was carried out by placing the J-ring around the slump cone, filling of concrete in slump cone and lifting it to allow concrete pass through the reinforcement. The maximum spread, $T_{500\,(J-Ring)}$, and the height difference between the centre (h_1) and outside of the ring (h_2) were measured. Block step value (S_H) can be calculated by using Eq. 3-2.

$$S_H = average(h_1 - h_2) \qquad \text{Eq. 3-2}$$

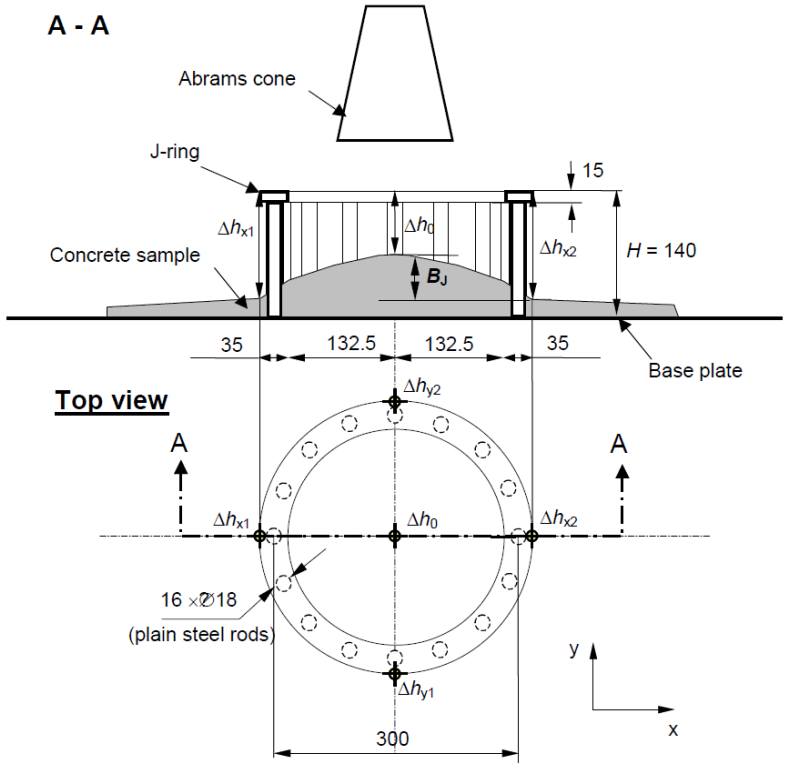

Figure 3.4: J-ring apparatus

3.2.3.4. Sieve Segregation Test

Sieve segregation test was used to assess concrete segregation resistance. The test began by allowing the mass of fresh concrete to stand still in a container for 15 minutes. The mass of pan was then measured as W_p on weighing balance. The actual mass of LWSCC used was recorded as W_c. It was then poured into sieve and allowed to pass through a sieve with an aperture of 4.75mm for 2 minutes. The weight of sieved portion was then recorded as W_{ps}. This value was then expressed as the percentage of total weight of LWSCC used by using Eq. 3-3.

$$\Pi = (W_{ps} - W_p)/W_c \times 100 \qquad \text{Eq. 3-3}$$

3.2.3.5. Visual Stability Index Test

Visual stability index (VSI) test was carried out by visual inspection of LWSCC before and after performing slump flow tests. The index values varied from 0 to 3. However, this method is highly dependent on the experience of the individual to evaluate segregation. The VSI criteria is shown in Table 3.3.

Table 3.3: VSI criteria

VSI value	Criteria
0	No evidence of segregation or bleeding.
1	No evidence of segregation and slight bleeding observed as a sheen on the concrete mass.
2	A slight mortar halo (≤ 10 mm) and/or aggregate pile in the centre of the concrete mass.
3	Clearly segregated by evidence of a large mortar halo (≥ 10 mm) and/or a large aggregate pile in the centre of the concrete mass.

3.2.4. Test on Hardened Properties

3.2.4.1. Strength Test

Concrete cube specimens with size of 100x100x100mm were casted and prepared which would be tested for compressive strength. Cylinder specimens of 100mm diameter and 200mm height were prepared and used for splitting tensile test. The fresh concrete after mixing were poured into two respective types of mould immediately after fresh concrete slump flow test. All the LWSCC specimens were allowed to self-compact without the aid of vibrator. The concrete specimens were demoulded after 24 hours of casting and cured in water until the day of testing. All the cubes and cylinders were tested by using 600kN capacity GOTECH universal testing machine. The compressive strength test was conducted in accordance with the standard procedure described in ASTM C39-18 and BS 1181-116 for cylinder and cube respectively. The method prescribed by Norma (2004) was used to carry out splitting tensile strength test.

3.2.4.2. Density

The relevant values of concrete density were determined when it was demoulded, air-dried and finally oven-dried. The demoulded density of concrete samples was determined immediately after the removal of concrete mould. The air-dry density was determined after the demoulded sample had been air dried. Oven-dry density of LWSCC was determined through the test prescribed in ASTM C567-14. The apparent mass of cylinder (G) was measured when it was completely submerged in water. The cylinder was allowed to air dry for 1 minute and the surface water was wiped with absorbent cloth. The mass was then recorded as saturated surface-dry cylinder (F). Concrete samples were then placed in an oven and continually weighted until there

was minimal change in the weight. The final weight recorded under room temperature was mass of oven-dry cylinder (D). The Oven-dry density can be calculated by using Eq. 3-4.

$$O_m = (D \times 997)/(F - G) \quad \text{Eq. 3-4}$$

3.2.4.3. Immersed Water Absorption

Immersed water absorption test was carried out in accordance to the procedure prescribed in ASTM C642-13. In the experiment, the prepared sample was weighted and then allowed to oven dry at 110°C for 24 hours. The sample was weighted again at room temperature after oven drying process. If the difference between two successive measured weights was more than 1g, oven drying process had to be repeated until the difference was less than 1g. This value was recorded as M_1. The sample was then immersed into water for 48 hours. After the immersion, the concrete surface was wiped by using absorbent cloth. The mass was recorded as M_2. The water absorption was calculated by using Eq. 3-5.

$$Water\ absorption = (M_2 - M_1)/M_1 \times 100 \quad \text{Eq. 3-5}$$

3.2.4.4. Strength under Elevated Temperature and Mass Loss

Concrete cube specimens were tested for compressive strength at 28-day and 90-day age. Similar heating method of Pathak and Siddique (2012) was adopted for this research. All the specimens were heated at a rate of 1°C/min up to specified temperature of 100,200 and 300°C. After the oven reached the specified temperature, the heating of specimens was continued for 1 hour in order to ensure uniform heating. All the specimens were allowed to cool at room temperature after 1 hour heating. The specimens were tested at room temperature for compressive strength in accordance to ASTM C39-18 procedures.

The mass loss test was to study the dehydration process of cement paste. The measurement of mass of each specimen was taken before and after heating. Prior to taking mass measurement, the specimens ought to achieve saturated surface dry condition in which all the pores were saturated and there was no film of water on surface.

3.3. LWSCC Mix Design

Currently, there is no standardized method for the mix design of LWSCC. Thus, particle packing method, which was originally proposed by Kanadasan and Razak (2014), was adopted to initiate the laboratory work. This method assumed that the voids between aggregates particles are filled by paste. Figure 3.6 shows the overall mix design procedure.

3.3.1. Particle Packing Method

Particle packing (PP) is defined as volume of packed aggregate particles in a unit volume (Glavind & Pedersen, 1999). The study is targeted at determining suitable LWSCC mix design method. The method recommends that PP test has to be carried out first. All the aggregates are pre-soaked in water for 24 hours and allowed to air dry till saturated surface dry condition (SSD) is achieved. Fixed amounts of fine and coarse aggregates are prepared in a known volume container. The aggregates are mixed thoroughly so that they are well-blended. A known volume of water is added until the water level covers the top surface of container, as illustrated in Figure 3.5. The total amount of voids can be found from the amount of water used which represents the amount of paste required for LWSCC. The PP ratio can be obtained by subtracting the void ratio from container volume.

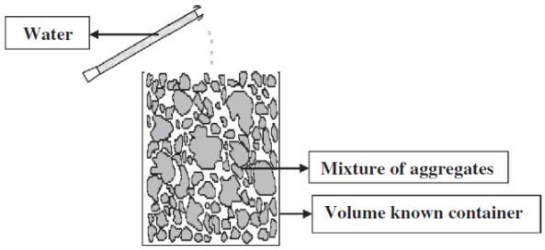

Figure 3.5: PP Test Illustration (Kanadasan & Razak, 2014)

3.3.2. Mix Design Algorithm

The procedures to determinate the LWSCC mix design is presented in this section.

Step 1: Determination of particle packing factor

The first step in proportioning LWSCC mix, which incorporates OPS as full coarse aggregates replacement, is to determine the particle packing factor between the

blended OPS as coarse aggregates and river sand as fine aggregates, using Eq. 3-6. The voids represent the minimum volume of paste required to lubricate the aggregates in order to produce flowing and filling ability of LWSCC (Kanadasan & Razak, 2014). A low PP ratio signifies that more paste is required to fill the porous voids of OPS aggregates. In contrast, a high PP ratio denotes that aggregates are tightly packed and a less amount of paste is required. The PP value is determined based on the procedure described in previous section.

$$PP = 1 - e \qquad \text{Eq. 3-6}$$

where PP is particle packing value and e is void ratio

Step 2: Calculation of aggregates content

The aggregate content of proposed LWSCC mix design can be determined from Eq. 3-7. The subscript of f/c agg in each term represents respective type of aggregate used and the ratio of each aggregate to total aggregates in a unit volume of LWSCC has been considered. The main concern of aggregates in this research is sand as fine aggregate and OPS as coarse aggregate. The optimum ratio of each aggregate to total aggregates was determined from the blended aggregates bulk density curve.

$$\mathrm{W_{f/c\ agg}} = \mathrm{PP} \times \mathrm{AR_{f/c\ agg}} \times \mathrm{SG_{f/c\ agg}} \times 1000 \qquad \text{Eq. 3-7}$$

where $\mathrm{W_{f/c\ agg}}$ is aggregate content (kg/m^3), $\mathrm{AR_{f/c\ agg}}$ is ratio of aggregate to total aggregates in volume and $\mathrm{SG_{f/c\ agg}}$ is specific gravity of aggregates.

Step 3: Calculation of cement content

Cement content must be chosen properly to ensure the concrete fresh properties as a SCC including filling ability, passing ability and segregation resistance fulfil the specified requirements while not to compromise the compressive strength. Good adjustment of cement content will ensure sufficient amount of cement paste is available to lubricate aggregates so as to attain self-compacting ability. The volume of cement can be determined using Eq. 3-8.

$$\mathrm{V_{cement}} = \mathrm{W_{cement}}/\mathrm{SG_{cement}} \qquad \text{Eq. 3-8}$$

where $\mathrm{V_{cement}}$ is volume of cement, $\mathrm{W_{cement}}$ is cement content (kg/m^3) and $\mathrm{SG_{cement}}$ is specific gravity of cement.

Step 4: Calculation of paste volume

The voids that exist in particle packing of aggregates represent the amount of paste required to be filled to ensure good concrete self-compacting ability. This can be calculated by using Eq. 3-9.

$$V_{paste} = 1 - PP \quad \text{Eq. 3-9}$$

where V_{paste} volume of paste

Step 5: Determination of water content

Water content can be calculated by water to binder (W/B) ratio using Eq. 3-10 and Eq. 3-11 . The actual W/B needs to be validated and adjusted by trial mix.

$$V_{water}/V_{cement} = W/B \quad \text{Eq. 3-10}$$

$$W_{water} = V_{water} \times SG_{water} \times 1000 \quad \text{Eq. 3-11}$$

where W/B is water to binder ratio, V_{water} is volume of water content, W_{water} is water content (kg/m^3) and SG_{water} is specific gravity of water.

Step 6: Determination of superplasticizer dosage

SP is an essential constituent to allow SCC to achieve followability and passing ability. However, excessive dosage of SP can cause severe bleeding and segregation. Determination of optimum SP can help SCC to achieve optimum performance. The SP content can be calculated by using Eq. 3-12. Adjustment of dosage has to be made through trial mix if its fresh properties do not fulfil the criteria in the EFNARC (2002).

$$W_{SP} = SP(\%) \times (W_{cement} + W_{SCM}) \quad \text{Eq. 3-12}$$

where W_{SP} is superplasticizer content (kg/m^3), $SP(\%)$ is superplasticizer dosage and W_{SCM} is supplementary cementitious material content (kg/m^3).

A sample calculation of mix design is presented in Appendix A. The mix proportion obtained from PP test is used as the baseline for LWSCC mix design. Fresh and hardened concrete tests in accordance with EFNARC (2002) are carried out to determine the mechanical properties to ensure that they fulfil the requirements of EFNARC (2002). The mix proportion is checked and adjusted accordingly with the requirements in Annex C of BIBM and ERMCO (2005). Figure 3.6 shows the flowchart for determining the mix proportion.

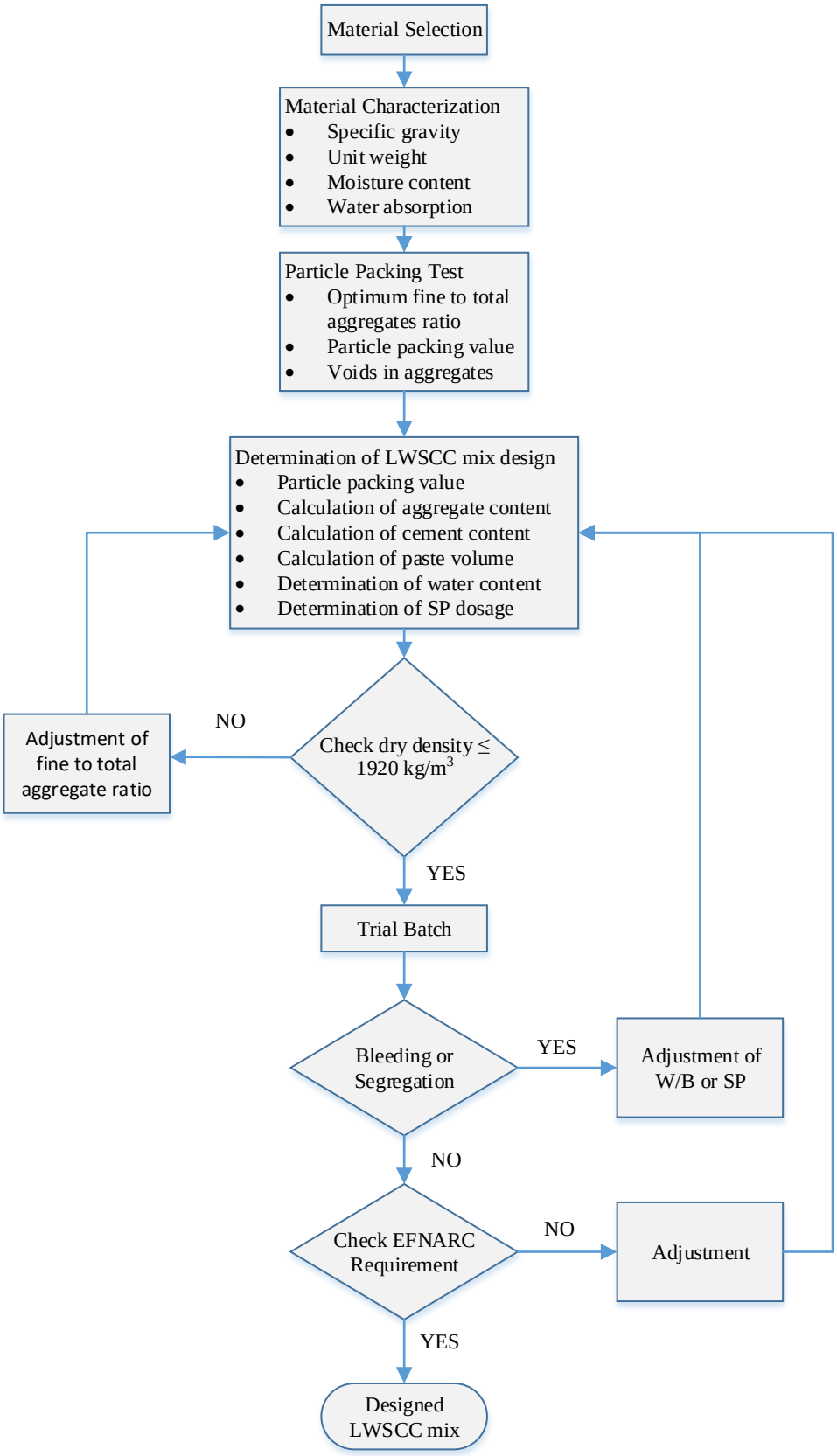

Figure 3.6: Flowchart for achieving LWSCC mix design

3.3.3. LWSCC Mix Proportion and Discussion

3.3.3.1. Trial Mix Discussion

Based on ASTMC29 , the relationships between bulk density as well as void ratio and aggregates ratio were established in Figure 3.7. For bulk density versus coarse to total aggregate ratio, it is noted that the bulk density decreased with increasing coarse aggregate content. It is because coarse aggregate (OPS) has lower specific gravity compared to fine aggregates (river sand). Lowest void ratio can be observed when the coarse to fine aggregates ratio is 1:1. This indicates that ratio of 50% of coarse aggregate and 50% fine aggregate is the optimum aggregate content for OPS and river sand combination. When coarse to total aggregate ratio is increased from 0.5 to 0.6, even though the density decreases, the void ratio exhibits a rising trend. This rising trend indicates more paste is required to fill in the voids. Several researchers have used coarse to total aggregate ratios of 0.5 (Floyd et al., 2015; Kanadasan & Razak, 2014) and 0.6 (Kanadasan & Razak, 2014; Li et al., 2017; Shi & Wu, 2005) in proportioning LWSCC. Even though coarse to total aggregate ratio of 0.6 could produce more economic mix, ratio of 0.5 was chosen for mix proportioning since this ratio produces the least voids.

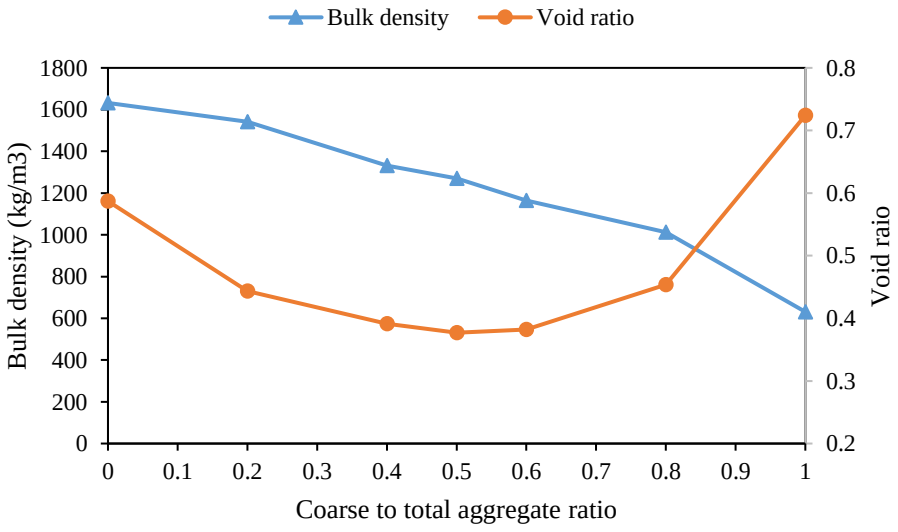

Figure 3.7: Influence of coarse to fine aggregate ratio on bulk density and void ratio

According to EFNARC (2002), the limit of air content is 2%. Nevertheless, air content of 1% was assumed in this research. A water to binder ratio of 0.35 was selected for this study. 1% of SP dosage was used to initiate the trial mix. Kanadasan and Razak (2014) recommended to use 420 kg/m^3 for cement content. As such, 420 kg/m^3 was used as cement content for the mix design calculation.

Several trial mixes of LWSCC have been designed and assessed before the mix proportion is to be finalized. These trial mix designs are presented in Appendix B. It was noticed that more cement paste is required to facilitate self-compacting ability for LWSCC incorporated with OPS as coarse aggregate. As such, the cement content was increased from 420 kg/m^3 to 520 kg/m^3. In order to compensate the increased cement content, the coarse to total aggregate ratio was increased from 0.5 to 0.6 by volume. This can reduce the density of proposed LWSCC. The SP dosage was increased from 1% to 1.65% in order to reduce the tendency of blockage.

3.3.3.2. Final Mix Proportion

As discussed in the previous section, the mix design of LWSCC using OPS as coarse aggregates was first determined by using particle packing theory and then assessed against EFNARC (2002) requirements. In the first trial, the fresh properties of LWSCC determined from particle packing theory did not fulfil the requirements of EFNARC (2002). Adjustment was made in order to obtain the mix design that fulfilled the requirements. Table 3.4 presents the finalized mix design to be studied. In this research study, 30% to 50% of fly ash replacements were made to the control mix. With the replacement of fly ash, the water demand was decreased, so as W/B was decreased from 0.33 to 0.31. The presence of fly ash was able to improve the packing of LWSCC which in turn reduced the water demand although fly ash exhibited characteristic of high affinity to water. The comparison of these four mix designs was made in the following section.

Table 3.4: Summary of mix design

Mix	M0	M30	M40	M50
Cement (kg/m^3)	520	364	312	260
Fly Ash (kg/m^3)	0	156	208	260
Water (kg/m^3)	171.6	161.2	161.2	161.2
Sand (kg/m^3)	715	715	715	715
Coarse Aggregate (kg/m^3)	455	455	455	455
SP (kg/m^3)	8.58	8.58	8.58	8.58
Air content	1%	1%	1%	1%
Water to binder ratio	0.33	0.31	0.31	0.31
Coarse Aggregate to total aggregate ratio	0.39	0.39	0.39	0.39

3.4. Fresh Properties

3.4.1. EFNARC Requirement

Several publications such as EFNARC (2002) and ACI-237 (2007) provide the guidelines to carry out workability tests for SCC. EFNARC (2002) is used as the workability assessment criteria in this research. The workability performance requirements for SCC are shown in Table 3.5. All the test results are assessed against these criteria. According to EFNARC (2002), these criteria are developed based on the current knowledge and research. However, not all of these criteria are suitable to be used for assessing LWSCC as it performs differently for SCC. LWSCC with fresh properties outside these criteria may be acceptable if it is able to perform properly under the required conditions. All the LWSCC mixes were assessed for fresh properties including filling ability (J-ring), passing ability (V-funnel and Slump flow) and segregation resistance (Visual segregation index and sieve stability).

Table 3.5: EFNARC requirement

Workability	Test	Class	Criteria
Filling ability	Slump Flow (mm)	SF1	550-650
		SF2	660-750
		SF3	760-850
	T500 (s)	VS1/VF1	≤ 2 V − Funnel ≤ 8
		VS2/VF2	≥ 2 time(s) $9 - 25$
Passing ability	Step height in J-ring (mm)	PA1	Sj ≤ 15 (59 mm bar spacing)
		PA2	Sj ≤ 15 (40 mm bar spacing)
	L-Box		0.8 - 0.1
	U-Box		0 - 30
Segregation Resistance	Sieve segregation (%)	SR1	≤ 20
		SR2	≤ 15

3.4.2. Experimental Test Results

As discussed in methodology section, LWSCC were assessed for fresh properties. The filling ability was assessed using J-ring test while passing ability was assessed through V-funnel and slump flow tests. Segregation resistance was assessed using visual segregation index and sieve stability tests. The fresh properties test results were shown in Table 3.6. These results are evaluated and discussed in the following section.

Table 3.6: Summary of fresh properties

Mixes		M0	M30	M40	M50
J-Ring	**T_{500} (s)**	10	9	8.4	7
	Dm (mm)	520	580	530	600
	Block Step (mm)	12.5	9.75	8.5	9.5
Slump flow	**T_{500} (s)**	5.04	4.38	4.35	1.82
	Dm (mm)	660	700	710	730
V-funnel	**T_{10s} (s)**	15	14	13	13
	T_{5min} (s)	25	18	18	17
Sieve segregation	**Sieved Portion (%)**	6.34	6.84	5.95	4.8
Visual Index	**Index**	1	1	1	1

3.4.3. Filling Ability

Filling ability is the mean to measure the ability of fresh LWSCC to flow and fill the formwork under self-weight without the need of external vibration. In this research,

slump flow and V-funnel tests have been carried out to assess the flow ability of LWSCC.

3.4.3.1. Slump Flow Test

Slump flow test is an essential basic test which gives the indicator of flow ability of SCC. All the LWSCC mix designs in this research have achieved the slump flow spread in the range of 660-730mm as shown in Figure 3.8. The measured slump flow values of all four mixes were within the range of 550-850mm which complied with the requirement of European guidelines (EGSCC, 2005). According to European Guidelines, all the four mixes were classified as class SF2 as the slump flow results fell within the range of 650-750mm. Class SF2 SCC is suitable for normal application such as walls and columns. The maximum spread of LWSCC tends to increase with the higher level fly ash replacement. It is a well-established fact that the use of FA in SCC can reduce the water demand required to achieve a given workability. On the other hand, incorporation of fly ash can reduce the need of superplasticiser at constant w/b ratio to obtain a given slump flow. Similar outcomes were observed by Yahia et al. (1999) and Ramanathan et al. (2013).

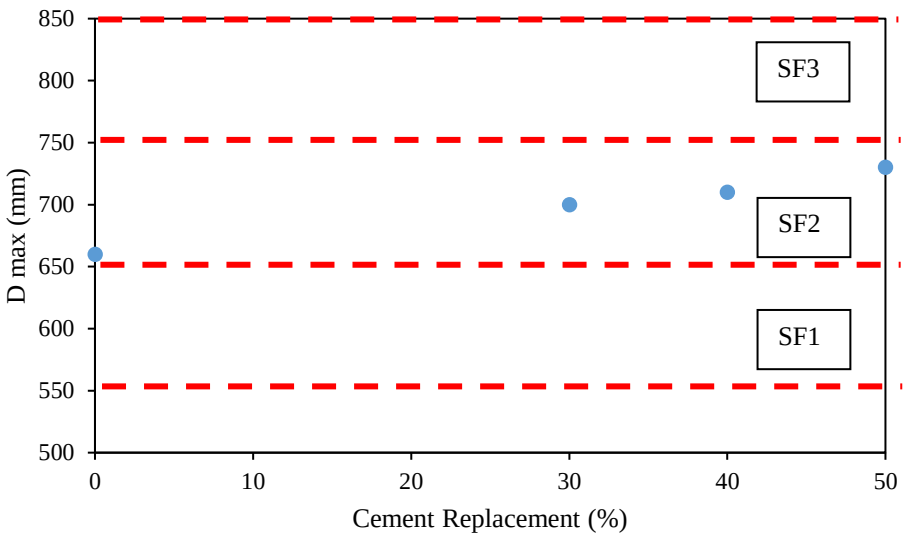

Figure 3.8: Comparison of maximum slump spread

3.4.3.2. T_{500} and V-Funnel Test

T_{500} and V-funnel flow times are used to assess the viscosity and stability of SCC respectively. Figure 3.9 and Figure 3.10 present the T_{500} and V-funnel flow times of

all mixes respectively. A low value of T_{500} and V-funnel flow time indicates that the fresh concrete possesses low plastic viscosity and therefore it has faster filling rate. The time to spread 500mm for four mixes fell in the range of 1.82 – 5.04s. The control mix, 30% and 40% were classified as class VS2 as the flow time was more than 2s while mix 50% was classified as class VS1. T_{500} was found to decrease with the increasing content of fly ash. V-funnel test was carried out in two conditions, which were when the funnel trap door was opened 10 seconds and 5 minutes after filling with LWSCC respectively. The V-funnel time was in the range of 13 -15s for T_{10s} and 17-25s for T_{5min}. Since the T_{10s} was more than 8s, all the LWSCC were classified as Class VF2 of European guidelines. The inverted cone shape of V-funnel restricts the concrete flow and the prolonged flow time can give the indication of fresh concrete blocking tendency. The control mix was found to have the highest v-funnel flow time. T_{10s} tended to decrease with the increase of fly ash replacement. Similar trend was found for T_{5min}. This is depicted in Figure 3.10. The relationship between T_{500} and V-funnel flow time is shown in Figure 3.11. Two mixes fall in VS2/VF2 category. According to EGSCC (2005), the mix that falls within VS2/VF2 region gives rise to good filling rate. The mixes which fall within this region can experience thixotropic effect that can help to reduce the formwork pressure. However, the resultant hardened concrete may experience blow hole finishing surface. Slump flow and flow times are highly dependent on the fly ash replacement level. As such, fly ash is found to be able to improve the filling ability of LWSCC. The capability of fly ash to improve the workability of LWSCC can be explained in terms of the spherical and smooth nature of fly ash particles which induce the ball bearing effect. Partial replacement of cement by fly ash can result in higher paste volume which in turn reduces the friction at the fine aggregate-paste interface. Consequently, the cohesiveness and plasticity of concrete improve. Hence, the improved concrete workability is achieved (Ramanathan et al., 2013). In short, incorporating fly ash as partial binder content in LWSCC with OPS as coarse aggregates has been proven by the filling ability results to have similar performance with conventional SCC.

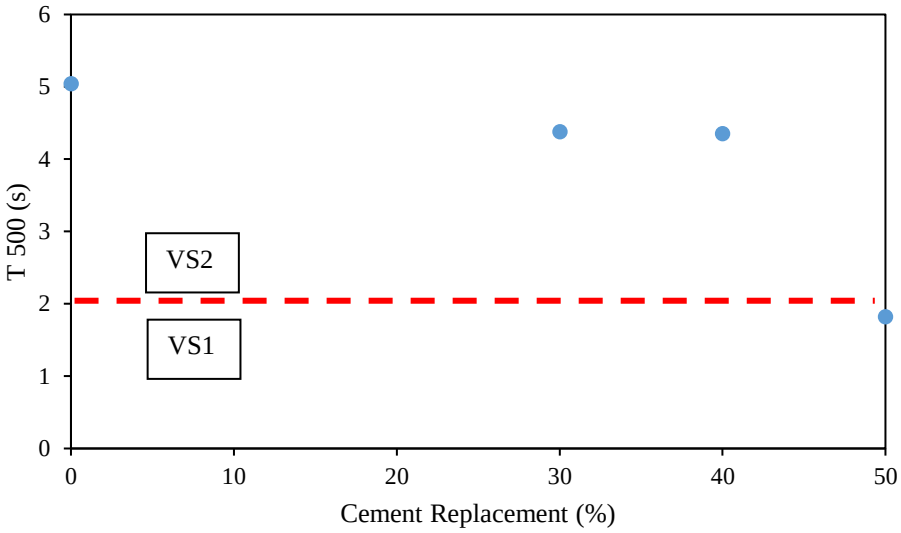

Figure 3.9: Comparison of slump flow time

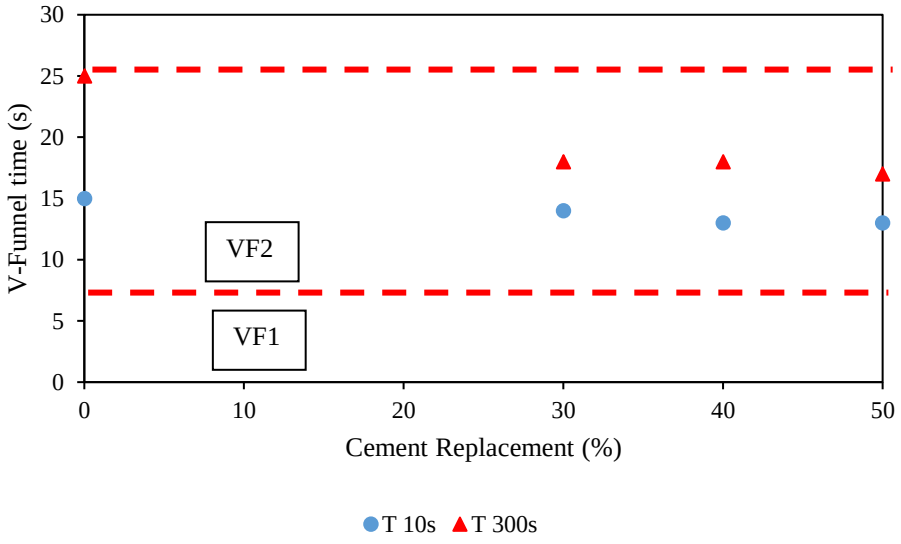

Figure 3.10: V-funnel time comparison

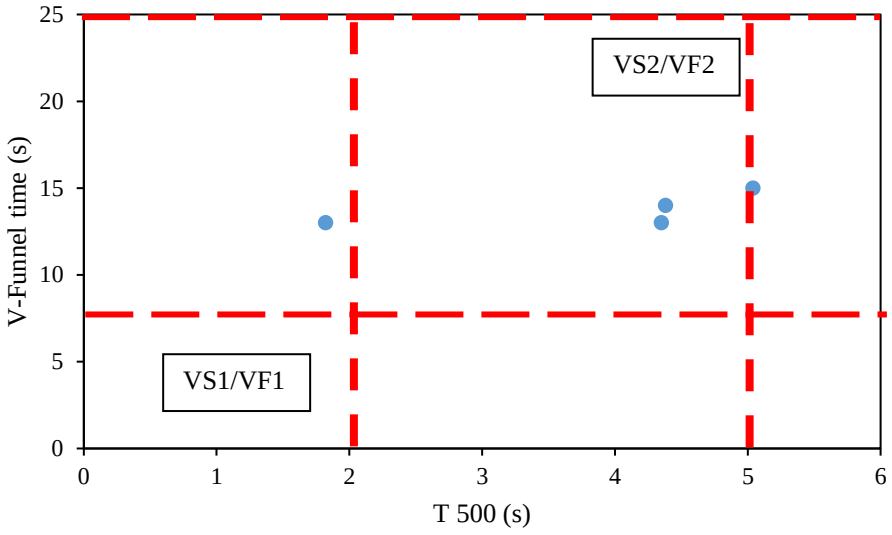

Figure 3.11: Viscosity class variation with T500 and V-funnel flow time

3.4.4. Passing Ability

Passing ability is assessed to determine the capability of a fresh LWSCC to flow through narrow openings in confined space such as congested reinforcement area, without segregation, loss of its uniform consistency or without blockage in the confined space. In this research, only J-ring test was carried out to determine the passing ability of LWSCC.

J-ring test was carried out to determine the passing ability of LWSCC. Three key parameters of J-ring test are indicated as T_{500} (time to spread 500mm diameter), D_m (maximum spread) and block step. The main concern is the block step value which is the difference between the height of concrete inside and outside of J-ring bars. Block step of 15mm is the acceptable limit for SCC in EGSCC (2005). From Table 3.6, the time used to spread 500m diameter is in the range of 7s to 10s while the maximum spread is ranging from 520mm to 600mm. These values are shown in Figure 3.12. The time taken to spread 500mm improved with the increasing replacement of fly ash in j-ring test. The block step is in the range of 9.5mm to 12.5mm. Higher block step values indicate higher viscosity whereby there is higher blockage tendency of coarse aggregate when the fresh SCC flows through steel reinforcements. Figure 3.13 shows the comparison of block step height. It can be seen that the block step height decreases when the fly ash replacement is increased from 0 to 40%. However, the block step height increases when fly ash replacement is increased from 40% to 50%. This

signifies that the passing ability of LWSCC improves with the replacement of fly ash up to 40%. In short, the replacement of fly ash in LWSCC offers better passing ability up to an optimum point.

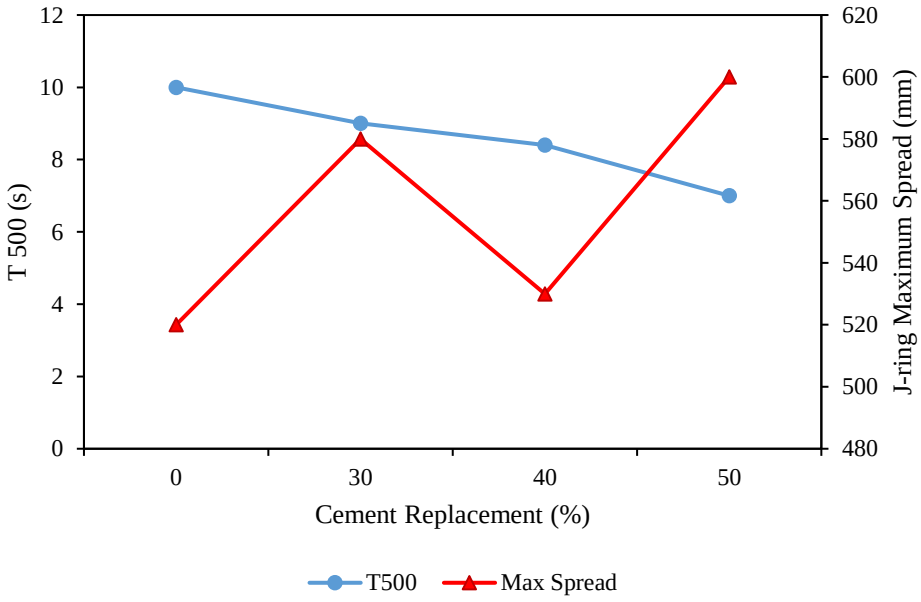

Figure 3.12: T 500 and max spread comparison

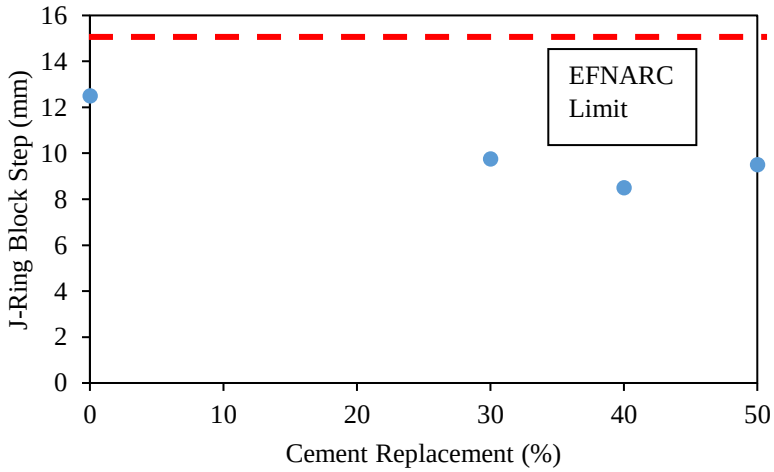

Figure 3.13: Comparison of j-ring block step height

3.4.5. Segregation Resistance

Segregation resistance is assessed to ensure the LWSCC remains homogeneous during the process of transporting, placing and after placing without any tendency to bleed and separation of aggregates from mortar. Sieve segregation and visual indexing are used to evaluate the segregation resistance of LWSCC in this study.

3.4.5.1. Sieve Segregation

The percentage of concrete mix that passes through 5mm sieve is expressed as segregation ratio. Figure 3.14 shows the comparison of segregation of LWSCC at different fly ash replacement. Lower segregation ratio indicates better segregation resistance of LWSCC. From the figure, all the four concrete mixes have achieved segregation ratio of less than 15%, which could be classified as class SR2 in segregation resistance. Class SR2 mixes are suitable for tall vertical application. All the LWSCC can be considered as quite consistent. During the trial stage, the binder content, w/b ratio, amount of SP and aggregates content were proportioned carefully in order to produce mixes with constant fresh concrete properties. By comparing the segregation ratio of control mix with 30% mix, 30% mix resulted in slightly poorer sieve segregation. However, as fly ash content increased, the segregation resistance was found to be improved up to 50% fly ash replacement.

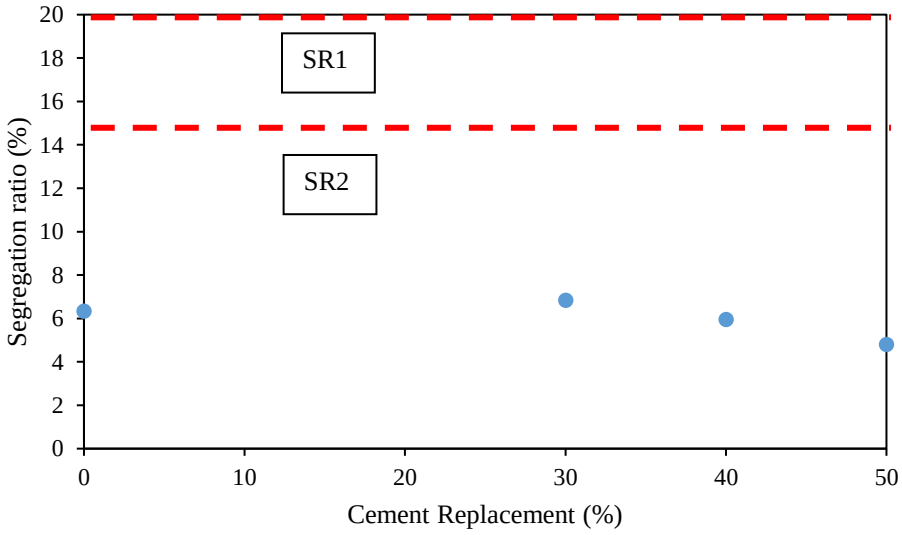

Figure 3.14: Comparison of segregation ratio

3.4.5.2. Visual Segregation Index

In this study, visual segregation indices were taken straight after the slump flow tests. These indices were recorded based on the presence of mortar halo and aggregates piling up at the centre of spread and any separation of aggregates and mortar at the edge. Figure 3.15 shows the VSI indices of all four LWSCC mix designs. All the mix designs show the VSI index of 1.0, which indicated no mortar halo or aggregate piled up at the centre and also minor evidence of air popping on the surface of LWSCC spread. Typical slump flow spread is shown in Figure 3.16. These VSI indices agreed with the results of sieve segregation and thus demonstrated satisfactory segregation resistance of the mix.

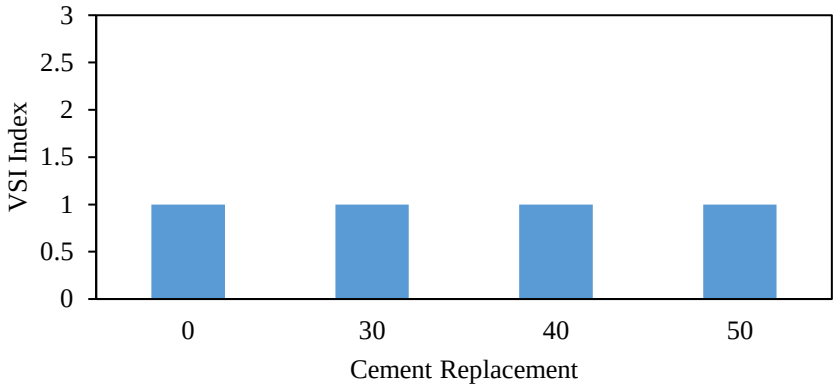

Figure 3.15: Comparison of VSI index

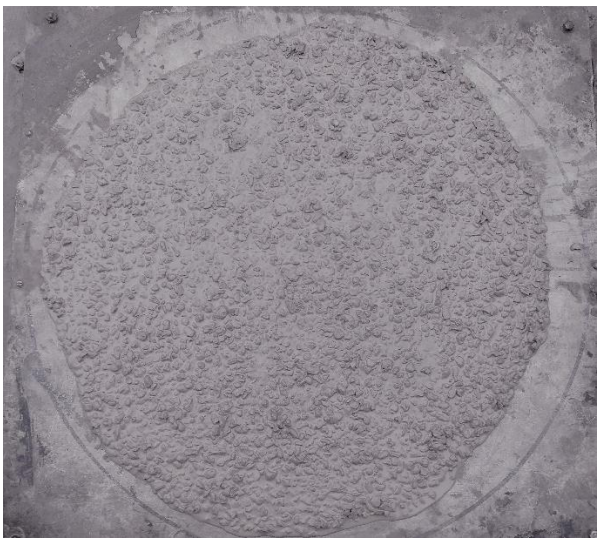

Figure 3.16: Typical slump flow appearance

These experiments have shown that the OPS based SCC satisfies the criteria of the fresh state properties of SCC such as filling ability, passing ability and segregation resistance. As such, the material can be potentially used as aggregates replacement in manufacturing SCC.

3.5. Hardened Properties under Room Temperature

3.5.1. Density

The density for all LWSCC mixes under fresh, air dry and oven dry conditions is shown in Table 3.7. Overall, all the mixes have achieved density in the range of 1800 kg/m^3 to 2000kg/m^3 for fresh density. The air dry density is about 40-70 kg/m^3 lower than fresh density while oven dry density is 125-175 kg/m^3 lower than fresh density. The comparisons of density between mixes under different conditions are illustrated in Figure 3.17. The density of control mix does not fall within the range of the specification stated by ASTM C330 which is 1120 to 1920 kg/m^3 for light weight concrete. Nevertheless, the control mix has attained about 17% lighter weight when compared to normal granite based concrete. It is noted that the density of concrete decreases with increasing replacement level of fly ash in the binder content of concrete. This reduction of density is due to the lower specific gravity of fly ash compared to cement. Similar trend of results was reported by Shafigh et al. (2016) with fly ash replacement up to 70% for normally vibrated OPS based concrete. A reduced in density of concrete can lead to better economic design of structure as dead load of structure is decreased significantly.

Table 3.7: Concrete density

Mix	Density (kg/m^3)		
	Demoulded	Air dry	Oven dry
M0	1918	1887	1832
M30	1900	1864	1771
M40	1881	1825	1731
M50	1843	1776	1668

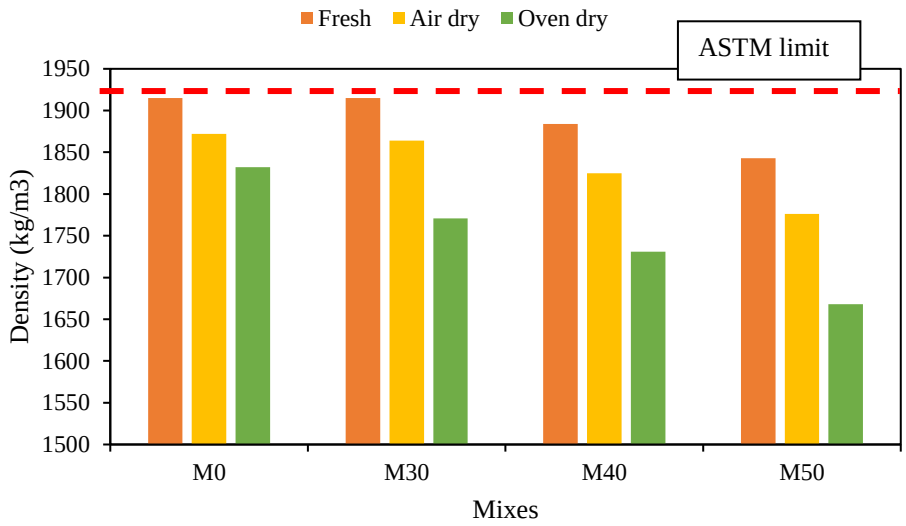

Figure 3.17: Comparison of mixes density

3.5.2. Compressive Strength at Room Temperature

Concrete compressive strength is regarded as the most important property which determines structural performance of the material. The compressive strength of LWSCC mixes at 7, 28 and 90 days is summarized in Table 3.8. The compressive strength for all mixes falls within the range of 13-27MPa at 7 days, 18-39MPa at 28 days and 24-41MPa at 90 days. Development of compressive strength for all LWSCC mixes is illustrated in Figure 3.18. The compressive strength improved with increasing age from 7 days to 90 days. Test results show that control mix achieved the highest compressive strength among all four mixes. When fly ash replacement level was increased from 30% to 50%, the compressive strength decreased drastically. From Figure 3.18, it is observed that the mixes that contain fly ash experienced slower rate of strength gain compared to control mix at early age. At the latter age, mixes that contained fly ash still experienced significant strength gain while control mix did not. Mix M30 achieved comparable strength to control mix M0 at 90 days. Similar trends were also observed in the studies of normally vibrated OPS based concrete studied by Kupaei et al. (2013) and Shafigh et al. (2016). These can be explained that the pozzolanic reactions in concrete have slowed down due to low calcium content in Class F fly ash, leading to significant delay in strength gain at early age. This effect is more significant when there is higher level of fly ash replacement.

For failure mode of LWSCC samples, it is observed that fracture occurred through the LWA particles. This observation indicates that aggregates are the weak point of the concrete matrix in LWSCC as all the failed samples exhibit aggregate fracture. In the study of normally vibrated OPS concrete, Okpala (1990) claimed that the failure of OPS concrete was governed by the breakdown of bond between aggregates and cement mortar. Mannan et al. (2006) also stated that OPS concrete failed due to lack of adhesion between OPS and cement paste. In the study of LWSCC, Floyd et al. (2015) reported similar observation in the study of expanded clay as LWA in LWSCC. Lotfy et al. (2015c) also reported that aggregate fracture was observed in failed sample after compression test for LWSCC. It has been demonstrated that the compressive strength of concrete highly depends on the stiffness of aggregates. Thus, it can be explained that cement mortar in LWSCC is typically stronger than LWA and contributes the most strength (Grabois et al., 2016). It is thus concluded that the individual strength of LWA is important in contributing to the compressive strength of LWSCC.

Table 3.8: Concrete compressive strength at different age

Mix	Compressive Strength (MPa)		
	7 days	28 days	90 days
M0	27.00	38.83	40.59
M30	24.67	32.17	36.01
M40	18.44	23.96	28.72
M50	13.34	18.72	24.43

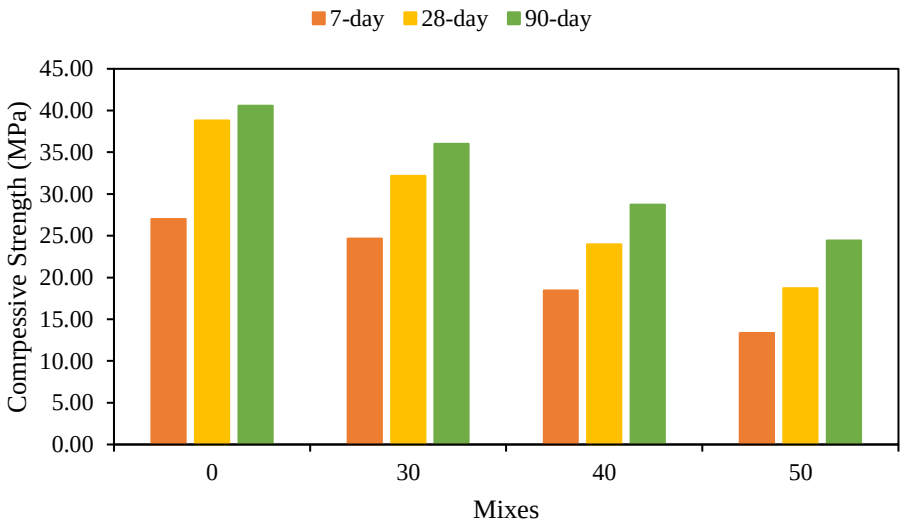

Figure 3.18: LWSCC compressive strength development with time

3.5.3. Tensile Splitting Strength

Splitting tensile strength is a material property which can be utilized to assess the diagonal tension resistance of LWSCC structure. The splitting tensile strength for OPS based SCC mixes at 7, 28 and 90 days is summarized in Table 3.9. The splitting tensile strength varies from 1.2- 2.2MPa at 7 days, 1.6-2.8MPa at 28 days and 2-2.8MPa at 90 days. ASTM C330 has specified a minimum value of 2MPa splitting tensile strength for LWA concrete. All the mixes except M50 have achieved 2MPa and above strength at 28 days. Development of LWSCC splitting tensile strength is shown in Figure 3.19. Splitting tensile strength is observed to increase as concrete ages. Similar to compressive strength, splitting tensile strength of concrete that contains fly ash experiences slower rate of strength gain. This effect is more significant at higher level of fly ash replacement. Splitting tensile strength decreases with increasing fly ash content.

Table 3.9: Concrete splitting tensile strength at different age

Mix	Splitting Tensile Strength (MPa)		
	7 days	28 days	90 days
M0	2.23	2.82	2.84
M30	2.09	2.54	2.75
M40	1.62	2.05	2.33
M50	1.20	1.62	2.07

Similar to granite based concrete, splitting tensile strength of OPS based SCC can also be correlated to its compressive strength. Relationship between compressive strength and splitting tensile strength is shown in Figure 3.20. The splitting tensile strength is noted to increase with increasing value of compressive strength. As shown in the experimental results, splitting tensile strength is about 7.2- 8.6% of compressive strength which is within the range of normally vibrated OPS based concrete reported by several researchers. Mahmud et al. (2009) reported values of 6-10% of their OPS based concrete compressive strength. Shafigh et al. (2012) also reported the values of 6.7-8.1% based on their extensive research on splitting tensile strength. A recent study on normally vibrated OPS based concrete with fly ash replacement by Shafigh et al. (2016) shows the values of 5-7%.

As illustrated in Figure 3.21, the ratio of splitting tensile strength to compressive strength decreases when the compressive strength of LWSCC increases. The trends agree with the findings of Shafigh et al. (2012) for normally vibrated OPS based concrete. This trend shows that OPS based SCC exhibits similar properties to normally vibrated OPS based concrete. The correlation between splitting tensile strength and compressive strength of concrete from various researchers are shown in Table 3.10. These equations are used to predict the splitting tensile strength and plotted in Figure 3.22 for comparison purpose. The vertical axis is expressed as ratio of calculated value to experimental value. It can be observed that the predicted values from equation of Farahani et al. (2017) are closest to the experimental results. The proposed equation by Felekoğlu et al. (2007) overestimates the splitting tensile strength as the equation is meant for granite based SCC. Contradictory to Felekoğlu et al. (2007), the equation proposed by Lotfy et al. (2015c) underestimates the splitting tensile strength as this equation is actually proposed for furnace slag, expanded clay and expanded shale based SCC. These findings demonstrated that the splitting tensile strength of concrete is highly dependent on the type of aggregates used. An equation for correlation of compressive strength with tensile splitting strength for OPS based SCC, which has been proposed in the present study is shown as Eq. 3-13 below:

$$f_t = 0.1803 f_{cu}^{0.7573} \quad (R^2 = 0.9896) \qquad \text{Eq. 3-13}$$

where f_t is splitting tensile strength and f_{cu} is ultimate cube strength of concrete.

Table 3.10: Splitting tensile strength equations from various researchers

Researchers	Equation	Description
Shafigh et al. (2010)	$0.2\sqrt[3]{f_c^2}$	Normally vibrated OPS concrete containing uncrushed OPS with compressive strength ranging from 17MPa to 37MPa
Shafigh et al. (2012)	$0.4887\sqrt{f_c}$	Normally vibrated OPS concrete containing crushed OPS
Shafigh et al. (2013)	$0.23f_c^{0.64}$	Normally vibrated OPS concrete containing crushed OPS and 10-50% fly ash
Farahani et al. (2017)	$0.146f_c^{0.835}$	Normally vibrated OPS concrete containing crushed and blended binder of OPC, RHA and FA
Lotfy et al. (2015c)	$0.177f_c^{1.33}$	Lightweight self-compacting concrete containing furnace slag, expanded clay and expanded shale as LWA
Felekoğlu et al. (2007)	$0.43f_c^{0.6}$	Self-compacting concrete with granite as aggregates

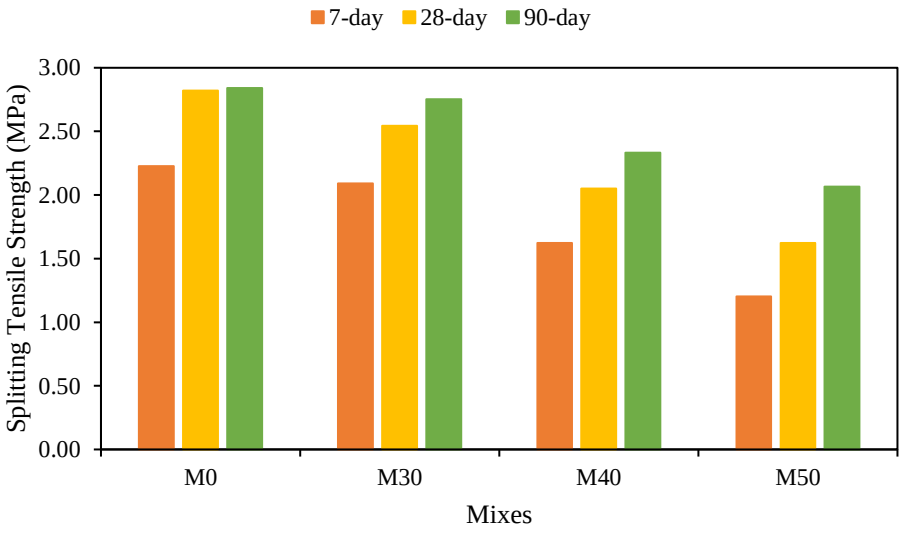

Figure 3.19: LWSCC splitting tensile strength development with time

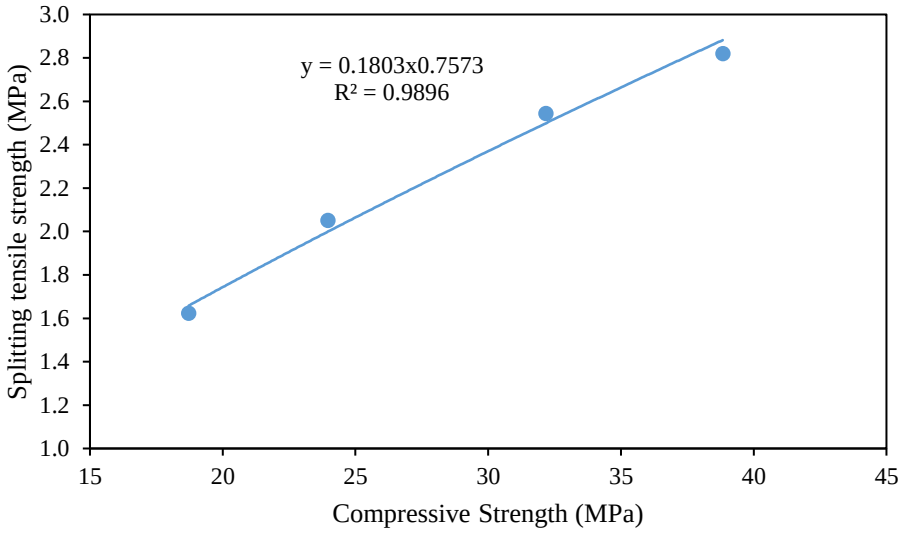

Figure 3.20: Correlation of LWSCC compressive strength to splitting tensile strength

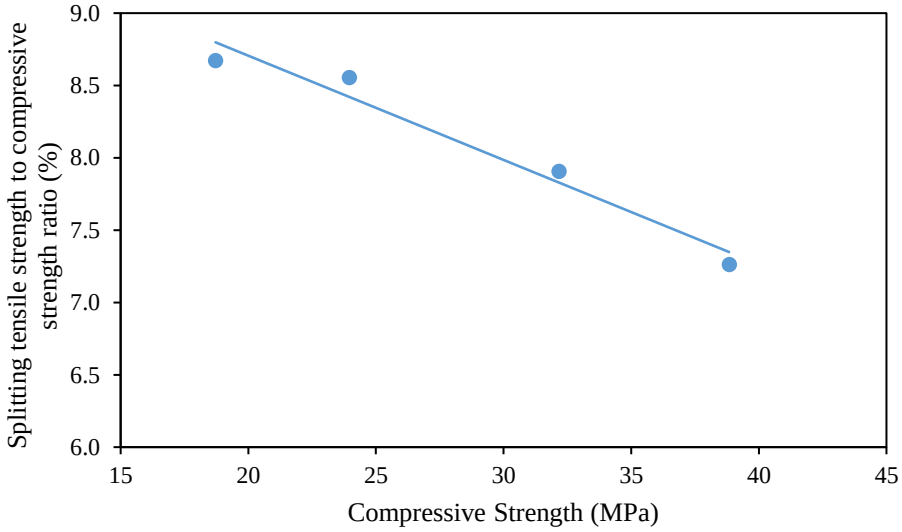

Figure 3.21: Correlation of compressive strength to ratio of splitting tensile to compressive strength

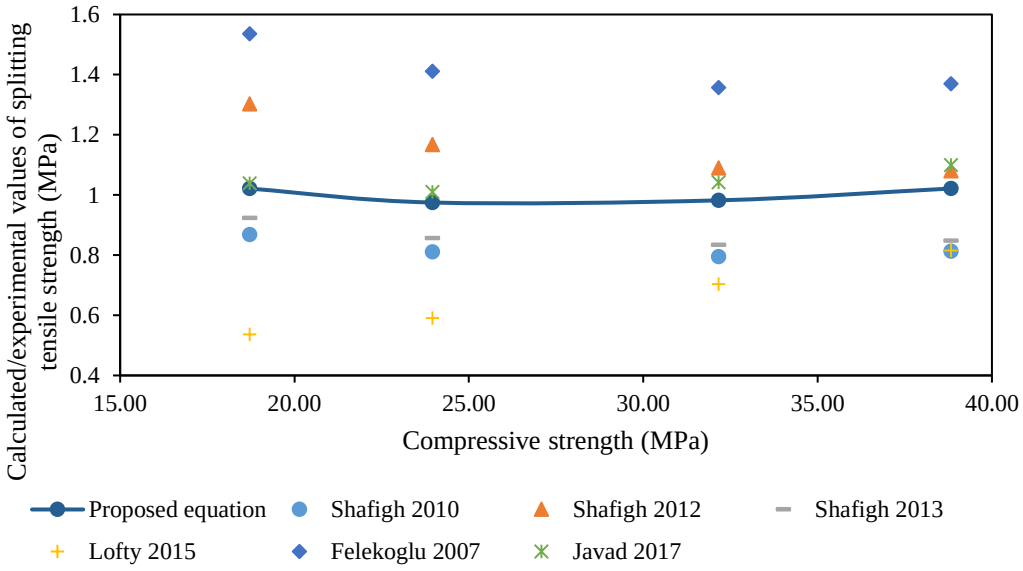

Figure 3.22: Relationship between 28-days compressive strength and calculated splitting tensile strength

3.5.4. SEM Analysis

The interfacial transition zones (ITZ) between binder and aggregates have been investigated by using SEM technique. This is to study the bonding characteristics between cement paste and aggregates of chosen LWSCC samples. The SEM images for Mix M0 at 28 days and 90 days are shown in Figure 3.23 and Figure 3.24 respectively. As shown in these two images, cement paste has considerably seeped into the surface pores of OPS aggregate in the interfacial transition zone (ITZ). This can enhance the interlocking bond between cement paste and aggregates.

The SEM images for Mix M50 at 28 days and 90 days are shown in Figure 3.25 and Figure 3.26. It can be noticed in Figure 3.25 that smooth spherical fly ash particles are still present, which shows that fly ash is still in the early stage of hydration as its initial shape is spherical. As such, the pozzolanic reactions of fly ash and cement are not complete in the initial phase of hydration (Saha, 2018). As concrete ages, the spherical shape of fly ash gradually decomposes. Figure 3.26 indicates that the spherical particles of fly ash are not as easily noticeable as the material is at the age of 90 days. These observations prove that the rate of hydration in concrete is reduced by fly ash. It is also observed that the aggregate surface is full of binder particles. The results showed good agreement with the finding of Alengaram et al. (2011) that finer

supplementary cementitious material could enhance the ITZ to improve the mechanical bonding.

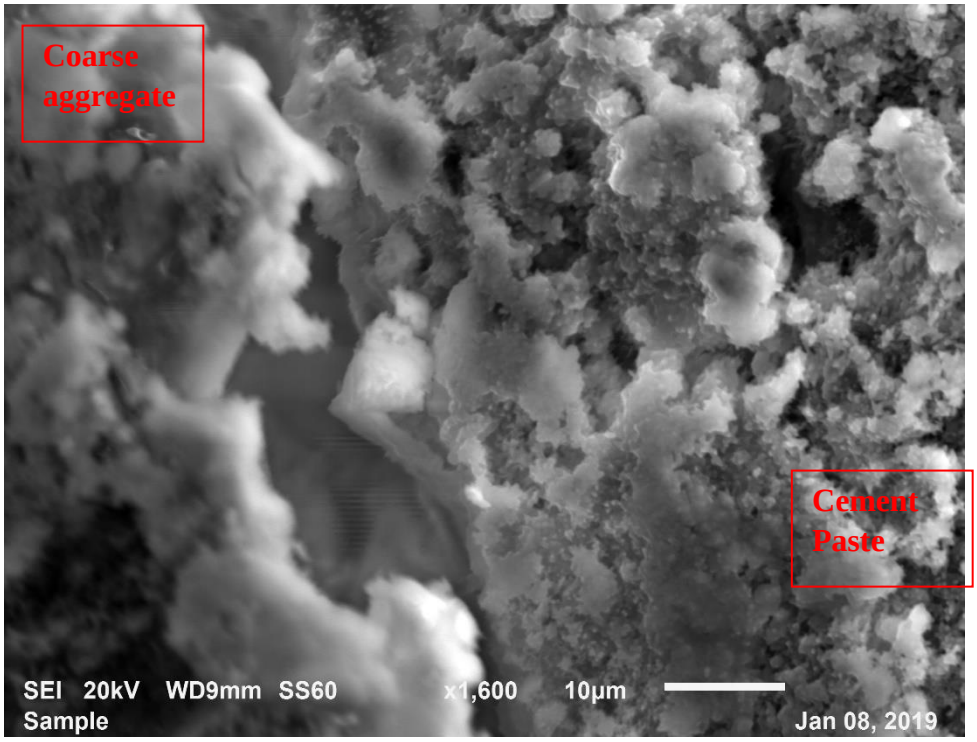

Figure 3.23: SEM image of ITZ of M0 at 28-day

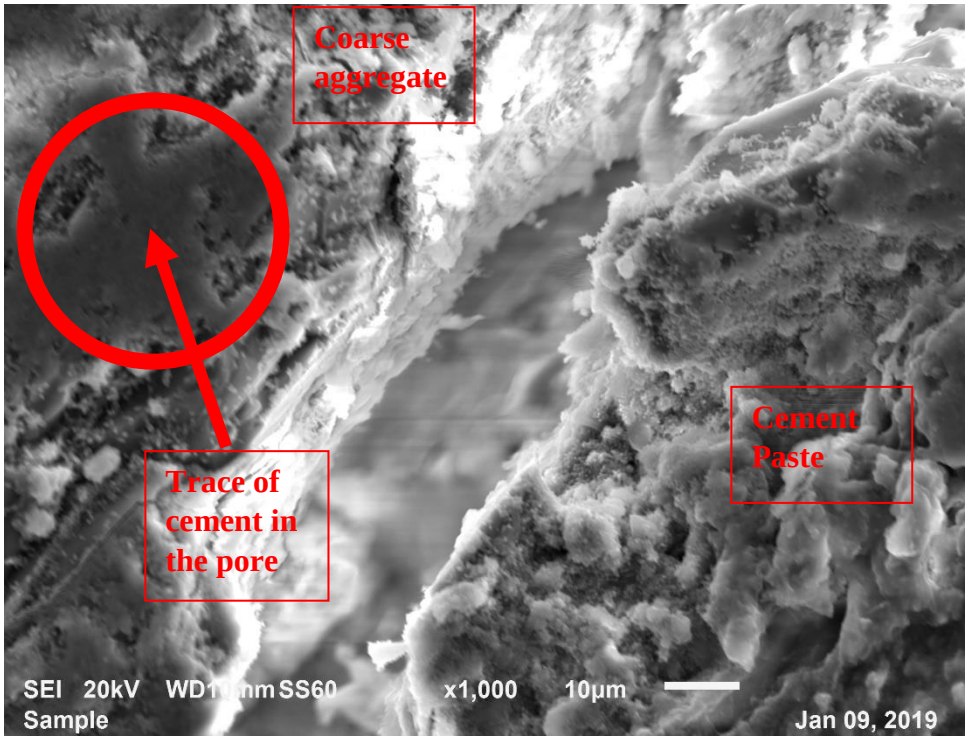

Figure 3.24: SEM image of ITZ of M0 at 90-day

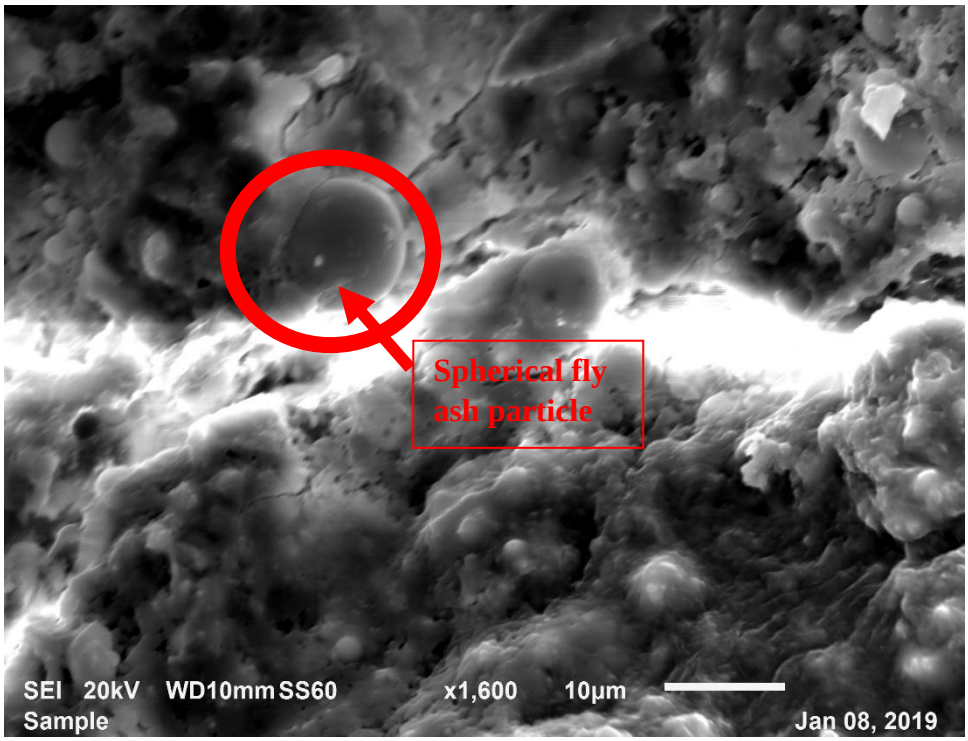

Figure 3.25: SEM image of ITZ of M50 at 28-day

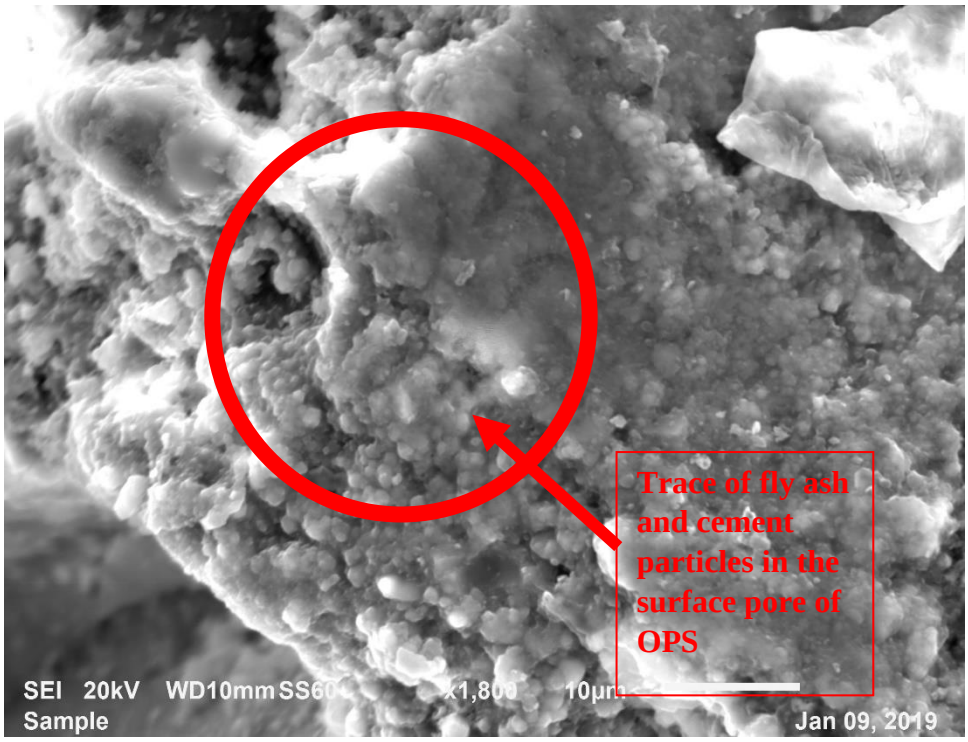

Figure 3.26: SEM image of aggregate part at ITZ of M50 at 90-day

3.5.5. Water Absorption

Concrete water absorption values of all four mix designs are shown in Table 3.11 and illustrated in Figure 3.27. The water absorption values for all mixes were 6.1-7.33% at 28 days and 4.47- 5.07% at 90 days. At 28-day age, control LWSCC mix had the lowest water absorption value among the four mixes. It is noticed that increasing the substitution of fly ash in OPS based LWSCC increases the water absorption at earlier age. This is due to fact that increasing of class F fly ash content in concrete reduces the hydration process at earlier age. At earlier age, the hydration process in high fly ash content concrete is not complete and capillary pores still exist which are highly permeable, resulting in higher water absorption (Fraay et al., 1989). Several researchers (Shafigh et al., 2013; Shafigh et al., 2016) have demonstrated that the water absorption of normally vibrated OPS increases with increasing of fly ash content. The study of Shafigh et al. (2013) shows that the water absorption of normally vibrated OPS concrete increases from 5.5% to 6.6%, 7% and 9.8% when fly ash content is increased from 0% to 10%, 30% and 50% respectively.

At 90-day age, concrete of all the four mixes shows reduction in water absorption. It is observed that the water absorption at 90 days reduced by 17%, 27%, 34% and 39% for M0, M30, M40 and M50 respectively when compared to 28-day. At 90-day age, for concrete incorporated with fly ash, the voids between particles of materials were filled with fly ash at higher percentage and thus the porosity of concrete was reduced. The texture and size of the fly ash particles are able to minimize the voids in between particles (Chindaprasirt et al., 2007). The experimental results in this study show that water absorption of LWSCC decreases with age especially those with higher fly ash content. The reason is that fly ash decreases the interconnectivity of the pore structure since it consumes $Ca(OH)_2$ from the cement paste and causes secondary calcium silicate to hydrate at later age (Kurda et al., 2019). However, the total porosity of concrete is increased with the incorporation of fly ash. Nevertheless, the ratio pore refinement to “pore size” is reduced (Filho et al., 2012).

Generally, all the concrete mixes exhibited water absorption of less than 8% at all ages. A. Neville (2008) stated good concrete must possess the water absorption value of less than 10%, the result of which can be determined from immersed water absorption test.

Table 3.11: Water absorption value of OPS based LWSCC

LWSCC Mix	Water Absorption (%)	
	28-day	90-day
M0	6.10	5.07
M30	6.40	4.66
M40	6.85	4.54
M50	7.33	4.47

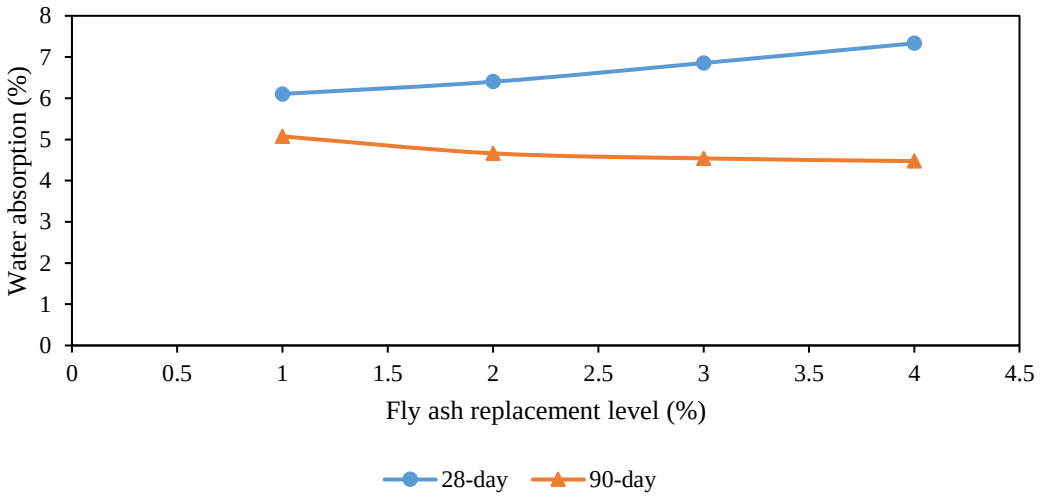

Figure 3.27: Water absorption of OPS based LWSCC

3.6. Hardened Properties under Elevated Temperature

3.6.1. Compressive Strength at Elevated Temperature

Table 3.12 shows the compressive strength of concrete manufactured from control mix (M0) and 40% fly ash mix (M40) under different temperature of heating at 28-day and 90-day of curing age. The relationship between compressive strength and temperature is illustrated in Figure 3.28. The relative strength ratio is defined as the ratio of given temperature to room temperature and it is presented in Table 3.13. At room temperature, concrete made from control mix and 40% fly ash mix achieved strength of 31.35MPa and 22.77MPa respectively at 28-day age while at 90-day age, they were 33.27 MPa and 25.04 MPa respectively. With 40% of fly ash replacement, it is observed that M2 attained 38% lower strength when compared to M1.

From Figure 3.28, it is noticed that both mixes at the age of 28 days and 90 days experienced strength reduction when temperature increased from room temperature up to 300°C. For 28-day concrete, strength reductions of about 24% and 12% were

observed in the temperature range of 24°C-100°C for M0 and M40 respectively. At the 90 days, about 14% and 10% strength reductions were observed for M0 and M40 respectively. There was a significant strength reduction in the temperature range of 100°C-200°C for both mixes. Strength reductions of 43% and 50% were noted in this temperature range for M0 and M40 at 28-day age respectively. Further minor strength reduction was noticed in the temperature range of 200°C-300°C at 28-day age. The compressive strength reduction was mainly due to expulsion of free water from internal pore and concrete dehydration at high temperature (Muthusamy & Kolandasamy, 2015). In the temperature range of 100°C-200°C, the heat energy was sufficient to cause phase transformation of cement paste which could cause shrinkage of cement paste and induce concrete cracks, resulting in significant strength loss (Wu et al., 2013). From Table 3.13, it is noticed that the strength loss was slightly less when the age of concrete was increased. It is also noticed that the incorporation of fly ash was able to reduce strength loss. At 300°C, the relative residual strength ratios of M0 were 0.16 and 0.21 for 28-day and 90-day age respectively while for M40 the ratios were 0.28 and 0.34 respectively.

Table 3.12. Compressive strength of concrete specimen at elevated temperature

Temperature (°C)	Mix Compressive strength (MPa)			
	M0		M40	
	28-day	90-day	28-day	90-day
Room Temperature	31.35	33.27	22.77	25.04
100	23.7	28.7	20.14	22.46
200	10.5	11.31	8.71	9.75
300	5.13	7.12	6.28	8.45

Table 3.13. Relative strength ratio at elevated temperature

Temperature (°C)	Relative Strength Ratio			
	M0		M40	
	28-day	90-day	28-day	90-day
Room Temperature	1	1	1	1
100	0.76	0.86	0.88	0.90
200	0.33	0.34	0.38	0.39
300	0.16	0.21	0.28	0.34

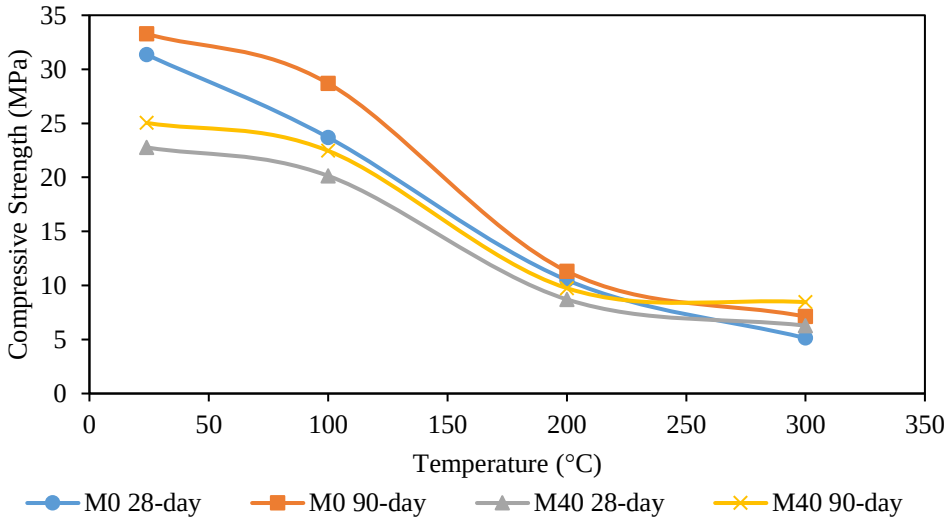

Figure 3.28. Compressive strength versus temperature

3.6.2. Mass Loss

The mass loss of concrete sample after heating is reported in Table 3.14 and illustrated in Figure 3.29. It was observed that the mass loss of concrete samples increased with increasing temperature. The increased in temperature resulted in an increased rate of evaporation of moisture in concrete and hence the weight loss. It is also noted that the mass loss of 28-day and 90-day samples were almost similar. OPS is an aggregate with porous cellular structure which can trap water inside pore. It was noticed that the rate of water loss increased within the temperature range of 200°C to 300°C. The water loss in this temperature range comes from disintegration of the C-S-H, carboaluminate hydrates and the dehydration of calcium silicate hydroxide. These observations are in good agreement with the findings of Pathak and Siddique (2012).

Table 3.14. Mass loss for LWSCC

Concrete Mix	Temperature, °C	Mass Loss, %	
		28days	91days
M0	25	0.84	0.88
	100	3.69	3.12
	200	14.17	14.41
	300	23.45	22.24
M40	25	1.52	0.69
	100	3.28	2.85
	200	13.76	12.72
	300	22.24	21.17

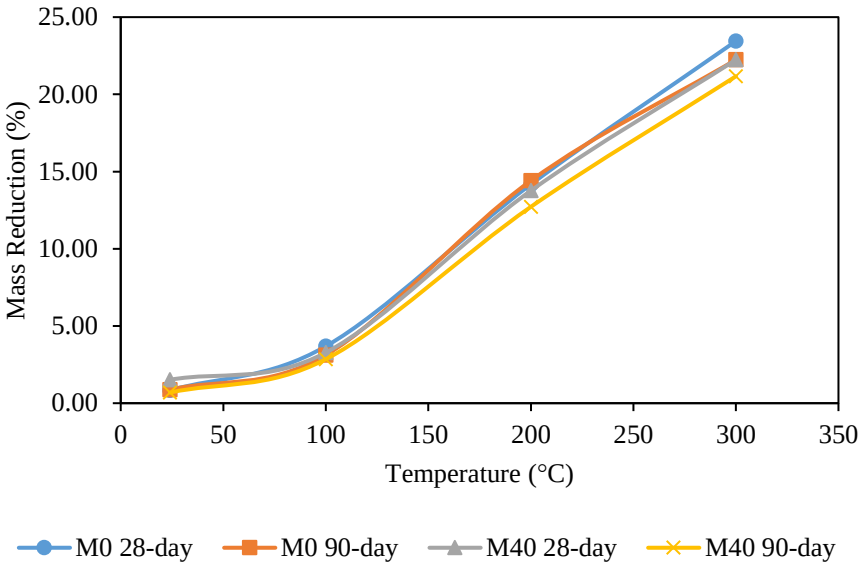

Figure 3.29. Weight loss

3.7. Concluding Remark

The LWSCC control mix design is successfully derived by using particle packing method. A thorough investigation has been performed on the fresh and hardened properties of control LWSCC mix design as well as the mixes with different proportions of fly ash replacement to the control mix. The following conclusions can be drawn:

1. LWSCC can be produced by using OPS as full replacement to normal weight aggregates (NWA), and also with partial fly ash replacement, the resultant concrete of which has satisfactorily achieved fresh state properties in respect of passing ability, filling ability and segregation resistance.
2. LWSCC with OPS as aggregates has achieved desirable slump flow spread in the range of 660-730mm.
3. Satisfactory V-funnel flow time that fulfils the European Guidelines has been achieved.
4. Good passing ability has been attained by OPS LWSCC with the block step in the range of 8-15mm.
5. Excellent segregation resistance with value in the range of 4-7% has been achieved.
6. All the fresh concrete properties of SCC using OPS as aggregates are improved with the replacement of fly ash.

7. The density of OPS based SCC is found to be 15%-23% lower than normal concrete. Replacement of Ordinary Portland Cement by fly ash has reduced the concrete density.
8. The compressive strength of LWSCC was in the range of 18 to 38MPa at 28 days. The compressive strength of LWSCC mix with fly ash replacement increases with curing age.
9. The splitting tensile strength of LWSCC is found in the range of 1.6-2.8MPa at 28 days. Splitting tensile strength falls in the range 7.2- 8.6% of its compressive strength. Its strength also improves with curing age.
10. As evidenced in SEM tests, cement paste has seeped into the pores of OPS aggregates giving rise to good bonding in the ITZ.
11. The water absorption of OPS based LWSCC is about 6%. With fly ash replacement, the water absorption has shown negative effect at early stage. As curing age increases, the water absorption of mix with fly ash improves and shows better value than the control mix.
12. When subjected to elevated temperature, the rate of strength reduction is less when concrete is aged. The OPS based LWSCC experiences strength reduction of nearly 84% and 79% at 28 days and 90 days respectively when subjected to temperature of 300°C.
13. The incorporation of fly ash in OPS based LWSCC is able to improve its residual strength at elevated temperature. With 40% fly ash incorporated, the concrete experiences strength reduction of nearly 72% and 66% at 28 days and 90 days respectively.
14. The mass loss of concrete increases with the rise in temperature. The incorporation of fly ash is able to slightly reduce the mass loss at elevated temperature.

4. Experimental Investigation on Wall Panels

4.1. Introduction

This chapter presents the experimental investigation on lightweight concrete wall panels. The experiment involved the axial load testing of lightweight concrete walls with various aspect ratios and slenderness ratios. Lightweight concrete wall specimens were casted by using LWSCC mixes developed in Chapter 3. A total of 24 specimens with 6 different configurations have been tested with pinned end condition at both ends.

The experimental outcomes, including failure mode, failure load and load-deflection, are discussed and then, used to evaluate the axial behaviour of lightweight concrete wall panels. Subsequently, based on the experimental results, study is made on the influence of aspect ratio and slenderness ratio on lightweight concrete wall.

In this research, current wall design equations from the standards ACI 318, AS3600, BS 8110 and Eurocode 2 are evaluated. Different parameters and factors have been taken into consideration by each of these four design equations. Nevertheless, the experimental results are compared to the calculated results from standard equations. The applicability and limitations of these design equations on lightweight concrete wall are also evaluated. Furthermore, calculated results from the existing design equations published by researchers are also compared with those obtained experimentally.

4.2. Experimental Programme

4.2.1. Specimen

A total of 24 specimens with 6 different configurations were prepared and tested. For wall panel with thickness of 60mm, slender wall panels were designed with slenderness ratio of 23 and aspect ratio of 5.3. As for wall specimen with 25mm thickness, the slenderness ratios were varied from 12 to 23 and the aspect ratios varied from 1.7 to 5.3. According to ACI and AS, minimum reinforcement ratio of 0.0015 must be provided in order to prevent cracking of concrete due to thermal stress. Reinforcement ratios of 0.0058 and 0.003 were provided for vertical and horizontal direction respectively. For wall with 60mm thickness, two layers of steel mesh of property described in Section 4.2.2.2 were used as reinforcement with 15mm concrete

cover. Single layer of reinforcement was provided for wall with 25mm thickness. The nominal diameter of steel mesh reinforcement was 5mm. The dimensions of designed wall panels are summarized in Table 4.1. Details of various types of wall panel specimen are illustrated in Figure 4.1 to Figure 4.6. Four specimens of each configuration were prepared.

Table 4.1: Specimen specification

Specimen	L (mm)	W (mm)	t (mm)	AR	SR	ρ_s	Mix
T25-AR1.8SR12	300	165	25	1.8	12	0.0059	M40
T25-AR1.8SR17	425	235	25	1.8	17	0.0059	M40
T25-AR1.8SR23	565	315	25	1.8	23	0.0059	M40
T25-AR3.1SR23	565	185	25	3.1	23	0.0059	M40
T25-AR5.3SR23	565	105	25	5.3	23	0.0059	M40
T60-AR5.3SR23	1400	260	60	5.3	23	0.0059	M40

Note: 'T' indicate thickness, 'AR' indicate aspect ratio, and 'SR' indicate slenderness ratio.

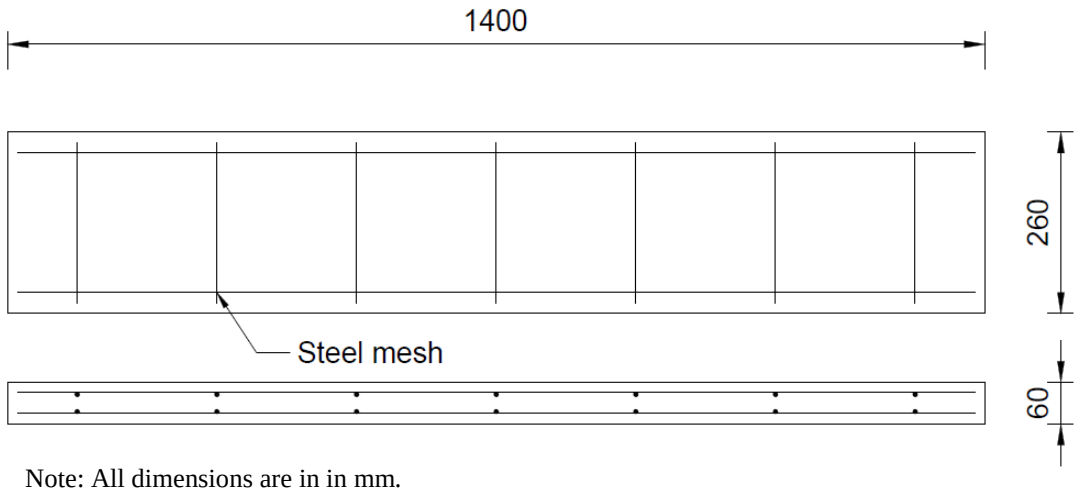

Note: All dimensions are in in mm.

Figure 4.1: T60-AR5.3SR23 specimen layout

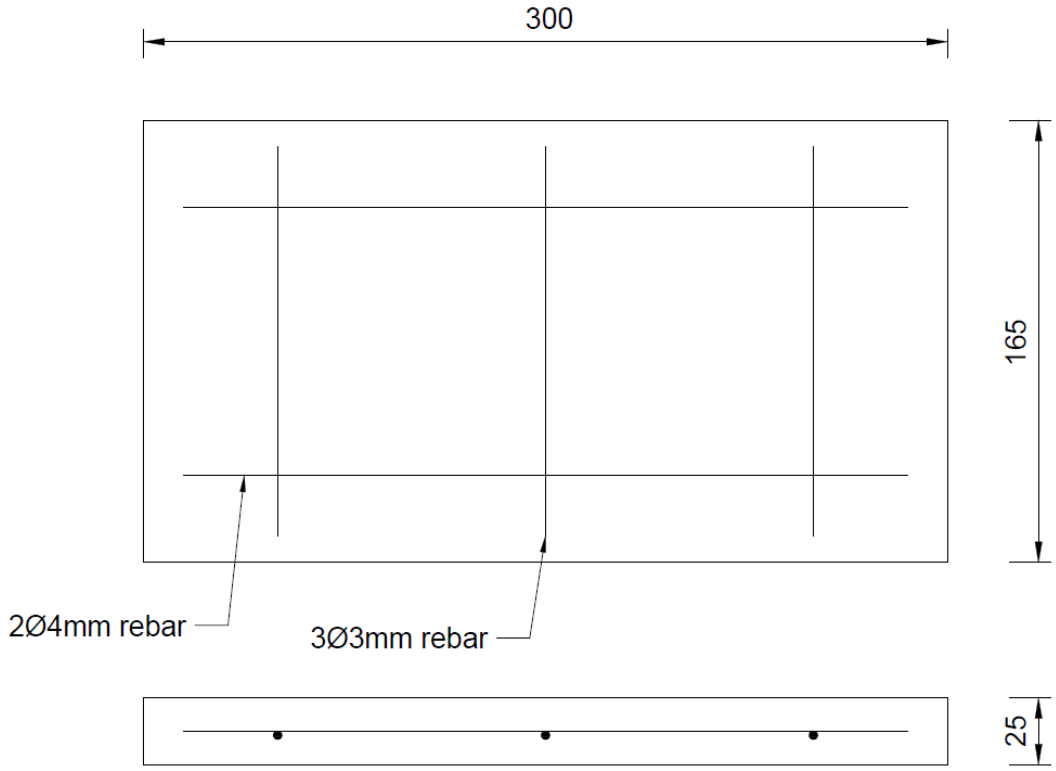

Note: All dimensions are in in mm.

Figure 4.2: T25-AR1.8SR12 specimen layout

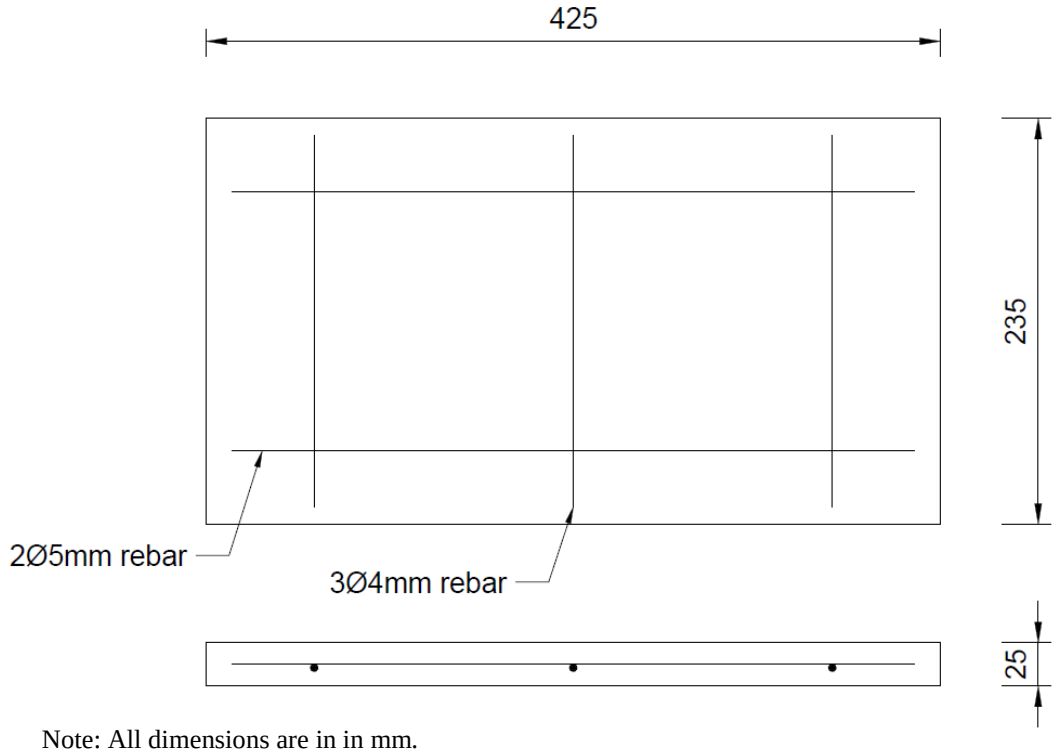

Note: All dimensions are in in mm.

Figure 4.3: T25-AR1.8SR17 specimen layout

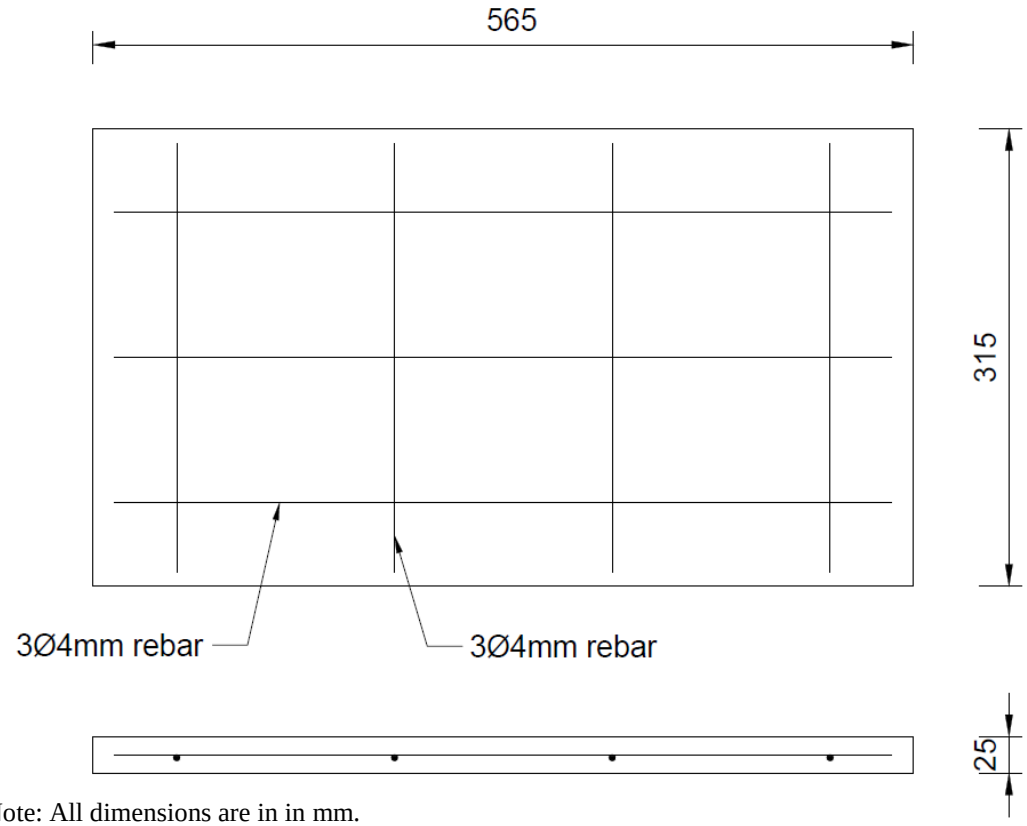

Note: All dimensions are in in mm.

Figure 4.4: T25-AR1.8SR23 specimen layout

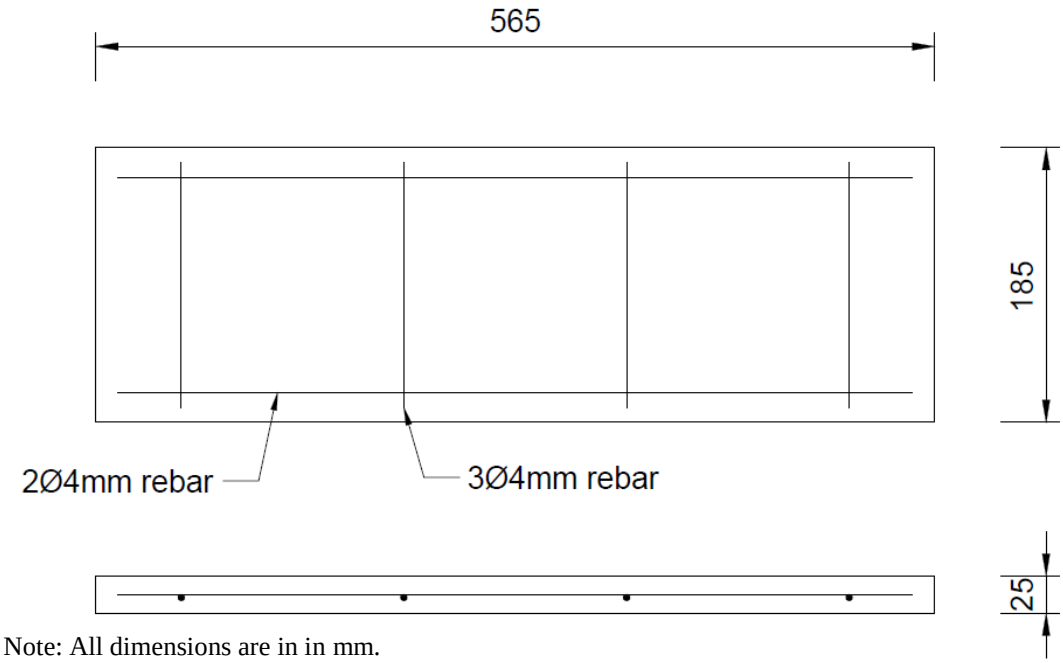

Note: All dimensions are in in mm.

Figure 4.5: T25-AR3.1SR23 specimen layout

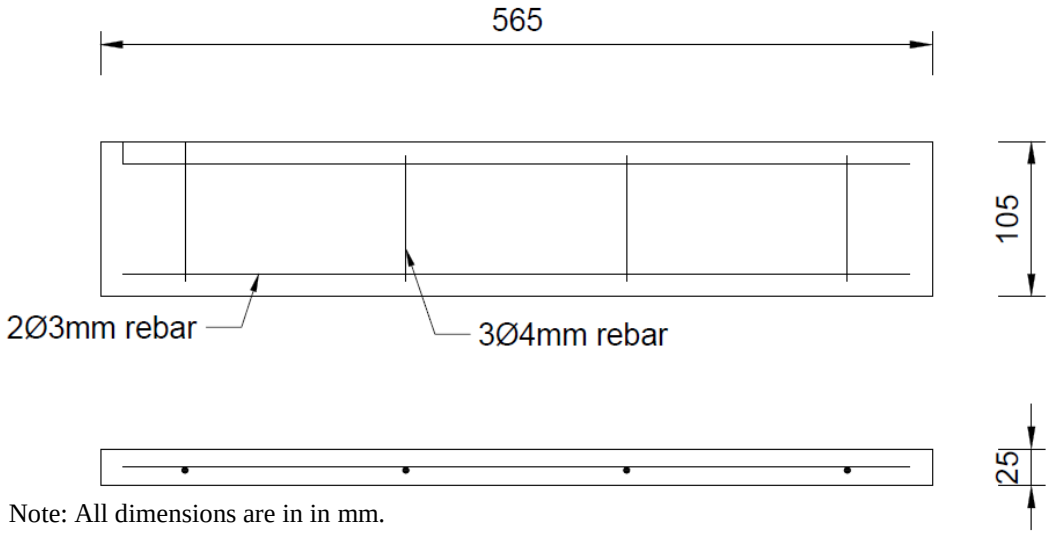

Note: All dimensions are in in mm.

Figure 4.6: T25-AR5.3SR23 specimen layout

4.2.2. Material Properties

4.2.2.1. Concrete

A lightweight self-compacting concrete mix proportion from the previous study in Chapter 3 was chosen for casting test specimens. Mix M40 was used and the detail of this mix proportion is summarized in Table 4.2. The uniaxial compressive strength of concrete cylinder for each wall specimen cast is furnished in Table 4.3.

Table 4.2: LWSCC mix design used for wall specimen

Mix	Cement (kg/m^3)	Fly Ash (kg/m^3)	Water (kg/m^3)	Sand (kg/m^3)	Coarse Aggregate (kg/m^3)	SP (kg/m^3)
M40	312	208	161.2	715	455	8.58

4.2.2.2. Steel

For wall specimen with 60mm thickness, Grade 300 steel mesh with diameter of 5mm and spacing of 200mm was used. Two layers of steel mesh were used with cover of 15mm and 30mm c/c spacing between two mesh. For 25mm thickness series, single layer of steel reinforcement was used. Since steel mesh with smaller diameter and spacing was not available, 25mm thickness wall specimen was reinforced by using steel reinforcing bar of sizes 3 to 4mm in diameter. The reinforcement ratios of 0.0059

and 0.0038 were provided for vertical and horizontal direction respectively in order to fulfil the minimum reinforcement requirement specified in ACI and AS3600.

4.2.3. Casting of Specimens

The formwork for specimen casting was prepared by using rectangular timber plank and plywood. All the wall panels were casted horizontally with one surface lying flat on the support to ensure no segregation of aggregates. Customized mortar spacer was used to provide cover for steel reinforcement at the bottom. Similar concrete batching procedures used in chapter 3 were adopted in casting concrete wall specimen. For fresh properties test, only slump flow test was carried out to indicate the workability of concrete. After completion of slump flow test, the fresh concrete was poured into formwork and cylinder mould without any physical vibration. Figure 4.7 shows freshly casted concrete wall specimen. The concrete wall specimens and cylinders were removed from formwork and moulds respectively after seven days of casting. For curing purpose during the first seven days after casting, a wet cotton cloth was put on the specimen surface and covered with plastic. Water was constantly added in order to maintain the moisture of cloth. After removal of formwork, all the specimens were fully wrapped in plastic and provided with moisture until the day of testing.

Figure 4.7: Freshly casted concrete wall specimen

Three specimens were prepared for each type of wall panel. For every batch of concreting, six test cylinders of standard size were prepared to obtain both compressive and tensile splitting strength of concrete at 7th, 14th and 28th day. Compressive strength obtained on the 28^{th} day was used as material properties in evaluating nominal load bearing capacity of wall by using design equations and Finite Element Analysis (FEA). The details of material strength obtained from the tests are summarized in Table 4.3.

4.2.4. Measurement of Specimen

The dimensions of hardened concrete wall specimens were measured and presented in Table 4.3. The actual eccentricity of each specimen during the setup was measured and the readings are shown in Table 4.3. The actual eccentricity value is also used in the numerical calculation and numerical modelling.

Table 4.3: Actual measurement, eccentricity and material properties

Specimen	Actual L (mm)	Actual W (mm)	Actual t (mm)	Actual eccentricity (mm)	Average compressive strength (MPa)	Average splitting tensile strength (MPa)
T25-AR1.8SR12-1	299	164	26	1.0	16.40	1.50
T25-AR1.8SR12-2	300	165	26	1.0	16.40	1.50
T25-AR1.8SR12-3	300	165	26	1.0	16.40	1.50
T25-AR1.8SR12-4	300	165	26	1.0	16.40	1.50
T25-AR1.8SR17-1	425	235	26	1.0	16.40	1.50
T25-AR1.8SR17-2	423	235	26	1.0	16.40	1.50
T25-AR1.8SR17-3	425	236	26	1.0	16.40	1.50
T25-AR1.8SR17-4	425	236	26	1.0	16.40	1.50
T25-AR1.8SR23-1	565	315	26	1.0	16.40	1.50
T25-AR1.8SR23-2	565	315	26	1.0	16.40	1.50
T25-AR1.8SR23-3	565	315	26	1.0	16.40	1.50
T25-AR1.8SR23-4	565	315	26	1.0	16.40	1.50
T25-AR3.1SR23-1	565	185	26	1.0	16.40	1.50
T25-AR3.1SR23-2	563	185	26	1.0	16.40	1.50
T25-AR3.1SR23-3	565	185	26	1.0	16.40	1.50
T25-AR3.1SR23-4	565	185	26	1.0	16.40	1.50
T25-AR5.3SR23-2	565	100	25	1.0	16.40	1.50
T25-AR5.3SR23-3	565	100	25	1.0	16.40	1.50
T60-AR5.3SR23-1	1400	260	62	2.5	13.70	1.10
T60-AR5.3SR23-2	1400	260	62	2.5	13.60	1.05
T60-AR5.3SR23-3	1399	260	61	2.5	13.30	1.04

Note: T25 series specimens were from the same batch of concrete.

4.2.5. Test Setup and Procedure

All the wall panels were tested with pinned connection at both the top and bottom end supports. Lotus Hydraulic Jack was used to transfer uniform load through a spreader beam as concentric load for T60 series specimen. As for T25 series, Gotech universal testing machine was used. For loading procedure, wall specimens were pre-loaded to 1kN to check and confirm that all the instruments were in working condition and to

eliminate the gaps. The load was then increased gradually until failure of the specimen. Linear Variable Displacement Transducers (LVDT) was installed at a quarter height, mid height and third quarter height of the wall to measure the horizontal displacement for wall specimen with 60mm thickness. For wall specimen with 25mm thickness, LVDT was only installed at mid height due to limit space. TML Data Logger TPS 530 was used to record the loading and displacement data. The support condition detail is showed in Figure 4.8. Figure 4.9 shows the test setup for T60 and T25 series. The behaviour of the specimens was observed and recorded throughout the tests.

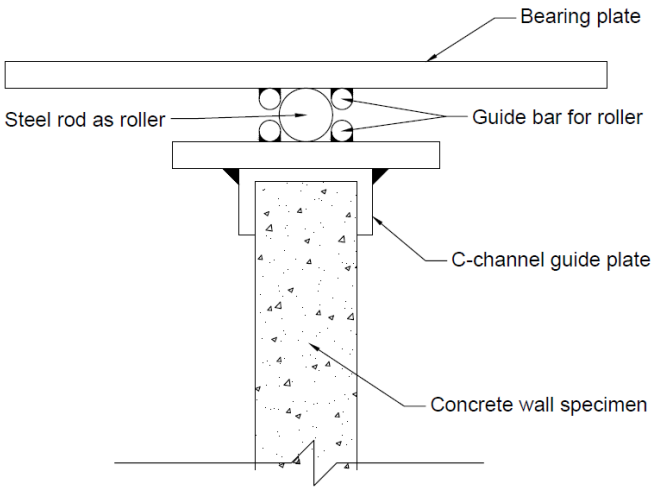

Figure 4.8: Detail of support condition

(a) **(b)**

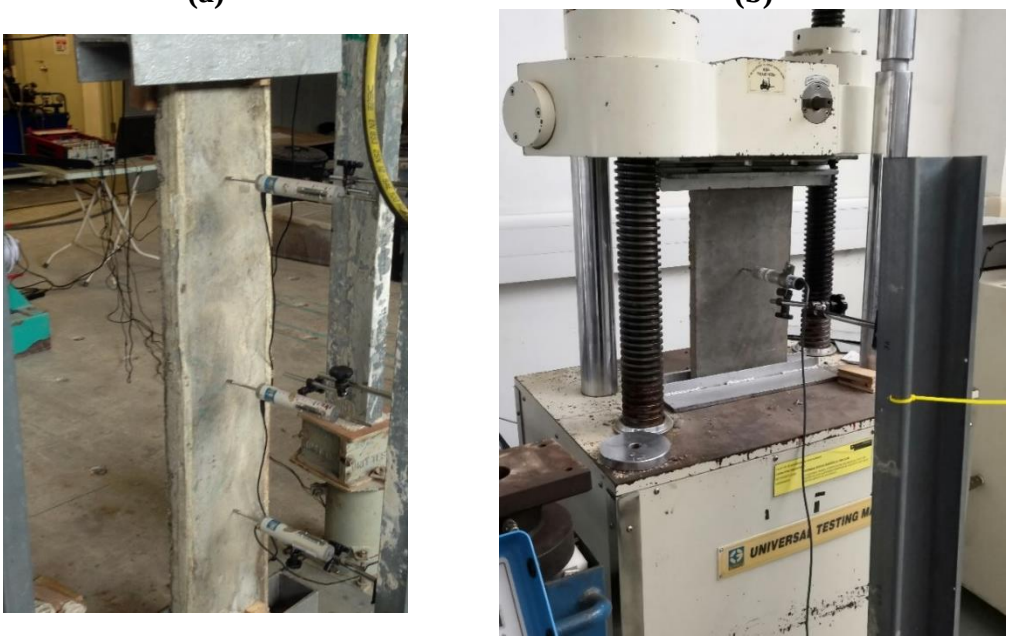

Figure 4.9: Experimental test setup for (a) T60 series, (b) T25 series

4.3. Test Results and Observation

4.3.1. Crack Patterns and Failure Mode

The failure characteristics of T60 series wall specimens are shown in Figure 4.11. Even though the wall specimens were designed to test under concentric loading, a small eccentricity still existed due to imperfection of fabrication of experimental setup components. A large horizontal crack was noticed at both sides of wall panel near the centre. Some cracks due to crushing were noticed at the loading surface and support end. T60-AR5.3SR23 specimen failed predominantly by buckling in a single curvature shape with maximum deflection at the centre. The slenderness ratio of the specimen was 23 and it was regarded as slender walls since it bended at mid height. This shows good agreement with the findings of Sam Fragomeni and Mendis (1996), in which concrete walls with slenderness ratio equal or greater than 20 could commonly fail by buckling with horizontal cracks at mid height.

The failure modes of T25 series specimens are shown in Figure 4.10 and Figure 4.11. Similar to T60 series wall, a small eccentricity also existed. Specimen T25-AR1.8SR12 with slenderness ratio of 12 failed by crushing as shown in Figure 4.10(a). An inclined crack was observed near the bottom end support. No obvious curvature and cracking were observed at mid height for the specimen. This shows good agreement with the findings of Saheb and Desayi (1989) that crushing is the predominant failure mode for concrete wall with low slenderness ratio even for lightweight concrete. Specimen T25-AR1.8SR17, T25-AR1.8SR23, T25-AR3.1SR23 and T25-AR15.3SR23 failed by bending at mid height. The slenderness ratios of these specimens were in the range of 17-23. Similarly, horizontal crack near the wall centre as well as some cracks near the support ends were also observed for these specimens. These specimens failed predominately by buckling since an obvious curvature shape with significant cracking at mid height were observed when they failed. This study shows good agreement with the findings of Oberlender (1975) and Saheb and Desayi (1989) that concrete wall failed by crushing at support end for wall with low slenderness ratio while those with high slenderness ratio failed by buckling at mid height.

With respect to walls of similar geometry ratio, both the larger wall (T60-AR5.3SR23) and smaller wall (T25-AR5.3SR23) have shown similar failure mode and cracking

patterns. As illustrated in Figure 4.11, both walls failed by buckling in a single curvature with a horizontal crack developed near the mid height. Similar stress distribution has been manifested in both cases. Thus, the effect of specimen size has been observed to be negligible.

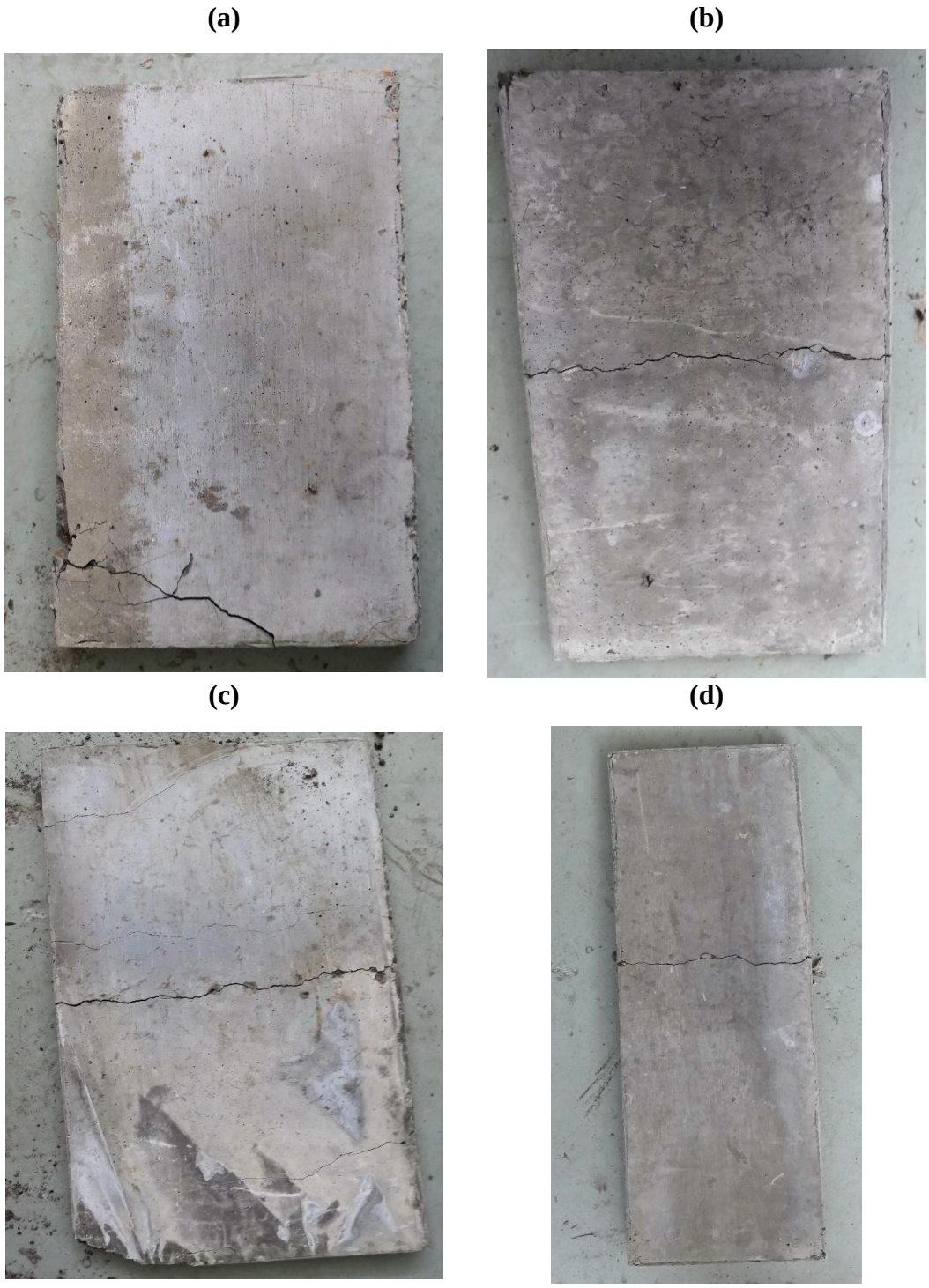

Figure 4.10: Failure mode of specimen (a) T25-AR1.8SR12, (b) T25-AR1.8SR17, (c) T25-AR1.8SR23 (d) T25-AR3.1SR23

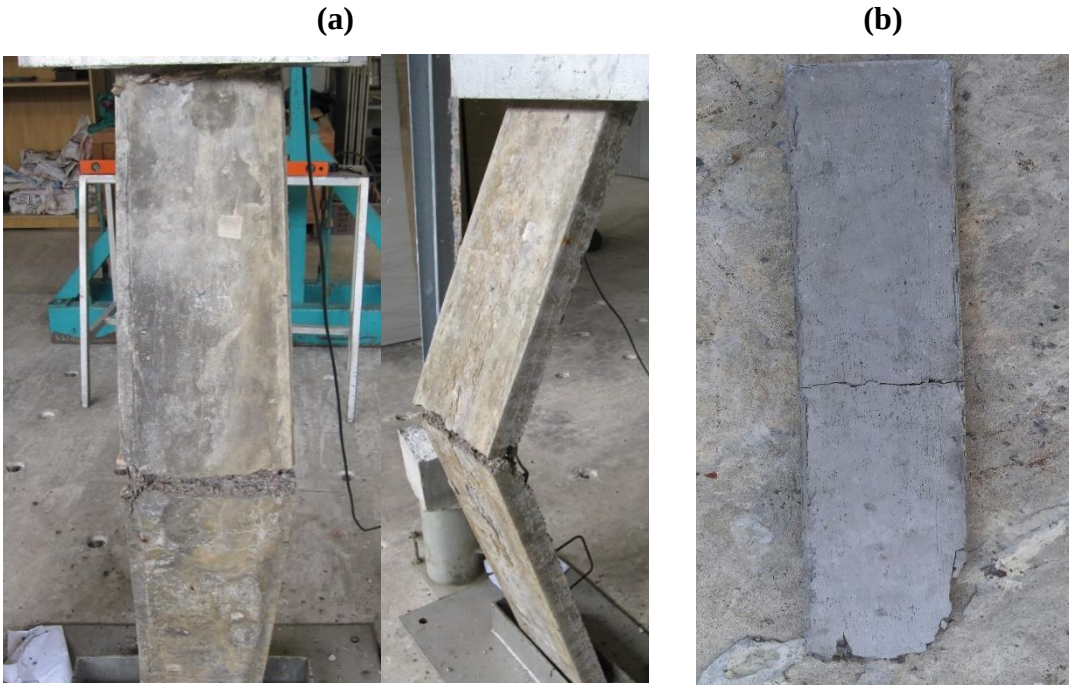

Figure 4.11: Failure mode of specimen: (a) T60-AR5.3SR23, (b) T25-AR5.3SR23

4.3.2. Load versus Deflection Behaviour

The axial load versus lateral deflection gives the structural deformation response of concrete wall under loading. Figure 4.12, Figure 4.13 and Figure 4.14 show the load versus lateral deflection profile of wall at top quarter, mid height and bottom quarter respectively for specimen T60-AR5.3SR23. These curves showed that the concrete wall specimens exhibited ductile behaviour with continuous increasing of lateral deflection with load. The curves showed linear behaviour in the initial loading region, followed by non-linear curve up to the ultimate failure load. The curves showed that only slight deflection was produced with increasing load in the linear region and the linearity was about 45-55% of ultimate failure load. In the nonlinear region, the lateral deflection increased rapidly as the load was increased. The deflection profile of specimens showed fairly uniform curvature along the height with maximum deflection at mid height.

For T25 series wall specimen, the load versus mid height lateral deflection curves are illustrated from Figure 4.15 to Figure 4.19. Similarly, the curves showed linear behaviour in the initial region and were followed by nonlinear trend up to failure.

Compared to T60 wall specimen, T25 wall exhibited smaller deflection at mid height. Among these five types of wall, specimen T25-AR1.8SR12 showed the lowest and negligible deflection as it failed by crushing.

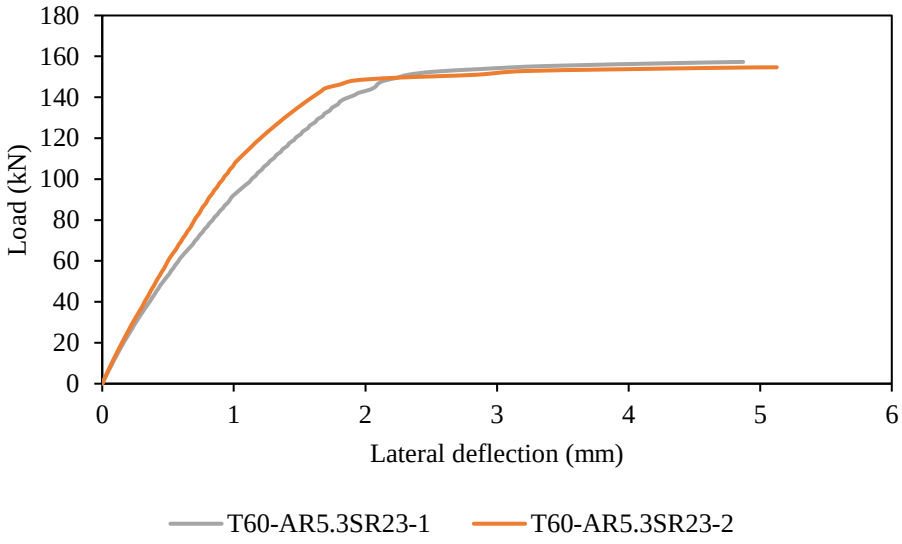

Figure 4.12: Load versus lateral deflection at top quarter of specimen T60-AR5.3SR23

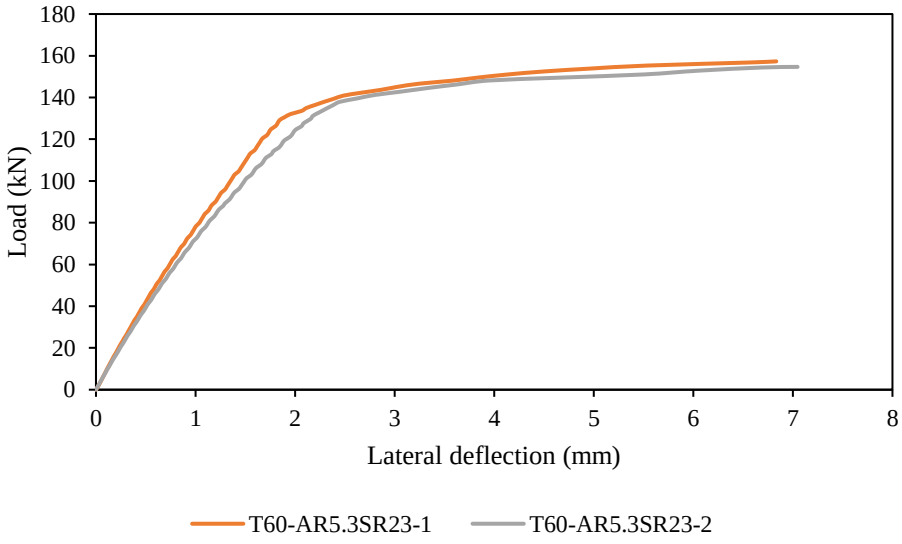

Figure 4.13: Load versus lateral deflection at mid height of specimen T60-AR5.3SR23

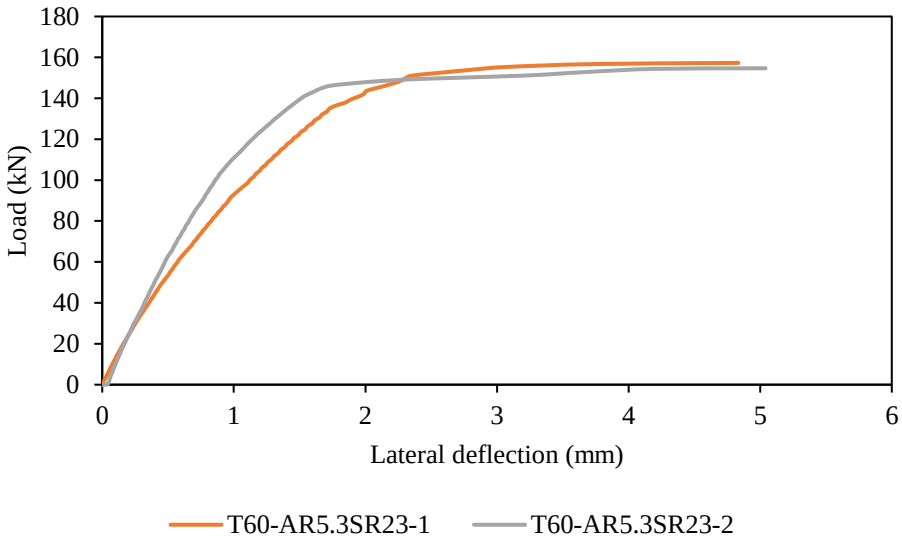

Figure 4.14: Load versus lateral deflection at bottom quarter of specimen T60-AR5.3SR23

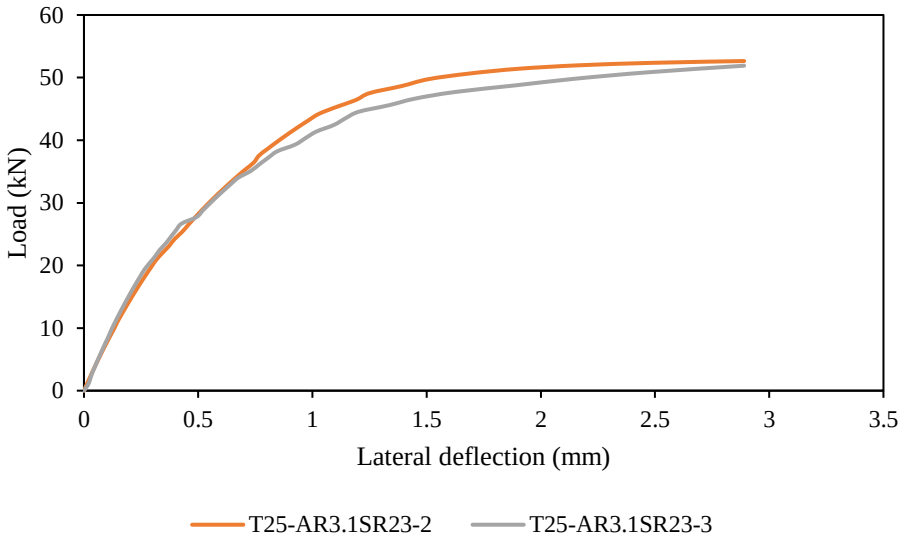

Figure 4.15: Load versus lateral deflection at mid height of specimen T25-AR1.8SR12

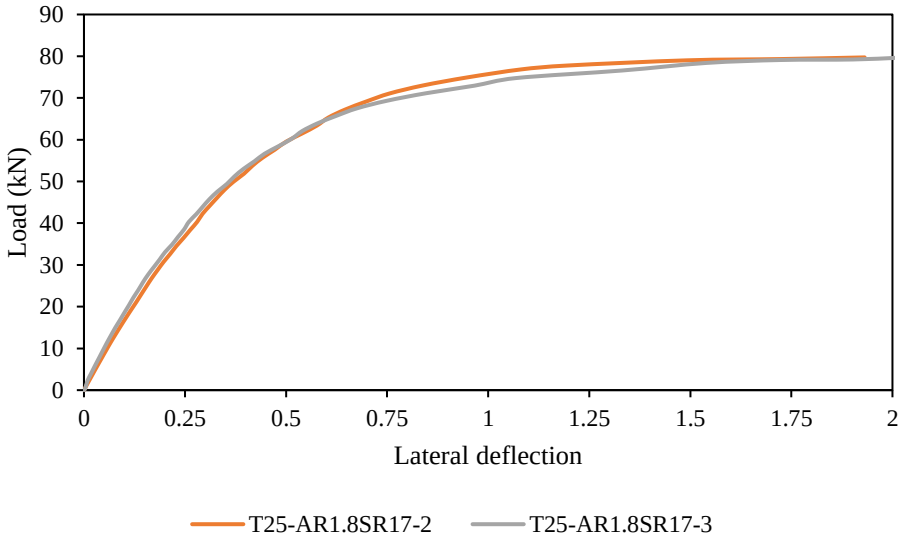

Figure 4.16: Load versus lateral deflection at mid height of specimen T25-AR1.8SR17

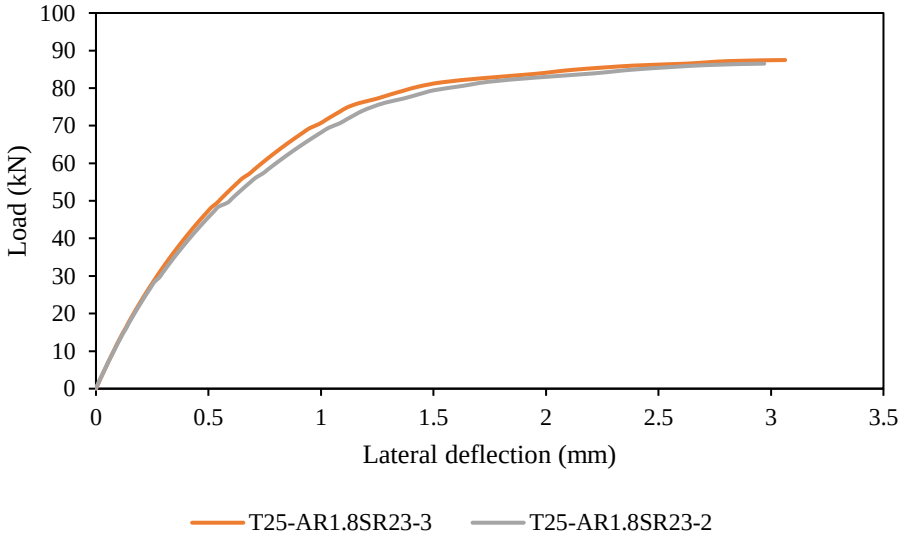

Figure 4.17: Load versus lateral deflection at mid height of specimen T25-AR1.8SR23

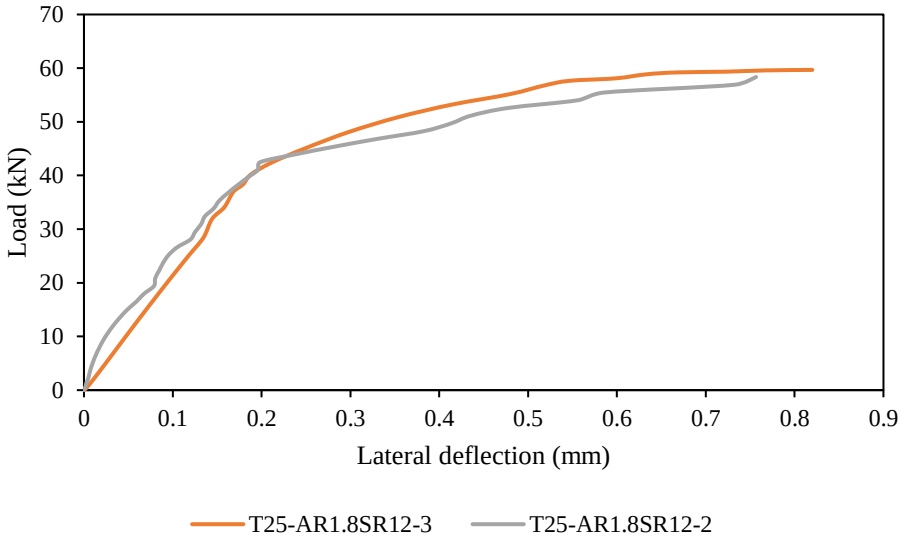

Figure 4.18: Load versus lateral deflection at mid height of specimen T25-AR3.1SR23

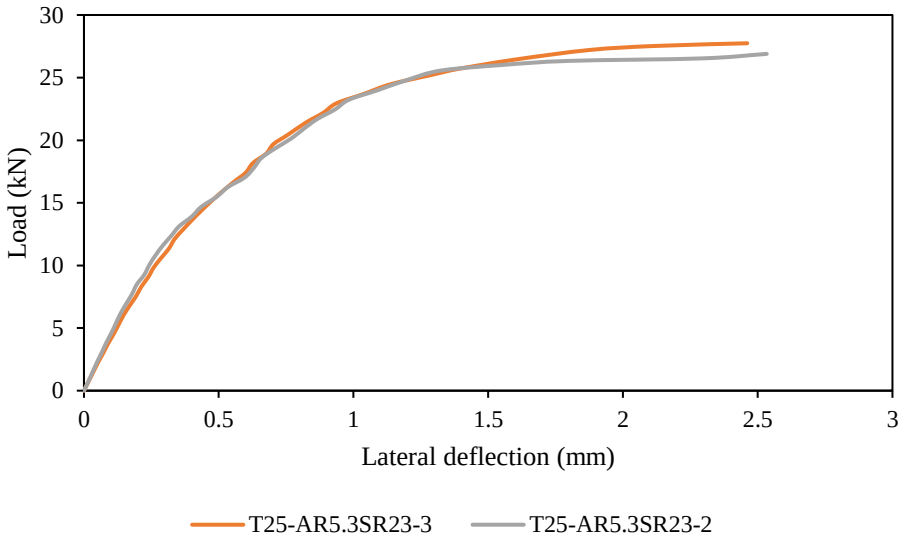

Figure 4.19: Load versus lateral deflection at mid height of specimen T25-AR5.3SR23

4.3.3. Failure Loads

The respective failure modes and loads of all specimens are summarized in Table 4.4. The failure loads are expressed as dimensionless values, which are axial strength ratios. This allows the discernible comparison of ultimate axial capacity of concrete wall specimens with different cross-sectional areas. The average axial strength ratios of test specimens are in the range of 0.64 to 0.83. Comparison of specimens with similar

geometry ratios showed that specimen T25-AR5.3SR23 and T60-AR5.3SR23 have close axial strength ratio. Both specimens have the same geometry ratio but different values of thickness. It can be established that concrete wall with similar geometry ratio has similar axial strength ratio even if its dimensions are different.

For comparison of axial strength ratio among all the specimens, it is noted that axial strength ratio decreased with increasing slenderness ratio from 0.83 to 0.64. It is observed that the increase of aspect ratio has insignificant effect on axial strength. The analysis of these two parameters are presented in the next section.

Table 4.4: Experimental results for concrete load bearing wall test

Specimen	Failure load (kN)	Average failure load P_{exp} (kN)	Standard Deviation	Failure mode	Axial Strength ratio $P_{exp}/f'cAg$	Average axial strength ratio $P_{exp}/f'cAg$
T25-AR1.8SR12-1	56.55	57.17	2.41	C	0.81	0.81
T25-AR1.8SR12-2	58.35			C	0.83	
T25-AR1.8SR12-3	59.68			C	0.85	
T25-AR1.8SR12-4	54.12			C	0.77	
T25-AR1.8SR17-1	77.72	78.00	2.25	B	0.78	0.78
T25-AR1.8SR17-2	79.72			B	0.80	
T25-AR1.8SR17-3	79.64			B	0.79	
T25-AR1.8SR17-4	74.92			B	0.74	
T25-AR1.8SR23-1	83.36	85.59	1.80	B	0.62	0.64
T25-AR1.8SR23-2	86.52			B	0.64	
T25-AR1.8SR23-3	87.48			B	0.65	
T25-AR1.8SR23-4	84.99			B	0.63	
T25-AR3.1SR23-1	50.49	51.20	1.31	B	0.64	0.65
T25-AR3.1SR23-2	52.65			B	0.67	
T25-AR3.1SR23-3	51.90			B	0.66	
T25-AR3.1SR23-4	49.76			B	0.63	
T25-AR5.3SR23-2	26.89	27.32	0.60	B	0.66	0.67
T25-AR5.3SR23-3	27.74			B	0.68	
T60-AR5.3SR23-1	157.30	155.06	2.25	B	0.71	0.71
T60-AR5.3SR23-2	155.07			B	0.71	
T60-AR5.3SR23-3	152.80			B	0.72	

Note: “B” indicates buckling and “C” indicates crushing.

4.3.3.1. Effect of Slenderness Ratio

In order to study the effect of slenderness ratio on lightweight concrete wall, axial strength ratio versus slenderness ratio curves are plotted and illustrated in Figure 4.20. It is noticed that axial strength ratio decreased nonlinearly with the increase of slenderness ratio. The reduction of strength was about 30% when the slenderness ratio increased from 12 to 23. For less slender wall T25-AR1.8SR12, the axial strength was close to the full cross-sectional capacity and its failure mode was characterized by material failure. Significant reduction was noticed when slenderness ratio was increased from 17 to 23. This finding showed that geometrical nonlinearity has great influence on the load carrying capacity of concrete wall (Huang et al., 2014). Failure of slender wall is dominated by buckling mode in which the lateral deflection increases due to vertical loading, thus inducing secondary eccentricity which causes the wall to fail before material failure.

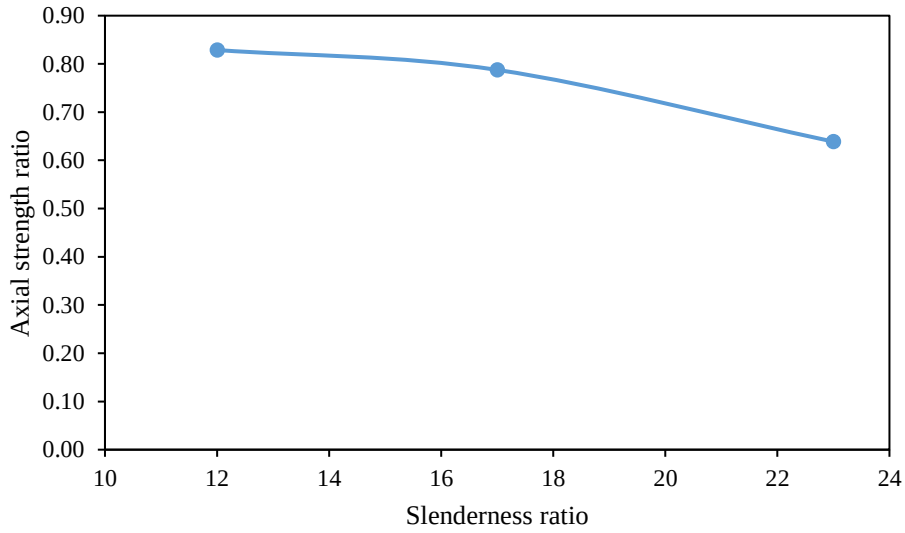

Figure 4.20: Axial strength ratio versus slenderness ratio

4.3.3.2. Effect of Aspect Ratio

To investigate the influence of aspect ratio, values of axial strength ratio are plotted against aspect ratio values and illustrated in Figure 4.21. It is observed that aspect ratio had negligible effect on the axial strength of concrete wall when aspect ratio was increased from 1.8 to 5.3 in the present study. A few researchers (Ganesan et al., 2013; Saheb & Desayi, 1989) stated that aspect ratio had great influence on the ultimate strength of concrete wall. Saheb and Desayi (1989) studied aspect ratio from 0.67 to 2

with low slenderness ratio of 12 and noticed that the axial strength ratio decreased from 0.72 to 0.66. The thickness of wall studied was 50mm. In the study of Ganesan et al. (2013), the slenderness ratio was fixed at 15 and aspect ratios were varied from 1 to 1.8. The results showed that the axial strength ratio decreased from 0.6 to 0.59 and then 0.5 when aspect ratio was increased from 1 to 1.5 and 1.875 respectively. The thickness of wall studied was 40mm. In this research, slenderness ratio of 23 was chosen to study the effect of aspect ratio. The effect of aspect ratio might not exist for concrete wall with high slenderness ratio. As for the slight improvement of axial strength ratio with decrease of aspect ratio which was claimed by the researchers (Ganesan et al., 2013; Saheb & Desayi, 1989), it could be due to margin of error since only one specimen was tested in both cases. According to Ho and Doh (2019), axial strength ratio of wall is influenced by aspect ratio through effective height when at least one of the edges of wall is supported. However, for wall under one-way action in this study, the side edges of concrete wall are not restrained. In this scenario, aspect ratio has no influence on wall axial strength ratio. Nevertheless, further investigation and discussion are to be carried out by using Finite Element modelling in section 5.5.

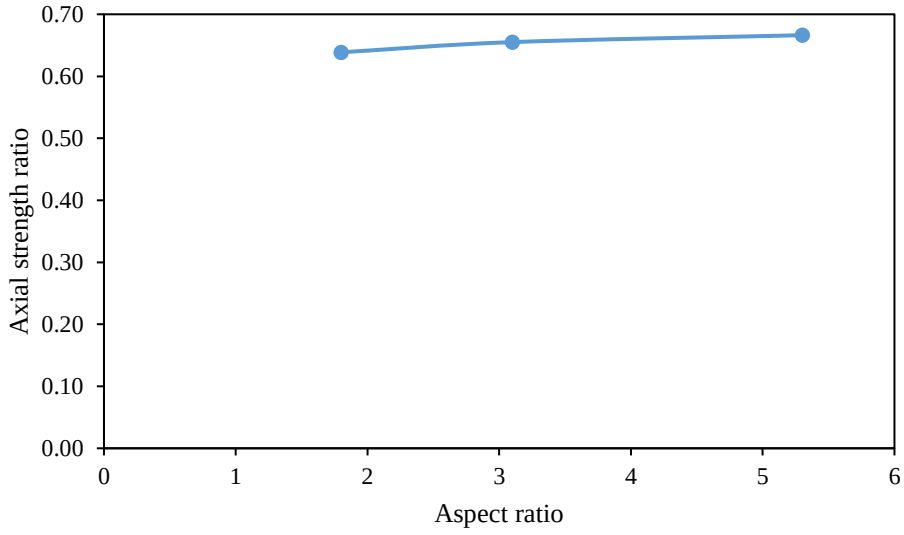

Figure 4.21: Axial strength ratio versus aspect ratio

4.3.4. Evaluation of Current Design Equations

4.3.4.1. Design Equations from Standards

The experimental results in this study are compared with the calculated results from design equations in standard ACI, AS 3600, BS and Eurocode 2 and the outcomes are

summarized in Table 4.5. The calculation details are presented in Appendix C. The ratios of experimental results to calculated results are also included. The experimental results are plotted in the envelopes of these design equations and the resultant graphs are illustrated in Figure 4.22.

Table 4.5: Comparison of experiment results and calculated results using various standard design equation

Specimens	P_{exp} (kN)	ACI		AS		BS		Eurocode 2	
		P_{cal} (kN)	P_{cal}/P_{exp} Ratio	P_{cal} (kN)	P_{cal}/P_{exp} Ratio	P_{cal} (kN)	P_{cal}/P_{exp} Ratio	P_{cal} (kN)	P_{cal}/P_{exp} Ratio
T25-AR1.8SR12	57.17	33.61	0.59	35.71	0.62	17.85	0.31	53.09	0.93
T25-AR1.8SR17	78.00	40.83	0.52	44.60	0.57	22.30	0.28	63.51	0.81
T25-AR1.8SR23	85.59	39.81	0.47	46.42	0.54	23.21	0.27	66.33	0.77
T25-AR3.1SR23	51.20	23.43	0.46	27.31	0.53	13.65	0.26	39.01	0.76
T25-AR5.3SR23	27.32	10.46	0.38	12.52	0.46	6.26	0.23	18.06	0.66
T60-AR5.3SR23	155.06	60.03	0.39	71.07	0.46	35.53	0.23	101.97	0.66
Mean			0.47		0.53		0.26		0.77
Standard deviation			0.08		0.06		0.03		0.10

It is noticed that the design equations from the standards have safely predicted the failure load of lightweight concrete wall. The P_{cal}/P_{exp} ratio of ACI equation varied from 0.38 to 0.58. The underestimation of ACI equation is mainly due to the assumption made by ACI equation that loading is applied within the eccentricity of t/6. The experiments in this research were carried out with almost concentric loading. Therefore, the gross underestimation made by ACI equation proves that it is not suitable to determine ultimate load of concrete wall with other eccentricities.

As for AS 3600 design equation, the P_{cal}/P_{exp} ratio is varied from 0.46 to 0.61. The ultimate strength of concrete wall loaded at different values of eccentricity can be determined by AS 3600 equation. However, this equation still underestimates the ultimate strength of lightweight wall without reduction factor, as shown in this research. For BS design equation, the P_{cal}/P_{exp} ratio is definitely lower than that of AS 3600 equation since BS equation uses lower factor of 0.3 instead of 0.6. The P_{cal}/P_{exp} ratio also varies from 0.35 to 0.45. The comparisons of experimental and calculated results have highlighted that AS 3600 equation has the limitation in which the equation is conservative and no parameter is allowed for lightweight concrete wall.

Among the design equations from the four standards, the one from Eurocode 2 gives load estimation with the best accuracy. The P_{cal}/P_{exp} ratio varies from 0.91 to 0.66. However, Eurocode 2 equation becomes less accurate when the slenderness ratio is increased. Nevertheless, this design equation takes into consideration the parameters similar to AS 3600 but appears to show better accuracy in results when compared with the latter. Unfortunately, similar to the other three standards, Eurocode 2 does not have the parameter to consider the effect of material property of lightweight concrete.

Generally, lightweight concrete wall has lower axial strength ratio due to its lower elastic modulus. However, the design equations provided by various design standards are still conservative in determining its ultimate capacity. None of the design equations provides factor to allow for lightweight concrete material property. This has demonstrated that modified equation is required to estimate the axial strength of concrete wall regardless of it being manufactured from lightweight or normal weight concrete.

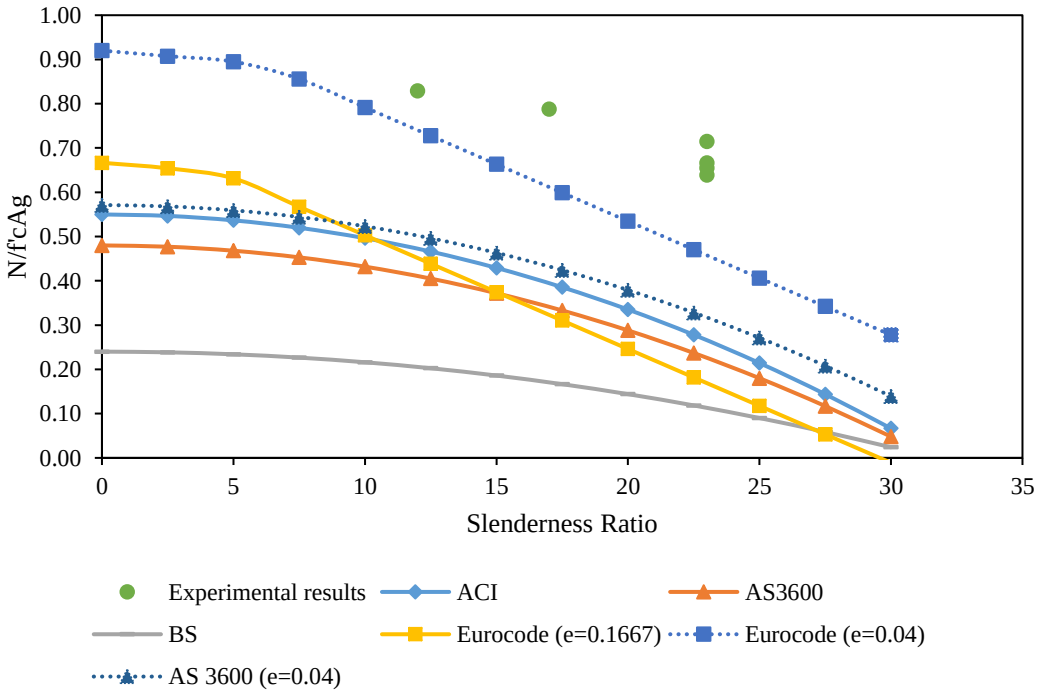

Figure 4.22: Experimental versus calculated results from standard equations

4.3.4.2. Design Equation from Previous Research

The experimental results are also compared with the results calculated from design equations proposed by various researchers. The comparisons are summarized in Table

4.6 and illustrated in Figure 4.23. The ratios of experimental result to calculated result are also included. The actual eccentricity is used in the calculation of ultimate axial capacity of concrete wall.

Similar to ACI equation, in the equations proposed by the researchers (Ganesan et al., 2012; Ganesan et al., 2013; Kripanarayanan, 1977; Oberlender, 1975; Pillai & Parthasarathy, 1977; Saheb & Desayi, 1989; Zielinski et al., 1983), load is assumed to be applied within the eccentricity of t/6. These equations yield values of P_{cal}/P_{exp} ratio in the range of 0.35-0.69, indicating that they are very conservative for lightweight concrete wall. As for the equation of Ganesan et al. (2012), P_{cal}/P_{exp} ratio is in the range of 0.45 – 0.85. This equation yields results close to the experimental results for specimen T25-AR1.8SR12, T25-AR1.8SR17, T25-AR1.8SR23 and T25-AR3.1SR23. Similar trend is observed for the calculated results from Ganesan et al. (2013) equation. As shown in Figure 4.23, the envelopes of these two equations showed an increasing trend of ultimate axial capacity when slenderness ratio was increased from 0 to 15. This increasing trench has brought the axial capacity envelope closer to the ultimate axial capacity of specimen T25-AR1.8SR12, T25-AR1.8SR17and T25-AR1.8SR23. This is the reason of the improved accuracy of these two equations in estimating the ultimate capacity of these specimens.

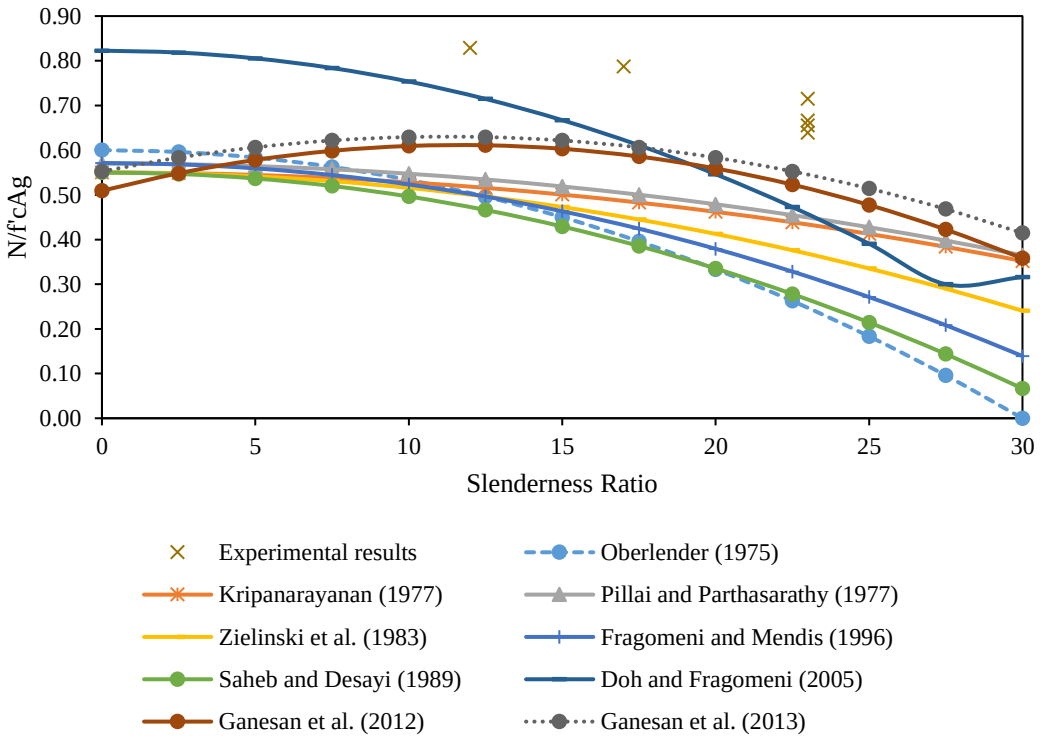

Figure 4.23: Experimental versus calculated results from previous researches

Sam Fragomeni and Mendis (1996) and Doh and Fragomeni (2005) modified the wall design equation from AS 3600. The calculated results of Sam Fragomeni and Mendis (1996) are similar to those calculated from AS 3600 equation since the authors only modified AS 3600 equation for high strength concrete. As for results determined by using equation proposed by Doh and Fragomeni (2005), the Pcal /Pexp ratio is improved compared with AS 3600 equation and is in the range of 0.64-0.92. This equation is improved by using a factor to allow for nonlinear contribution of compressive strength with axial load carrying capacity. However, none of the equations has taken into consideration the effect of lightweight concrete which has lower elastic modulus and higher ductility as material properties.

Table 4.6: Comparison of experimental results with calculated results using design equation from previous research

Specimen	P_{exp} (kN)	Oberlender (1975)		Kirpanarayan (1977)		Pillai and Parthasarathy (1977)		Zielinski et al (1983)		Saheb and Desayi (1989)		Sam Fragomeni and Mendis (1996)		Doh and Fragomeni (2005)		Ganesan (2012)		Ganesan (2013)	
		P_{cal} (kN)	P_{cal}/P_{exp} Ratio	P_{cal} (kN)	P_{cal}/P_{exp} Ratio	P_{cal} (kN)	P_{cal}/P_{exp} Ratio	P_{cal} (kN)	P_{cal}/P_{exp} Ratio	P_{cal} (kN)	P_{cal}/P_{exp} Ratio	P_{cal} (kN)	P_{cal}/P_{exp} Ratio	P_{cal} (kN)	P_{cal}/P_{exp} Ratio	P_{cal} (kN)	P_{cal}/P_{exp} Ratio	P_{cal} (kN)	P_{cal}/P_{exp} Ratio
T25-AR1.8SR12	57.17	35.91	0.63	36.57	0.64	37.90	0.66	36.36	0.64	37.66	0.66	35.71	0.62	51.43	0.90	43.38	0.76	46.36	0.81
T25-AR1.8SR17	78.00	42.39	0.54	49.31	0.63	51.10	0.66	49.04	0.63	45.84	0.59	44.60	0.57	64.23	0.82	60.45	0.77	64.66	0.83
T25-AR1.8SR23	85.59	38.30	0.45	59.92	0.70	62.10	0.73	59.59	0.70	44.72	0.52	46.42	0.54	66.86	0.78	72.82	0.85	79.32	0.93
T25-AR3.1SR23	51.20	22.55	0.44	35.21	0.69	36.49	0.71	35.01	0.68	25.79	0.50	27.31	0.53	39.33	0.77	36.96	0.72	43.00	0.84
T25-AR5.3SR23	27.32	9.66	0.35	17.33	0.63	17.96	0.66	17.23	0.63	11.52	0.42	12.52	0.46	18.03	0.66	12.17	0.45	17.47	0.64
T60-AR5.3SR23	155.06	56.35	0.36	95.92	0.62	99.40	0.64	95.38	0.62	67.35	0.43	71.07	0.46	108.02	0.70	71.91	0.46	100.54	0.65
Mean			0.46		0.65		0.68		0.65		0.52		0.53		0.77		0.67		0.78
Standard deviation			0.11		0.03		0.03		0.03		0.09		0.06		0.09		0.17		0.11

4.4. Summary

In this chapter, the experimental results of lightweight concrete wall panel subjected to axial loading have been presented, discussed and analysed. Five different types of lightweight concrete walls with 25mm thickness and one lightweight concrete wall with 60mm have been tested with pinned-end condition. In total, testing has been performed on 24 lightweight concrete wall specimens.

Generally, concrete wall of low slenderness ratio value failed by crushing while wall of higher slenderness ratio value failed by buckling in a single curvature shape with horizontal cracks at mid height. The load versus lateral deflection curves showed linear behaviour in the initial loading region, followed by non-linear behaviour up to the ultimate failure load. It is noted that the ultimate axial capacity of lightweight wall decreases with increasing of slenderness ratio. As for aspect ratio, it is concluded from the experimental results that it has little effect on the ultimate axial capacity of slender wall.

The experimental failure loads are compared with design equations from various standards and researchers. It is noticed that all the available design equations are conservative. None of them takes into consideration of the material properties of lightweight concrete. Such simplified design equations are not able to capture the nonlinearity of concrete and it is necessary to derive an improved design equation. Further investigations of parameters that affect the ultimate axial capacity of concrete wall are explored by using finite element analysis in Chapter 5.

5. Numerical Modelling and Analysis

5.1. Introduction

Finite element analysis (FEA) is one of the most powerful tools which can be deployed to model engineering structures so as to provide more precise solutions to engineering problems. This chapter presents the details of finite element model development for lightweight concrete wall panel subjected to axial compression loading. In this study, ABAQUS 6.14 is used in finite element analysis of concrete wall panel. The ABAQUS finite element software is used to construct the wall model and three dimensional 8-node reduced integration brick element, C3D8R, is utilized for the concrete wall. Concrete Damaged Plasticity (CDP), a constitutive model based on the combination of damage mechanics and plasticity, is used in modelling the concrete material of wall under axial loading. The results of developed FEA model are verified and validated by using experimental results from chapter 4.

5.2. Concrete Damaged Plasticity

Concrete Damaged Plasticity (CDP) is a material model derived by incorporating two main failure mechanisms of concrete, which are the tensile cracking and compression crushing. It has been chosen as concrete material model in this research because it is able to capture the stiffness degradation and damage to the concrete as the concrete either cracks in tension or crushes in compression. The information so obtained is useful in the comparison of the FEA results with experimental results. The feature of this model is that it offers powerful capability in modelling quasi-brittle material, which is concrete, in quasi-static analysis. CDP model of ABAQUS was developed based on the research of Lubliner et al. (1989), Lee and Fenves (1998).

5.2.1. Strain Rate

In CDP model, the concrete stress in both tension and compression exhibits a linear elastic relationship before the concrete elements reach the value of σ_{to} and σ_{co}. These stresses correspond to the tensile failure stress and initial compressive yield stress respectively. The total strain rate of concrete comprises of elastic strain rate ($\dot{\varepsilon}^{e}$) and plastic strain rate ($\dot{\varepsilon}^{pl}$) as indicated in Eq. 5-1.

$$\dot{\varepsilon} = \dot{\varepsilon}^{e} + \dot{\varepsilon}^{pl} \quad \text{Eq. 5-1}$$

5.2.2. Effective Stress and Evolution of the Scalar Damage Factor

The stress-strain relationship of concrete is represented by using scalar damaged elasticity as below:

$$\sigma = (1 - d) D_0^{el} : (\varepsilon - \varepsilon^{pl}) \quad \text{Eq. 5-2}$$

where D_0^{el} is the initial elastic stiffness of concrete and d is the scalar damage parameter/ stiffness degradation values. In ABAQUS, two hardening variables, which are equivalent plastic strain $\tilde{\varepsilon}_t^{pl}$ and $\tilde{\varepsilon}_c^{pl}$ in tension and compression respectively, are used to represent the damaged state of CDP model in tension and compression. Under axial loading conditions, transformation of the uniaxial stress-strain curves into stress versus plastic strain curves can take the form of

$$\sigma_t = \sigma_t\left(\tilde{\varepsilon}_t^{pl}, \dot{\varepsilon}_t^{pl}, \theta, f_i\right) \quad \text{Eq. 5-3}$$

$$\sigma_c = \sigma_c\left(\tilde{\varepsilon}_c^{pl}, \dot{\varepsilon}_c^{pl}, \theta, f_i\right) \quad \text{Eq. 5-4}$$

where θ is the temperature and f_i is other pre-defined field variables. The equivalent plastic strains are then computed as below:

$$\tilde{\varepsilon}_t^{pl} = \int_0^t \dot{\tilde{\varepsilon}}_t^{pl}\, dt \quad \text{Eq. 5-5}$$

$$\tilde{\varepsilon}_c^{pl} = \int_0^t \dot{\tilde{\varepsilon}}_c^{pl}\, dt \quad \text{Eq. 5-6}$$

For concrete which is uniaxially loaded in tension and compression, the effective plastic strain rates are respectively represented by

$$\dot{\tilde{\varepsilon}}_t^{pl} = \dot{\varepsilon}_{t11}^{pl} \quad \text{Eq. 5-7}$$

$$\dot{\tilde{\varepsilon}}_c^{pl} = \dot{\varepsilon}_{c11}^{pl} \quad \text{Eq. 5-8}$$

When unloaded from any point on the strain softening part of stress-strain curve, the elastic stiffness of concrete tends to be degraded. This degradation is represented by two damaged function (d_t and d_c), which are expressed as the function of plastic strains, temperature and field variables, as shown in Eq. 5-9 and Eq. 5-10. These damaged variables take the value from zero, which indicates unimpaired material stiffness, to one, depicting the total loss of stiffness.

$$d_t = d_t\left(\tilde{\varepsilon}_t^{pl}, \theta, f_i\right) \quad \text{Eq. 5-9}$$

$$d_c = d_c\left(\tilde{\varepsilon}_c^{pl}, \theta, f_i\right) \quad \text{Eq. 5-10}$$

Figure 5.1 and Figure 5.2 illustrate the stress-strain relation of concrete subjected to tension and compression respectively. In the figures, E_o represent the initial undamaged elastic stiffness of concrete. The stress-strain relationships of concrete which is subjected to uniaxial tension and compression loadings are characterized by Eq. 5-11 and Eq. 5-12 respectively.

$$\sigma_t = (1-d)E_o\left(\varepsilon_t - \tilde{\varepsilon}_t^{pl}\right) \quad \text{Eq. 5-11}$$

$$\sigma_c = (1-d)E_o\left(\varepsilon_c - \tilde{\varepsilon}_c^{pl}\right) \quad \text{Eq. 5-12}$$

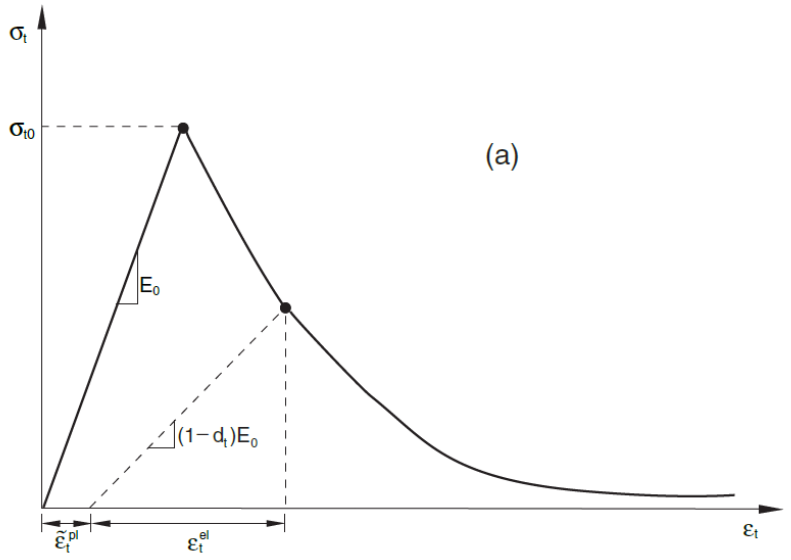

Figure 5.1: Reponses of concrete under uniaxial loading in tension

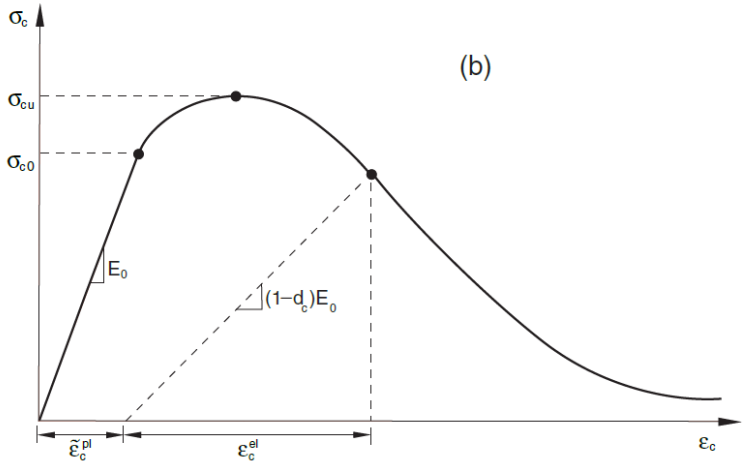

Figure 5.2: Reponses of concrete under uniaxial loading in compression

As concrete starts to crack and the consequent cracking propagates, the available load-carrying cross-sectional area is reduced, resulting in increase of the effective stress. The effective cohesion stress in tension and that in compression are represented by Eq. 5-13 and Eq. 5-14 respectively. These two stresses are used to determine the yield surface size.

$$\bar{\sigma}_t = E_o\left(\varepsilon_t - \tilde{\varepsilon}_t^{pl}\right) \quad \text{Eq. 5-13}$$

$$\bar{\sigma}_c = E_o\left(\varepsilon_c - \tilde{\varepsilon}_c^{pl}\right) \quad \text{Eq. 5-14}$$

The modulus elasticity *E* of concrete damaged plasticity is expressed as the function of scalar degradation variable, d as Eq. 5-15.

$$E = (1-d)E_o \quad \text{Eq. 5-15}$$

As a function of stress state and the uniaxial damage variables in both tension and compression (s_t and s_c), the stiffness degradation variable is represented by Eq. 5-16.

$$(1-d) = (1-s_t d_c)(1-s_c d_t) \;\; 0 \le s_t, s_c \le 1 \quad \text{Eq. 5-16}$$

where s_t and s_c are function of stress state which account for stiffness recovery effect. These variables are characterized by Eq. 5-17 and Eq. 5-18.

$$s_t = 1 - w_t r*(\sigma_{11}) \;\; 0 \le w_t \le 1 \quad \text{Eq. 5-17}$$

$$s_c = 1 - w_c\left(1 - r*(\sigma_{11})\right) \;\; 0 \le w_c \le 1 \quad \text{Eq. 5-18}$$

where

$$r*(\sigma_{11}) = H(\sigma_{11}) = \begin{cases} 1 \; if \; \sigma_{11} > 0 \\ 0 \; if \; \sigma_{11} < 0 \end{cases} \quad \text{Eq. 5-19}$$

The weight factor w_t and w_c are material properties that are responsible for the recovery of tensile and compressive stiffness when the load is reversed. The equivalent plastic strains are then determined from Eq. 5-20 and Eq. 5-21.

$$\dot{\tilde{\varepsilon}}_t^{pl} = r * \dot{\varepsilon}_{11}^{pl} \quad \text{Eq. 5-20}$$

$$\dot{\tilde{\varepsilon}}_c^{pl} = -(1 - r*)\dot{\varepsilon}_{11}^{pl} \quad \text{Eq. 5-21}$$

5.2.3. Hardening Variable

Two independent hardening variables, which are $\tilde{\varepsilon}_t^{pl}$ and $\tilde{\varepsilon}_c^{pl}$, have been introduced by Lee and Fenves (1998) in CDP to control the damaged states in tension and compression respectively. $\tilde{\varepsilon}_t^{pl}$ is equivalent plastic strain in tension while $\tilde{\varepsilon}_c^{pl}$ is that in compression. The hardening variables are then evolved to the form of Eq. 5-22.

$$\tilde{\varepsilon}^{pl} = \begin{bmatrix} \tilde{\varepsilon}_t^{pl} \\ \tilde{\varepsilon}_c^{pl} \end{bmatrix};\ \dot{\tilde{\varepsilon}}^{pl} = h(\bar{\sigma}, \tilde{\varepsilon}^{pl}) \cdot \dot{\varepsilon}^{pl} \qquad \text{Eq. 5-22}$$

Increasing values of the hardening variables signify micro cracking and crushing in the concrete. These variables are closely related to the evolution of yield surface and degradation of elastic stiffness. They also have close relationship with the dissipated fracture energy which is responsible for generating micro-cracks.

5.2.4. Yield Function

The yield criterion implemented is based on the modified Drucker-Prager yield surface by using two independent parameter by Lee and Fenves (1998) to take into consideration of the different evolution of strength subject to tension and compression. The first parameter, which represents the ratio of biaxial compressive yield stress σ_{b0} to uniaxial yield stress σ_{c0}, adapts the yield surface in biaxial stress state as illustrated in Figure 5.3. As for the second parameter Kc, it transforms the form of deviatoric cross-section from the initial circular shape into a smooth triangular form as shown in Figure 5.4. The yield function is defined as Eq. 5-23.

$$F(\bar{\sigma}, \tilde{\varepsilon}^{pl}) = \frac{1}{1-\alpha}(\bar{q} - 3\alpha\bar{p} + \beta(\tilde{\varepsilon}^{pl})\langle\hat{\bar{\sigma}}_{max}\rangle - \gamma\langle-\hat{\bar{\sigma}}_{max}\rangle) - \bar{\sigma}_c(\tilde{\varepsilon}_c^{pl}) \leq 0 \qquad \text{Eq. 5-23}$$

where α and γ are dimensionless material constant.

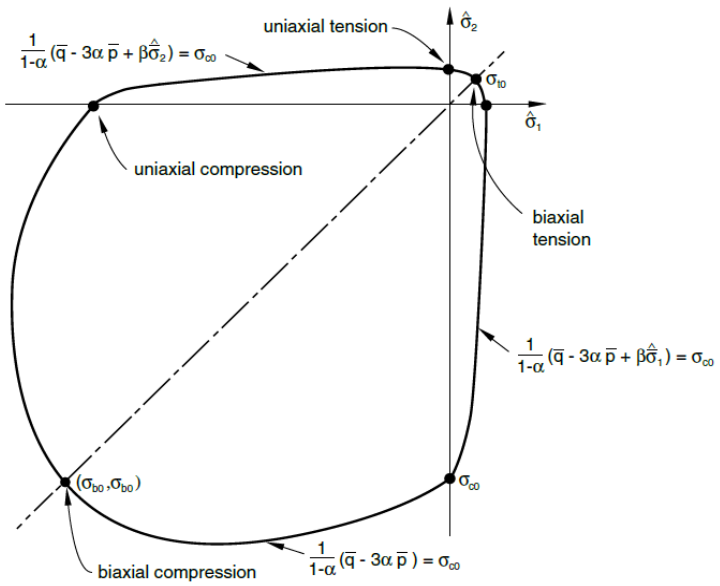

Figure 5.3: Yield surface in plane stress state

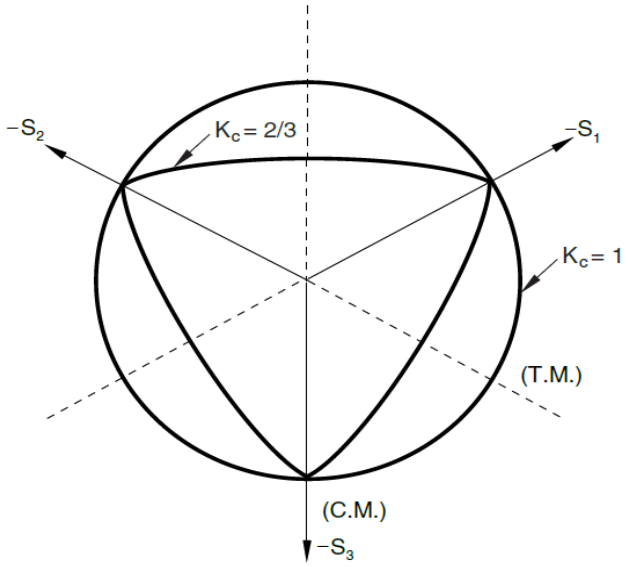

Figure 5.4: Yield surfaces in deviatoric plane, corresponding to different values of K_c

The effective hydrostatic pressure is defined as Eq. 5-24.

$$\bar{p} = -\frac{1}{3}\bar{\sigma}:I \qquad \text{Eq. 5-24}$$

The Von Mises equivalent effective stress is defined as Eq. 5-25.

$$\bar{q} = \sqrt{\frac{3}{2}\bar{S}:\bar{S}} \qquad \text{Eq. 5-25}$$

The deviatoric part of effective stress is represented by Eq. 5-26.

$$\bar{S} = \bar{p}I + \bar{\sigma} \qquad \text{Eq. 5-26}$$

where $\hat{\bar{\sigma}}_{max}$ is maximum eigenvalue of $\bar{\sigma}$. $\beta(\tilde{\varepsilon}^{pl})$ function is given by Eq. 5-27.

$$\beta(\tilde{\varepsilon}^{pl}) = \frac{\bar{\sigma}_c\left(\tilde{\varepsilon}_c^{pl}\right)}{\bar{\sigma}_t\left(\tilde{\varepsilon}_t^{pl}\right)}(1-\alpha) - (1+\alpha) \qquad \text{Eq. 5-27}$$

where $\bar{\sigma}_c$ and $\bar{\sigma}_t$ are the effective compression and tensile cohesion stresses respectively. The yield function is reduced to well-known Drucker-Prager yield function in biaxial compression ($\hat{\bar{\sigma}}_{max} = 0$). Parameter α takes the form of Eq. 5-28.

$$\alpha = \frac{\sigma_{b0} - \sigma_{c0}}{2\sigma_{b0} - \sigma_{c0}} \qquad \text{Eq. 5-28}$$

where σ_{b0} and σ_{c0} are initial equibiaxial and uniaxial compressive yield stress respectively. According to Lubliner et al. (1989), the experimental value of σ_{b0}/σ_{c0}

ratio of concrete ranges from 1.10 to 1.16, making the α value to fall in the range of 0.08 to 0.12.

The coefficient γ only appears in triaxial compression when $\hat{\bar{\sigma}}_{max} < 0$. Value of γ is calculated from the yield condition ratio of tensile and compressive meridians. The relationship between these two meridians is represented by Eq. 5-29.

$$K_c = \frac{\bar{q}_{TM}}{\bar{q}_{CM}} \qquad \text{Eq. 5-29}$$

Default value of 2/3 for Kc is recommended for Concrete Damaged Plasticity Model in ABAQUS, but the model limits the permissible value to $0.5<Kc\leq1.0$. The coefficient γ is calculated by Eq. 5-30.

$$\gamma = \frac{3(1-K_c)}{2K_c - 1} \qquad \text{Eq. 5-30}$$

5.2.5. Non-associated Potential Flow

Concrete is proven to be a material that undergoes large volumetric changes under loading. As such, non-associated flow rule is suitable to control the dilatancy in the plastic-damage model (Lee & Fenves, 1998). In ABAQUS, CDP model uses non-associated flow rule as defined in Eq. 5-31.

$$\dot{\varepsilon}^{pl} = \dot{\lambda}\frac{\delta G(\bar{\sigma})}{\delta \bar{\sigma}} \qquad \text{Eq. 5-31}$$

where $\dot{\varepsilon}^{pl}$is the plastic strain rate, G is the flow potential function and $\dot{\lambda}$ is a non-negative scalar hardening parameter. The flow function G used in this study is a hyperbolic Drucker-Prager function and is given by Eq. 5-32.

$$G = \sqrt{(\epsilon\sigma_{t0}\tan\varphi)^2 + \bar{q}^2} - \bar{p}\tan\varphi \qquad \text{Eq. 5-32}$$

where φ is the angle of dilation determined in the *p*-*q* plane at high confining pressure, σ_{t0} is uniaxial tensile strength, and ϵ is eccentricity of the potential flow which defines the rate at which the function approaches the asymptote. Figure 5.5 illustrates the flow potential curve within the $p-q$ plane. The function asymptotically approaches linear Drucker—Prager flow potential as confining pressure increases, and later the hydrostatic pressure axis is intersected at 90°. ABAQUS manual states that the default value for the eccentricity is equal to 0.1, which shows that the concrete has the same dilation angle through a wide range of confining pressure stresses.

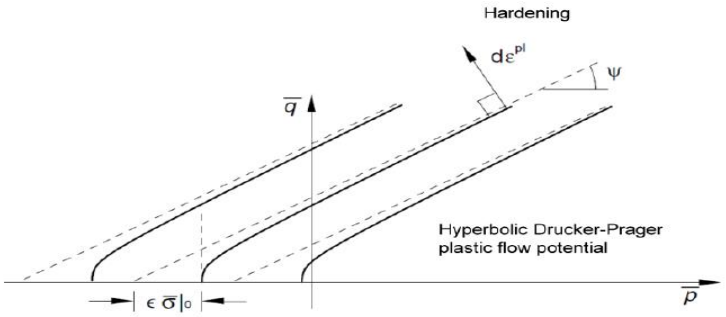

Figure 5.5: Hyperbolic Drucker-Prager flow potential function

5.2.6. Viscoplastic Regularization

Softening behaviour and stiffness degradation of solid model often result in severe convergence problems. This issue is obvious where there is significant change of slope of tensile stress-strain curve at peak stress for tensile loaded model. Viscoplastic regularization of constitutive model is commonly applied to overcome these convergence difficulties. ABAQUS adopts a generalization of Devaut-Lions approach which allows the stresses to be outside yield surface. For non-zero viscosity parameter, viscoplastic strain rate tensor $\dot{\varepsilon}_v^{pl}$ is defined as Eq. 5-33.

$$\dot{\varepsilon}_v^{pl} = \frac{1}{\mu}\left(\varepsilon^{pl} - \varepsilon_v^{pl}\right) \qquad \text{Eq. 5-33}$$

where μ is the viscosity parameter which represents the relaxation of viscoplastic system and ε^{pl} is the plastic strain determined in the inviscid solution. As viscoplastic strain rate is introduced, viscous stiffness degradation variable d_v can be expressed as Eq. 5-34.

$$\dot{d}_v^{pl} = \frac{1}{\mu}(d - d_v) \qquad \text{Eq. 5-34}$$

where *d* is the degradation variable of the inviscid model. The viscoplastic stress-strain relationship is given as Eq. 5-35.

$$\sigma = (1 - d_v)D_0^{el}:\left(\varepsilon - \varepsilon_v^{pl}\right) \qquad \text{Eq. 5-35}$$

Once viscoplastic regularization is implemented, all the model output will be based on viscous plastic strain and viscous elastic stiffness degradation values. The use of small value of viscosity parameter can generally improve convergence rate of concrete model in the softening regime.

5.3. Finite Element Modelling

5.3.1. Model Geometry

All the concrete walls in this research are modelled based on the experimental data from Chapter 4. Concrete component was modelled as 3D deformable solid while steel reinforcement was modelled as 3D deformable wire. The actual dimensions of wall specimens from experiment are used in the modelling and these are summarized in Table 5.1. The model geometry is illustrated in Figure 5.6.

Table 5.1: Wall geometric properties

Specimen	Actual H (mm)	Actual W (mm)	Actual t (mm)	Actual eccentricity (mm)
T25 - AR1.8SR12	299.67	164.67	26.00	1
T25 - AR1.8SR17	424.33	235.33	26.00	1
T25 - AR1.8SR23	565.00	315.00	26.00	1
T25 - AR3.1SR23	564.33	185.00	26.00	1
T25 - AR5.3SR23	565.00	109.67	25.33	1
T60 - AR5.3SR23	1399.67	260.00	61.67	2.5

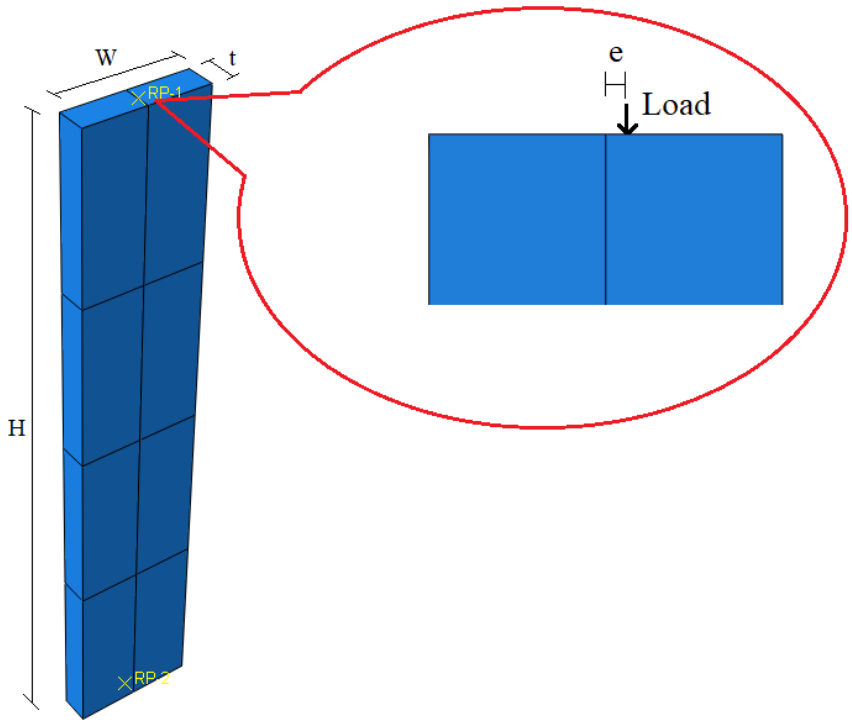

Figure 5.6: Model geometry

5.3.2. Material Property

5.3.2.1. Concrete in Compression

Uniaxial stress-strain graph of concrete is essential to model the structural behaviour of concrete components. According to Lim and Ozbakkaloglu (2014), for a given compressive strength, lightweight concrete exhibits more ductile stress-strain behaviour under compression loading compared to normal weight concrete. This is shown in Figure 5.7. The stress-strain model of normal weight concrete is not suitable to be used. The empirical stress-strain model of unconfined concrete in compression proposed by Yang et al. (2014), which is applicable to lightweight, normal weight and high strength concrete, is chosen to be used in this research.

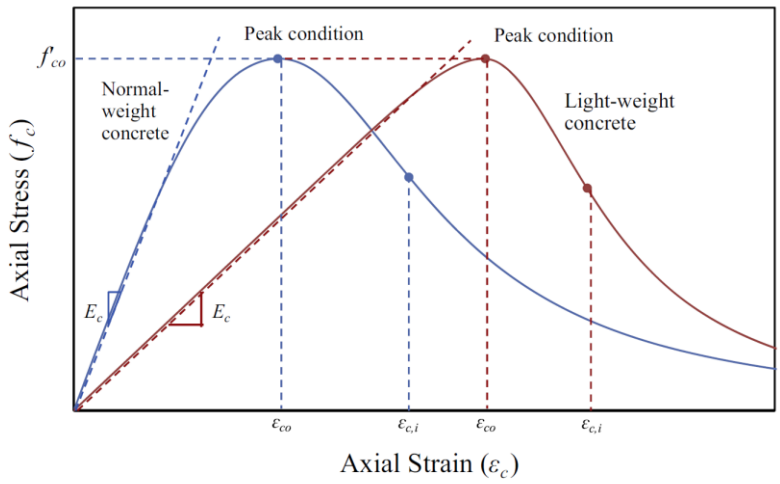

Figure 5.7: Comparison of stress-strain curve of normal and light-weight concrete (Lim & Ozbakkaloglu, 2014)

The stress-strain model of Yang et al. (2014) is represented by a parabola with peak stress at its vertex. The mathematical expression of the non-linear curve is in the form of Eq. 5-36 and illustrated in Figure 5.8.

$$y = \frac{\beta_2 x}{x^{\beta_2} + \beta_1} \qquad \text{Eq. 5-36}$$

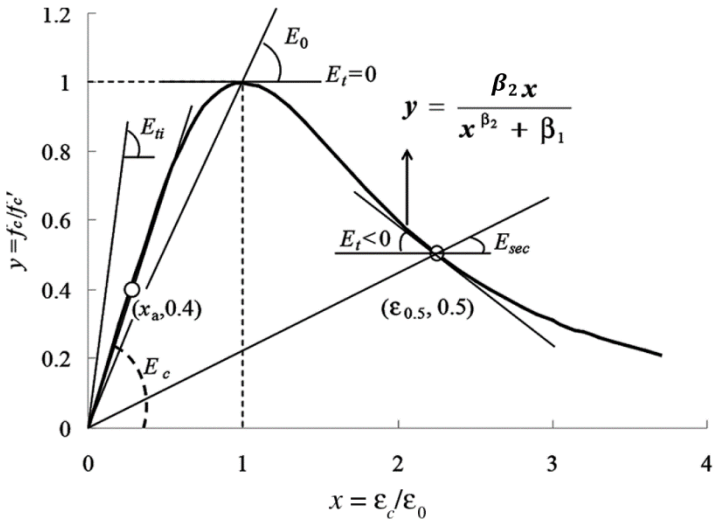

Figure 5.8: Stress-strain model of unconfined concrete in compression proposed by Yang et al. (2014)

The peak strain which corresponds to peak stress is given by Eq. 5-37 and the strain that correlates with the 50% of peak stress in the descending branch is given by Eq. 5-38.

$$\varepsilon_0 = 0.0016e^{240\frac{f_c'}{E_c}} \quad \text{Eq. 5-37}$$

$$\varepsilon_{0.5} = 0.0035e^{1.2\left\{\left(\frac{10}{f_c'}\right)\left(\frac{w_c}{2300}\right)\right\}^{1.75}} \quad \text{Eq. 5-38}$$

The stress-strain relationship of concrete in Eq. 5-36 is further processed and represented by Eq. 5-39. This model is pertinent to concrete with compressive strength from 10 to 180MPa and density from 1200 to 4500kg/m^3.

$$f_c = \left[\frac{(\beta_1 + 1)\left(\frac{\varepsilon_c}{\varepsilon_0}\right)}{\left(\frac{\varepsilon_c}{\varepsilon_0}\right)^{\beta_1+1} + \beta_1}\right] f_c' \quad \text{Eq. 5-39}$$

The parameters β_1 of ascending and descending branches are determined from Eq. 5-40 and Eq. 5-41 respectively.

$$\beta_1 = 0.2e^{0.73\xi} \; for \; \varepsilon_c \leq \varepsilon_0 \quad \text{Eq. 5-40}$$

$$\beta_1 = 0.41e^{0.77\xi} \; for \; \varepsilon_c > \varepsilon_0 \quad \text{Eq. 5-41}$$

$$\xi = \left(\frac{f_c'}{10}\right)^{0.67}\left(\frac{2300}{w_c}\right)^{1.17} \quad \text{Eq. 5-42}$$

Yang et al. (2014) also proposed an equation from statistical analysis to estimate the elastic modulus of concrete as given in Eq. 5-43.

$$E_c = 8470(f_c')^{\frac{1}{3}}\left(\frac{w_c}{2300}\right)^{1.17} \quad \text{Eq. 5-43}$$

The elastic modulus equations of concrete provided in AS 3600 are given as Eq. 5-44 and Eq. 5-45.

$$E_c = \rho^{1.5}\left(0.043\sqrt{f_c'}\right) \text{ for } f_c' \leq 40\text{MPa} \quad \text{Eq. 5-44}$$

$$E_c = \rho^{1.5}\left(0.024\sqrt{f_c' + 0.12}\right) \text{ for } f_c' > 40\text{MPa} \quad \text{Eq. 5-45}$$

A comparison has been made for the elastic modulus of concrete determined from experimental test, AS 3600 equation and Yang et al. (2014) equation as shown Table 5.2. It is clear that the elastic modulus determined from experiment is close to the value determined from AS 3600 equation. The value determined from equation of Yang et al. (2014) tends to overestimate the elastic modulus of LWSCC used in this research. As such, the equation of AS 3600 is used to estimate elastic modulus of concrete used in the parametric study.

Table 5.2: Comparison of elastic modulus

Yang et al. (2014)	AS3600	Experimental
15214	12155	12047

The comparison of stress-strain curves determined from experimental test and empirical model is illustrated in Figure 5.9. It is found that the curve computed from empirical model is close to the experimental.

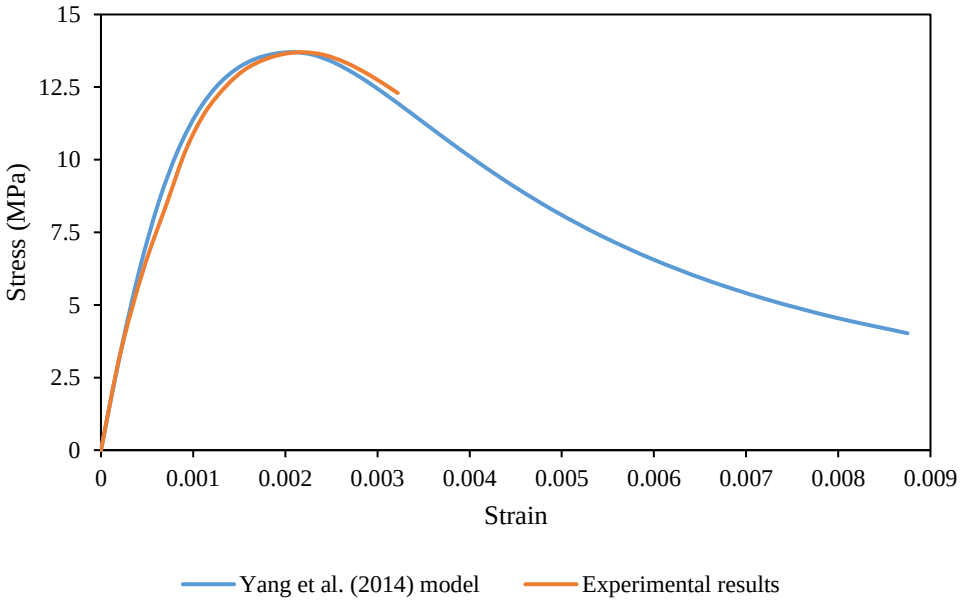

Figure 5.9: Experimental stress-strain curve vs empirical model

The total strains of raw stress-strain curve are converted into inelastic strain by using Eq. 5-46. Also, the compression damaged parameters are determined by using Eq. 5-47.

$$\varepsilon_i = \varepsilon_{c.t} - \frac{\sigma_c}{E_c} \qquad \text{Eq. 5-46}$$

$$d_c = 1 - \frac{\sigma_c}{\sigma_{max}} \qquad \text{Eq. 5-47}$$

The final concrete damaged plasticity properties of lightweight concrete in compression are summarized in Table 5.3 .

Table 5.3: Input values for compressive behaviour in Concrete Damaged plasticity

Compression Behaviour		Compression Damage		Checking	
Stress σ_c (MPa)	**Inelastic Strain ε_i**	**Damage d_c**	**Inelastic strain ε_i**	**Plastic Strain**	**(1-dc)E**
0	0	0	0	0	12154.51
3.32	0	0	0	0	12154.51
6.22	0	0	0	0	12154.51
8.56	0	0	0	0	12154.51
10.34	0	0	0	0	12154.51
11.63	0.00009	0	0.00009	0.00009	12154.51
12.53	0.00023	0	0.00023	0.00023	12154.51
13.12	0.00039	0	0.00039	0.00039	12154.51
13.47	0.00057	0	0.00057	0.00057	12154.51
13.65	0.00076	0	0.00076	0.00076	12154.51
13.70	0.00097	0	0.00097	0.00097	12154.51
13.61	0.00119	0.01	0.00119	0.00118	12073.47
13.34	0.00144	0.03	0.00144	0.00141	11831.09
12.89	0.00173	0.06	0.00173	0.00166	11436.65
12.30	0.00206	0.10	0.00206	0.00194	10909.31
11.58	0.00242	0.15	0.00242	0.00225	10275.54
10.78	0.00283	0.21	0.00283	0.00259	9565.83
9.93	0.00327	0.28	0.00327	0.00296	8811.13
9.06	0.00375	0.34	0.00375	0.00337	8039.98
8.20	0.00427	0.40	0.00427	0.00382	7276.51
7.37	0.00483	0.46	0.00483	0.00431	6539.56
6.59	0.00544	0.52	0.00544	0.00486	5842.60
5.85	0.00610	0.57	0.00610	0.00545	5194.23
5.18	0.00681	0.62	0.00681	0.00611	4599.06
4.57	0.00759	0.67	0.00759	0.00684	4058.52
4.03	0.00843	0.71	0.00843	0.00763	3571.80

5.3.2.2. Concrete in Tension

It is necessary to define tension stiffening of concrete in order to model the realistic structural behaviour of concrete. The tensile strength of concrete is commonly governed by the type of aggregates used and the compressive strength of concrete. Tensile strength of concrete can be determined through direct tension, cylinder splitting and flexural tests.

In ABAQUS, uniaxial tension properties of concrete are required in CDP model. In order to obtain uniaxial tensile strength of lightweight concrete, splitting tensile

strength is determined through laboratory test. It was then converted into uniaxial tensile strength by using Eq. 5-48 from the guidelines of AS 3600.

$$\sigma_{ct} = 0.9 f_{ct.sp} \qquad \text{Eq. 5-48}$$

The tension stiffening model of Wahalathantri et al. (2011) has been chosen in this research. This model was originally proposed by Hillerborg et al. (1976) and modified by Nayal and Rasheed (2006) to avoid discontinuity in global response. The model of Nayal and Rasheed (2006) comprises of two regions, which are primary and secondary cracking stage, as shown in Figure 5.10.

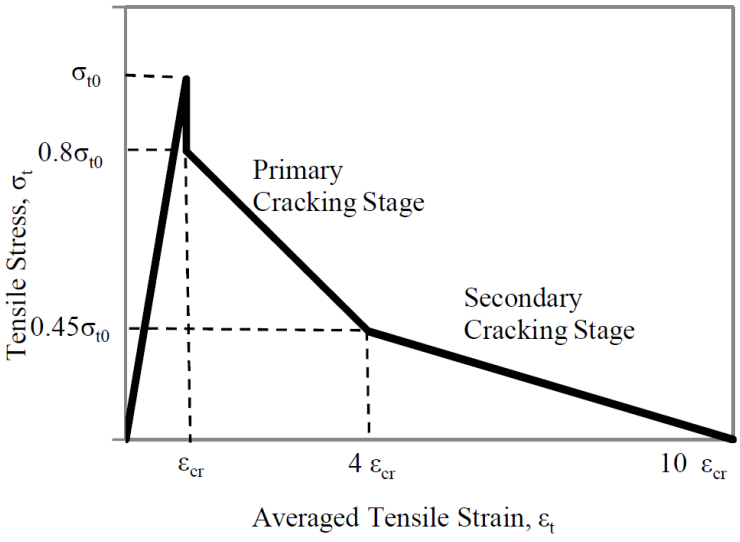

Figure 5.10: Tension stiffening model proposed by Nayal and Rasheed (2006)

The model was then modified by Wahalathantri et al. (2011) in order to avoid runtime errors in ABAQUS as shown in Figure 5.11. The critical tensile strain is calculated by using uniaxial tensile strength and Eq. 5-49.

$$\varepsilon_{t.cr} = \frac{\sigma_{ct}}{E_c} \qquad \text{Eq. 5-49}$$

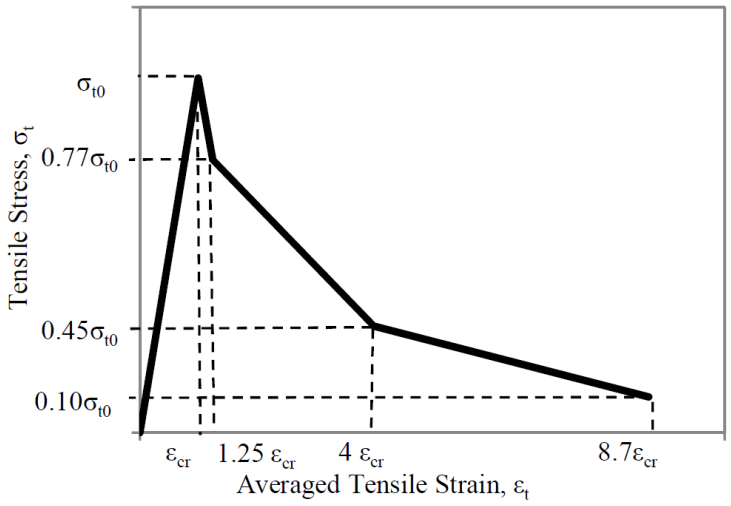

Figure 5.11: Modified tension stiffening model by Wahalathantri et al. (2011) for ABAQUS

Figure 5.12 shows the tensile stress-strain curve of lightweight concrete in this research computed by using equation of Wahalathantri et al. (2011).

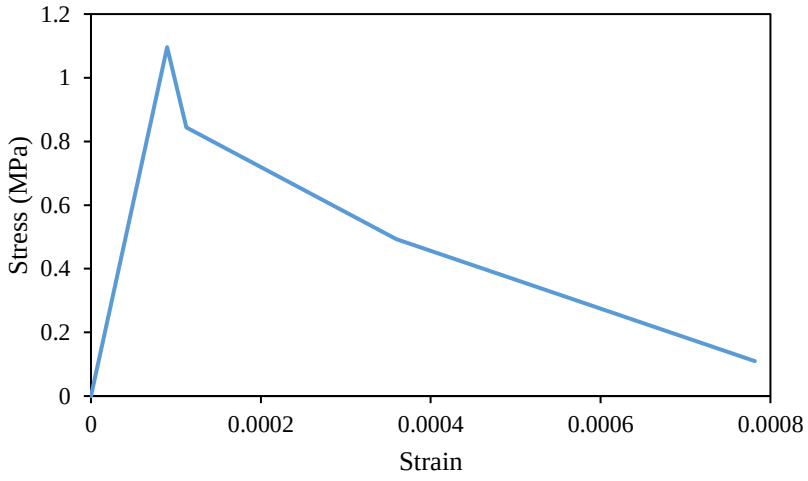

Figure 5.12: Tensile stress-strain curve of lightweight concrete based on Wahalathantri et al. (2011)

The total strains of raw stress-strain curve are converted into inelastic strain by using Eq. 5-50. Also, the compression damaged parameters are determined by using Eq. 5-51.

$$\varepsilon_t^{ck} = \varepsilon_{t.cr} - \frac{\sigma_t}{E_c} \qquad \text{Eq. 5-50}$$

$$d_t = 1 - \frac{\sigma_t}{\sigma_{t.max}} \qquad \text{Eq. 5-51}$$

The concrete damaged plasticity properties of lightweight concrete in tension to be inputted in ABAQUS are summarized in Table 5.4.

Table 5.4: Input values for tensile behaviour in Concrete Damaged plasticity

Tensile Behaviour		Tensile Damage		Checking
Stress σ_t (MPa)	**Inelastic Strain $\varepsilon_{t.cr}$**	**Damage dt**	**Inelastic strain ε_t^{ck}**	**Plastic Strain**
0	0	0	0	0
1.10	0	0	0	0
0.84	0.00004313	0.23	0.00004313	0.00002066
0.49	0.00031895	0.55	0.00031895	0.00004941
0.11	0.00077267	0.9	0.00077267	0.00008086

5.3.2.3. Steel Reinforcement

The stress-strain curve of reinforced steel bar is determined in accordance to ASTM A370 and shown in Figure 5.13. The engineering stresses determined in laboratory test are converted into true stresses by using Eq. 5-52.

$$\sigma_{true} = \sigma(1 + \varepsilon_{eng}) \qquad \text{Eq. 5-52}$$

The true strains are determined from engineering strain by using Eq. 5-53.

$$\varepsilon_{plastic}^{pl} = ln(1 + \varepsilon_{eng}) - \frac{\sigma}{E_s} \qquad \text{Eq. 5-53}$$

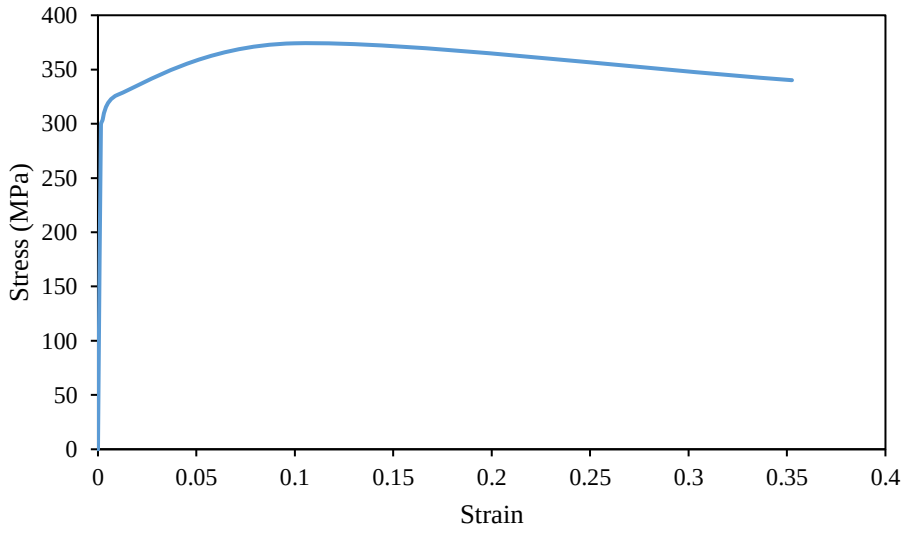

Figure 5.13: Stress-strain curve of steel reinforcement

The input of steel reinforcement properties in ABAQUS is shown in Table 5.5.

Table 5.5: Stress-strain curve of steel reinforcement

E	200000 MPa		
Engineering stress σ_{eng} (MPa)	**Engineering strain ε_{eng}**	**True stress σ_{true} (MPa)**	**True plastic strain $\varepsilon_{plastic}^{pl}$**
0	0	0	0.00000
299.00	0.00150	299.45	0.00000
302.77	0.00220	303.44	0.00068
326.69	0.01000	329.96	0.00830
374.16	0.09985	411.52	0.09311
340.15	0.35251	460.05	0.29967

5.3.3. CDP Input Parameters

Five parameters are required to be inputted in CDP model, which are dilation angle, eccentricity, σ_{b0}/σ_{c0} ratio, K_c and viscosity parameter. Sensitivity study has been performed to determine the best values for these parameters. The following section elaborates how these parameters are chosen. The load versus mid height deflection curve of specimen T60-AR5.3SR23 is used as validation in the sensitivity study.

5.3.3.1. Dilation Angle (ψ)

Dilation angle (ψ) represents the inclination of the plastic strain at high confining pressure as mentioned previously. Material with the low value exhibits brittle behaviour while material with high value indicates high ductile behaviour. Sensitivity study has been carried out to determine the best value for lightweight concrete as shown in Figure 5.14. It is noted that the variation of dilation angle has little effect on ultimate capacity. However, this variation has some effect on failure lateral displacement. The default value of 31° is chosen as it best fits the test results.

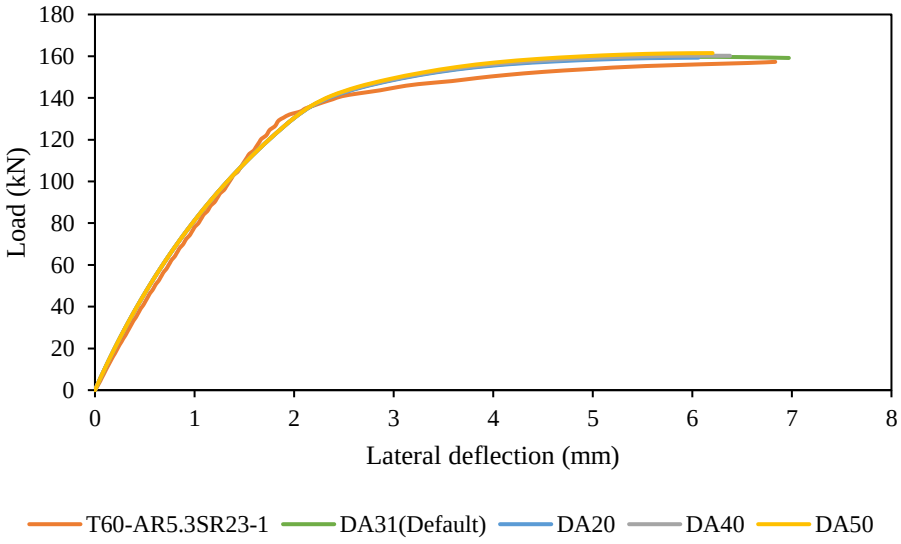

Figure 5.14: Dilation angle sensitivity study

5.3.3.2. Eccentricity

Eccentricity determines the rate at which the function approaches the asymptote. Convergence issue can be arisen if a lower value is used. It is shown in Figure 5.15 that the change of eccentricity value does little effect to the load versus deflection curve. Thus, the default value is chosen.

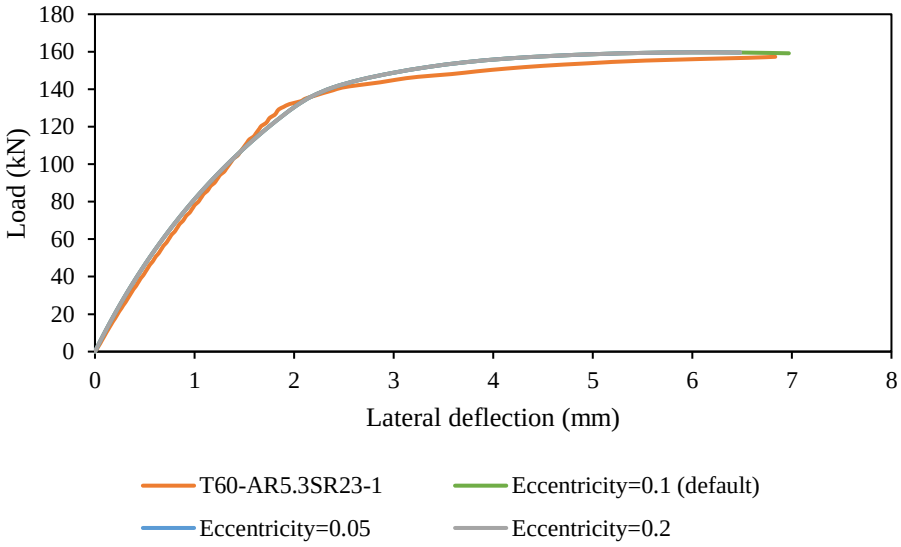

Figure 5.15: Eccentricity sensitivity study

5.3.3.3. Initial Biaxial to Uniaxial ratio

The initial biaxial to uniaxial ratio plays an important role in the determination of failure criterion for concrete. From the sensitivity study illustrated in Figure 5.16, the default value is chosen since the variation of this parameter does not obviously affect the load versus deflection curve.

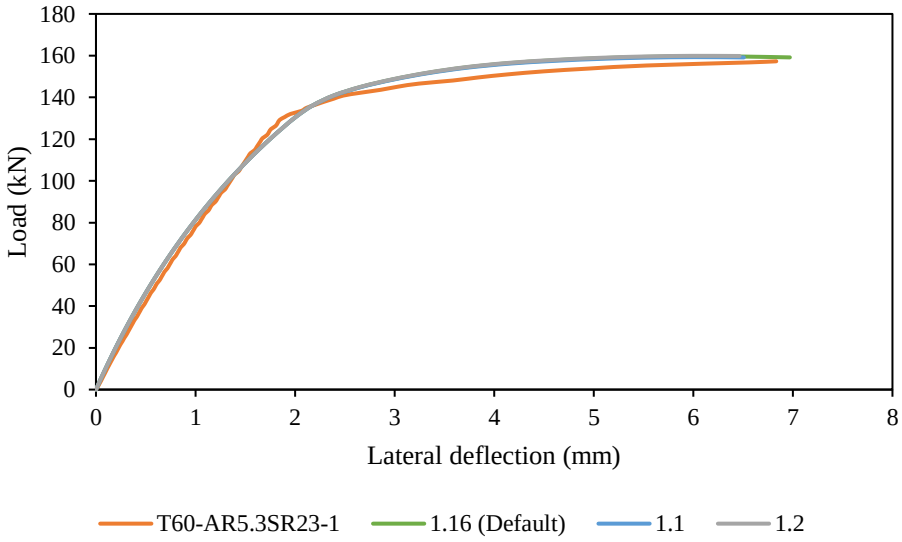

Figure 5.16: Biaxial to uniaxial ratio sensitivity study

5.3.3.4. K_c Parameter

K_c is defined as the ratio of the second stress invariant on the tensile meridian, ($\bar{q}_{TM}$), to the compressive meridian, ($\bar{q}_{TM}$), which is adopted for different evolutions of strength under tension and compression. The common value of K_c for concrete is 0.667. The sensitivity study illustrated in Figure 5.17 shows that the default value fits the experimental results well. Therefore, the default value is chosen.

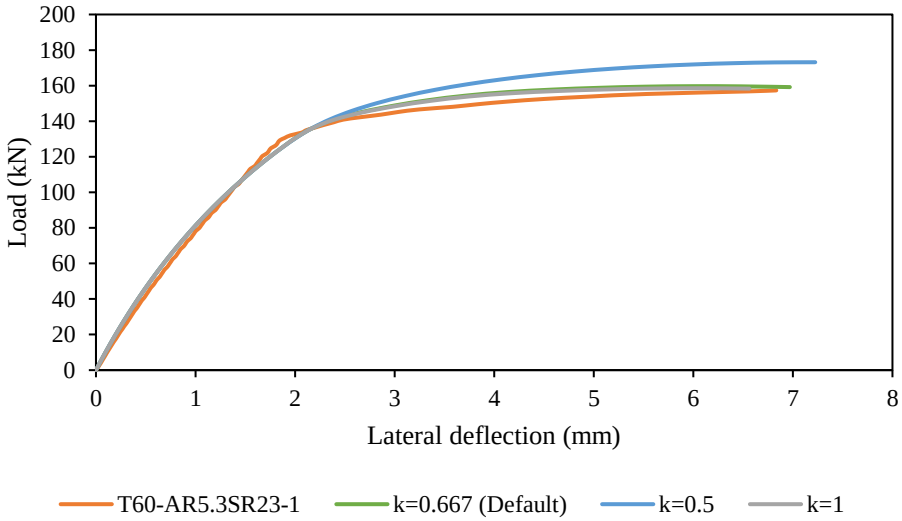

Figure 5.17: K_c sensitivity study

5.3.3.5. Viscosity Parameter

Viscosity parameter is defined to characterize the relaxation time of the visco-plastic system. By proper defining this parameter, convergence issue can be overcome without compromising the accuracy of results. In Figure 5.18, it is noticed that the variation of viscosity parameter from 0.0001 to 0.001 has little effect on ultimate axial capacity. However, the ultimate axial capacity increases significantly when viscosity parameter is increased from 0.001 to 0.01. The value of 0.001 is chosen as it best fits the experimental results and also with this value, slightly lesser computation time is required.

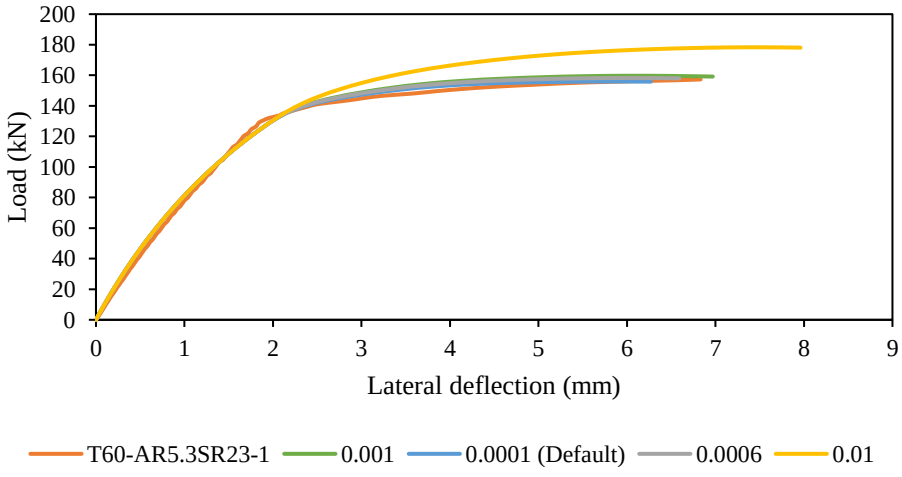

Figure 5.18: Viscosity parameter sensitivity study

5.3.3.6. Chosen Input Parameter

The material parameters of CDP model used for lightweight concrete wall modelling is summarized in Table 5.6.

Table 5.6: Material parameters for CDP model

Parameters	Values
Dilation angle	31°
Eccentricity	0.1
Initial biaxial/uniaxial ratio, σ_{c0}/σ_{b0}	1.16
K_c	0.667
Viscosity	0.001

5.3.4. Contact

The interaction between concrete and reinforcing steel bars are modelled by using "Embedded Region" constraint in the ABAQUS. Steel reinforcement is embedded into the concrete body as shown in Figure 5.19. This type of constraint defines the truss elements as the "embedded region" and the solid continuum concrete as the "host region". The nodes of the embedded region become tied to the nodes of the host region, and thus the translational degrees of freedom of the rebars are constrained to that of the concrete. Steel reinforcement is assumed to be perfectly bonded into concrete and its contribution to axial strength is taken into consideration.

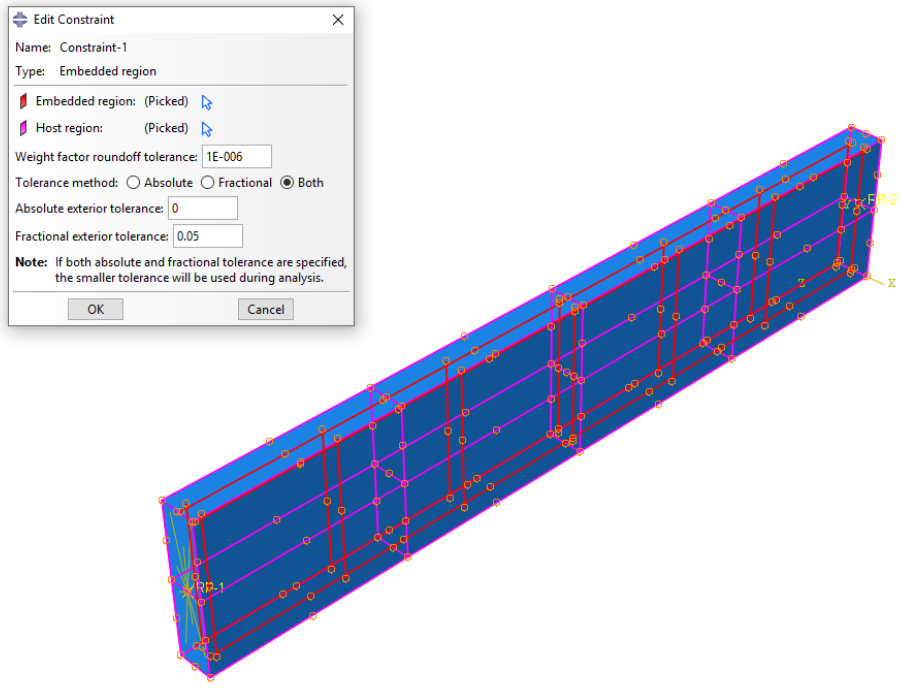

Figure 5.19: Embedment of steel reinforcement into concrete

5.3.5. Element Type

Concrete component is modelled by using "continuum" element as it is more suitable for three dimensional non-linear material that possesses the characteristics of plasticity and large deformation. Three dimensional brick elements, C3D8 and C3D8R which are shown in Figure 5.20, are common elements used in modelling concrete. C3D8 is a fully integrated linear hexahedral element with eight Gauss points. C3D8 commonly experiences shear locking issue and requires finer mesh to solve it, resulting in longer simulation time. C3D8R is a three dimensional 8-node reduced integration brick element with one Gauss point at the centre. Due to only one integration point, C3D8R is able to eliminate shear locking issue. However, when this element is subjected to bending, the strain energy in the element will be assumed to be zero and thus this element has no stiffness under this loading. Hourglassing phenomenon can occur which can cause significant distortion in the mesh. ABAQUS offers an artificial stiffness and damping method to control the hourglass. For modelling of concrete wall in this research, C3D8R is used since it is able to avoid shear locking issue and less computational time is required when compared to C3D8 element.

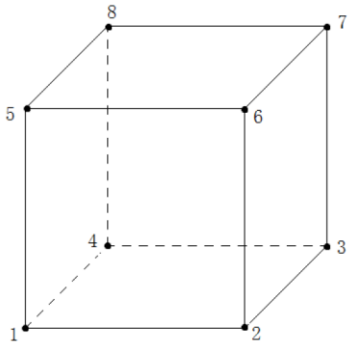

Figure 5.20: 8 nodes brick element

The steel reinforcement materials are modelled by using T3D2 truss elements. T3D2 is three dimensional two-node straight truss element.

5.3.6. Boundary Conditions

Both ends of concrete wall are modelled as pinned end conditions to simulate the actual support condition of laboratory test. Reference points (RP) are created at both ends. All the boundary conditions and applied load are specified at respective reference points. The boundary and loading conditions are illustrated in Figure 5.21. Coupling constraint technique is used to constraint the action of selected surface to the reference points. For the boundary condition at the top of wall, translation is prevented for x and y-directions while z-direction is allowed to be free so that load can be applied to the wall. For bottom boundary condition, the translation in all three directions are retrained. The loading is applied in the form of imposed displacement at reference point. Displacement controlled loading is chosen in order to study the post-failure behaviour of concrete wall. This displacement is large enough to ensure the failure of wall.

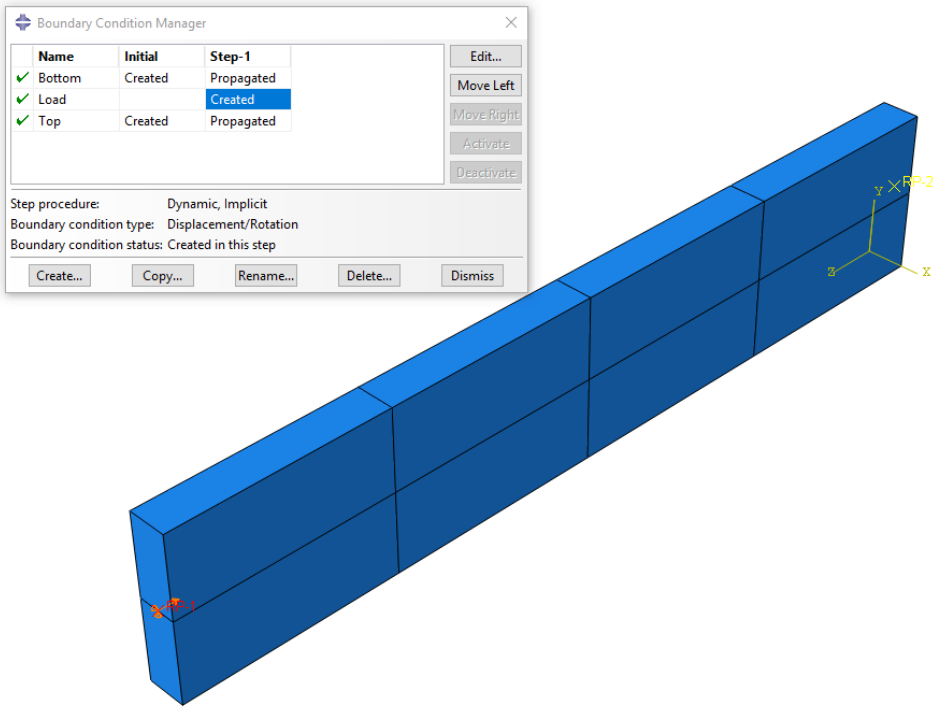

Figure 5.21: Boundary and loading condition used in wall model

5.3.7. Time Step Configuration

Analysis procedure is one of the important steps in carrying out FEA modelling. ABAQUS provides both implicit and explicit solvers for solving FEA problems. According to Coelho et al. (2015), implicit method is more suitable for static and quasi-static simulations with smooth geometric and material non-linearity. However, the unconditionally stable implicit method can encounter difficulty in modelling three dimensional model. It is because the tangent stiffness matrix increases dramatically and causes divergence issue if the reduction of time increment continues. On the other hand, explicit solver provides a more robust solution to convergence problem in which the equilibrium state is determined by adjusting forces and displacements to remove residual penetration without any need of convergence check. Generally, explicit solver incorporated technique by introducing artificial mass scaling to reduce the solution time. Yet, this method accelerates quasi-static analysis but leads to undesirable inertial effect. This effect is commonly minimized by keeping the ratio of kinetic energy to internal energy below 5%. Sun et al. (2000) compared both implicit and explicit methods and concluded that explicit solver is more suitable for fast contact such as impact loading while implicit solver is more suitable for slow contact problems. As

such, quasi-static analysis of implicit solver in ABAQUS/Standard is chosen for modelling since it is not affected by undesirable inertial effects.

In implicit method, Newton's method is incorporated to solve nonlinear equilibrium equations in the step, in which a series of iterations is carried out to obtain equilibrium in each increment. Automatic incrementation option is incorporated so that the increment size will be determined automatically based on computational efficiency. A maximum value of 10000 has been inputted for maximum increment number to ensure sufficient number of increment for model to achieve convergence. Since concrete structural member is highly nonlinear, a value of $1x10^{-15}$ is used for minimum increment size to prevent premature termination of analysis due to small increment size. In implicit dynamic solver, the maximum increment size will be based on the specified value of initial increment size. The software will not exceed the user-defined value of the maximum increment size. The nonlinear behaviour of concrete member cannot be captured properly if large increment size is used in the analysis. A value of 0.01 has been used for the initial increment size as recommended by ABAQUS Manual . Even though implicit quasi-static analysis is not affected by inertial force, the ratio of kinetic energy to internal energy will be checked to be below 5% to ensure quasi-static condition.

5.3.8. FEA Simulation Procedures

The overall procedures to carry out FEA modelling using ABAQUS 6.14 are illustrated in the flow chart as shown in Figure 5.22.

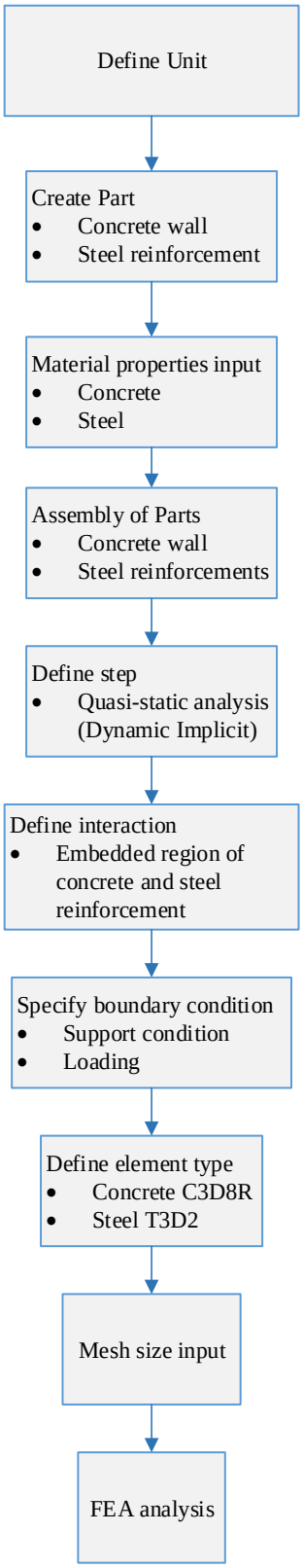

Figure 5.22: Finite Element Analysis Procedure

5.4. Model Verification

5.4.1. Quasi-static Analysis Verification

In order to obtain satisfactory quasi-static solution, the energy level of whole model must be checked throughout the stage of analysis by keeping kinetic energy below 5% of total internal energy. Figure 5.23 shows the comparison of total internal energy and kinetic energy. It is noted that the kinetic energy of entire model is below 5% of total internal energy throughout the analysis. This indicated that inertial effect which can disturb the accuracy of solution is negligible. The default time period is adequate to generate reasonable quasi-static solution.

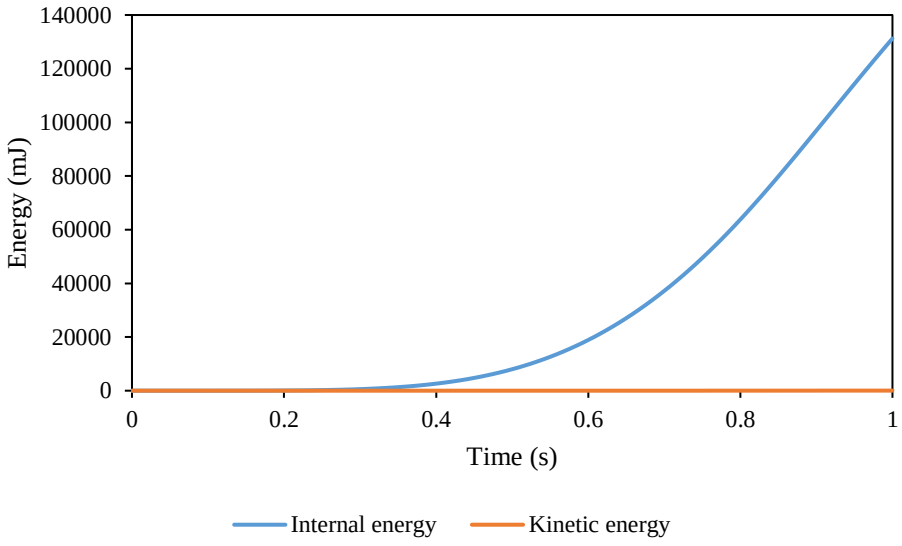

Figure 5.23: Comparison of energy at different loading stage for specimen T60-AR5.3SR23

5.4.2. Mesh Convergence Study

The use of finer mesh can improve the accuracy results of finite element model. However, more computational cost will be required if finer mesh is used. Mesh convergence study has been carried out in order to determine the appropriate mesh size and it is summarized in Table 5.7. Figure 5.24 and Figure 5.25 show the variation of ultimate axial load capacity with the number of elements. To determine suitable mesh, the number of elements is varied from 3678 to 103552. It is observed that the ultimate axial capacity does not change much when the number of elements is increased to more than 19240. As for mid height displacement, convergence is achieved at 46160 number

of elements. Use of mesh density of 30000 to 70000 elements should be able to produce reasonably accurate solutions. Mesh density of 50000 elements is chosen for modelling lightweight concrete wall because not only it produces reasonable accurate results, it also requires optimum computational time.

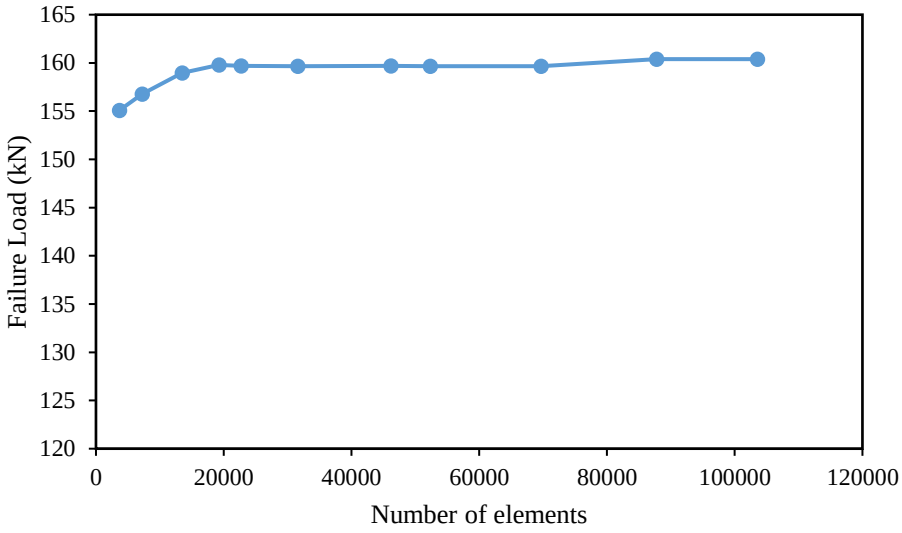

Figure 5.24: Mesh convergence study for specimen T60-AR5.3SR23 (Failure load)

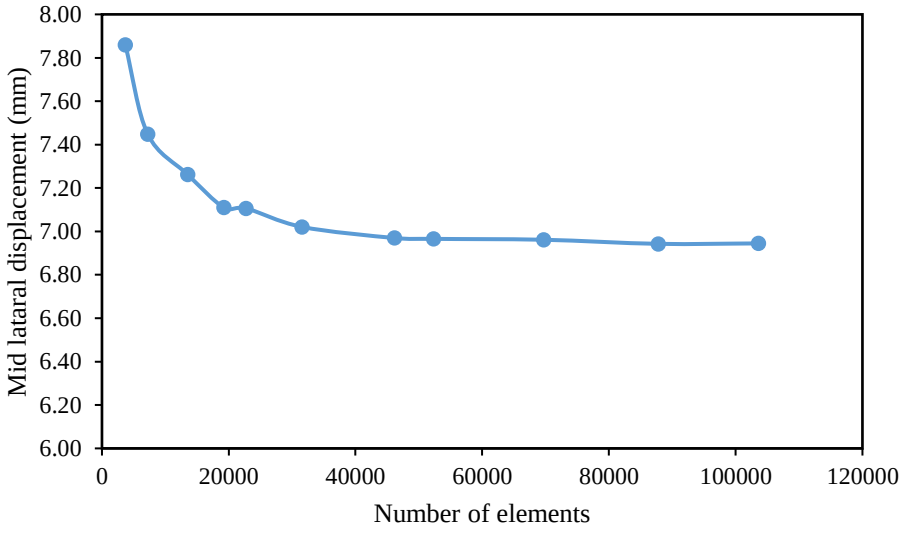

Figure 5.25: Mesh convergence study for specimen T60-AR5.3SR23 (Mid lateral displacement)

Table 5.7: Summary of mesh convergence study

Mesh size (mm)	Number of elements	Ultimate axial capacity (kN)	Mid lateral displacement (mm)
6	103552	160.39	6.94
6.5	87762	160.39	6.94
7	69660	159.67	6.96
7.5	52316	159.67	6.97
8	46160	159.68	6.97
9	31562	159.66	7.02
10	22724	159.69	7.11
11	19240	159.79	7.11
12	13496	158.97	7.26
15	7212	156.77	7.45
18	3678	155.09	7.86

5.4.3. Experimental Results

In this section, the models described in previous sections are verified against experimental results. Comparison of failure mode, load versus deflection behaviour and ultimate axial load capacity are carried out and discussed.

5.4.3.1. Failure Mode

The failure modes of all the lightweight concrete wall panels predicted by FEA models are verified by the recorded experimental failure modes. Comparison of failure mode has been made between experimental tests and FEA models. Figure 5.26 to Figure 5.31 show the comparison of experimental and FEA failure mode for all concrete wall specimens. In ABAQUS, the maximum principle plastic strain can be used to show the crack pattern of concrete. For specimen T25-AR1.8SR12 as shown in Figure 5.27, FEA model has predicted crushing failure mode. Plastic strains are concentrated at the bottom support and no curvature is exhibited by T25-AR1.8SR12 FEA model. This is because the stress has surpassed compressive crushing strength of concrete before reaching tensile strength in Concrete Damaged Plasticity (CDP) due to the low slenderness ratio of specimen. This has caused localized crushing failure.

The FEA model has predicted specimen T60-AR5.3SR23, T25-AR1.8SR17, T25-AR1.8SR23, T25-AR3.1SR23 and T25-AR5.3SR23 to be failed in buckling failure mode. It is noted that plastic strains concentrate at the mid height of these specimens. Specifically, a horizontal crack develops at the mid height of wall panel. These

specimens show uniaxial curvature deformation with maximum deflection at mid height. These FEA models exhibit similar failure mode to that of the experimental test. Cracking pattern and failure mode of lightweight concrete wall have been well predicted by CDP model in ABAQUS.

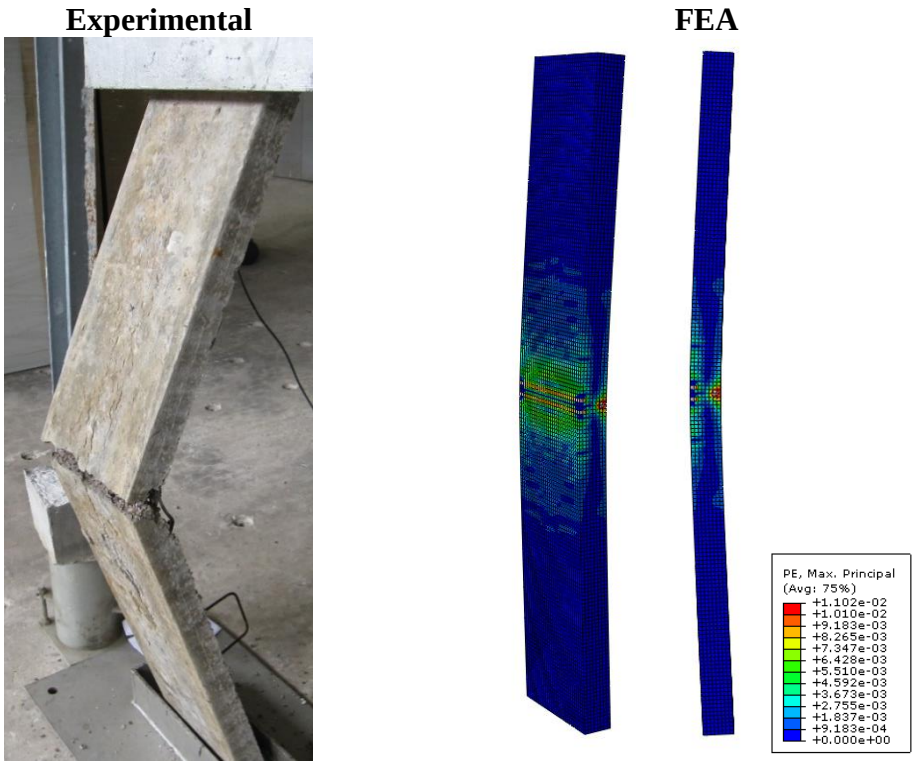

Figure 5.26: Experimental versus FEA failure mode of wall T60-AR5.3SR23

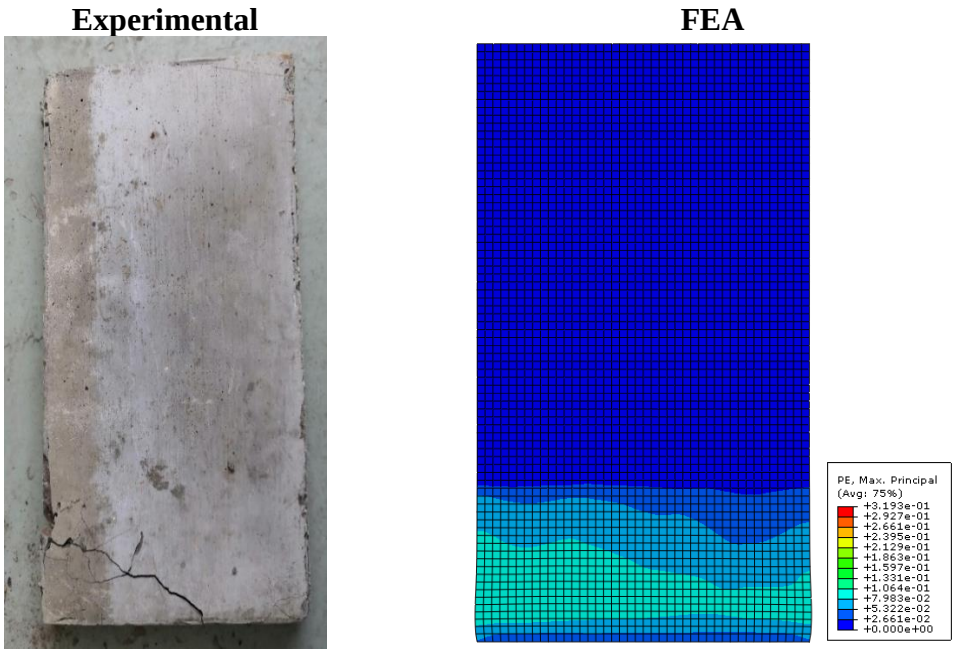

Figure 5.27: Experimental versus FEA failure mode of wall T25-AR1.8SR12

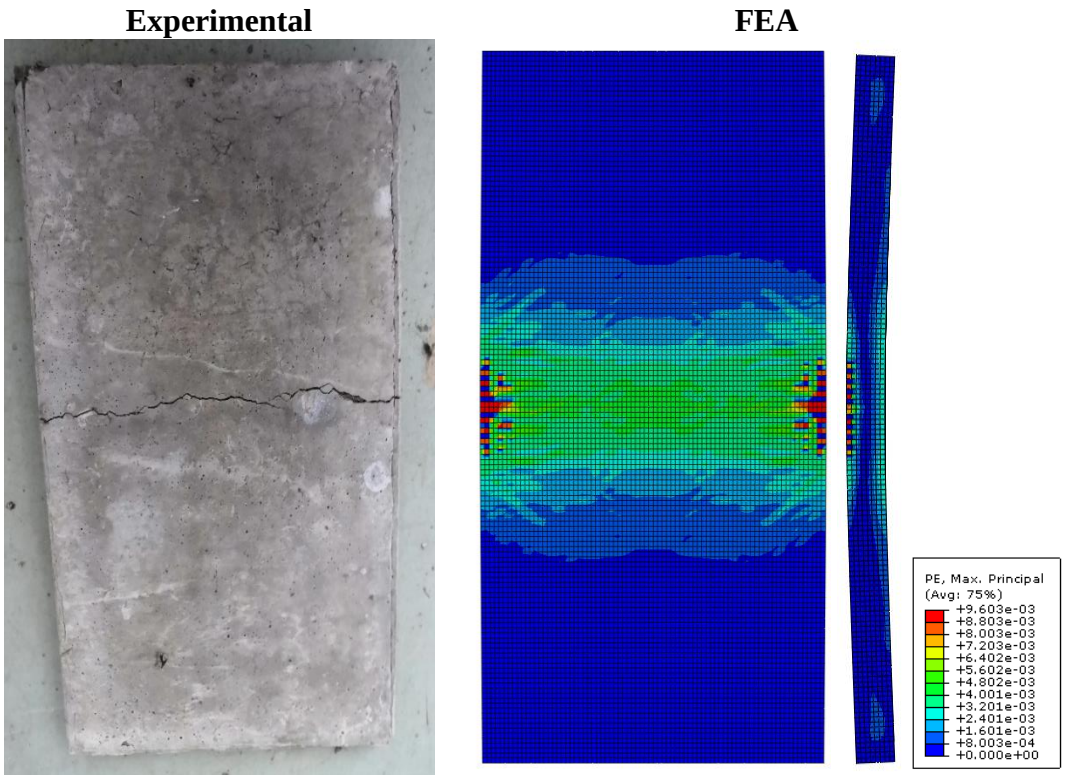

Figure 5.28: Experimental versus FEA failure mode of wall T25-AR1.8SR17

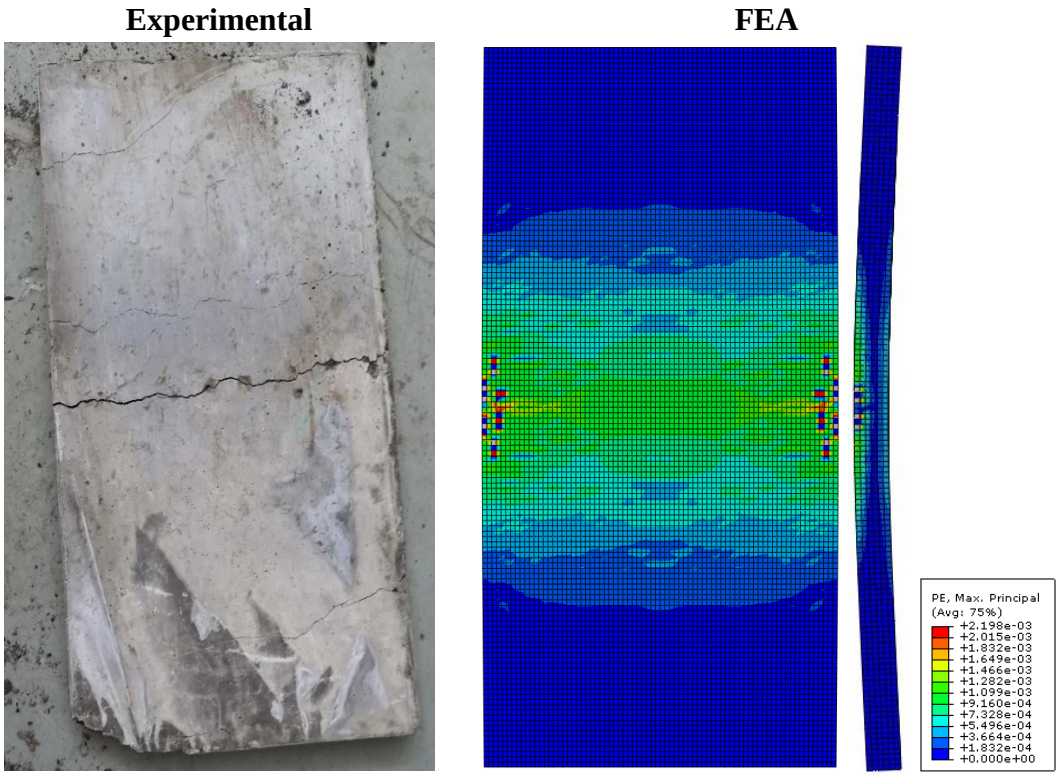

Figure 5.29: Experimental versus FEA failure mode of wall T25-AR1.8SR23

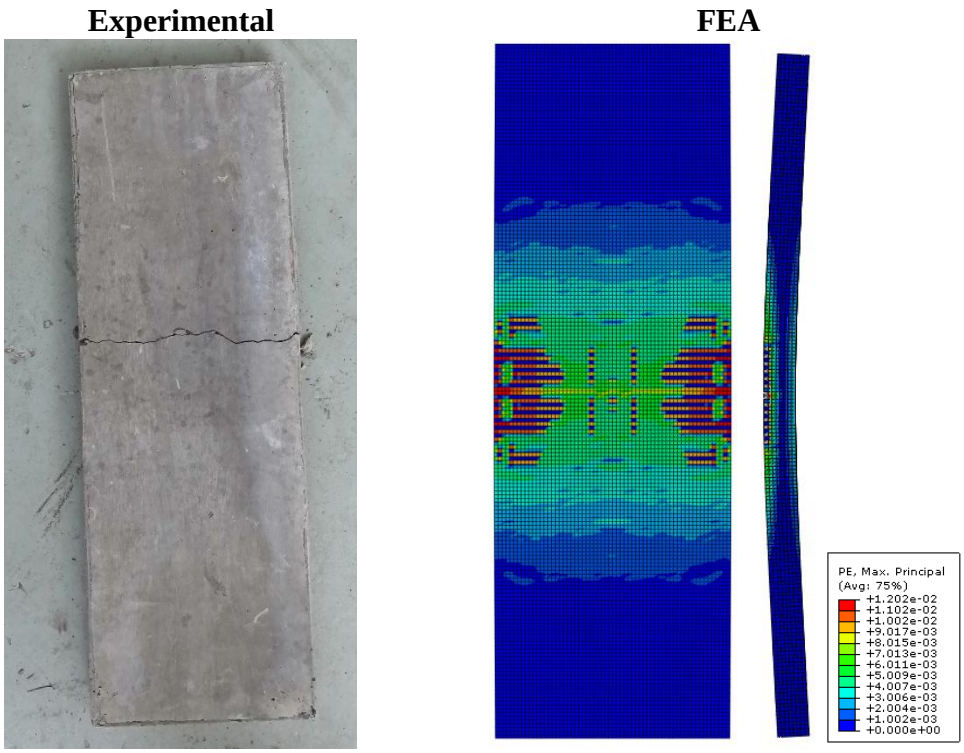

Figure 5.30: Experimental versus FEA failure mode of wall T25-AR3.1SR23

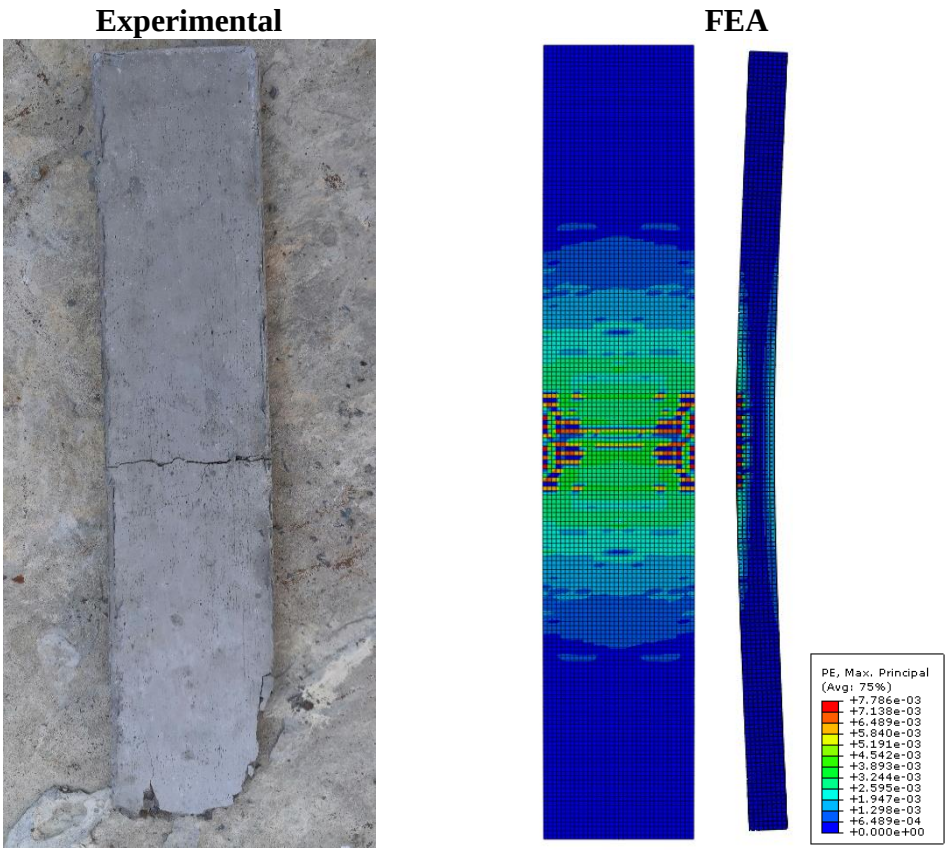

Figure 5.31: Experimental versus FEA failure mode of wall T25-AR5.3SR23

5.4.3.2. Comparison of Axial Load versus Deflection

The load versus deflection curves obtained from FE analyses of the six different walls are shown from Figure 5.32 to Figure 5.39 and they are compared with those experimentally measured. The load versus deflection curves at the top quarter, middle and bottom quarter of wall specimen T60-AR5.3SR23 are illustrated in Figure 5.32, Figure 5.33 and Figure 5.34 respectively. The load versus deflection curves at mid-height of T25 series walls are compared and shown in Figure 5.35 to Figure 5.39. It can be observed that the FEA results with respect to the ultimate axial capacity and deflections are in good agreement with the experimental results. In general, FE model has shown slightly stiffer response at the nonlinear region. This is mainly because in the modelling, idealistic concrete material characteristics are assumed. The comparison demonstrates that CDP model in ABAQUS gives a good prediction of the non-linear load-deflection behaviour of lightweight concrete wall as the modelling results correlate well with experimental values.

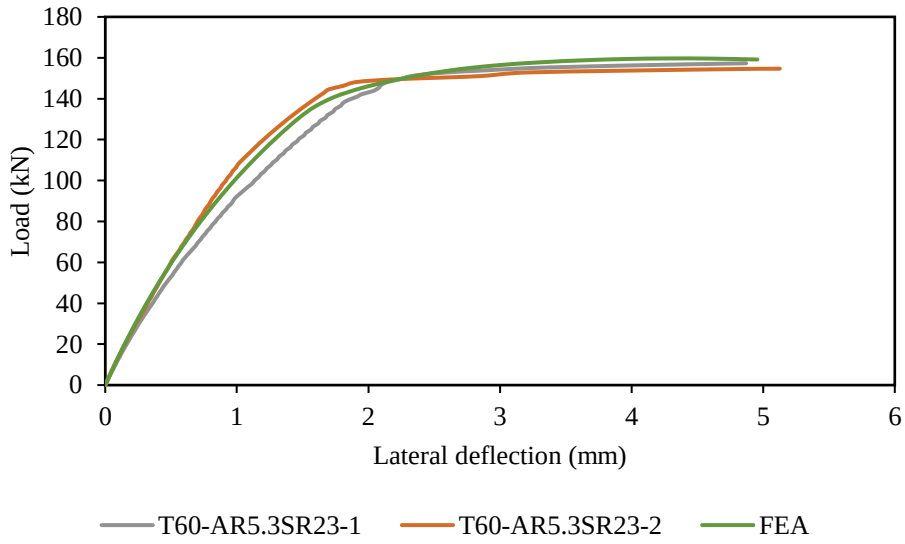

Figure 5.32: Experimental and FEA load versus top quarter deflection curves (T60-AR5.3SR23)

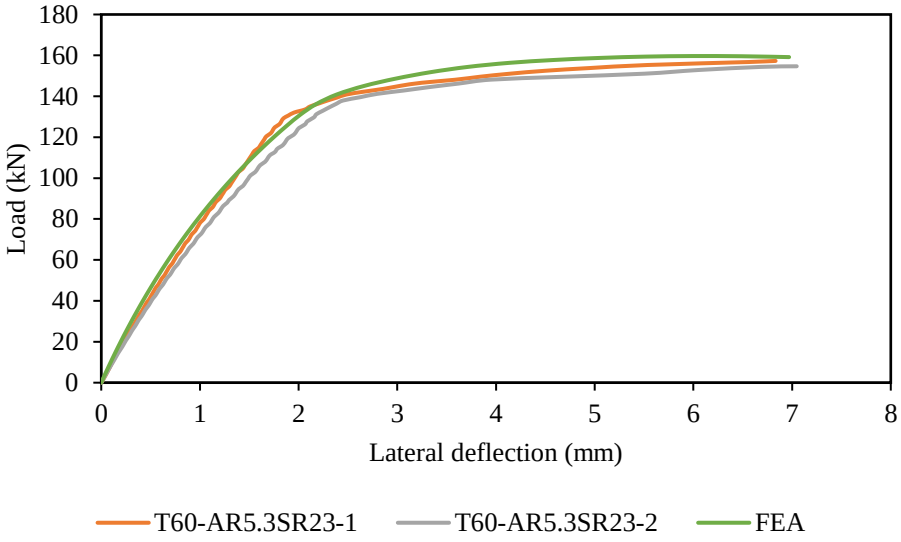

Figure 5.33: Experimental and FEA load versus mid height deflection curves (T60-AR5.3SR23)

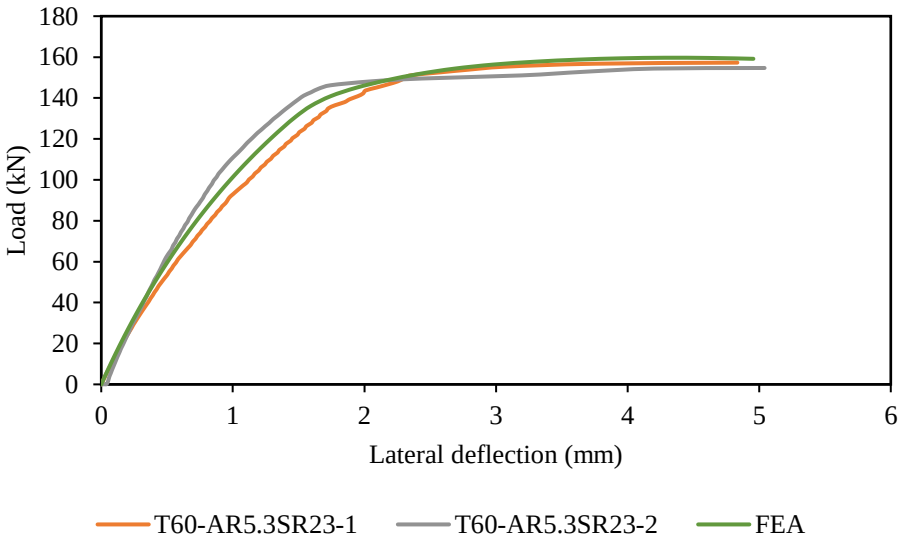

Figure 5.34: Experimental and FEA load versus bottom quarter deflection curves (T60-AR5.3SR23)

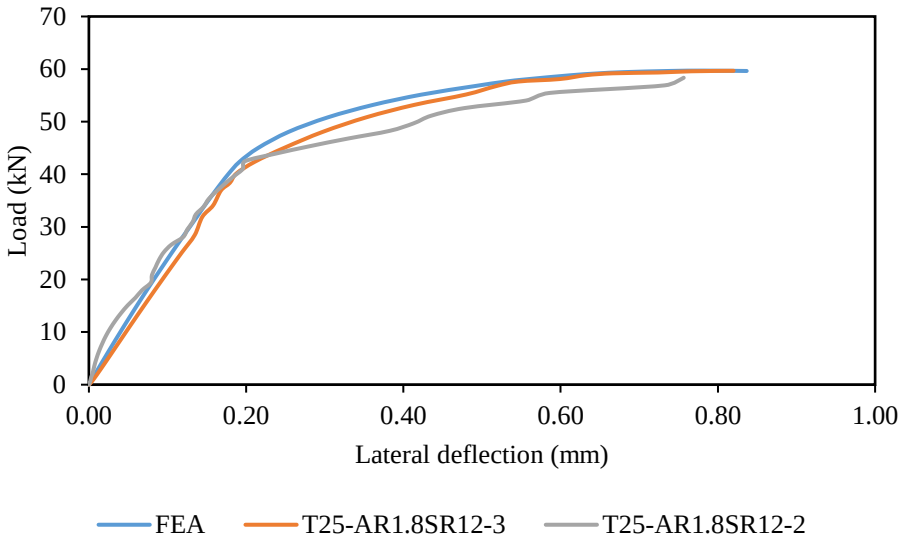

Figure 5.35: Experimental and FEA load versus mid height deflection curves (T25-AR1.8SR12)

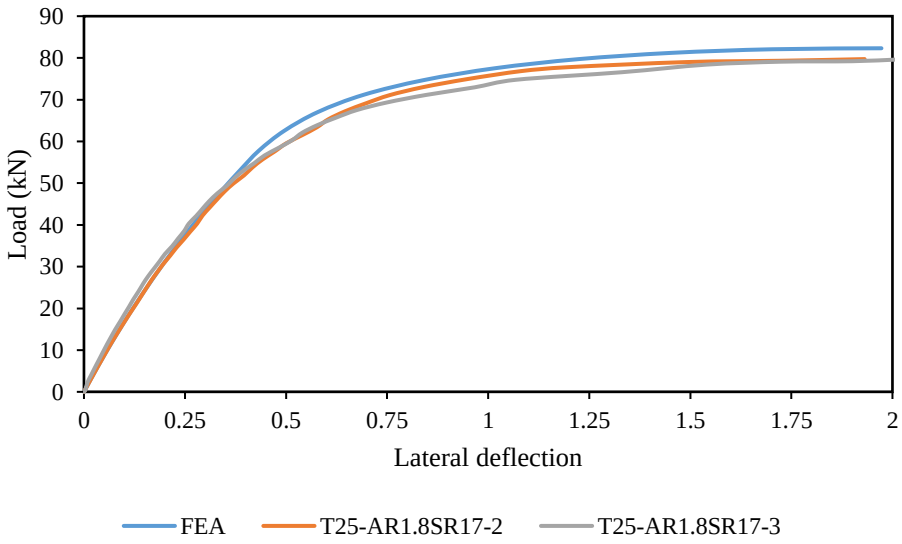

Figure 5.36: Experimental and FEA load versus mid height deflection curves (T25-AR1.8SR17)

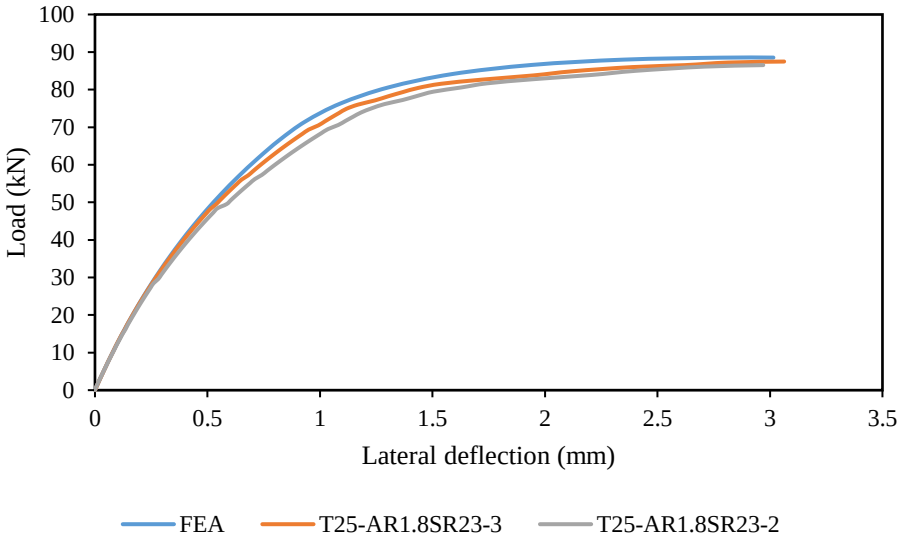

Figure 5.37: Experimental and FEA load versus mid height deflection curves (T25-AR1.8SR23)

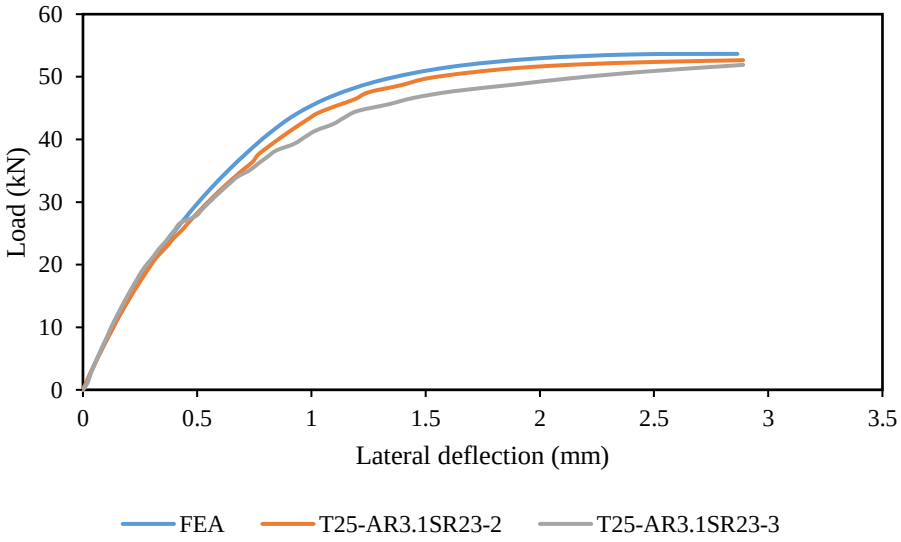

Figure 5.38: Experimental and FEA load versus mid height deflection curves (T25-AR3.1SR23)

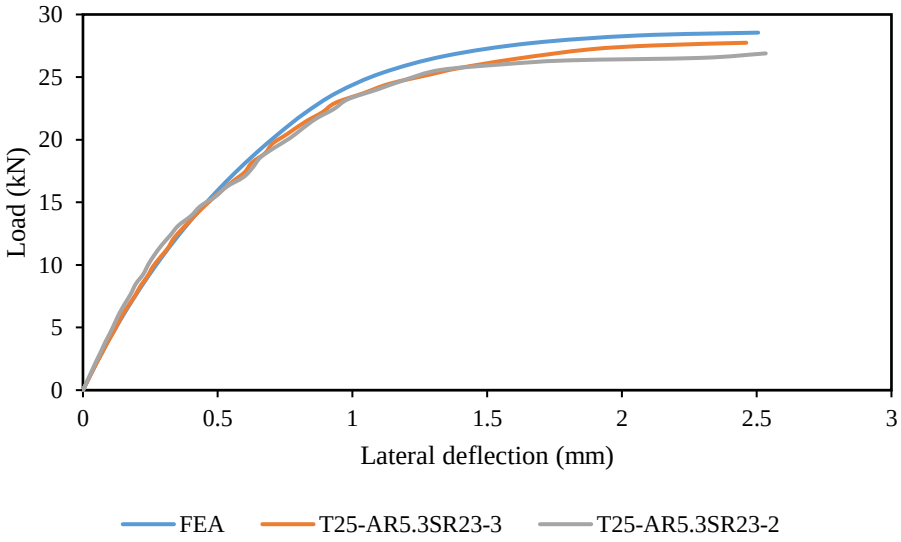

Figure 5.39: Experimental and FEA load versus mid height deflection curves (T25-AR5.3SR23)

5.4.3.3. Ultimate Axial Capacity

Table 5.8 summarizes the comparisons between FEA results and experimental results for all lightweight wall panels in terms of ultimate axial capacity. FEA and experimental results are expressed as P_{FEA}/P_{exp} ratio for comparison purpose.

Table 5.8: Comparison of experimental and FEA results

Sample	Pexp (kN)	PFEA(kN)	Percentage of error (%)	Ratio
T25-AR1.8SR12	57.17	59.71	4.43	1.04
T25-AR1.8SR17	78.00	82.31	5.53	1.06
T25-AR1.8SR23	85.59	88.53	3.43	1.03
T25-AR3.1SR23	51.20	53.55	4.58	1.05
T25-AR5.3SR23	27.32	28.55	4.51	1.05
T60-AR5.3SR23	155.06	159.68	2.98	1.03
Mean				1.04
Standard				0.01

The comparison indicates all the P_{FEA}/P_{exp} ratios are greater than 1, varying from 1.03 to 1.05, with mean value of 1.04 and standard deviation of 0.01. The P_{FEA}/P_{exp} ratios for T25 series are 1.03, 1.04, 1.03, 1.04 and 1.05 for AR1.8SR12, AR1.8SR17, AR1.8SR23, AR3.1SR23 and AR5.3SR23 respectively. For T60 series, the P_{FEA}/P_{exp}

ratio for AR5.3SR23 is 1.03. The comparison of results shows that the predicted ultimate axial capacity of FEA model is satisfactory though with slight overestimation. The slight discrepancies of FEA results are mainly due to the idealistic nature of FEA model including materials and boundary conditions. CDP model gives more accurate prediction of ultimate axial capacity of lightweight concrete wall when compared to the results calculated by using design equations of various design standards.

For further comparison of FEA results and experimental results, coefficient of determination (R-squared) is computed, as illustrated in Figure 5.40. The resulting R-square value is 0.9998 which shows a good agreement between FEA and experimental results.

From the comparison between FEA results and those obtained experimentally in respect of failure mode, load versus deflection behaviour and ultimate axial capacity, it is demonstrated that CDP model in ABAQUS can accurately predict the structural behaviour of axially loaded wall. This also clearly demonstrates the reliability of ABAQUS as a powerful tool for the analysis of concrete wall under axial loading.

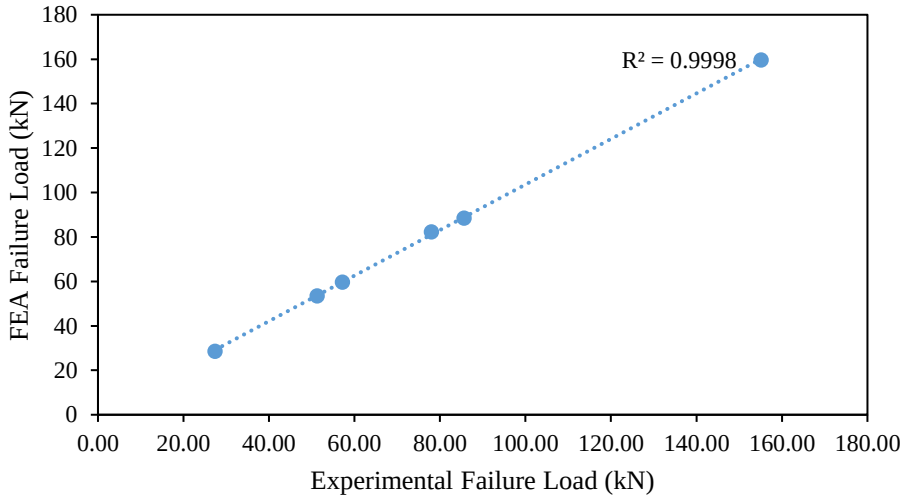

Figure 5.40: Comparison of FEA and experimental failure load

5.4.4. Comparative Study

In order to establish the effectiveness of FEA as a tool for predicting failure mode and ultimate load of concrete wall, the constructed FEA models for lightweight concrete wall are also benchmarked with the published experimental results of normal strength and high strength concrete walls. Figure 5.42 shows the comparisons of failure mode of FEA and published experimental results (Doh & Fragomeni, 2005) for specimen

OWNS3 and OWHS4. According to Doh and Fragomeni (2005), the wall panels tested under one-way action failed by buckling in a single curvature shape with horizontal cracks near mid height. It is observed that FEA model is able to predict the failure mechanism of concrete wall accurately, in which plastic strains are concentrated at the mid height of wall and a horizontal crack is developed near the mid height.

Table 5.9 shows the comparison of FEA result and published experimental results (Doh & Fragomeni, 2005; Saheb & Desayi, 1989). The ratios of FEA to experimental results vary from 0.9 to 1.12, with mean of 1.03 and standard deviation of 0.07. Coefficient of determination (R-squared) is also computed for comparing FEA results with published experimental results, as shown in Figure 5.41. The resulting R-square value is 0.9764 which shows a good agreement between FEA and published experimental results. It is demonstrated that the proposed model is able to predict the failure loads of concrete wall with slenderness ratio up to 40. It is also established that the proposed model is able to predict the failure load of concrete wall with different compressive strength of concrete correctly. Generally, all the FEA results showed slight overestimation of failure load. The slight discrepancies of FEA results are mainly due to the idealistic nature of FEA model including materials and boundary conditions. Thus, the FEA results have shown a good agreement with published experimental results.

Table 5.9: Comparison of published experimental result and FEA result

Researcher	Specimen	H (mm)	L (mm)	t (mm)	SR	f'c (MPa)	P_{exp} (kN)	P_{FEA} (kN)	P_{FEA}/P_{exp} Ratio
Saheb and Desayi (1989)	WSR1	450	300	50	9	21.7	214.18	192.40	0.90
	WSR2	600	400	50	12	21.7	254.10	246.87	0.97
	WSR3	900	600	50	18	21.7	298.92	319.10	1.07
	WSR4	1350	900	50	27	21.7	373.65	409.67	1.10
	WSTV4	600	900	50	12	25.2	704.14	787.66	1.12
	WSTV7	1200	800	50	24	22.8	463.28	430.94	0.93
	WSTH6	1200	800	50	24	20.2	348.74	362.97	1.04
Doh and Fragomeni (2005)	OWNS3	1400	1400	40	35	52	426.70	462.25	1.08
	OWNS4	1600	1600	40	40	51	441.50	443.63	1.00
	OWHS2	1200	1200	40	30	78.2	482.70	504.00	1.04
	OWHS3	1400	1400	40	35	63	441.50	462.45	1.05
	OWHS4	1600	1600	40	40	75.9	455.80	495.71	1.09
Mean									1.03
Standard Deviation									0.07

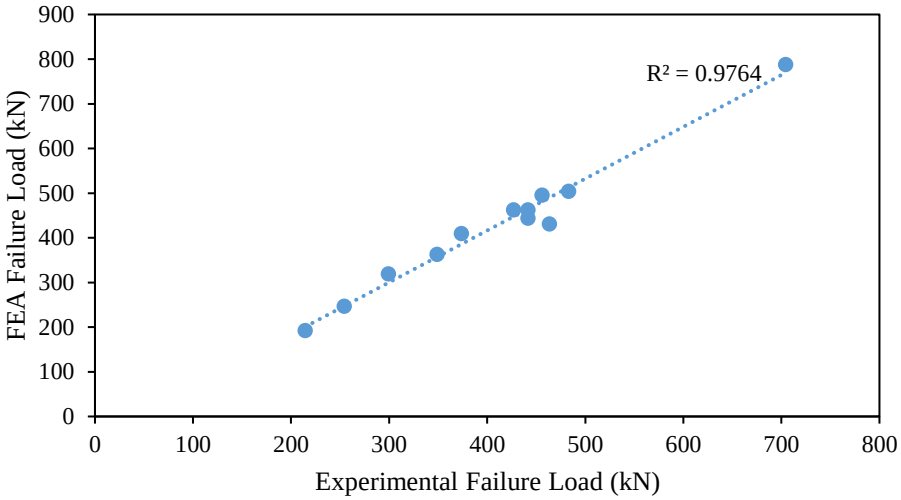

Figure 5.41: Comparison of FEA and published experimental failure load

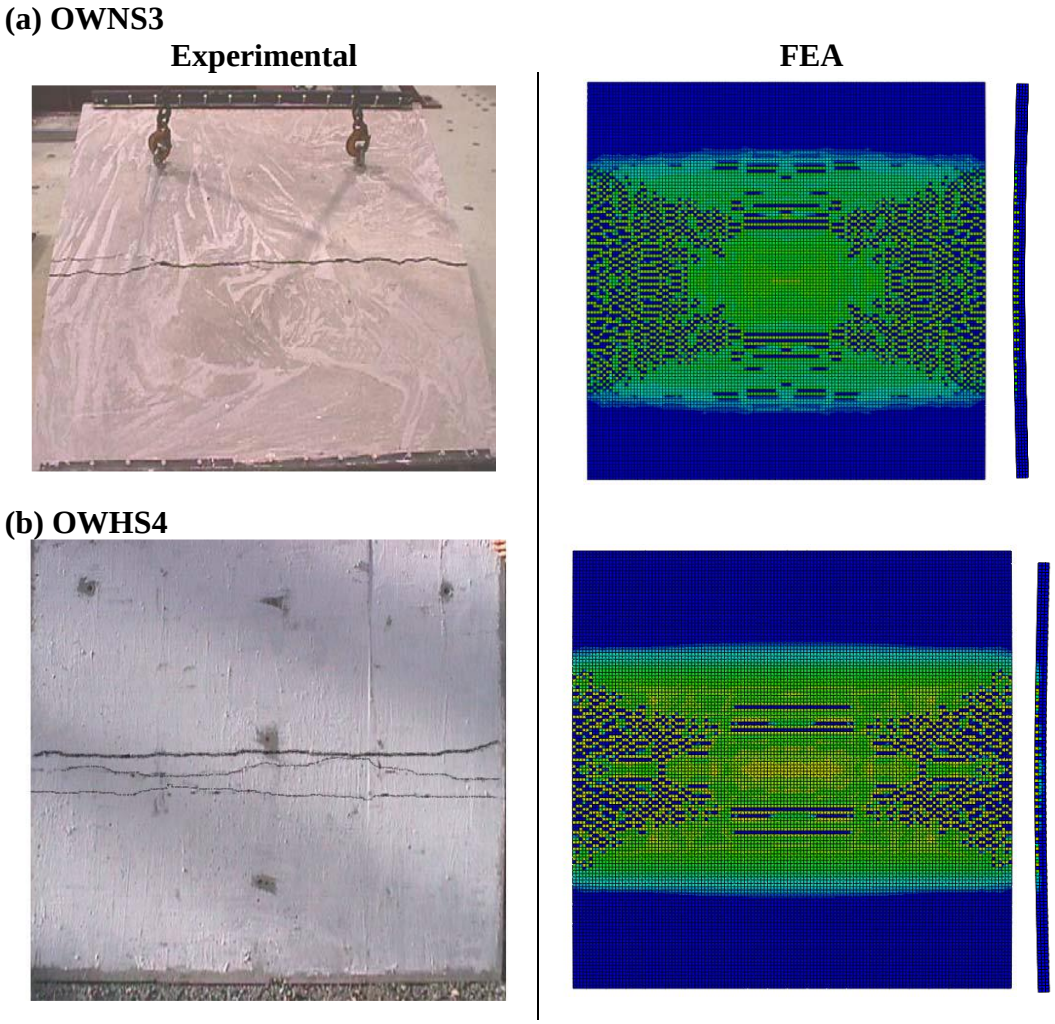

Figure 5.42: Published experimental versus FEA failure mode

5.5. Parametric Studies

It has been demonstrated in previous section that the results obtained from FEA model have shown good agreement with experimental results as well as the experimental results in the published literature. Hence, the developed FEA model can be used to carry out parametric study on the axial strength of concrete wall. A series of parametric studies was carried out to study the effect of slenderness ratio, eccentricity, aspect ratio, concrete strength, elastic modulus and tensile strength on the axial capacity of concrete wall. The effect of each parameter was demonstrated by comparing the axial strength ratio of each wall. The failure loads of concrete wall in parametric study are documented in Appendix D. All the walls in the parametric study contain two layers of steel reinforcement with reinforcement ratio of 0.0059 and yield stress of 300MPa. The range of each parameter studied is summarized in Table 5.10.

Table 5.10: Range of parametric studies

Parameters	Slenderness ratio	Eccentricity	Aspect ratio	Compressive strength (MPa)	Density (kg/m^3)	Tensile to compressive strength (%)
Range	23	t/600	0.5	13.7	1600	5
	27	t/20	0.75	25	1800	8
	30	t/12	1	40	2000	10
	35	t/6	2	60	2200	
	40		3	80	2400	
	45		4			
	50		5.3			

5.5.1. Effect of Slenderness Ratio

Slenderness ratio is a significant parameter that affects the axial strength ratio of concrete wall. Figure 5.43 to Figure 5.45 show the curves of axial strength ratio versus slenderness ratio with different values of eccentricity and aspect ratio. In the study, the slenderness ratio is varied from 23 to 50. The slenderness ratio parameter is studied with 3 different eccentricities (t/600, t/12, t/6) and 3 different aspect ratios (0.5, 1, 5.3). It is noted that the shape of curve is sensitive to the change of eccentricity. At the eccentricity of t/600, the decrease in axial strength ratio with increase in slenderness ratio gives a downward concave curvature shape as illustrated in Figure 5.43. When

the eccentricity is increased to t/12, the shape of curve becomes flat and shows a slight upward concave shape as shown in Figure 5.44. The concave shape of curve becomes more noticeable when eccentricity is increased to t/6 as illustrated in Figure 5.45. The initial eccentricity is important in deciding the profile of axial strength versus slenderness ratio curve. Comparison also shows that concrete wall with different aspect ratio also has similar curve shape.

From Figure 5.43 to Figure 5.45, it is important to note that the axial strength of concrete wall decreases non-linearly with the increase of slenderness ratio due to geometric non-linearity. At t/600 eccentricity and with aspect ratio fixed at 5.3, the axial strength ratio of wall decreases from 0.904 to 0.406 when slenderness ratio is increased from 23 to 50. About 55% strength reduction is observed. Likewise, when eccentricity is increased to t/12 and t/6, the axial strength ratio decreases from 0.614 to 0.213 and 0.419 to 0.149 respectively when slenderness ratio is increased from 23 to 50. At the eccentricity of t/12 and t/6, about 65% strength reduction is observed when the slenderness ratio is increased. It is crucial to note that concrete wall with slenderness ratio greater than 30, and even up to 50, is still able to sustain load. This has further highlighted the limitation of design equations in standard in which negative strength value is resulted for slenderness ratio more than 30. This study also confirms the previous findings of Doh and Fragomeni (2005).

The concrete wall with larger slenderness ratio has longer effective length. It has the higher tendency to buckle and therefore its lateral deflection increases significantly when loaded. The significant increase of lateral deflection results in increase of secondary moment and hence reduces axial strength ratio. The axial strength ratio decreases non-linearly with the increase of slenderness ratio.

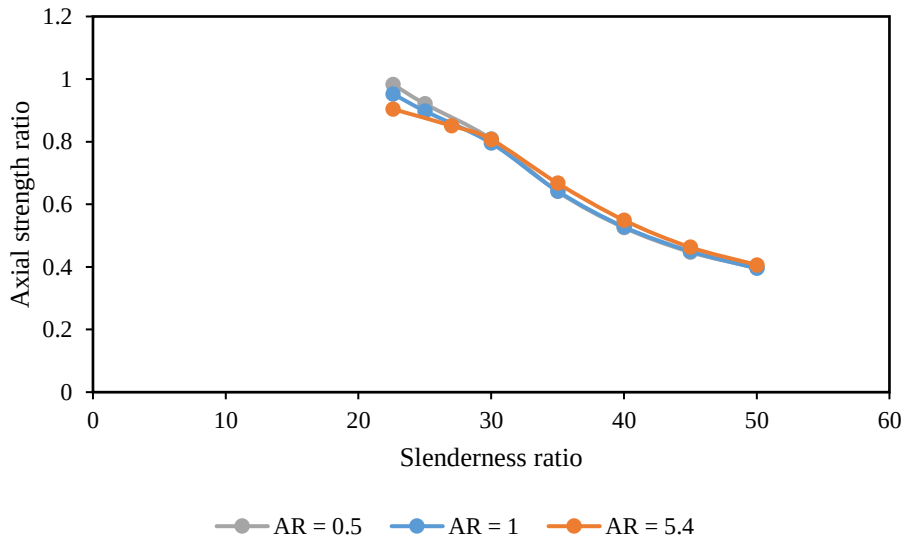

Figure 5.43: Axial strength ratio versus slenderness ratio (AR = 0.5, 1, 5.3, e = t/600, f'_c = 13.7MPa, ρ = 1800kg/m^3, f_t/ f'_c=0.08)

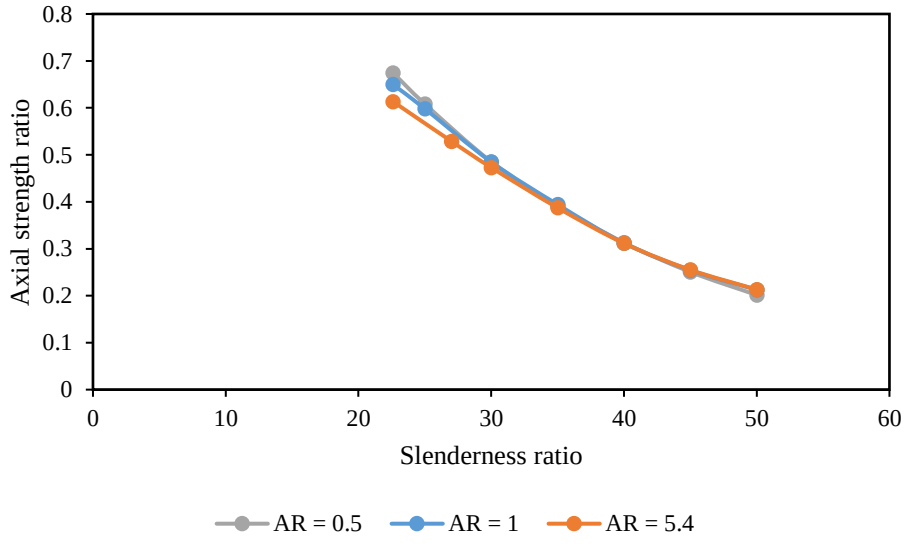

Figure 5.44: Axial strength ratio versus slenderness ratio (AR = 0.5, 1, 5.3, e = t/12, f'_c = 13.7MPa, ρ = 1800kg/m^3, f_t/ f'_c=0.08)

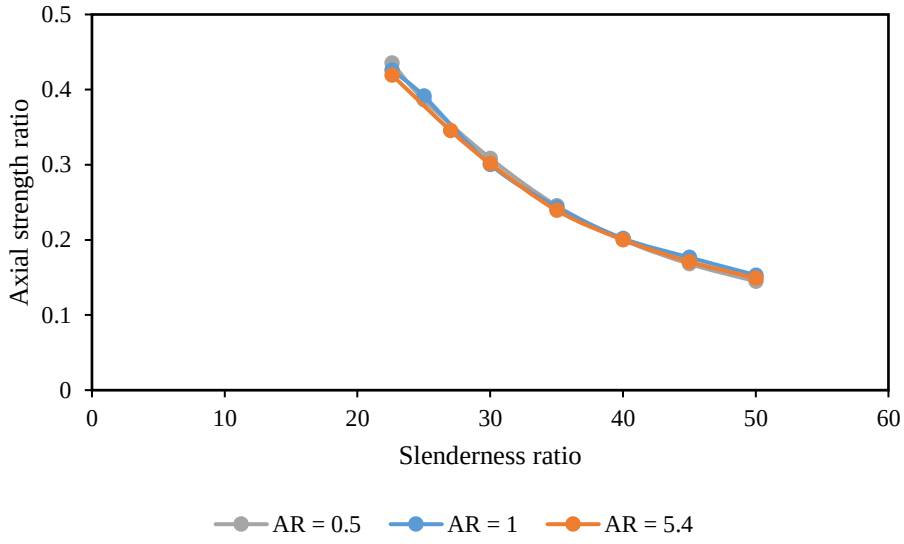

Figure 5.45: Axial strength ratio versus slenderness ratio (AR = 0.5, 1, 5.3, e = t/6, f'_c = 13.7MPa, ρ = 1800kg/m^3, f_t/f'_c=0.08)

5.5.2. Effect of Eccentricity

Eccentricity exists when the applied load is offset from the centroid of wall, creating bending stress along with the axial stress. The investigation of eccentricity effect is carried out at values of t/600 to t/20, t/12 and t/6. Figure 5.46 illustrates the change of axial strength ratio with slenderness ratio at different eccentricity. The concrete compressive strength and aspect ratio are fixed at 13.7MPa and 5.3 respectively. As discussed previously, the shape of axial strength versus slenderness ratio curve changes from downward concave shape to upward concave shape when the eccentricity is increased. At low eccentricity of t/600, the reduction of axial strength ratio with slenderness ratio is more significant when compared to higher eccentricity. The most remarkable strength reduction is observed in the slenderness ratio interval of 30 to 40. Strength reduction tapers off in the range of 40 to 50. When the eccentricity is increased to t/20 and subsequently t/12, smooth axial strength ratio reduction is observed, without a significant reduction interval of slenderness ratio. Similarly, strength reduction is also observed to taper off in the slenderness ratio range of 40 to 50. At eccentricity of t/6, it is noted that reduction of axial strength ratio with increase of slenderness ratio is less severe. This can be explained that at higher eccentricity, the primary moment due to eccentricity is relatively large when compared to secondary moment. At lower slenderness ratio of 23, axial strength ratio decreases from 0.904 to

0.694, 0.614 and 0.419 when eccentricity is increased from t/600 to t/20, t/12 and t/6 respectively. At high slenderness ratio of 50, when eccentricity is increased from t/600 to t/20, t/12 and t/6, the axial strength ratio decreases from 0.406 to 0.243, 0.213 and 0.149 respectively. The change of axial strength ratio versus slenderness ratio envelope with eccentricity shows similar trend to that of reinforced concrete column (Warner et al., 1998). For concrete wall with one side edge restrained (Ho & Doh, 2019), the envelope of axial strength ratio versus slenderness ratio also changes from downward concave shape to upward concave shape when the eccentricity is increased.

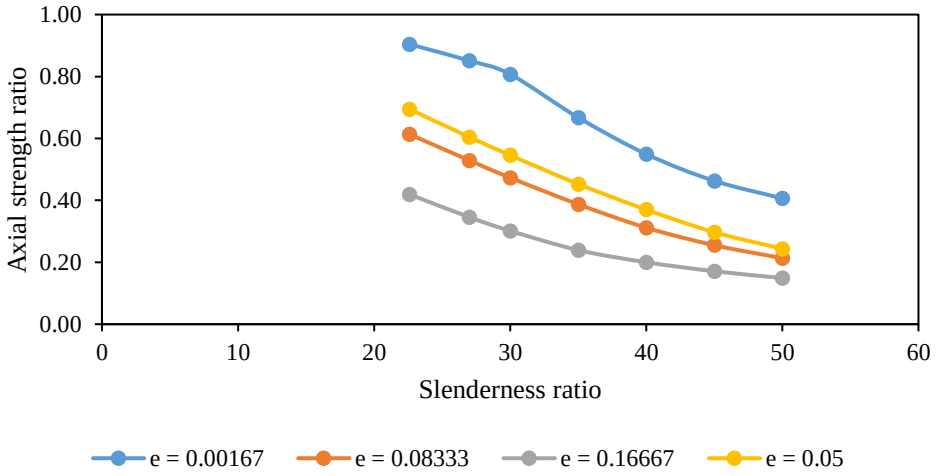

Figure 5.46: Axial strength ratio versus slenderness ratio (AR = 5.3, e = t/600, t/20, t/12, t/6, f'_c = 13.7MPa, ρ = 1800kg/m^3, f_t/ f'_c=0.08)

5.5.3. Effect of Aspect Ratio

To evaluate the effect of aspect ratio, aspect ratio is varied from 0.5 to 5.3 with eccentricity applied at t/12 and t/6. Figure 5.47 and Figure 5.48 illustrate the axial strength ratio versus aspect ratio with eccentricity applied at t/12 and t/6 respectively. As observed from Figure 5.47, at t/12 eccentricity and 23 slenderness ratio, aspect ratio has little effect on axial strength ratio when the aspect ratio is more than 1. When aspect ratio is decreased from 1 to 0.75 and 0.5, the axial strength ratio increases from 0.65 to 0.66 and 0.675 respectively. At 40 slenderness ratio, the change of aspect ratio has negligible effect on axial strength ratio. When eccentricity is increased to t/6 as shown in Figure 5.48, the effect of aspect ratio diminishes even in the range of 0.5 to 1.

The aspect ratio is observed to have little effect on axial strength ratio at higher eccentricity. These findings contrast with previous finding reported in literature

(Ganesan et al., 2012; Saheb & Desayi, 1989). According to Ho and Doh (2019), axial strength ratio of wall is influenced by aspect ratio through effective height when the at least one of the edges of wall is supported. For wall under one-way action in this research, the side edges of concrete wall are not supported. There is no active lateral restraint to support the edges of wall which can reduce effective height. The slight improvement of axial strength ratio with decrease of aspect ratio is mainly due to the increased stability by self-weight when the length of wall is increased.

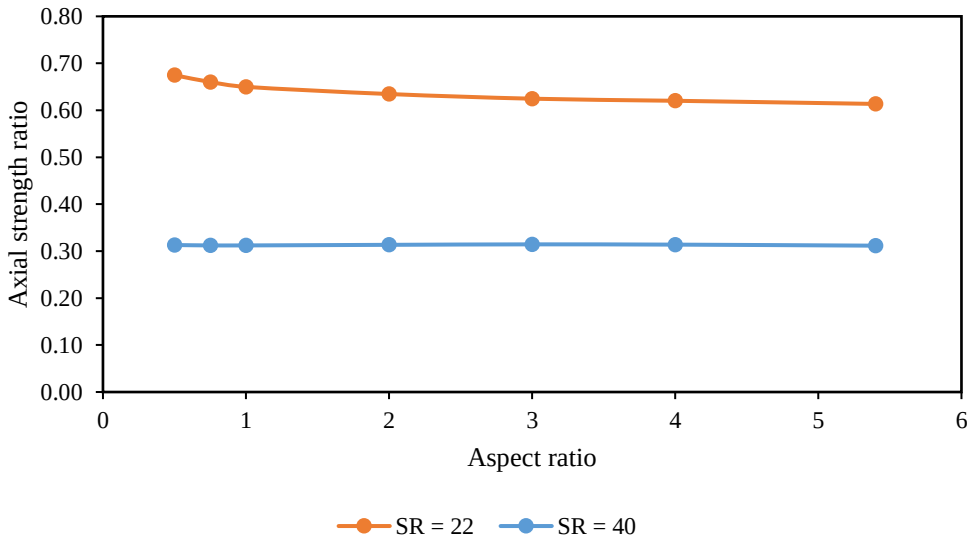

Figure 5.47: Axial strength ratio versus aspect ratio
(AR = 0.5, 0.75, 1, 2, 3, 4, 5.3, e = t/12, f'_c = 13.7MPa, ρ = 1800kg/m^3, f_t/f'_c=0.08)

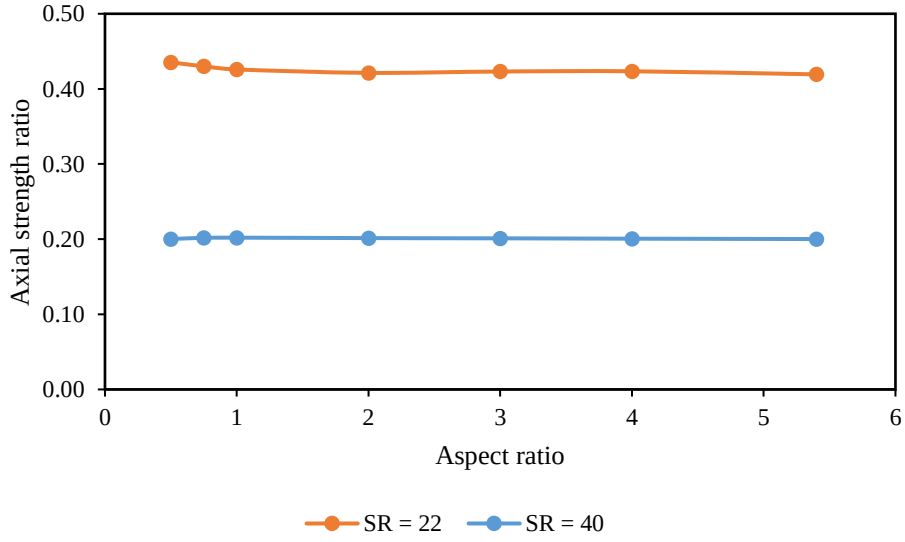

Figure 5.48: Axial strength ratio versus aspect ratio
(AR = 0.5, 0.75, 1, 2, 3, 4, 5.3, e = t/6, f'_c = 13.7MPa, ρ = 1800kg/m^3, f_t/f'_c=0.08)

5.5.4. Effect of Concrete Strength

Table 5.11 shows the comparison of ultimate axial capacity of concrete wall when compressive strength is varied from 13.7 to 80MPa. For comparison purpose, the load increment ratio is expressed with reference to 13.7MPa compressive strength as base. It is noted that ultimate capacity increases with the increase of compressive strength. However, the increase in ultimate axial capacity is not directly proportional to increment of concrete compressive strength. For instance, when slenderness ratio is fixed at 22.6 and at eccentricity of t/20, the ultimate capacity increases by 1.62, 2.32, 2.9 and 3.32 times when compressive strength is increased from 13.7MPa to 25, 40, and 80 MPa respectively. As noted in Table 5.11, the percentage of strength increment also differs from the effect of slenderness ratio. To clarify this, at fixed eccentricity of t/20 and compressive strength of 80MPa, the ratio of strength increase is 3.32, 2.45, 2.13 and 2.14 for slenderness ratio of 23, 30, 40 and 50 respectively. Interestingly, at lower slenderness ratio range of 23 to 30, the ratio of ultimate capacity increases due to increment of compressive strength. However, the increase magnitude of this ratio is lower with the increase of eccentricity value. However, this trend is opposite to that of slenderness ratio in the range of 40 to 50.

The ultimate axial capacity of concrete wall is expressed as axial strength ratio and summarized in Table 5.12. It is noted that axial strength ratio decreases with increase of concrete compressive strength. Typically, at slenderness ratio of 30 and eccentricity of t/6, the axial strength ratio decreases by 23%, 37%, 50% and 57% respectively when concrete strength is increased from 13.7MPa to 25, 40, and 80 MPa. The influences of concrete strength on the axial strength of concrete wall at eccentricity of t/20, t/12 and t/6 are further illustrated in Figure 5.49, Figure 5.50 and Figure 5.51 respectively. These figures showed that the envelope decreases when compressive strength of concrete increases. This is in good agreement with Doh and Fragomeni (2005) that the ultimate capacity increases non-linearly with increase of compressive strength of concrete. This is mainly due to the nonlinearity which arises from aggregate interlock at the crack, tensile cracking and compression crushing of material (Bathe et al., 1989). Eventually, ultimate axial strength ratio of concrete wall decreases with increasing of compressive strength and its value is also affected by slenderness ratio and eccentricity value. The current design equations from standards do not consider the effect of

nonlinear relationship of axial capacity and compressive strength. Linear extrapolation for high strength concrete can lead to unsafe design.

Table 5.11: Effect of compressive strength

f'c (MPa)	H/t	Failure Load (kN)			Load increment ratio		
		t/20	t/12	t/6	t/20	t/12	t/6
13.7	22.6	153.35	135.49	92.61	1	1	1
	30	162.26	140.62	89.63	1	1	1
	40	147.73	124.41	79.90	1	1	1
	50	119.88	104.99	73.50	1	1	1
25	22.6	249.12	216.01	141.78	1.62	1.59	1.53
	30	243.99	203.80	125.50	1.50	1.45	1.40
	40	198.26	167.96	111.26	1.34	1.35	1.39
	50	160.63	141.87	102.44	1.34	1.35	1.39
40	22.6	355.15	304.48	188.37	2.32	2.25	2.03
	30	317.12	260.81	163.94	1.95	1.85	1.83
	40	250.64	214.48	146.36	1.70	1.72	1.83
	50	205.25	181.13	134.22	1.71	1.73	1.83
60	22.6	444.83	368.80	220.62	2.90	2.72	2.38
	30	360.54	300.59	196.46	2.22	2.14	2.19
	40	285.33	247.39	176.36	1.93	1.99	2.21
	50	234.07	208.47	160.07	1.95	1.99	2.18
80	22.6	508.62	426.93	251.89	3.32	3.15	2.72
	30	397.27	335.13	225.27	2.45	2.38	2.51
	40	314.93	275.88	203.50	2.13	2.22	2.55
	50	256.64	232.11	182.42	2.14	2.21	2.48

Table 5.12: Comparison of axial strength ratio

f'c (MPa)	H/t	Axial strength ratio			Comparison		
		t/20	t/12	t/6	t/20	t/12	t/6
13.7	22.6	0.694	0.614	0.419	1	1	1
	30	0.546	0.473	0.302	1	1	1
	40	0.370	0.312	0.200	1	1	1
	50	0.243	0.213	0.149	1	1	1
25	22.6	0.618	0.536	0.352	0.89	0.87	0.84
	30	0.450	0.376	0.231	0.82	0.79	0.77
	40	0.272	0.231	0.153	0.74	0.74	0.76
	50	0.179	0.158	0.114	0.73	0.74	0.76
40	22.6	0.551	0.472	0.292	0.79	0.77	0.70
	30	0.365	0.300	0.189	0.67	0.64	0.63
	40	0.215	0.184	0.126	0.58	0.59	0.63
	50	0.143	0.126	0.093	0.59	0.59	0.63
60	22.6	0.460	0.381	0.228	0.66	0.62	0.54
	30	0.277	0.231	0.151	0.51	0.49	0.50
	40	0.163	0.141	0.101	0.44	0.45	0.50
	50	0.108	0.097	0.074	0.45	0.45	0.50
80	22.6	0.394	0.331	0.195	0.57	0.54	0.47
	30	0.229	0.193	0.130	0.42	0.41	0.43
	40	0.135	0.118	0.087	0.37	0.38	0.44
	50	0.089	0.081	0.063	0.37	0.38	0.43

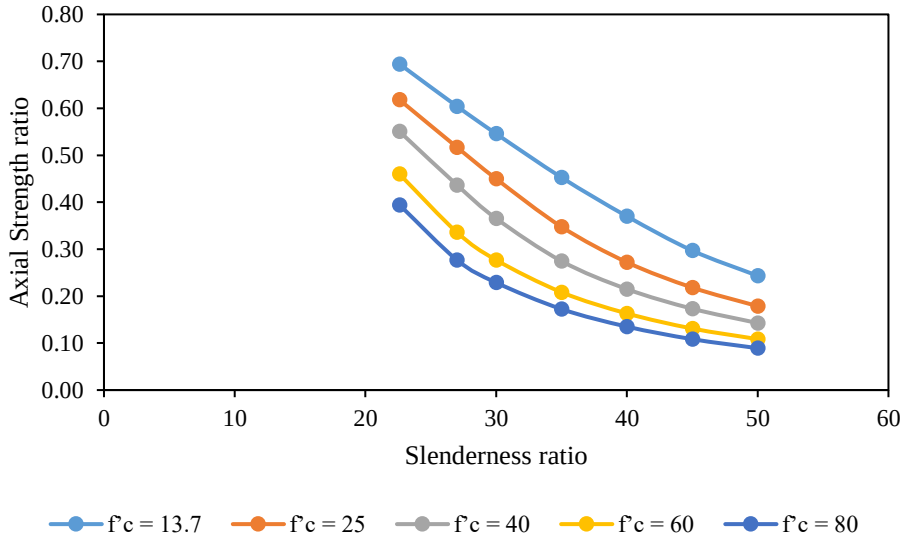

Figure 5.49: Axial strength ratio versus slenderness ratio
(AR = 5.3, e = t/20, f'_c = 13.7, 25, 40, 60, 80MPa, ρ = 1800kg/m^3, f_t/f'_c=0.08)

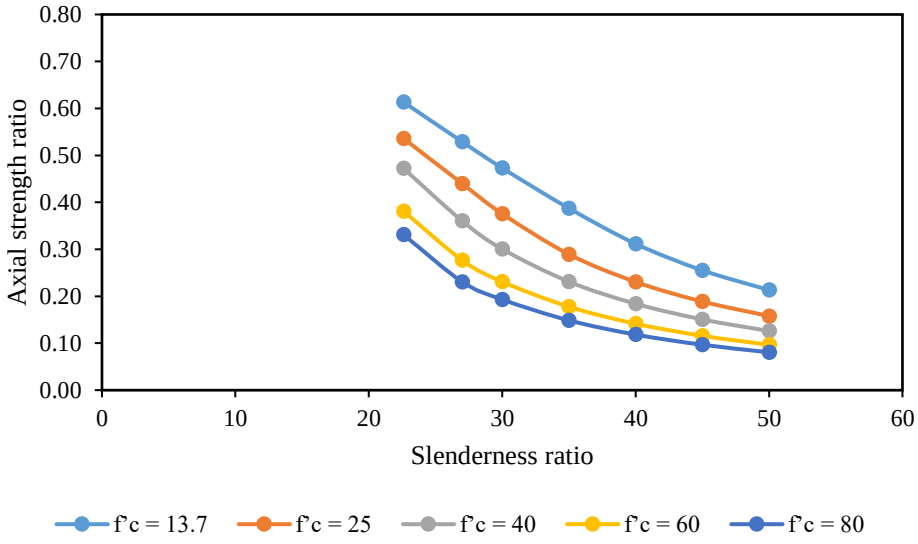

Figure 5.50: Axial strength ratio versus slenderness ratio (AR = 5.3, e = t/12, f'_c = 13.7, 25, 40, 60, 80MPa, ρ = 1800kg/m^3, f_t/f'_c=0.08)

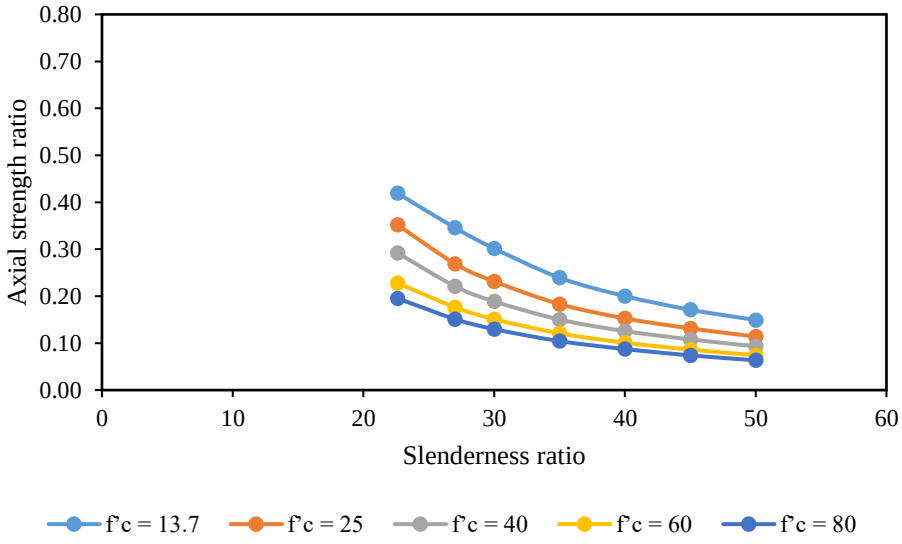

Figure 5.51: Axial strength ratio versus slenderness ratio (AR = 5.3, e = t/6, f'_c = 13.7, 25, 40, 60, 80MPa, ρ = 1800kg/m^3, f_t/f'_c=0.08)

5.5.5. Effect of Elastic Modulus

Elastic modulus of concrete is varied to study its effect on axial capacity of concrete wall. The elastic modulus is determined from the density of concrete by using Eq. 5-44. The range of density of concrete for this study is from 1600 to 2400kg/m^3 and the FEA results are summarized in Table 5.13. For comparison purpose, the load ratios are

expressed with reference to the load at density of 2400 kg/m^3 as base. Decrease in elastic modulus with constant low eccentricity and low slenderness ratio results in decrease in both ultimate axial capacity and axial strength ratio. It can be seen from Table 5.13 that P_{fea}/P_{2400} ratio decreases as elastic modulus of concrete decreases. At eccentricity of t/20 and slenderness ratio 23, by decreasing the elastic modulus from 18713 to 10186MPa, the axial strength decreases by 7%. The effect of elastic modulus reduction on axial capacity is more pronounced with increase of slenderness ratio. At eccentricity of t/20 and slenderness ratio of 50, decrease of elastic modulus has resulted in 39% strength reduction. For higher values of eccentricity and constant slenderness ratio, the axial capacity of wall also decreases with decreasing of elastic modulus. For example, at 23 slenderness ratio, when elastic modulus decreases from 18713 to 10186MPa, the axial capacity decreases by 7%, 8% and 13% for eccentricity of t/20, t/12 and t/6 respectively.

The plots of axial strength ratio versus slenderness ratio with different elastic modulus at eccentricity of t/20, t/12 and t/6 are illustrated in Figure 5.52, Figure 5.53 and Figure 5.54 respectively. It is observed that the curves of axial strength ratio versus slenderness ratio shift downward when the elastic modulus of concrete decreases at a given compressive strength. As mentioned previously, lightweight concrete exhibits more ductile stress-strain behaviour under compression when compared to normal weight concrete at a given compressive strength. This is due to the reduced elastic modulus resulting from the use of lightweight aggregate in concrete. The ultimate load capacity of concrete wall under axial loading depends on not only the axial stiffness of wall but also the flexural stiffness of the wall section. The flexural stiffness of concrete wall is used to resist the moment induced by both eccentric loading and second order effect resulting from lateral deflection. The reduced elastic modulus of lightweight concrete results in reduced flexural stiffness which is required for resisting moment produced by eccentricity and slenderness effect, and hence, reduced axial capacity. However, all the current simplified design equations from design standards and published literature do not consider the effect of elastic modulus. The effect of elastic modulus must be considered in the design equation in order to safely predict the axial capacity of lightweight concrete wall.

Table 5.13: Effect of elastic modulus (f'c=13.7MPa)

ρ (kg/m^3)	E (MPa)	H/t	Eccentricity								
			t/20			t/12			t/6		
			P_{fea} (kN)	P_{fea}/ f'cAg	P_{fea}/ P_{2400}	P_{fea} (kN)	P_{fea}/ f'cAg	P_{fea}/ P_{2400}	P_{fea} (kN)	P_{fea}/ f'cAg	P_{fea}/ P_{2400}
1600	10186	23	149	0.68	0.93	131	0.59	0.92	87	0.40	0.87
		30	152	0.51	0.86	128	0.43	0.83	78	0.26	0.75
		40	126	0.32	0.71	107	0.27	0.69	70	0.18	0.67
		50	102	0.21	0.61	90	0.18	0.62	64	0.13	0.64
1800	12155	23	153	0.69	0.96	135	0.61	0.95	93	0.42	0.92
		30	162	0.55	0.92	141	0.47	0.91	90	0.30	0.85
		40	148	0.37	0.84	124	0.31	0.80	80	0.20	0.76
		50	120	0.24	0.72	105	0.21	0.73	73	0.15	0.73
2000	14236	23	156	0.71	0.97	138	0.63	0.97	96	0.43	0.96
		30	168	0.57	0.95	147	0.50	0.95	97	0.33	0.92
		40	162	0.41	0.92	140	0.35	0.90	90	0.22	0.85
		50	138	0.28	0.83	120	0.24	0.83	82	0.17	0.81
2200	16423	23	158	0.72	0.99	141	0.64	0.99	98	0.44	0.98
		30	173	0.58	0.98	152	0.51	0.98	102	0.34	0.97
		40	171	0.43	0.97	150	0.37	0.96	98	0.25	0.93
		50	154	0.31	0.93	134	0.27	0.93	92	0.19	0.91
2400	18713	23	160	0.73	1	143	0.65	1	100	0.45	1
		30	177	0.60	1	155	0.52	1	105	0.35	1
		40	177	0.44	1	156	0.39	1	105	0.26	1
		50	166	0.34	1	145	0.29	1	101	0.21	1

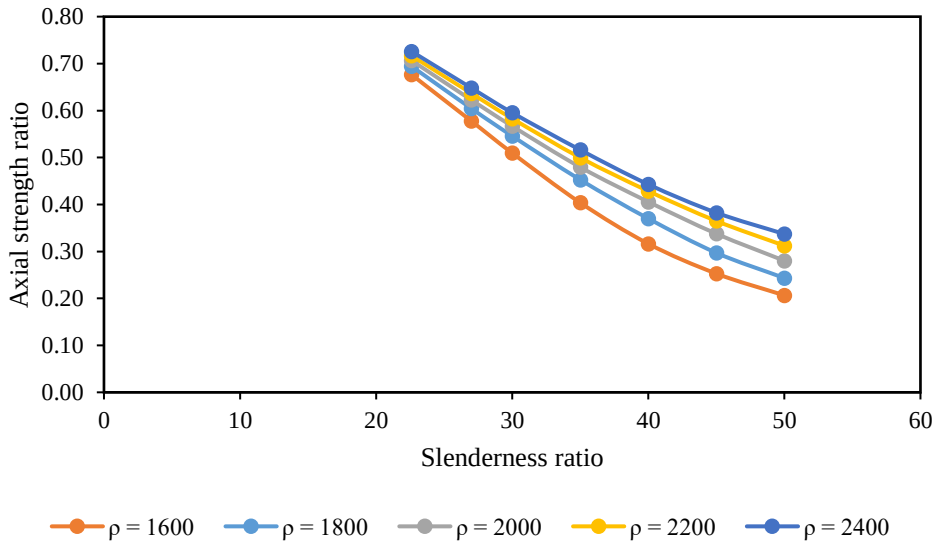

Figure 5.52: Axial strength ratio versus slenderness ratio (AR = 5.3, e = t/20, f'$_c$ = 13.7MPa, ρ = 1600, 1800, 2000, 2200, 2400kg/m^3, f_t/ f'$_c$=0.08)

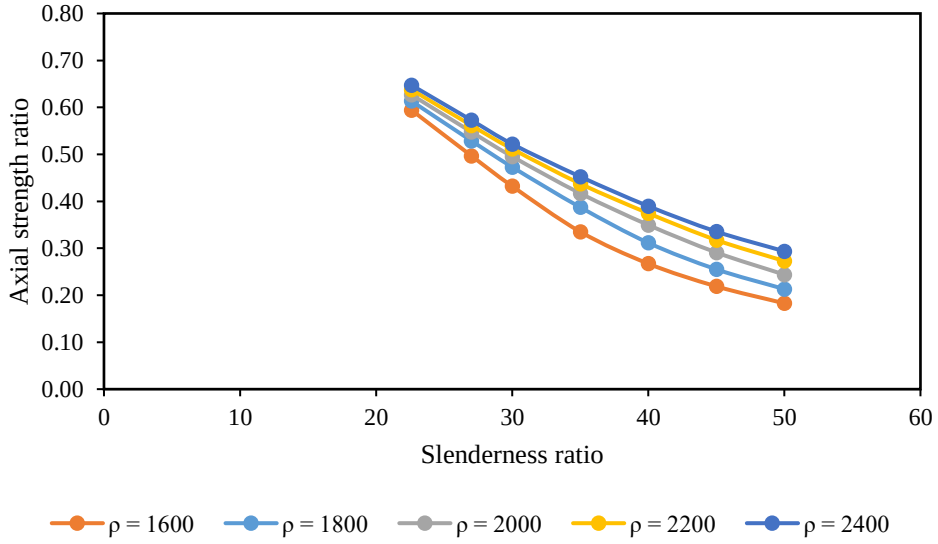

Figure 5.53: Axial strength ratio versus slenderness ratio (AR = 5.3, e = t/12, f'$_c$ = 13.7MPa, ρ = 1600, 1800, 2000, 2200, 2400kg/m^3, f_t/ f'$_c$=0.08)

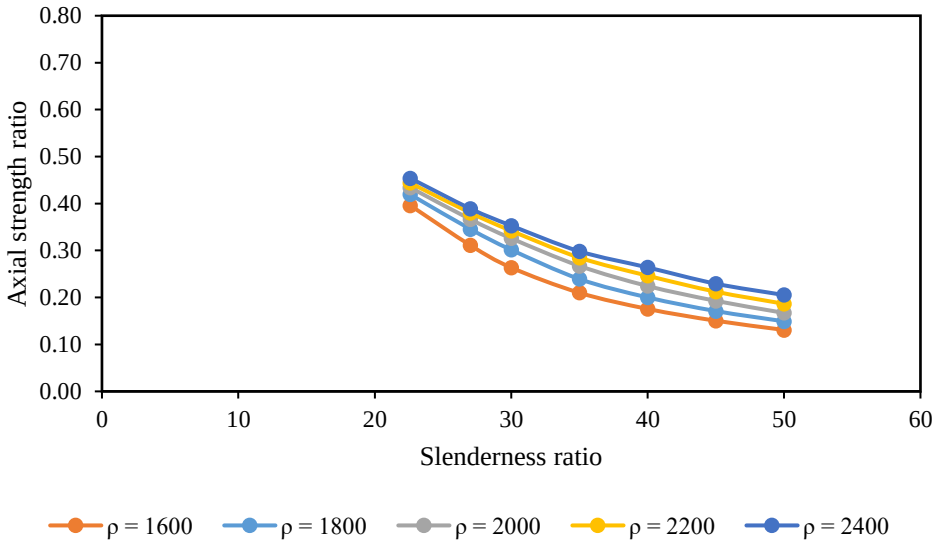

Figure 5.54: Axial strength ratio versus slenderness ratio (AR = 5.3, e = t/6, f'$_c$ = 13.7MPa, ρ = 1600, 1800, 2000, 2200, 2400kg/m^3, f_t/ f'$_c$=0.08)

5.5.6. Effect of Tensile Strength

The tensile strength of concrete is insignificant for structural member loaded under pure compression. However, in many occasions, concrete has to resist tensile stress resulting from load which is applied with eccentricity, even if it is reinforced with steel.

This is particularly important for lightweight concrete since tensile strength of concrete is highly dependent on the type of lightweight aggregate used. Table 5.14 shows the effect of tensile strength on axial load capacity of concrete wall. For comparison purpose, load increment ratio is expressed with reference to 0.05 as base. At eccentricity of t/12, it can be observed that tensile strength of concrete has little effect on axial capacity of wall. Under eccentricity of t/12, the improvement of axial capacity by increased tensile strength is low particularly in the slenderness ratio range of 23 to 35. At slenderness ratio of 50, the axial capacity increases by 9% when tensile strength ratio is increased to 0.15. In Figure 5.55, it is noted that the curves with different tensile strengths overlap one another at the front region but divert slightly at the back region.

When eccentricity is increased to t/6, the tensile strength of concrete has noticeable effect on axial capacity of concrete wall as shown in Figure 5.56. At slenderness ratio of 23 and eccentricity of t/6, the ultimate axial capacity of wall increases from 90.96kN to 92.61 and 99.26 respectively when tensile strength ratio is increased from 0.05 to 0.15. About 2% and 9% of strength improvement is observed. When slenderness ratio increases, the improvement of ultimate capacity is more obvious. At slenderness ratio of 50, when tensile strength ratio is increased from 0.05 to 0.15, the axial capacity increases by 23%. Nevertheless, though the tensile ratio has increased at high slenderness ratio, there is no pronounced increase in strength magnitude. Thus, the increased tensile strength of concrete is able to provide slightly more flexural stiffness to resist the induced moment due to eccentricity and hence marginally increases ultimate axial capacity. Since the effect of concrete tensile strength is insignificant, it is normally ignored in the calculation of axial compressive capacity (Warner et al., 1998). Therefore, tensile strength parameter is not considered in the derivation of concrete wall axial strength equations.

Table 5.14: Effect of tensile strength

Eccentricity		t/12		t/6		t/12	t/6
f't/f'c	H/t	P_{fea} (kN)	P_{fea} /f'cAg	P_{fea} (kN)	P_{fea} /f'cAg	Increment ratio	
0.05	22.6	134.00	0.607	90.96	0.412	1	1
	27	140.22	0.524	89.46	0.334	1	1
	30	138.75	0.467	84.82	0.285	1	1
	35	131.68	0.378	77.02	0.221	1	1
	40	120.75	0.302	73.33	0.184	1	1
	45	109.44	0.248	69.36	0.157	1	1
	50	102.22	0.207	67.83	0.138	1	1
0.08	22.6	135.49	0.614	92.61	0.419	1.01	1.02
	27	141.52	0.529	92.48	0.346	1.01	1.03
	30	140.62	0.473	89.63	0.302	1.01	1.06
	35	134.89	0.387	83.34	0.239	1.02	1.08
	40	124.41	0.312	79.90	0.200	1.03	1.09
	45	112.71	0.255	75.55	0.171	1.03	1.09
	50	104.99	0.213	73.50	0.149	1.03	1.08
0.15	22.6	137.69	0.623	99.26	0.449	1.03	1.09
	27	144.09	0.539	101.28	0.379	1.03	1.13
	30	143.78	0.484	99.23	0.334	1.04	1.17
	35	138.84	0.399	95.16	0.273	1.05	1.24
	40	131.00	0.328	91.28	0.229	1.08	1.24
	45	119.02	0.269	86.67	0.196	1.09	1.25
	50	111.04	0.225	83.52	0.170	1.09	1.23

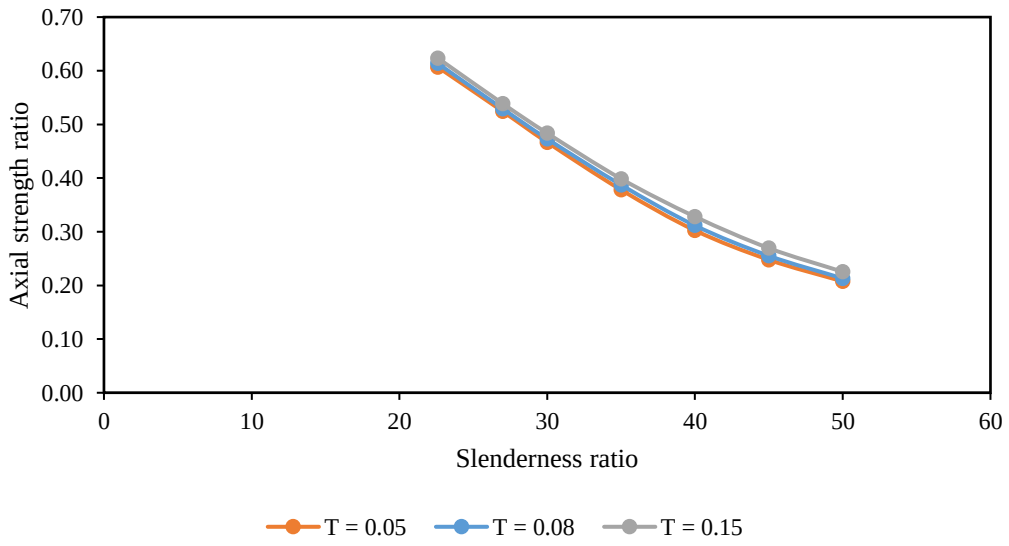

Figure 5.55: Axial strength ratio versus slenderness ratio
(AR = 5.3, e = t/12, f'_c = 13.7MPa, ρ = 1800kg/m^3, f_t/ f'_c= 0.05, 0.08, 0.15)

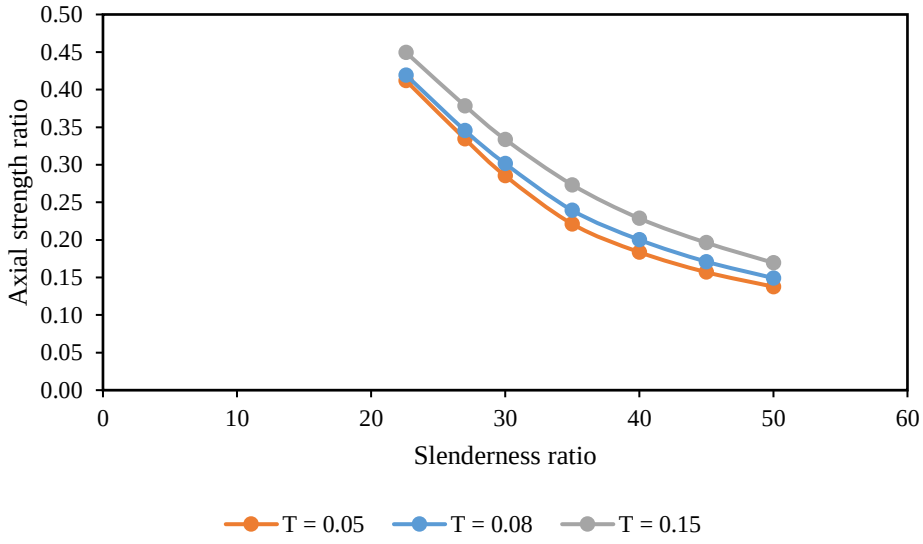

Figure 5.56: Axial strength ratio versus slenderness ratio (AR = 5.3, e = t/6, f'_c = 13.7MPa, ρ = 1800kg/m^3, f_t/f'_c= 0.05, 0.08, 0.15)

5.6. Concluding Remark

This study in this chapter presents the numerical modelling of concrete wall panel under axial loading by using Concrete Damaged Plasticity (CDP) in ABAQUS. The models are validated by using the results obtained from experimental tests and also benchmarked with the results in published literature. The models developed are subsequently used to perform parametric study on the factors that influence the axial capacity of concrete wall. From the consequential results, the following conclusions can be drawn:

1. Generally, CDP model is able to predict the failure modes, load-deflection behaviour and ultimate axial capacity of lightweight concrete well. The FEA results have showed slightly higher ultimate axial capacity compared to experimental results.
2. Comparative studies of published and FEA results show that FEA is an effective technique to model the structural behaviour of concrete wall.
3. Parametric study on the effects of slenderness ratio shows that the axial strength ratio decreases with increase of slenderness ratio. It has been demonstrated that concrete wall is still able to sustain loading for slenderness ratio more than 30.

4. Eccentricity is important in determining the envelope of axial strength ratio versus slenderness ratio.
5. The parametric study shows that aspect ratio has little effect on axial strength ratio. The effect of aspect ratio diminishes with increasing of either slenderness ratio or eccentricity value.
6. The ultimate axial capacity increases non-linearly with increase of compressive strength of concrete. The axial strength ratio is found to decrease when compressive strength increases.
7. A decrease in elastic modulus of concrete results in reduced ultimate axial capacity and axial strength ratio of wall.
8. Tensile strength is found to have less effect on axial strength ratio at lower slenderness ratio and eccentricity value. The effect of tensile strength becomes marginally more pronounced at higher eccentric loading and slenderness ratio.

6. Rational Design Method

6.1. Introduction

The experimental and numerical modelling works done in this research provide a good framework for deriving a generalized equation that can be used to design the axial capacity of lightweight concrete, normal strength concrete and high strength concrete walls. Although researchers have derived several equations to determine the ultimate load capacity of concrete wall under axial loading, these equations have limitations in application due to their conservativeness and over-simplicity. Lightweight concrete generally has reduced elastic stiffness due to the use of weaker lightweight aggregates. This can increase the tendency of structural concrete load bearing wall to buckle and hence lower its load carrying capacity. To overcome the shortcomings of the existing equations, in this chapter, two new design equations are proposed by using both the experimental and numerical modelling results. The assumption, validation and comparative studies of the proposed design equations are also elaborated in this chapter.

6.2. Proposed Design Equation

Based on the experimental tests and numerical simulations from the previous two chapters, it is noted with better insight that the axial capacity of concrete wall is affected by not only its geometry non-linearity but also its material properties. However, as discussed in chapter 2, there are limitations in the current design equations from the standards. The current design equations from AS 3600 and Eurocode consider only the effect of slenderness ratio and eccentricity. The design equation from ACI 318 considers only slenderness ratio. In any case, the equations are only applicable for slenderness ratio up to 30. Besides, they are not suitable for designing lightweight concrete wall. The results obtained from FEA parametric studies have shown that the axial strength ratio decreases as the elastic modulus of concrete decreases due to the use of lightweight aggregate. Furthermore, axial strength of concrete wall increases non-linearly with increase of compressive strength. Notably, the existing design equations do not consider the effects of both compressive strength and elastic modulus. As such, there is a need to enhance the design equations to

determine the axial capacity of concrete wall with better accuracy. In this section, a new semi-empirical equation is proposed to take into consideration of material compressive strength and elastic modulus.

The proposed design equation is derived based on concrete stress block of wall cross section and regression analysis. The following are the assumptions made in equation derivation:

1. The wall must contain minimum reinforcement in both vertical and horizontal directions as specified by the AS3600.
2. The loads are applied within the stress block of the section.
3. The wall behaves as one-way wall under axial loading.
4. The largest eccentricity ratio that can be applied without cracking is only allowed up to $e/t \leq 1/6$.

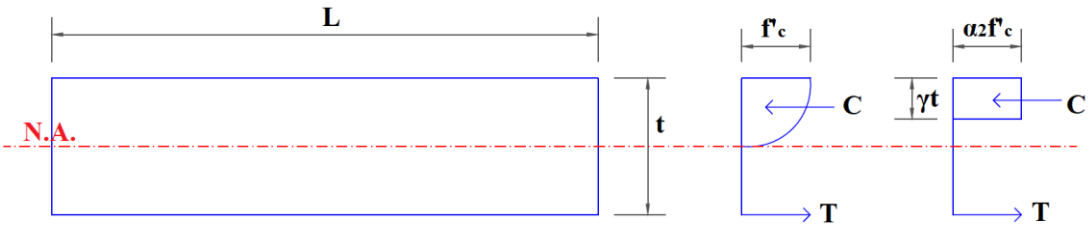

Figure 6.1: Concrete stress block

Figure 6.1 shows the stress block of concrete wall cross section. From the equivalent rectangular stress block, the compression force can be determined as Eq. 6-1.

$$P_{us} = \alpha_2 \gamma f'_c A_g \qquad \text{Eq. 6-1}$$

where

α_2 = $0.85 - 0.0015 f'_c$, $\alpha_2 \geq 0.67$

γ = $0.97 - 0.0025 f'_c$, $\gamma \geq 0.67$

f'_c = Compressive strength of concrete

A_g = Cross sectional area of wall

Eccentricity and slenderness ratio parameters are introduced into Eq. 6-1 by using regression analyses of FEA results. The details of regression analyses are shown in Figure 6.2 for eccentricity ratio at t/20, t/12 and t/6 respectively. Similar approaches of Saheb and Desayi (1989) and Ganesan et al. (2013) are taken in this equation

derivation. Notwithstanding, instead of using quadratic regression for the effect of slenderness ratio, exponential function has shown better fitting and it is therefore adopted in this equation derivation. From Figure 6.2, the regression equations show the same argument value in exponential function with different constant values. Hence, another regression analysis has been carried out to introduce the constant value for different eccentricity, as shown in Figure 6.3. Eq. 6-1 then becomes Eq. 6-2.

$$P_{us1} = \alpha_2 \gamma f'_c A_g exp(-0.038\lambda) e_L \qquad \text{Eq. 6-2}$$

where

$$exp(-0.038\lambda) e_L \leq 1$$

The eccentricity parameter is determined from

$$e_L = 7.77 e_r + 2.51 \qquad \text{Eq. 6-3}$$

where

λ = Slenderness ratio

e_L = Eccentricity parameter

e_r = Eccentricity ratio of applied load

Eq. 6-2 is rearranged with f'c expressed in terms of other variables and this effective f'c value is then plotted against the actual f'c as illustrated in Figure 6.4. From the regression analysis, compressive strength of concrete is represented by a power function of f'_c variable raised to a fixed power of 0.68. This is to account for the non-linear increase in axial capacity as concrete strength increases. Eq. 6-2 is subsequently transformed into Eq. 6-4.

$$P_{us2} = 2.24 \alpha_2 \gamma f'^{0.68}_c A_g exp(-0.038\lambda) e_L \qquad \text{Eq. 6-4}$$

(a)

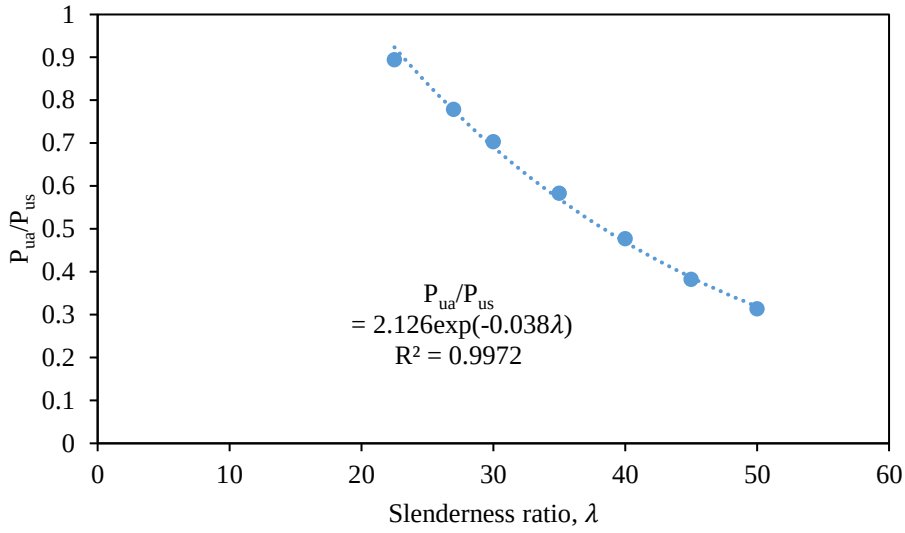

(b)

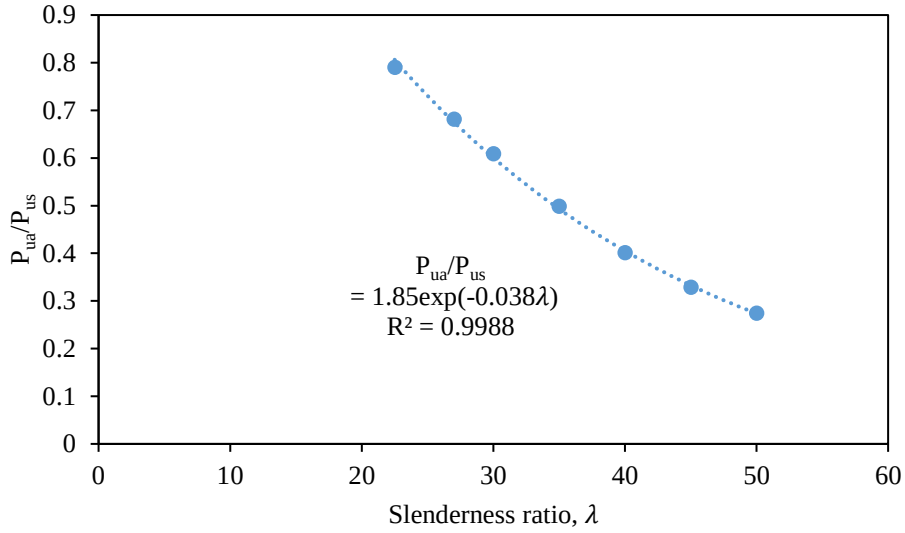

(c)

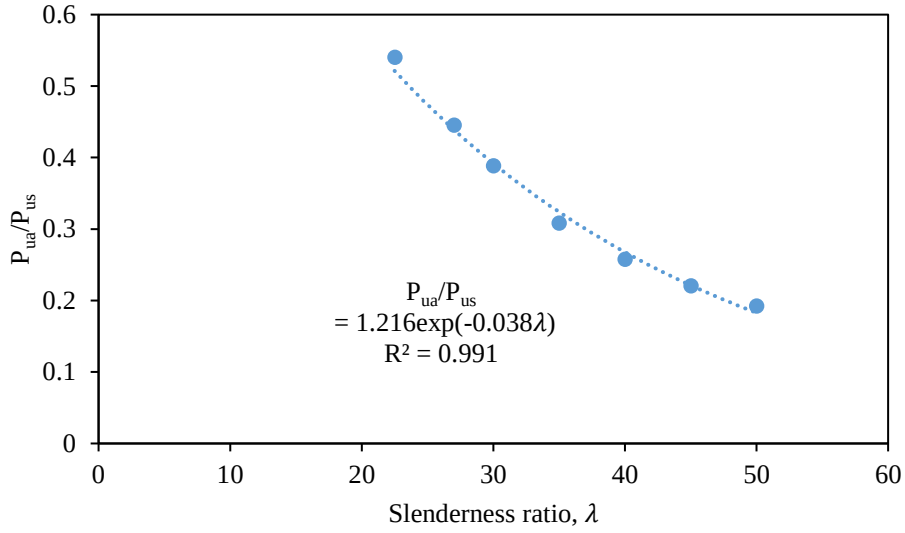

Note: P_{ua} is FEA result

Figure 6.2: Regression analysis for λ at, (a) e = t/20; (b) e= t/12; (c) e = t/6

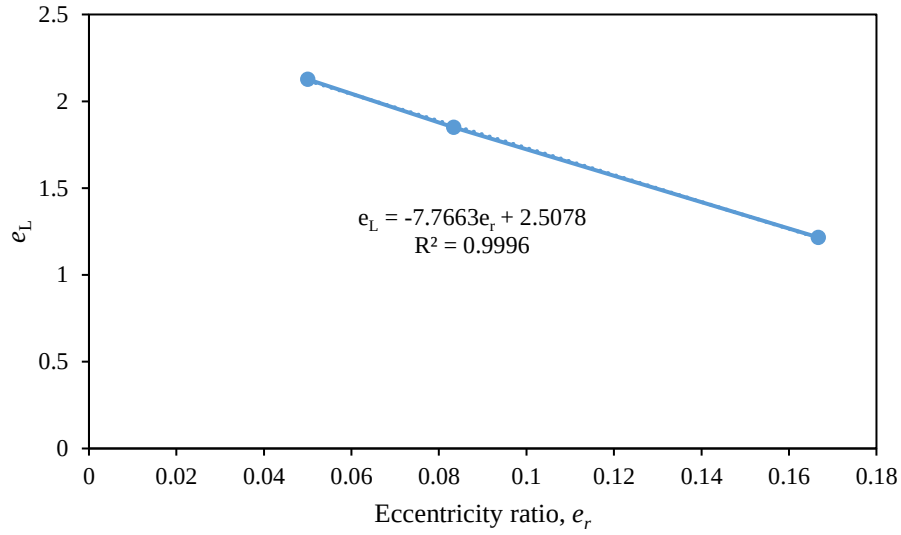

Figure 6.3: Regression analysis for parameter *e*

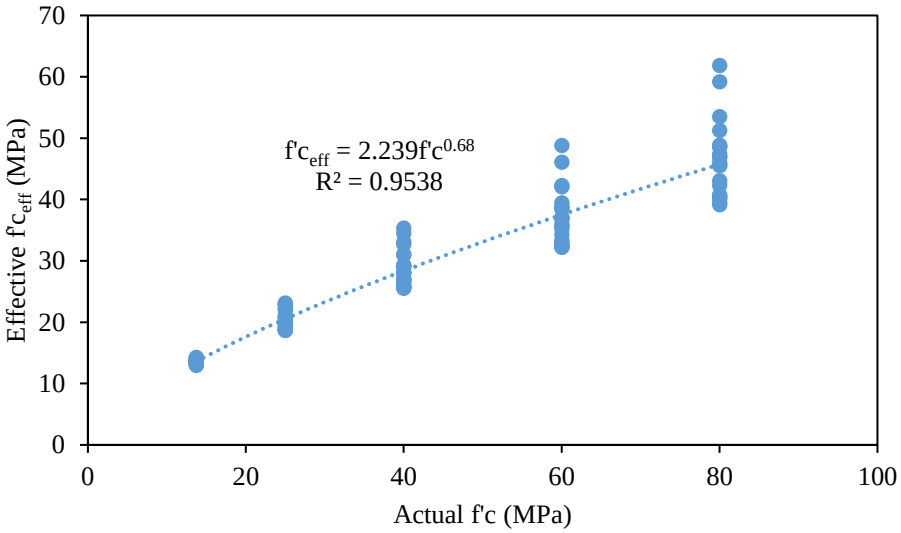

Figure 6.4: Regression analysis for f'c

Another factor, *E* variable, has been introduced to account for the effect of different values of concrete elastic modulus on its axial capacity. In order to introduce the factor for elastic modulus, the values of P_{ua}/P_{us2} from FEA results and Eq. 6-4 are plotted against *E*, as shown in Figure 6.5. *E* variable is also represented by a power function raised to a fixed power of 0.48. This factor has been calibrated from the results of FE-model by using regression analysis. The final design equation is depicted as Eq. 6-5.

$$P_u = 2.73\alpha_2\gamma f'^{0.68}_c A_g exp(-0.038\lambda) e_L E^{0.48} \qquad \text{Eq. 6-5}$$

The elastic modulus parameter, E can be determined from Eq. 6-6.

$$E = \frac{E_c}{E_{2400}} \qquad \text{Eq. 6-6}$$

where

E = Elastic modulus parameter

E_c = Elastic modulus of concrete

E_{2400} = Reference elastic modulus of concrete when ρ=2400kg/m^3

By using the relationship of material elastic modulus with density as shown in AS 3600, Eq. 6-6 can further be expressed in terms of material density as indicated in Eq. 6-7.

$$E = \frac{\rho^{1.5}}{2400^{1.5}} \qquad \text{Eq. 6-7}$$

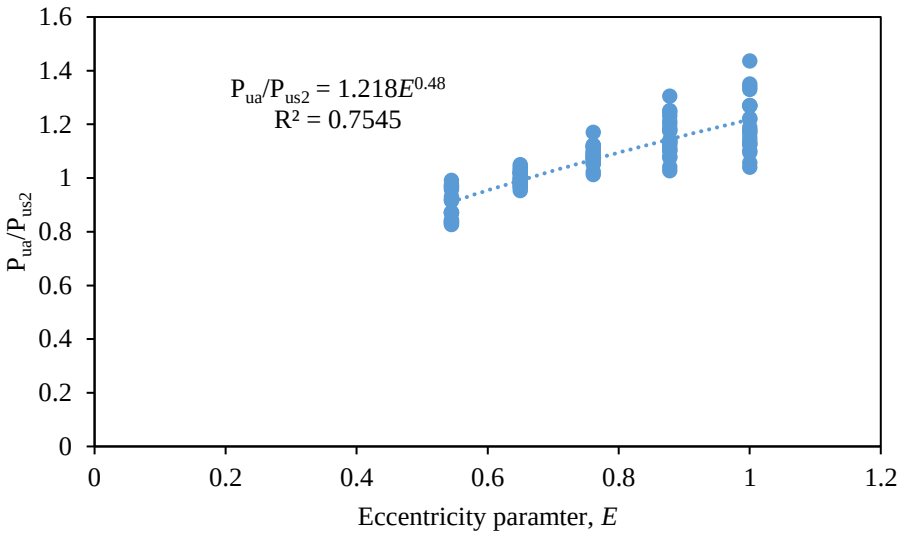

Figure 6.5: Regression analysis for parameter *E*

From the equation Eq. 6-5, axial strength of concrete wall varies with eccentricity (e_L) and slenderness ratio (λ). Non-linear increase in axial strength with compressive strength ($f'^{0.68}_c$) is reflected in the equation. Furthermore, the axial strength reduction due to the use of lightweight aggregate is allowed for through elastic modulus parameter (E).

6.3. Proposed Equation by using RSM

6.3.1. Prediction Model

Another equation can be derived by using response surface methodology (RSM). In RSM, a collection of statistical techniques is used to determine a response of interest which is influenced by several variables. By using results in regression analysis, a response to several independent input variables can be obtained. Second order quadratic RSM prediction model for axial strength of concrete wall is developed as Eq. 6-8. The ultimate axial capacity is expressed as axial strength ratio in the Eq. 6-8. Five parameters are chosen as prediction variable and the range of each variable used are summarized in Table 6.1. The input data for RSM is can be found in Appendix E.

$$P_u/f'_c A_g = (1.58203 - 0.0495916\lambda - 3.35892e_r - 0.128903\,C + 0.678011E + 0.0579191\lambda e_r + 0.000685507\lambda\,C - 0.00286346\,\lambda E + 0.104136e_r C - 0.790131e_r E + 0.00287261CE + 0.000425184\lambda^2 - 0.478367{e_r}^2 + 0.00629655C^2 - 0.186515E^2) \quad \text{Eq. 6-8}$$

where

λ = Slenderness ratio

e_L = Eccentricity ratio, e/t

C = Compressive strength parameter, $f'_c/10$

E = Elastic modulus parameter, E_c/E_{2400}

Table 6.1: Parameter ranges for RSM

Variables	Min	Centre	Max
λ	15	32.5	50
e_L	0.05 (t/20)	0.108	0.167 (t/6)
C	1	4.5	8
E	0.446	0.723	1

6.3.2. ANOVA and Model Fitness

Analysis of variance (ANOVA) has been carried out to determine the significance of each term in the model and the results are summarized in Table 6.2. ANOVA is assessed through F-test and lack of fit test. F-test is used to measure the significance of the model under investigation with respect to the variance of all the terms at the desired significance level. p-value is used to determine the statistical significance of results at a confidence level (0.05 in this case). F-value of the proposed model is 99.70 and the p-value is less than 0.0001. This has implied that the model has only 0.01% chance that an F-value of this large could occur due to noise and has indicated that the model is significant. The prediction model has shown insignificant lack of fit since the F-value and p-value for this category are 4.10 and 0.0665 respectively. The Lack of Fit F-value of 4.1 implies that there is a 6.65% chance that a Lack of Fit F-value of this large could occur due to noise.

The R^2 value of the proposed model is 0.9894 and the adjusted R^2 value is 0.9794. All the adequacy measures are close to 1, indicating good correlation between actual and predicted results. The predicted R^2 value is reported as 0.9274, which is in good agreement with adjusted R^2 value for adequate model. Adeq precision is reported as 40.4, which is greater than 4, indicating a good signal to noise ratio and it can be used to navigate the design space. Figure 6.6 shows a plot of predicted versus actual values of axial strength ratio. This figure confirms that the established model is good and suitable, since the residuals from the prediction of responses are small and the values are close to the line.

Table 6.2: ANOVA of RSM

Source	Sum of Squares	df	Mean Square	F-value	p-value	
Model	2.07	14	0.1478	99.7	< 0.0001	significant
A-SR	1.19	1	1.19	799.51	< 0.0001	
B-e	0.1736	1	0.1736	117.05	< 0.0001	
C-C	0.2953	1	0.2953	199.15	< 0.0001	
D-Ec	0.0813	1	0.0813	54.81	< 0.0001	
AB	0.056	1	0.056	37.74	< 0.0001	
AC	0.0282	1	0.0282	19.02	0.0006	
AD	0.0031	1	0.0031	2.08	0.1699	
BC	0.0072	1	0.0072	4.88	0.0431	
BD	0.0026	1	0.0026	1.76	0.2045	
CD	0.0001	1	0.0001	0.0837	0.7763	
A^2	0.0439	1	0.0439	29.63	< 0.0001	
B^2	6.87E-06	1	6.87E-06	0.0046	0.9466	
C^2	0.0154	1	0.0154	10.4	0.0057	
D^2	0.0005	1	0.0005	0.3579	0.5586	
Residual	0.0222	15	0.0015			
Lack of Fit	0.0198	10	0.002	4.1	0.0665	insignificant
Pure Error	0.0024	5	0.0005			
Cor Total	2.09	29				

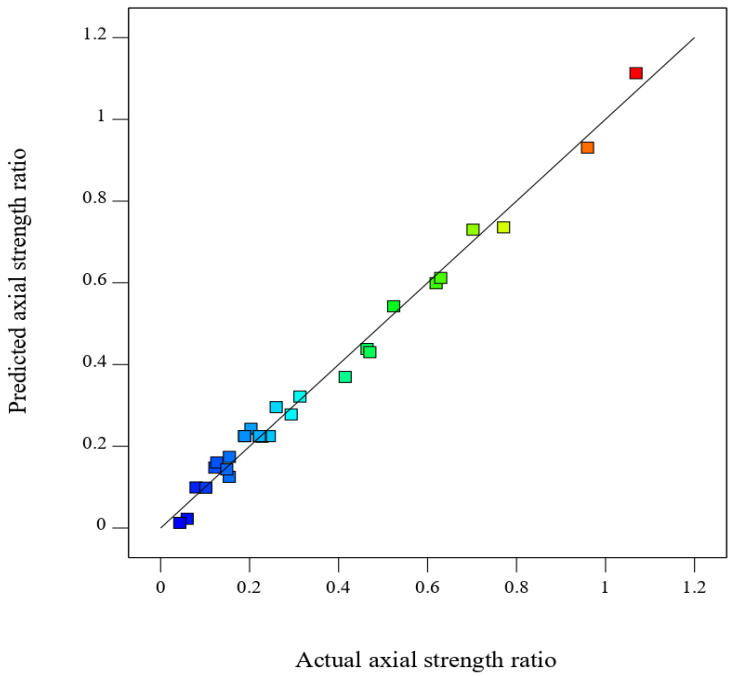

Figure 6.6: Predicted versus actual values of axial strength ratio

6.4. Evaluation of Proposed Equation

6.4.1. Experimental Results

In order to verify the validity of the proposed equation, comparisons are made between the calculated results from the proposed equations and the experimental results. Table 6.3 shows the calculated results from the proposed and the existing equations while Table 6.4 shows the comparison of normalized axial strengths. For clarity, the sample calculations are presented in Appendix C. As seen in Table 6.4, the P_{cal}/P_{exp} ratios for the proposed equation Eq. 6-5 have varied from 0.84 to 1 with mean value of 0.93 and standard deviation of 0.06. The calculated results from Eq. 6-5 are slightly conservative in predicting the axial strength of lightweight concrete wall with all P_{cal}/P_{exp} ratio less than 1. Comparison of the experimental results with those calculated from Eq. 6-5 is illustrated in Figure 6.7. It is observed that all the experimental results are very close to the equality line. This has demonstrated that the proposed equation Eq. 6-5 is satisfactory in estimating the axial strength of lightweight concrete wall.

As for the calculated results determined from Eq. 6-8, the P_{cal}/P_{exp} ratio values varied from 1.06 to 1.31 with mean value of 1.14 and standard deviation of 0.09. All the results showed higher values than those obtained experimentally. It is observed that the equation showed fairly good prediction of axial capacity for specimen T25-AR1.8SR12. This is mainly because the slenderness ratio of 12 falls outside the range of the proposed equation. The equation proposed from RSM method is only applicable to the range of variable used in the derivation. The comparison of the experimental results with the calculated results from Eq. 6-8 is graphically shown in Figure 6.8. Contradictory to Eq. 6-5, all the calculated results from Eq. 6-8 are above equality line. Apart from specimen T25-AR1.8SR12, all the other results are close to the line.

As discussed in section 4.3.4, none of the existing equations give a good axial strength prediction of lightweight concrete wall. As shown in Table 6.4, the two proposed design equations give better prediction of axial capacity of lightweight concrete wall compared to the existing equations. Nevertheless, inter-comparison of the calculated results between Eq. 6-5 and Eq. 6-8 indicates that Eq. 6-5 shows better accuracy in prediction of the experimental results in this research.

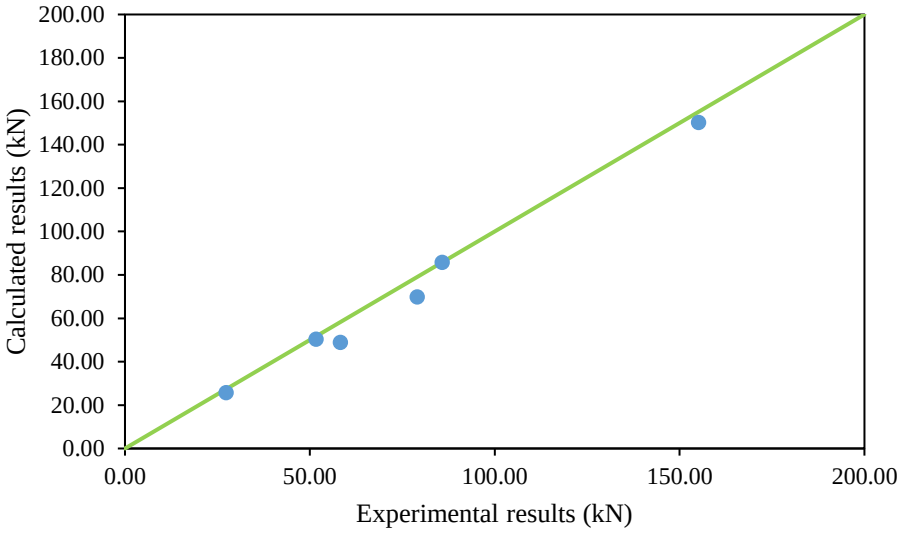

Figure 6.7: Calculated (Eq. 6-5) versus experimental results

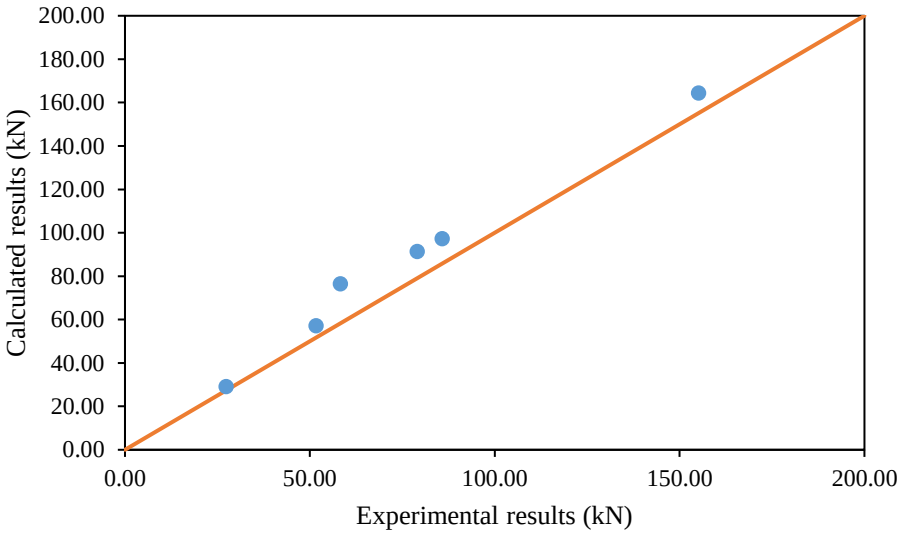

Figure 6.8: Calculated (Eq. 6-8) versus experimental results

Table 6.3: Calculated ultimate load

Specimen	Pexp	ACI 318	AS 3600	Eurocode	Eq. 2-16	Eq. 2-18	Eq. 2-21	Eq. 2-22	Eq. 2-23	Eq. 2-24	Eq. 6-5	Eq. 6-8
T25-AR1.8SR12	58.19	33.61	35.71	53.09	37.66	35.71	51.43	43.38	46.36	344.83	48.82	76.43
T25-AR1.8SR17	79.02	40.83	44.60	63.51	45.84	44.60	64.23	60.45	64.66	487.40	69.76	91.34
T25-AR1.8SR23	85.79	39.81	46.42	66.33	44.72	46.42	66.86	72.82	79.32	641.92	85.70	97.27
T25-AR3.1SR23	51.68	23.43	27.31	39.01	25.79	27.31	39.33	36.96	43.00	377.00	50.33	57.13
T25-AR5.3SR23	27.32	10.46	12.52	18.06	11.52	12.52	18.03	12.17	17.47	191.99	25.63	29.09
T60-AR5.3SR23	155.06	60.03	71.07	101.97	67.35	71.07	108.02	71.91	100.54	405.97	150.26	164.30

Note: all units are in kN.

Table 6.4: Comparison of normalized failure load

Specimen	ACI 318	AS 3600	Eurocode	Eq. 2-16	Eq. 2-18	Eq. 2-21	Eq. 2-22	Eq. 2-23	Eq. 2-24	Eq. 6-5	Eq. 6-8
T25-AR1.8SR12	0.58	0.61	0.91	0.65	0.61	0.88	0.75	0.80	5.93	0.84	1.31
T25-AR1.8SR17	0.52	0.56	0.80	0.58	0.56	0.81	0.76	0.82	6.17	0.88	1.16
T25-AR1.8SR23	0.46	0.54	0.77	0.52	0.54	0.78	0.85	0.92	7.48	1.00	1.13
T25-AR3.1SR23	0.45	0.53	0.75	0.50	0.53	0.76	0.72	0.83	7.30	0.97	1.11
T25-AR5.3SR23	0.38	0.46	0.66	0.42	0.46	0.66	0.45	0.64	7.03	0.94	1.06
T60-AR5.3SR23	0.39	0.46	0.66	0.43	0.46	0.70	0.46	0.65	2.62	0.97	1.06
Mean	0.46	0.53	0.76	0.52	0.53	0.77	0.66	0.78	6.09	0.93	1.14
Standard Deviation	0.08	0.06	0.10	0.09	0.06	0.08	0.17	0.11	1.81	0.06	0.09

Note: all values are expressed as P_{cal}/P_{exp} ratio.

6.4.2. Published Results

To further verify the applicability of the proposed equations, the predicted concrete axial strengths are compared to the experimental data published in the relevant literatures. Table 6.5 shows the comparison of the published results with those calculated using the proposed equations. Comparison of normalized axial strengths is presented in Table 6.6. The details of the published results can be found in Appendix F. As noted from these two tables, the P_{cal}/P_{exp} ratios for the proposed equation Eq. 6-5 vary from 0.83 to 1.16 with a mean value of 0.95 and a standard deviation of 0.11. It can be seen that the proposed equations give improved estimation of axial strength of normal weight concrete wall when compared with the existing equations. For high strength concrete wall, the axial strength prediction from Eq. 6-5 shows slight overestimation for specimen OWHS3 and OWHS4 (Doh & Fragomeni, 2005) with P_{cal}/P_{exp} ratios of 1.14 and 1.11 respectively. The compressive strengths of these specimens are 63 and 75.9MPa respectively while the slenderness ratios are 35 and 40 respectively. As for high strength concrete wall of Sam Fragomeni and Mendis (1996), the calculated results from Eq. 6-5 are slightly conservative with P_{cal}/P_{exp} ratios of 0.92, 0.96 and 0.89 for specimen 2b, 5b and 6b respectively. The compressive strengths of these specimens are 65.4, 59.7 and 67.4MPa respectively whereas the slenderness ratios are 15, 20 and 25 respectively. These comparisons manifest that the proposed equations can give a good prediction of the ultimate capacity of the normal weight high strength slender wall. Comparisons of the published experimental and calculated results from Eq. 6-5 are further illustrated in Figure 6.9. It can be seen that these results are close to equality line and are uniformly distributed on both sides of the line. The comparisons demonstrate that the predicted results obtained from Eq. 6-5 have shown a good agreement with the published experimental results.

As for Eq. 6-8, P_{cal}/P_{exp} ratios are in the range of 0.65 to 1.36 with mean and standard deviation of 1.05 and 0.21 respectively. Figure 6.10 shows a plot of the calculated results versus the published experimental results. It is noted that the points in the plot are more scattered compared to those in Figure 6.9. For this reason, Eq. 6-8 has been shown to have fair capability in predicting the axial strength of concrete wall. A contributing factor to this shortfall is that some of the published experimental results fall outside the range of the equation. Furthermore, by comparing the results calculated

using Eq. 6-5 with those from Eq. 6-8, Eq. 6-5 shows better accuracy in predicting the published experimental results.

The comparisons have manifested that these proposed equations yield more accurate prediction of the axial strength of concrete wall. Hence, they can be regarded as improved equations for designing axially loaded concrete wall.

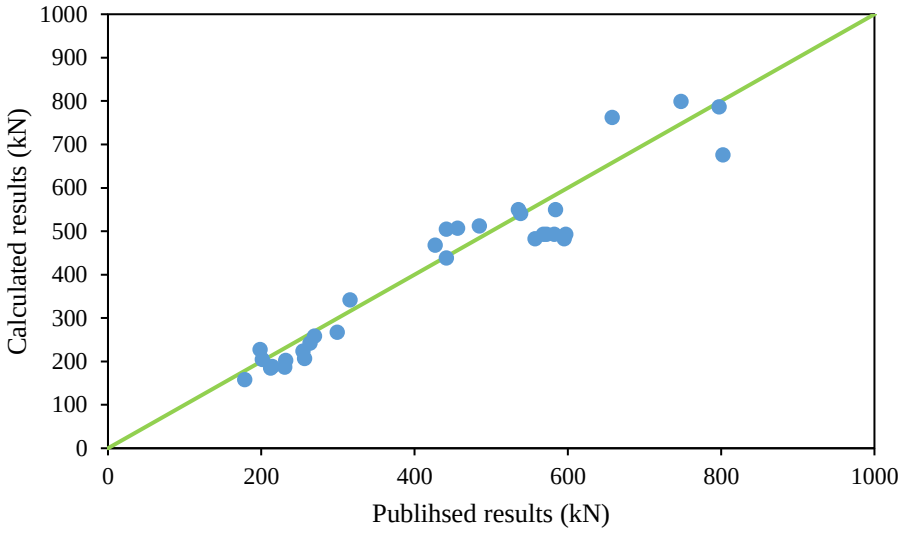

Figure 6.9: Calculated (Eq. 6-5) versus published results

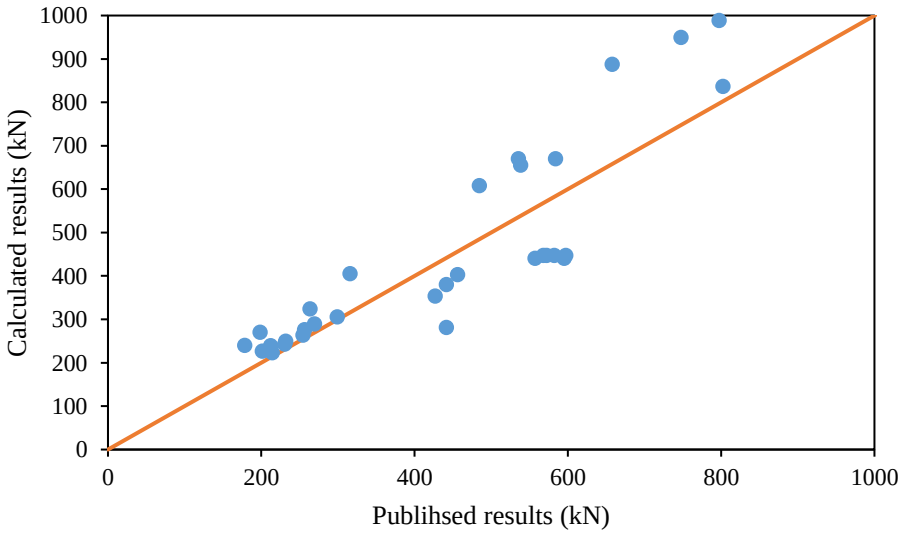

Figure 6.10: Calculated (Eq. 6-8) versus published results

Table 6.5: Calculated and published results

Authors	Specimen	ACI 318	AS 3600	Eurocode	Eq. 2-16	Eq. 2-18	Eq. 2-21	Eq. 2-22	Eq. 2-23	Eq. 2-24	Eq. 6-5	Eq. 6-8
Saheb and Desayi (1989)	WAR1	380	330	363	442	330	464	522	530	453	512	609
	WAR2	253	220	242	286	220	309	336	347	302	341	406
	WAR3	169	147	161	182	147	206	213	224	202	227	270
	WSR1	132	115	137	142	115	162	154	162	150	188	223
	WSR2	164	142	157	177	142	202	207	218	196	223	264
	WSR3	196	169	155	211	169	239	295	312	273	267	306
	WSTV2	428	372	409	507	372	504	597	607	511	549	670
	WSTV3	428	372	409	557	372	504	657	667	511	549	670
	WSTH2	417	362	398	484	362	495	571	580	497	541	656
Doh and Fragomeni (2005)	OWNS3	-314	-315	-406	-357	-310	341	605	854	1394	468	354
	OWNS4	-1010	-940	-875	-1149	-933	345	21	414	1306	439	282
	OWHS3	-381	-381	-492	-430	-352	390	728	1029	1689	505	381
	OWHS4	-1503	-1399	-1302	-1689	-1220	455	31	609	1943	506	403
Ganesan et al. (2013)	OPCAR1	186	161	162	207	161	187	262	281	300	186	243
	GPCSR1	200	174	191	231	174	203	271	285	301	206	276
	GPCAR1	182	157	159	203	157	184	257	275	294	184	240
Sam Fragomeni and Mendis (1996)	2a	213	183	156	218	183	198	279	328	323	202	250
	2b	329	283	241	334	258	269	427	501	498	242	325
	5a	153	129	84	157	129	147	316	356	433	205	227
	5b	256	215	140	260	202	210	521	587	724	258	289
	6b	231	201	202	235	181	189	265	301	374	158	240

(Contd.)

Authors	Specimen	ACI 318	AS 3600	Eurocode	Eq. 2-16	Eq. 2-18	Eq. 2-21	Eq. 2-22	Eq. 2-23	Eq. 2-24	Eq. 6-5	Eq. 6-8
Kripanarayanan (1977)	A6	469	409	551	553	409	598	543	560	321	762	888
	C4	577	501	504	594	501	643	753	801	436	676	837
	C5	624	543	633	678	543	712	755	785	442	786	989
	C6	507	442	597	579	442	631	569	587	348	799	950
Robinson et al. (2013)	R5	164	112	-46	186	112	320	499	815	259	482	441
	R6	164	112	-46	186	112	320	499	815	259	482	441
	R11	172	118	-48	172	116	331	462	755	272	493	448
	R12	172	118	-48	172	116	331	462	755	272	493	448
	R13	172	118	-48	172	116	331	462	755	272	493	448
	R14	172	118	-48	172	116	331	462	755	272	493	448

Note: all units are in kN.

Table 6.6: Comparison of normalized calculated and published results

Authors	Specimen	ACI 318	AS 3600	Eurocode	Eq. 2-16	Eq. 2-18	Eq. 2-21	Eq. 2-22	Eq. 2-23	Eq. 2-24	Eq. 6-5	Eq. 6-8
Saheb and Desayi (1989)	WAR1	0.78	0.68	0.75	0.91	0.68	0.96	1.08	1.09	0.94	1.06	1.26
	WAR2	0.80	0.70	0.77	0.91	0.70	0.98	1.07	1.10	0.96	1.08	1.28
	WAR3	0.85	0.74	0.81	0.92	0.74	1.04	1.07	1.13	1.02	1.15	1.36
	WSR1	0.61	0.54	0.64	0.66	0.54	0.76	0.72	0.76	0.70	0.88	1.04
	WSR2	0.64	0.56	0.62	0.70	0.56	0.79	0.81	0.86	0.77	0.88	1.04
	WSR3	0.65	0.56	0.52	0.71	0.56	0.80	0.99	1.04	0.91	0.89	1.02
	WSTV2	0.80	0.70	0.76	0.95	0.70	0.94	1.12	1.14	0.96	1.03	1.25
	WSTV3	0.73	0.64	0.70	0.95	0.64	0.86	1.13	1.14	0.88	0.94	1.15
	WSTH2	0.77	0.67	0.74	0.90	0.67	0.92	1.06	1.08	0.92	1.01	1.22
Doh and Fragomeni (2005)	OWNS3	-0.74	-0.74	-0.95	-0.84	-0.73	0.80	1.42	2.00	3.27	1.10	0.83
	OWNS4	-2.29	-2.13	-1.98	-2.60	-2.11	0.78	0.05	0.94	2.96	0.99	0.64
	OWHS3	-0.86	-0.86	-1.11	-0.97	-0.80	0.88	1.65	2.33	3.83	1.14	0.86
	OWHS4	-3.30	-3.07	-2.86	-3.71	-2.68	1.00	0.07	1.34	4.26	1.11	0.88
Ganesan et al. (2013)	OPCAR1	0.81	0.70	0.70	0.90	0.70	0.81	1.14	1.22	1.30	0.81	1.05
	GPCSR1	0.78	0.68	0.75	0.90	0.68	0.79	1.06	1.11	1.18	0.81	1.08
	GPCAR1	0.86	0.74	0.75	0.96	0.74	0.87	1.21	1.30	1.39	0.87	1.13
Sam Fragomeni and Mendis (1996)	2a	0.92	0.79	0.67	0.94	0.79	0.86	1.20	1.41	1.39	0.87	1.08
	2b	1.25	1.07	0.92	1.27	0.98	1.02	1.62	1.90	1.89	0.92	1.23
	5a	0.76	0.64	0.42	0.78	0.64	0.73	1.57	1.77	2.15	1.02	1.13
	5b	0.95	0.80	0.52	0.97	0.75	0.78	1.94	2.18	2.69	0.96	1.07
	6b	1.30	1.13	1.13	1.32	1.02	1.06	1.49	1.69	2.10	0.89	1.35

(Contd.)

Authors	Specimen	ACI 318	AS 3600	Eurocode	Eq. 2-16	Eq. 2-18	Eq. 2-21	Eq. 2-22	Eq. 2-23	Eq. 2-24	Eq. 6-5	Eq. 6-8
Kripanarayanan (1977)	A6	0.71	0.62	0.84	0.84	0.62	0.91	0.83	0.85	0.49	1.16	1.35
	C4	0.72	0.62	0.63	0.74	0.62	0.80	0.94	1.00	0.54	0.84	1.04
	C5	0.78	0.68	0.79	0.85	0.68	0.89	0.95	0.98	0.55	0.99	1.24
	C6	0.68	0.59	0.80	0.78	0.59	0.84	0.76	0.79	0.47	1.07	1.27
Robinson et al. (2013)	R5	0.27	0.19	-0.08	0.31	0.19	0.54	0.84	1.37	0.43	0.81	0.74
	R6	0.29	0.20	-0.08	0.33	0.20	0.57	0.90	1.46	0.46	0.87	0.79
	R11	0.30	0.20	-0.08	0.30	0.20	0.57	0.79	1.30	0.47	0.85	0.77
	R12	0.29	0.20	-0.08	0.29	0.19	0.56	0.77	1.26	0.46	0.83	0.75
	R13	0.30	0.21	-0.08	0.30	0.20	0.58	0.81	1.32	0.47	0.86	0.78
	R14	0.30	0.21	-0.08	0.30	0.20	0.58	0.81	1.33	0.48	0.87	0.79
Mean		0.38	0.30	0.25	0.41	0.31	0.82	1.03	1.30	1.33	0.95	1.05
Standard Deviation		0.97	0.89	0.89	1.08	0.83	0.15	0.40	0.40	1.06	0.11	0.21

Note: all values are expressed as P_{cal}/P_{exp} ratio.

6.5. Concluding Remark

The current design equations from the standards are not suitable for predicting the axial capacities of lightweight concrete walls. To prevail over the shortcomings, experimental and numerical modelling are performed in this study to derive two enhanced design equations which can be used to predict the axial capacities of the walls within this lightweight category. Furthermore, the proposed equations consider the effects of elastic modulus and at the same time are incorporated with the factors to allow for slenderness ratio, eccentricity and non-linear strength increment of compressive strength. The applicability of the proposed design equations is evaluated on lightweight, normal and high strength concrete wall panels. The comparison outcome has manifested that the proposed equations are able to predict the axial capacity of concrete wall, regardless of the types of concrete, and be them the lightweight, normal or high strength. Thus, this has demonstrated the effectiveness and versatility of the proposed equations to estimate the axial capacity of concrete wall. Comparatively, Eq. 6-5 shows more suitability than Eq. 6-8 in practical application.

7. Conclusions and Future Recommendation

7.1. Introduction

With scrupulous design, lightweight concrete wall can provide good structural performance. However, limited relevant literature on lightweight concrete wall restricts its application in construction. This thesis presents the research on the axially loaded lightweight concrete wall panel through experimental tests and finite element analyses. Furthermore, lightweight self-compacting concrete (LWSCC) mix design was developed and used as material for concrete wall panel. A series of experimental tests were carried out to study the behaviour of lightweight concrete wall under axial loading. The current design equations were evaluated using the experimental results. Numerical model was developed by using commercial finite element analysis software ABAQUS, followed by a series of extensive parametric study through numerical simulation. Due to limited application of the existing design equations in lightweight concrete wall, the experimental and numerical results were then used in the development of generalized design equations for determining axial capacity of concrete wall. This study can further enhance the understanding of lightweight concrete wall panel under axial loading.

This chapter concludes the main outcomes of this research in respect of each and every objective. Moreover, a discussion on new and plausible ideas for future research is also provided.

7.2. Conclusions

7.2.1. Conclusions from Objective 1

To develop lightweight self-compacting concrete mix design, incorporating fly ash as partial replacement of cement and oil palm shell (OPS) as replacement of coarse aggregates.

Four LWSCC mix designs were developed by using particle packing method. The mix designs were incorporated with fly ash as partial replacement of cement while oil palm shell (OPS) as replacement of coarse aggregates. The developed LWSCC mixes have

been found to be satisfactory in terms of fresh and hardened concrete properties. The following conclusions may be drawn:

1. LWSCC with OPS as aggregates has achieved desirable slump flow spread in the range of 660-730mm.
2. Satisfactory V-funnel flow time that fulfils the European Guidelines has been achieved.
3. Considerable passing ability has been attained by OPS LWSCC with the block step in the range of 8-15mm.
4. Excellent segregation resistance with value in the range of 4-7% has been achieved.
5. All the fresh concrete properties of SCC using OPS as aggregates are improved with the replacement of fly ash.
6. The density of OPS based SCC is found to be 15%-23% lower than normal concrete. Replacement of Ordinary Portland Cement by fly ash has reduced the concrete density.
7. The compressive strength of LWSCC was in the range of 18 to 38MPa on the 28th day. The compressive strength of LWSCC mix with fly ash replacement increases with curing age.
8. The splitting tensile strength of LWSCC is found to be in the range of 1.6-2.8MPa on the 28th day. Splitting tensile strength is about 7.2- 8.6% of its compressive strength. Its strength also improves with curing age.
9. As evidenced in SEM tests, cement paste has seeped into the pores of OPS aggregates giving rise to good bonding in the ITZ.
10. The water absorption of OPS based LWSCC is about 6%. With fly ash replacement, the water absorption has shown negative effect at early stage. As curing age increases, the water absorption of mix with fly ash improves and shows better value than the control mix.
11. When subjected to elevated temperature, the rate of strength reduction is less when concrete is aged. The OPS based LWSCC experiences strength reduction of nearly 84% and 79% at 28-day and 90-day ages respectively when subjected to temperature of 300°C.

7.2.2. Conclusions from Objective 2

To assess experimentally the behaviour of axially loaded lightweight concrete wall panel.

A series of tests were conducted on lightweight concrete wall panels loaded under uniaxial loading. A total of 24 lightweight concrete wall specimens were tested. Based on the test results, the following conclusions can be drawn:

1. In general, concrete wall with low slenderness ratio fails by crushing while for slender wall, buckling failure mode is dominant regardless of the wall thickness.
2. The load-deflection behaviour shows linear responses in the initial loading region and is followed by non-linear response up to ultimate failure load.
3. The results of parametric studies show that the ultimate axial strength of lightweight wall decreases with increasing of slenderness ratio while the aspect ratio has insignificant effect on the strength.
4. From the comparisons, the existing design equations from both the standards and previous researches are conservative and not suitable to be used for lightweight concrete wall. None of them takes into consideration of the materials properties of lightweight concrete. Improvement of current design equation is required.

7.2.3. Conclusions from Objective 3

To model the lightweight concrete wall panel by using Finite Element Analysis (FEA) software, ABAQUS and to carry out parametric studies so as to examine the effects of slenderness ratio, eccentricity, compressive strength, tensile strength and elastic modulus on the strength of concrete wall panel.

The ABAQUS finite element software was used to construct the wall model and three dimensional 8-node reduced integration brick element, C3D8R, was utilized for the concrete material. Concrete material was simulated by using constitutive model, concrete damaged plasticity (CDP). The FEA results were validated against those from the experiments and relevant published literatures. In general, the FEA model showed good agreement with the experimental results in terms of load-deflection curve, failure mode and failure load. Based on the results obtained from numerical investigation and parametric studies, the following conclusions can be drawn:

1. CDP model is able to simulate realistically the behaviour of concrete wall under axial loading, in terms of failure modes, load-deflection behaviour and ultimate axial capacity.
2. From the results of parametric study on the effects of slenderness ratio, it has been demonstrated that concrete wall is still able to sustain loading for slenderness ratio more than 30 and the axial strength ratio decreases nonlinearly with the increase of slenderness ratio.
3. The envelope of axial strength ratio versus slenderness ratio is greatly influenced by the eccentricity of load.
4. The parametric study shows that the aspect ratio has insignificant effect on the axial strength. The effect of aspect ratio diminishes with increasing of either slenderness ratio or eccentricity values.
5. The ultimate axial capacity increases non-linearly with the increase of compressive strength of concrete. The axial strength ratio is found to decrease when compressive strength increases.
6. Elastic modulus of concrete is the key parameter affecting the ultimate axial strength of lightweight concrete wall. Decrease in elastic modulus of concrete results in reduced ultimate axial capacity and axial strength ratio of wall.
7. Tensile strength is found to have less effect on axial strength ratio.

7.2.4. Conclusions from Objective 4

To develop a rational design methodology in the form of design equation to evaluate the axial load bearing capacity of concrete wall panel, inclusive of that manufactured from lightweight concrete.

Two new design equations have been developed based on the experimental and numerical results. The main outcomes from this investigation can be concluded as follows:

1. Two design equations are proposed to determine the axial strength of concrete wall. The first equation is derived based on equivalent rectangular stress block concept and incorporated with factors while the second equation is derived purely based on statistical method, response surface methodology.

2. The proposed equations allow for the effect of elastic modulus and at the same time are incorporated with factors to consider the slenderness ratio, eccentricity and non-linear strength increment of compressive strength of the concrete.
3. It has been demonstrated that the proposed equations Eq. 6-5 and Eq. 6-8 are able to well predict the axial capacity of walls manufactured from lightweight, normal and high strength concrete. This has confirmed the effectiveness and versatility of the proposed equations to estimate the axial capacity of concrete wall.

7.3. Recommendations & Future Works

This research has achieved all the objectives. Based on the work conducted and concluded findings, the following recommendations are made for future research works:

1. For concrete mix, more research with regard to the long term durability behaviour of LWSCC incorporated with OPS such as shrinkage, creep, corrosion and bond strength is required.
2. Tests were carried out with pin-pin end conditions in this research. Study on the effect of different end support conditions such as pin-fix, fix-fix, free-pin and free-fix can be extended.
3. This research was carried out with no support on side edges. Research can be further extended with one or both side edges supported with pinned or fixed condition. Design equation can be further developed to account for this effect.
4. Opening on wall surface is commonly allowed for door, windows and architectural requirements. Further study on the effect of elastic modulus on concrete wall with different openings can be examined.
5. Further study of time-dependent factors such as creep, shrinkage and thermal stress on the behaviour of axially loaded lightweight concrete wall is recommended.

References

211, A. C. (1992). *Standard Practice for Selecting Proportions for Structural Lightweight Concrete (ACI 211.2-91)*.

213, A. C. (2014). *Guide for structural lightweight-aggregate concrete*.

Abaqus. (2012). *Abaqus Analysis User's Manual* (V6.14 ed ed.).

Abdizadeh, N., Zekavati, A., & Afshin, H. (2009). Mix Design of Structural Self-compacting Concrete Using Void-Bulk Density Method.

Abdullah, A. (1984). *Basic strength properties of lightweight concrete using agricultural wastes as aggregates.* Paper presented at the Proceedings of international conference on low-cost housing for developing countries, Roorkee, India.

ACI-213. (2003). *Guide for Structural Lightweight-aggregate Concrete*.

ACI-237. (2007). 237.". *ACI 237R-07–Self-Consolidating Concrete". American Concrete Institute*.

ACI Committee 318. (2005). Building code requirements for structural concrete (ACI 318-05) and commentary (ACI 318R-05). : Farmington Hills, Mich. :American Concrete Institute.

Aïtcin, P. (2016). Supplementary cementitious materials and blended cements. *Science and Technology of Concrete Admixtures*(2nd), 53-73.

Alengaram, U. J., Al Muhit, B. A., & bin Jumaat, M. Z. (2013). Utilization of oil palm kernel shell as lightweight aggregate in concrete–a review. *Construction and Building Materials, 38*, 161-172.

Alengaram, U. J., Mahmud, H., & Jumaat, M. Z. (2011). Enhancement and prediction of modulus of elasticity of palm kernel shell concrete. *Materials & Design, 32*(4), 2143-2148.

Andiç-Çakır, Ö., & Hızal, S. (2012). Influence of elevated temperatures on the mechanical properties and microstructure of self consolidating lightweight aggregate concrete. *Construction and Building Materials, 34*, 575-583. doi:10.1016/j.conbuildmat.2012.02.088

Ardalan, R. B., Joshaghani, A., & Hooton, R. D. (2017). Workability retention and compressive strength of self-compacting concrete incorporating pumice powder and silica fume. *Construction and Building Materials, 134*, 116-122.

Aslam, M., Shafigh, P., & Jumaat, M. Z. (2016). Oil-palm by-products as lightweight aggregate in concrete mixture: a review. *Journal of Cleaner Production, 126*, 56-73.

Aslani, F., Ma, G., Wan, D. L. Y., & Muselin, G. (2018). Development of high-performance self-compacting concrete using waste recycled concrete aggregates and rubber granules. *Journal of Cleaner Production, 182*, 553-566.

ASTM C150/C150M-12: Standard specification for Portland cement: ASTM International West Conshohocken, PA, USA.

ASTM C618-12a, Standard Specification for Coal Fly Ash and Raw or Calcined Natural Pozzolan for Use in Concrete: ASTM International, West Conshohocken, PA, 2012, www.astm.org.

ASTM C642-13, Standard Test Method for Density, Absorption, and Voids in Hardened Concrete: ASTM International, West Conshohocken, PA, 2013, www.astm.org.

ASTM A370-14, Standard Test Methods and Definitions for Mechanical Testing of Steel Products: ASTM International, West Conshohocken, PA, 2014, www.astm.org.

ASTM C567 / C567M-14, Standard Test Method for Determining Density of Structural Lightweight Concrete: ASTM International, West Conshohocken, PA, 2014, www.astm.org.

ASTM C29 / C29M-17a, Standard Test Method for Bulk Density ("Unit Weight") and Voids in Aggregate: ASTM International, West Conshohocken, PA, 2017, www.astm.org.

ASTM C330 / C330M-17a, Standard Specification for Lightweight Aggregates for Structural Concrete: ASTM International, West Conshohocken, PA, 2017, www.astm.org.

ASTM C494 / C494M-17, Standard Specification for Chemical Admixtures for Concrete: ASTM International, West Conshohocken, PA, 2017, www.astm.org.

ASTM C39 / C39M-18, Standard Test Method for Compressive Strength of Cylindrical Concrete Specimens: ASTM International, West Conshohocken, PA, 2018, www.astm.org.

Atiş, C. D. (2003). High-volume fly ash concrete with high strength and low drying shrinkage. *Journal of Materials in Civil Engineering, 15*(2), 153-156.

Australia, S. 2018. Concrete structures (AS 3600:2018). Retrieved from Standards Online.

Bathe, K.-J., Walczak, J., Welch, A., & Mistry, N. (1989). Nonlinear analysis of concrete structures. *Computers & Structures, 32*(3-4), 563-590.

BIBM, C., & ERMCO, E. (2005). EFNARC. 2005. The European guidelines for Self-compacting concrete: specification, production and use. *SCC European Project Group*.

Bogas, J. A., Gomes, A., & Pereira, M. F. C. (2012). Self-compacting lightweight concrete produced with expanded clay aggregate. *Construction and Building Materials, 35*, 1013-1022. doi:10.1016/j.conbuildmat.2012.04.111

Bouzoubaa, N., & Lachemi, M. (2001). Self-compacting concrete incorporating high volumes of class F fly ash: Preliminary results. *Cement and Concrete Research, 31*(3), 413-420.

Bozkurta, N., & Taşkin, V. (2017). Design of Self Compacting Lightweight Concrete Using Acidic Pumice with Different Powder Materials. *Acta Physica Polonica, A., 132*(3).

Chai, W. W. S., Lee, D. T. C., & Ng, C. K. (2014). *Improving the properties of oil palm shell (OPS) concrete using polyvinyl alcohol (PVA) coated aggregates.* Paper presented at the Advanced Materials Research.

Chindaprasirt, P., Chotithanorm, C., Cao, H., & Sirivivatnanon, V. (2007). Influence of fly ash fineness on the chloride penetration of concrete. *Construction and Building Materials, 21*(2), 356-361.

Choi, Y. W., Kim, Y. J., Shin, H. C., & Moon, H. Y. (2006). An experimental research on the fluidity and mechanical properties of high-strength lightweight self-compacting concrete. *Cement and Concrete Research, 36*(9), 1595-1602.

Claeson, C., & Gylltoft, K. (1998). Slender high-strength concrete columns subjected to eccentric loading. *Journal of Structural Engineering, 124*(3), 233-240.

Coelho, A. M. G., Mottram, J. T., & Harries, K. A. (2015). Finite element guidelines for simulation of fibre-tension dominated failures in composite materials validated by case studies. *Composite Structures, 126*, 299-313.

Corinaldesi, V., & Moriconi, G. (2015). Use of synthetic fibers in self-compacting lightweight aggregate concretes. *Journal of Building Engineering, 4*, 247-254. doi:10.1016/j.jobe.2015.10.006

Crisfield, M. (1986). Snap ‐ through and snap ‐ back response in concrete structures and the dangers of under ‐ integration. *International Journal for Numerical Methods in Engineering, 22*(3), 751-767.

Dinakar, P., Babu, K., & Santhanam, M. (2008). Durability properties of high volume fly ash self compacting concretes. *Cement and Concrete Composites, 30*(10), 880-886.

Doh, J.-H., & Fragomeni, S. (2005). Evaluation of experimental work on concrete walls in one and two-way action. *Australian journal of structural engineering, 6*(1), 37-52.

Domagała, L. (2015). The effect of lightweight aggregate water absorption on the reduction of water-cement ratio in fresh concrete. *Procedia Engineering, 108*, 206-213.

Duan, Z. H., & Poon, C. S. (2014). Properties of recycled aggregate concrete made with recycled aggregates with different amounts of old adhered mortars. *Materials & Design, 58*, 19-29.

Dymond, B. Z. (2007). *Shear strength of a PCBT-53 girder fabricated with lightweight, Self-consolidating concrete.* Virginia Polytechnic Institute and State University.

Specification and Guidelines for Self-Compacting Concrete: Surrey, UK: EFNARC, Association House.

EGSCC. (2005). The European Guidelines for Self-Compacting Concrete.

Etxeberria, M., Vázquez, E., Marí, A., & Barra, M. (2007). Influence of amount of recycled coarse aggregates and production process on properties of recycled aggregate concrete. *Cement and Concrete Research, 37*(5), 735-742.

Fanning, P., & Kelly, O. (2000). Smeared crack models of RC beams with externally bonded CFRP plates. *Computational Mechanics, 26*(4), 325-332.

Farahani, J. N., Shafigh, P., Alsubari, B., Shahnazar, S., & Mahmud, H. B. (2017). Engineering properties of lightweight aggregate concrete containing binary and ternary blended cement. *Journal of Cleaner Production, 149*, 976-988.

Felekoğlu, B., Türkel, S., & Baradan, B. (2007). Effect of water/cement ratio on the fresh and hardened properties of self-compacting concrete. *Building and environment, 42*(4), 1795-1802.

Filho, J. H., Medeiros, M. d., Pereira, E., Helene, P., & Isaia, G. (2012). High-volume fly ash concrete with and without hydrated lime: chloride diffusion coefficient

from accelerated test. *Journal of Materials in Civil Engineering, 25*(3), 411-418.

Floyd, R. W., Hale, W. M., & Bymaster, J. C. (2015). Effect of aggregate and cementitious material on properties of lightweight self-consolidating concrete for prestressed members. *Construction and Building Materials, 85*, 91-99. doi:10.1016/j.conbuildmat.2015.03.084

Fraay, A., Bijen, J., & De Haan, Y. (1989). The reaction of fly ash in concrete a critical examination. *Cement and Concrete Research, 19*(2), 235-246.

Fragomeni, S., & Mendis, P. (1996). Improved axial load formulae for normal and high strength reinforced concrete walls. *Australian Civil Engineering Transactions, 38*(2/3/4), 71.

Fragomeni, S., & Mendis, P. (1999). Applicability of current ACI318 wall design formula for high strength concrete walls. *Advances in Structural Engineering, 2*(2), 103-108.

Gamino, A., Sousa, J., Manzoli, O., & Bittencourt, T. (2010). A comparative study between smeared and embedded crack models for finite element analysis of reinforced concrete beams. *Proc. of FraMCo S. Korean Concrete Institute*.

Ganesan, N., Indira, P., & Prasad, S. R. (2012). Strength and behavior of SFRSCC and SFRC wall panels under one-way in-plane action *High Performance Fiber Reinforced Cement Composites 6* (pp. 279-286): Springer.

Ganesan, N., Indira, P., & Santhakumar, A. (2013). Prediction of ultimate strength of reinforced geopolymer concrete wall panels in one-way action. *Construction and Building Materials, 48*, 91-97.

Gibigaye, M., Godonou, G. F., Katte, R., & Degan, G. (2017). Structured mixture proportioning for oil palm kernel shell concrete. *Case Studies in Construction Materials, 6*, 219-224.

Glavind, M., & Pedersen, E. (1999). *Packing calcuations applied for concrete mix design.* Paper presented at the Utilizing Ready Mixed Concrete and Mortar: Proceedings of the International Conference Held at the University of Dundee, Scotland, UK on.

Gopi, R., Revathi, V., & Kanagaraj, D. (2015). Light Expanded Clay Aggregate and Fly Ash Aggregate as Self Curing Agents in Self Compacting Concrete. *ASIAN JOURNAL OF CIVIL ENGINEERING (BHRC), 16*(7), 1025-1035.

Grabois, T. M., Cordeiro, G. C., & Toledo Filho, R. D. (2016). Fresh and hardened-state properties of self-compacting lightweight concrete reinforced with steel

fibers. *Construction and Building Materials, 104*, 284-292. doi:10.1016/j.conbuildmat.2015.12.060

Gungat, L., Putri, E. E., & Makinda, J. (2013). Effects of oil palm shell and curing time to the load-bearing capacity of clay subgrade. *Procedia Engineering, 54*, 690-697.

Helmuth, R. (1987). *Fly ash in cement and concrete*.

Hillerborg, A., Modéer, M., & Petersson, P.-E. (1976). Analysis of crack formation and crack growth in concrete by means of fracture mechanics and finite elements. *Cement and Concrete Research, 6*(6), 773-781.

Ho, N. M., & Doh, J. H. (2018). Experimental and numerical investigations of axially loaded RC walls restrained on three sides. *The Structural Design of Tall and Special Buildings, 27*(7), e1459.

Ho, N. M., & Doh, J. H. (2019). Prediction of ultimate strength of concrete walls restrained on three sides. *Structural Concrete*.

Huang, Y., Hamed, E., Chang, Z.-T., & Foster, S. J. (2014). Theoretical and experimental investigation of failure behavior of one-way high-strength concrete wall panels. *Journal of Structural Engineering, 141*(5), 04014143.

Hubertova, M., & Hela, R. (2007). The effect of metakaolin and silica fume on the properties of lightweight self consolidating concrete. *Special Publication, 243*, 35-48.

Hubertová, M., & Hela, R. (2013). Durability of Lightweight Expanded Clay Aggregate Concrete. *Procedia Engineering, 65*, 2-6. doi:10.1016/j.proeng.2013.09.002

Hwang, C.-L., & Hung, M.-F. (2005). Durability design and performance of self-consolidating lightweight concrete. *Construction and Building Materials, 19*(8), 619-626.

Illidge, F. B. (2010). *Acoustic emission techniques and cyclic load testing load testing for integrity evaluation of self-compacting normal and self-compacting.* PhD thesis. University of South Carolina, USA.

EN 1992-1-1 Eurocode 2: Design of concrete structures - Part 1-1: General ruels and rules for buildings: London: BSi.

Method for Determination of Compressive Strength of Concrete Cubes (BS 1881-116: 1983): London.

Jacobsen, S., & Arntsen, B. (2008). Aggregate packing and-void saturation in mortar and concrete proportioning. *Materials and Structures, 41*(4), 703-716.

Jalal, M., Pouladkhan, A., Harandi, O. F., & Jafari, D. (2015). Comparative study on effects of Class F fly ash, nano silica and silica fume on properties of high performance self compacting concrete. *Construction and Building Materials, 94*, 90-104.

Juenger, M. C., Snellings, R., & Bernal, S. A. (2019). Supplementary cementitious materials: New sources, characterization, and performance insights. *Cement and Concrete Research, 122*, 257-273.

Jumaat, M. Z., Alengaram, U. J., & Mahmud, H. (2009). Shear strength of oil palm shell foamed concrete beams. *Materials & Design, 30*(6), 2227-2236.

Juradin, S., Baloević, G., & Harapin, A. (2012). Experimental Testing of the Effects of Fine Particles on the Properties of the Self-Compacting Lightweight Concrete. *Advances in Materials Science and Engineering, 2012*, 1-8. doi:10.1155/2012/398567

Kaffetzakis, M. I., & Papanicolaou, C. G. (2012). Mix Proportioning method for lightweight aggregate SCC (LWASCC) based on the optimum packing point concept *Innovative Materials and Techniques in Concrete Construction* (pp. 131-151): Springer.

Kaffetzakis, M. I., & Papanicolaou, C. G. (2016a). Bond behavior of reinforcement in Lightweight Aggregate Self-Compacting Concrete. *Construction and Building Materials, 113*, 641-652. doi:10.1016/j.conbuildmat.2016.03.081

Kaffetzakis, M. I., & Papanicolaou, C. G. (2016b). Lightweight Aggregate Self-Compacting Concrete (LWASCC) semi-automated mix design methodology. *Construction and Building Materials, 123*, 254-260. doi:10.1016/j.conbuildmat.2016.07.012

Kanadasan, J., & Razak, H. A. (2014). Mix design for self-compacting palm oil clinker concrete based on particle packing. *Materials & Design, 56*, 9-19. doi:10.1016/j.matdes.2013.10.086

Khaleel, O. R., Al-Mishhadani, S. A., & Abdul Razak, H. (2011). The Effect of Coarse Aggregate on Fresh and Hardened Properties of Self-Compacting Concrete (SCC). *Procedia Engineering, 14*, 805-813. doi:10.1016/j.proeng.2011.07.102

Khatib, J. (2008). Performance of self-compacting concrete containing fly ash. *Construction and Building Materials, 22*(9), 1963-1971.

Kim, Y. J., Choi, Y. W., & Lachemi, M. (2010). Characteristics of self-consolidating concrete using two types of lightweight coarse aggregates. *Construction and Building Materials, 24*(1), 11-16. doi:10.1016/j.conbuildmat.2009.08.004

Kripanarayanan, K. (1977). *Interesting aspects of the empirical wall design equation.* Paper presented at the Journal Proceedings.

Kupaei, R. H., Alengaram, U. J., Jumaat, M. Z. B., & Nikraz, H. (2013). Mix design for fly ash based oil palm shell geopolymer lightweight concrete. *Construction and Building Materials, 43*, 490-496.

Kupfer, H., Hilsdorf, H. K., & Rusch, H. (1969). *Behavior of concrete under biaxial stresses.* Paper presented at the Journal proceedings.

Kurda, R., de Brito, J., & Silvestre, J. D. (2019). Water absorption and electrical resistivity of concrete with recycled concrete aggregates and fly ash. *Cement and Concrete Composites, 95*, 169-182.

Kurt, M., Aydin, A. C., Gül, M. S., Gül, R., & Kotan, T. (2015). The effect of fly ash to self-compactability of pumice aggregate lightweight concrete. *Sadhana, 40*(4), 1343-1359.

Kurt, M., Kotan, T., Gül, M. S., Gül, R., & Aydin, A. C. (2016). The effect of blast furnace slag on the self-compactability of pumice aggregate lightweight concrete. *Sadhana, 41*(2), 253-264.

Kwasny, J., Sonebi, M., Taylor, S. E., Bai, Y., Owens, K., & Doherty, W. (2012). Influence of the Type of Coarse Lightweight Aggregate on Properties of Semilightweight Self-Consolidating Concrete. *Journal of Materials in Civil Engineering, 24*(12), 1474-1483. doi:10.1061/(asce)mt.1943-5533.0000527

Lahkega, O. V. T. N. I., & Stenah, V. B. V. P. (2011). Evaluation of the strength variation of normal and lightweight self-compacting concrete in full scale walls. *Materiali in tehnologije, 45*(6), 571-577.

Law, D. S. Y. W., Aslani, F., & Ma, G. (2018). Lightweight Self-Compacting Concrete Incorporating Perlite, Scoria, and Polystyrene Aggregates. *Journal of Materials in Civil Engineering, 30*(8), 04018178.

Leabu, V. F. (1959). *Problems and performance of precast concrete wall panels.* Paper presented at the Journal Proceedings.

Lechner, T., & Fischer, O. (2015). Stabilitätsverhalten von schlanken Wandscheiben aus Normal ‐ und Ultrahochleistungsbeton. *Beton ‐ und Stahlbetonbau, 110*(5), 328-339.

Lee, J., & Fenves, G. L. (1998). Plastic-damage model for cyclic loading of concrete structures. *Journal of engineering mechanics, 124*(8), 892-900.

Li, J., Chen, Y., & Wan, C. (2017). A mix-design method for lightweight aggregate self-compacting concrete based on packing and mortar film thickness theories. *Construction and Building Materials, 157*, 621-634.

Liao, F., & Huang, Z. (2018). Modeling Cracks of Reinforced Concrete Slabs under Fire Conditions. *Journal of Structural Engineering, 144*(5), 04018030.

Liew, K., Sojobi, A., & Zhang, L. (2017). Green concrete: Prospects and challenges. *Construction and Building Materials, 156*, 1063-1095.

Lim, J. C., & Ozbakkaloglu, T. (2014). Stress–strain model for normal-and light-weight concretes under uniaxial and triaxial compression. *Construction and Building Materials, 71*, 492-509.

Liu, M. (2010). Self-compacting concrete with different levels of pulverized fuel ash. *Construction and Building Materials, 24*(7), 1245-1252.

Liu, X., Chia, K. S., & Zhang, M.-H. (2011). Water absorption, permeability, and resistance to chloride-ion penetration of lightweight aggregate concrete. *Construction and Building Materials, 25*(1), 335-343.

Lo, T., Tang, P., Cui, H., & Nadeem, A. (2007). Comparison of workability and mechanical properties of self-compacting lightweight concrete and normal self-compacting concrete. *Materials Research Innovations, 11*(1), 45-50.

Lotfy, A., Hossain, K. M., & Lachemi, M. (2015a). Mix design and properties of lightweight self-consolidating concretes developed with furnace slag, expanded clay and expanded shale aggregates. *Journal of Sustainable Cement-Based Materials*, 1-27.

Lotfy, A., Hossain, K. M. A., & Lachemi, M. (2015b). Lightweight Self-consolidating Concrete with Expanded Shale Aggregates: Modelling and Optimization. *International Journal of Concrete Structures and Materials, 9*(2), 185-206. doi:10.1007/s40069-015-0096-5

Lotfy, A., Hossain, K. M. A., & Lachemi, M. (2015c). Mix design and properties of lightweight self-consolidating concretes developed with furnace slag, expanded clay and expanded shale aggregates. *Journal of Sustainable Cement-Based Materials, 5*(5), 297-323. doi:10.1080/21650373.2015.1091999

Lothenbach, B., Scrivener, K., & Hooton, R. (2011). Supplementary cementitious materials. *Cement and Concrete Research, 41*(12), 1244-1256.

Lubliner, J., Oliver, J., Oller, S., & Onate, E. (1989). A plastic-damage model for concrete. *International Journal of solids and structures, 25*(3), 299-326.

Mahmud, Jumaat, M., & Alengaram, U. (2009). Influence of sand/cement ratio on mechanical properties of palm kernel shell concrete. *Journal of Applied Sciences, 9*(9), 1764-1769.

Mahmud, H. (2010). Mix design and mechanical properties of oil palm shell lightweight aggregate concrete: a review. *International journal of the physical sciences, 5*(14).

Malárics, V., & Müller, H. (2010). Evaluation of the splitting tension test for concrete from a fracture mechanical point of view. *Proceedings of FraMCos-7. Fracture mechanics of concrete and concrete structures, Korea*, 709-716.

Malhotra, V. (2002). High-performance high-volume fly ash concrete. *Concrete international, 24*(7), 30-34.

Mannan, M., Alexander, J., Ganapathy, C., & Teo, D. (2006). Quality improvement of oil palm shell (OPS) as coarse aggregate in lightweight concrete. *Building and environment, 41*(9), 1239-1242.

Mannan, M., Basri, H., Zain, M. F. M., & Islam, M. (2002). Effect of curing conditions on the properties of OPS-concrete. *Building and environment, 37*(11), 1167-1171.

Mannan, M., & Ganapathy, C. (2001). Long-term strengths of concrete with oil palm shell as coarse aggregate. *Cement and Concrete Research, 31*(9), 1319-1321.

Mannan, M., & Ganapathy, C. (2004). Concrete from an agricultural waste-oil palm shell (OPS). *Building and environment, 39*(4), 441-448.

Mazaheripour, H., Ghanbarpour, S., Mirmoradi, S., & Hosseinpour, I. (2011). The effect of polypropylene fibers on the properties of fresh and hardened lightweight self-compacting concrete. *Construction and Building Materials, 25*(1), 351-358.

Mehta, K. P. (2001). Reducing the environmental impact of concrete. *Concrete international, 23*(10), 61-66.

Mo, K. H., Chin, T. S., Alengaram, U. J., & Jumaat, M. Z. (2016). Material and structural properties of waste-oil palm shell concrete incorporating ground granulated blast-furnace slag reinforced with low-volume steel fibres. *Journal of Cleaner Production, 133*, 414-426.

Mohamad, N., Goh, W. I., Abdullah, R., Samad, A. A. A., Mendis, P., & Sofi, M. (2017). Structural performance of FCS wall subjected to axial load. *Construction and Building Materials, 134*, 185-198.

Mohammadi, Y., Mousavi, S., Rostami, F., & Danesh, A. (2015). The effect of silica fume on the properties of self-compacted lightweight concrete. *Current World Environment, 10*(Special-Issue1), 381-388. doi:10.12944/CWE.10.Special-Issue1.48

Muthusamy, S., & Kolandasamy, P. (2015). Lightweight self-consolidating concrete at high temperatures. *Građevinar, 67*(04.), 329-338.

Nadim, W. (2012). Modern methods of construction. *Construction innovation and process improvement*, 209-233.

Nagaratnam, B. H., Rahman, M. E., Mirasa, A. K., Mannan, M. A., & Lame, S. O. (2016). Workability and heat of hydration of self-compacting concrete incorporating agro-industrial waste. *Journal of Cleaner Production, 112*, 882-894. doi:10.1016/j.jclepro.2015.05.112

Nayal, R., & Rasheed, H. A. (2006). Tension stiffening model for concrete beams reinforced with steel and FRP bars. *Journal of Materials in Civil Engineering, 18*(6), 831-841.

Nepomuceno, M. C., Oliveira, L., & Lopes, S. M. R. (2012). Methodology for mix design of the mortar phase of self-compacting concrete using different mineral additions in binary blends of powders. *Construction and Building Materials, 26*(1), 317-326.

Nepomuceno, M. C., Pereira-de-Oliveira, L., Lopes, S. M. R., & Franco, R. M. C. (2016). Maximum coarse aggregate's volume fraction in self-compacting concrete for different flow restrictions. *Construction and Building Materials, 113*, 851-856.

Nepomuceno, M. C., Pereira-de-Oliveira, L., & Pereira, S. F. (2014). Methodology for the mix design of self-compacting concrete using different mineral additions in binary blends of powders. *Construction and Building Materials, 64*, 82-94. doi:10.1016/j.conbuildmat.2014.04.021

Nepomuceno, M. C., Pereira-de-Oliveira, L., & Pereira, S. F. (2018). Mix design of structural lightweight self-compacting concrete incorporating coarse lightweight expanded clay aggregates. *Construction and Building Materials, 166*, 373-385.

Properties of concrete CTP-VVP: Malaysia.

Neville, A. M. (1995). *Properties of concrete*.

Norma, A. (2004). C496/C496M-11, Standard test method for splitting tensile strength of cylindrical concrete specimens. *ASTM International, West Conshohocken, PA*, 469-490.

Oberlender, G. D. (1975). STRENGTH INVESTIGATION OF PRECAST REINFORCED CONCRETE LOAD-BEARING WALL PANELS.

Ohno, H., Kawai, T., Kuroda, Y., & Ozawa, K. (1993). *Development of vibration-free high strength lightweight concrete and its application.* Paper presented at the Proceeding of FIP Symposium.

Okafor, F. O. (1988). Palm kernel shell as a lightweight aggregate for concrete. *Cement and Concrete Research, 18*(6), 901-910.

Okpala, D. (1990). Palm kernel shell as a lightweight aggregate in concrete. *Building and environment, 25*(4), 291-296.

Owaid, H. M., Hamid, R. B., & Taha, M. R. (2012). A review of sustainable supplementary cementitious materials as an alternative to all-Portland cement mortar and concrete. *Australian Journal of Basic and Applied Sciences, 6*(9), 287-303.

Pantzaris, T., & Mohd Jaaffar, A. (2002). Properties and utilization of palm kernel oil. *Palmas (Colombia)*.

Papanicolaou, C. G., & Kaffetzakis, M. I. (2010). Pumice aggregate self-compacting concrete (PASCC). *Proceedings of SCC2010, Montreal*, 1286-1295.

Pathak, N., & Siddique, R. (2012). Properties of self-compacting-concrete containing fly ash subjected to elevated temperatures. *Construction and Building Materials, 30*, 274-280.

Mechanical properties of Lightweight Aggregate Concrete: EuroLightcon.

Pierce, K. (2007). *Performance of lightweight aggregate in self consolidating concrete.* Paper presented at the Masters Abstracts International.

Pillai, S. U., & Parthasarathy, C. (1977). Ultimate strength and design of concrete walls. *Building and environment, 12*(1), 25-29.

Popescu, C., Sas, G., Blanksvärd, T., & Täljsten, B. (2015). Concrete walls weakened by openings as compression members: A review. *Engineering Structures, 89*, 172-190. doi:10.1016/j.engstruct.2015.02.006

Rahman Sobuz, H., Hasan, N. M. S., Tamanna, N., & Islam, M. S. (2014). Structural lightweight concrete production by using oil palm shell. *Journal of Materials, 2014*.

Rajamanickam, G., & Vaiyapuri, R. (2016). Self compacting self curing concrete with lightweight aggregates. *Građevinar, 68*(04.), 279-285.

Ramanathan, P., Baskar, I., Muthupriya, P., & Venkatasubramani, R. (2013). Performance of self-compacting concrete containing different mineral admixtures. *KSCE Journal of Civil Engineering, 17*(2), 465-472. doi:10.1007/s12205-013-1882-8

Robinson, G. P., Palmeri, A., & Austin, S. A. (2013). Design methodologies for one way spanning eccentrically loaded minimally or centrally reinforced pre-cast RC panels. *Engineering Structures, 56*, 1945-1956.

Rodriguez de Sensale, G., Rodriguez Viacava, I., & Aguado, A. (2015). Simple and Rational Methodology for the Formulation of Self-Compacting Concrete Mixes. *Journal of Materials in Civil Engineering, 28*(2), 04015116.

Saha, A. K. (2018). Effect of class F fly ash on the durability properties of concrete. *Sustainable environment research, 28*(1), 25-31.

Saheb, S. M., & Desayi, P. (1989). Ultimate strength of RC wall panels in one-way in-plane action. *Journal of Structural Engineering, 115*(10), 2617-2630.

Samad, S., & Shah, A. (2017). Role of binary cement including Supplementary Cementitious Material (SCM), in production of environmentally sustainable concrete: A critical review. *International Journal of Sustainable Built Environment, 6*(2), 663-674.

Samson, G., Phelipot-Mardelé, A., & Lanos, C. (2016). A review of thermomechanical properties of lightweight concrete. *Magazine of Concrete Research, 69*(4), 201-216.

Sanjayan, J. (2000). Load capacity of slender reinforced concrete walls governed by flexural cracking strength of concrete. *Magazine of Concrete Research, 52*(3), 169-176.

Seddon, A. (1956). Concrete walls in compression under short-term axial and eccentric loads. *IABSE (International Association for Bridge and Structural Engineering), Zürich, Switzerland*.

Senaratne, S., Gerace, D., Mirza, O., Tam, V. W., & Kang, W.-H. (2016). The costs and benefits of combining recycled aggregate with steel fibres as a sustainable, structural material. *Journal of Cleaner Production, 112*, 2318-2327.

Serri, E., Suleiman, M., & Mydin, M. O. (2015). The effect of curing environment on oil palm shell lightweight concrete mechanical properties and thermal conductivity. *Advances in Environmental Biology, 9*(4), 222-225.

Sethy, K. P., Pasla, D., & Chandra Sahoo, U. (2016). Utilization of high volume of industrial slag in self compacting concrete. *Journal of Cleaner Production, 112*, 581-587. doi:10.1016/j.jclepro.2015.08.039

Shafigh, P., Johnson Alengaram, U., Mahmud, H. B., & Jumaat, M. Z. (2013). Engineering properties of oil palm shell lightweight concrete containing fly ash. *Materials & Design, 49*(Supplement C), 613-621. doi:https://doi.org/10.1016/j.matdes.2013.02.004

Shafigh, P., Jumaat, M. Z., & Mahmud, H. (2010). Mix design and mechanical properties of oil palm shell lightweight aggregate concrete: a review. *International journal of the physical sciences, 5*(14), 2127-2134.

Shafigh, P., Jumaat, M. Z., & Mahmud, H. (2011). Oil palm shell as a lightweight aggregate for production high strength lightweight concrete. *Construction and Building Materials, 25*(4), 1848-1853.

Shafigh, P., Jumaat, M. Z., Mahmud, H. B., & Hamid, N. A. A. (2012). Lightweight concrete made from crushed oil palm shell: Tensile strength and effect of initial curing on compressive strength. *Construction and Building Materials, 27*(1), 252-258. doi:10.1016/j.conbuildmat.2011.07.051

Shafigh, P., Nomeli, M. A., Alengaram, U. J., Mahmud, H. B., & Jumaat, M. Z. (2016). Engineering properties of lightweight aggregate concrete containing limestone powder and high volume fly ash. *Journal of Cleaner Production, 135*, 148-157.

Shanker, M. (2016). Experimental Investigation on Self Compacting Concrete using Light Weight Aggregates. *International Journal of Advanced Science and Engineering Research, 1*(1).

Shi, C., & Wu, Y. (2005). Mixture proportioning and properties of self-consolidating lightweight concrete containing glass powder. *ACI Materials Journal, 102*(5), 355-363.

Shi, C., Wu, Z., Lv, K., & Wu, L. (2015). A review on mixture design methods for self-compacting concrete. *Construction and Building Materials, 84*, 387-398.

Shi, C., & Yang, X. (2005). *Design and application of self-compacting lightweight concrete*. Paper presented at the SCC'2005-China: 1st International Symposium on Design, Performance and Use of Self-Consolidating Concrete.

Sonebi, M., Grunewald, S., & Walraven, J. (2007). Filling ability and passing ability of self-consolidating concrete. *ACI Materials Journal, 104*(2), 162.

Sun, J., Lee, K., & Lee, H. (2000). Comparison of implicit and explicit finite element methods for dynamic problems. *Journal of Materials Processing Technology, 105*(1-2), 110-118.

Teo, D., Mannan, M. A., Kurian, V., & Ganapathy, C. (2007). Lightweight concrete made from oil palm shell (OPS): structural bond and durability properties. *Building and environment, 42*(7), 2614-2621.

Topçu, İ. B., & Uygunoğlu, T. (2010). Effect of aggregate type on properties of hardened self-consolidating lightweight concrete (SCLC). *Construction and Building Materials, 24*(7), 1286-1295. doi:10.1016/j.conbuildmat.2009.12.007

Tripathi, M., Sahu, J., Ganesan, P., Monash, P., & Dey, T. (2015). Effect of microwave frequency on dielectric properties of oil palm shell (OPS) and OPS char synthesized by microwave pyrolysis of OPS. *Journal of Analytical and Applied Pyrolysis, 112*, 306-312.

Tviksta, L. (2000). Guideline for SCC. *Brite EuRam, Task, 9*, 3-11.

Uygunoğlu, T., & Topçu, İ. B. (2009). Thermal expansion of self-consolidating normal and lightweight aggregate concrete at elevated temperature. *Construction and Building Materials, 23*(9), 3063-3069.

Vakhshouri, B., & Nejadi, S. (2016). Mix design of light-weight self-compacting concrete. *Case Studies in Construction Materials, 4*, 1-14. doi:10.1016/j.cscm.2015.10.002

Wahalathantri, B. L., Thambiratnam, D., Chan, T., & Fawzia, S. (2011). *A material model for flexural crack simulation in reinforced concrete elements using ABAQUS.* Paper presented at the Proceedings of the first international conference on engineering, designing and developing the built environment for sustainable wellbeing.

Warner, R. F., Rangan, B., Hall, A., & Faulkes, K. (1998). *Concrete structures*.

Wu, X., Wu, Z.-m., Zheng, J.-j., Ueda, T., & Yi, S.-h. (2013). An experimental study on the performance of self-compacting lightweight concrete exposed to elevated temperature. *Magazine of Concrete Research, 65*(13), 780-786.

Xiao, J., Li, J., & Zhang, C. (2005). Mechanical properties of recycled aggregate concrete under uniaxial loading. *Cement and Concrete Research, 35*(6), 1187-1194.

Yahia, A., Tanimura, M., Shimabukuro, A., Shimoyama, Y., & Tochigi, T. (1999). *Effect of mineral admixtures on rheological properties of equivalent self-compacting concrete mortar.* Paper presented at the Proc., 7th East Asia-Pacific Conf. on Structural Engineering and Construction.

Yang, K.-H., Mun, J.-H., Cho, M.-S., & Kang, T. H.-K. (2014). Stress-Strain Model for Various Unconfined Concretes in Compression. *ACI Structural Journal, 111*(4).

Yew, M. K., Bin Mahmud, H., Ang, B. C., & Yew, M. C. (2014). Effects of oil palm shell coarse aggregate species on high strength lightweight concrete. *The Scientific World Journal, 2014*.

Zielinski, Z., Troitski, M., & El-Chakieh, E. (1983). Bearing capacity tests on precast concrete thin-wall ribbed panels. *PCI journal, 28*(3), 88-103.

Appendices

A. Mix Design Calculations

A calculation example to determine the LWSCC mix design by using particle packing method is shown below.

General properties:

$\mathrm{AR_{f\,agg}} = 0.5$

$\mathrm{SG_{f\,agg}} = 2.64$

$\mathrm{AR_{c\,agg}} = 0.5$

$\mathrm{SG_{c\,agg}} = 1.19$

$\mathrm{W_{cement}} = 420\mathrm{kg/m^3}$

$\mathrm{SG_{cement}} = 3.14$

$\mathrm{SG_{water}} = 1$

From laboratory test, $e = 0.377$

Step 1: Determination of particle packing factor

$$PP = 1 - e$$
$$= 1 - 0.377$$
$$= 0.623$$

Step 2: Calculation of aggregates content

$$\mathrm{W_{f\,agg}} = \mathrm{PP} \times \mathrm{AR_{f\,agg}} \times \mathrm{SG_{f\,agg}} \times 1000$$
$$= 0.623 \times 0.5 \times 2.64 \times 1000$$
$$= 822\mathrm{kg/m^3}$$

$$\mathrm{W_{c\,agg}} = \mathrm{PP} \times \mathrm{AR_{c\,agg}} \times \mathrm{SG_{c\,agg}} \times 1000$$
$$= 0.623 \times 0.5 \times 1.19 \times 1000$$
$$= 370\mathrm{kg/m^3}$$

Step 3: Calculation of cement content

$$\mathrm{V_{cement}} = \mathrm{W_{cement}}/\mathrm{SG_{cement}}$$

$$= \frac{420}{3.14}$$
$$= 0.134\text{m}^3$$

Step 4: Calculation of paste volume

$$V_{paste} = 1 - PP$$
$$= 1 - 0.623$$
$$= 0.377\text{m}^3$$

Step 5: Determination of water content

$$V_{water}/V_{cement} = W/B = 0.8657$$

$$V_{water} = W/B \times V_{cement}$$
$$= 0.8657 \times 0.134$$
$$= 0.116$$
$$W_{water} = V_{water} \times SG_{water} \times 1000$$
$$= 0.116 \times 1 \times 1000$$
$$= 116\text{kg/m}^3$$

Step 6: Determination of superplasticizer dosage

$$SP = 1\%$$

$$W_{SP} = SP(\%) \times (W_{cement} + W_{SCM})$$
$$= 0.01 \times 420$$
$$= 4.2\text{kg/m}^3$$

The calculated LWSCC mix design is summarized in Table A.1.

Table A.1: Summary of calculated mix design

Water (kg/m^3)	116
Cement (kg/m^3)	450
Coarse aggregate (kg/m^3)	370
Fine aggregate (kg/m^3)	822
SP (kg/m^3)	4.2
Total weight (kg/m^3)	1762.2

B. Trial Mix

The details and results of trial mixes are summarized in Table B.1.

Table B.1: Summary of trial mix design

Trial Mix	1	2	3	4	5	6	7	8	9	10
W/B	0.26	0.3	0.3	0.3	0.3	0.3	0.3	0.3	0.33	0.33
Water (kg/m^3)	116	135	135	135	150	156	156	156	171.6	171.6
Cement (kg/m^3)	450	450	450	450	500	520	520	520	520	520
Sand (kg/m^3)	370	370	626	715	715	715	715	715	715	715
OPS (kg/m^3)	882	882	626	455	455	455	455	455	455	455
Sp(%)	1	1	1	1	1	1	1.5	1.65	1.65	1.5
SP (kg/m^3)	4.2	4.2	4.2	4.2	5	5.2	7.8	8.58	8.58	7.8
Dm (mm)	300	392	438	510	543	563	586	610	660	648
T_{500} (s)	-	-	-	-	10	7	6.78	6.21	5.04	5.63
Blockstep (mm)	25	24.22	20.13	18.67	15.68	15.18	14.37	13.21	12.5	12.9
T_{10s} (s)	-	-	-	-	-	24	21	18	15	17
Sieved portion (%)	-	-	-	-	-	3	3.56	4.38	6.34	5.64
Visual observation	The mix too dry	Aggregates were not fully covered by paste	Aggregates were not fully covered by paste	Some of the aggregates were not covered by paste	Similar observation	High viscosity	High viscosity	High viscosity	Satisfied	high viscosity
Corrective action	increase w/b	increase fine aggregates	increase fine aggregates	increase cement content	Further increase cement content	increase SP	increase SP	increase w/b	Check SP 1.5%	

(contd.)

Trial Mix	11	12	13	14
W/B	0.33	0.33	0.31	0.28
Water (kg/m^3)	171.6	171.6	161.2	145.6
Fly Ash (kg/m^3)	156	156	156	156
Cement (kg/m^3)	364	364	364	364
Sand (kg/m^3)	715	715	715	715
OPS (kg/m^3)	455	455	455	455
Sp(%)	1.65	1	1	1
SP (kg/m^3)	8.58	5.72	5.72	5.72
Dm (mm)	900	781	700	564
T_{500} (s)	2	3.54	4.38	6.44
Blockstep (mm)	7	8	9.75	10.26
T_{10s} (s)	10	13.2	14	18
Sieved portion (%)	16	10.17	6.84	4.31
Visual observation	Severe bleeding		Satisfied	Blockage in V-funnel
Corrective action	Reduce SP	Reduce water content	check 0.28 w/b	

C. Design Calculations

Sample calculation to determine the ultimate axial capacity of concrete wall by using the equations from the design standards, published literatures and proposed equations is presented as follows.

C.1. Design Parameters

Specimen T60-AR5.3SR23

H = 1400 mm
L = 260mm
t = 62mm
f'_c = 13.7MPa
e = 2.5mm
E_c = 12047MPa
f_{sy} = 299MPa
ρ_v = 0.0058
A_{st} = 94.489mm^2

C.2. Design Standard

ACI 318:

$$P_u = 0.55 f'_c A_c \left[1 - \left(\frac{kH}{32t}\right)^2\right]$$

$$= 0.55 \times 13.7 \times 16120 \left[1 - \left(\frac{1 \times 1400}{32 \times 62}\right)^2\right] \times 10^{-3}$$

$$= 60.03\text{kN}$$

AS 3600:

$$e_a = \frac{H_{we}^2}{2500 t_w}$$

$$= \frac{1400^2}{2500 \times 62}$$

$$= 12.71$$

$$N_u = (t_w - 1.2e - 2e_a)0.6f_c'b$$
$$= (62 - 1.2 \times 2.5 - 2 \times 12.71) \times 0.6 \times 13.7 \times 260 \times 10^{-3}$$
$$= 71.07\text{kN}$$

BS 8110:

$$e_a = \frac{H_{we}^2}{2500t_w}$$
$$= \frac{1400^2}{2500 \times 62}$$
$$= 12.71$$

$$n_w = 0.3(t_w - 1.2e - 2e_a)f_{cu}'$$
$$= (62 - 1.2 \times 2.5 - 2 \times 12.71) \times 0.3 \times 13.7 \times 260 \times 10^{-3}$$
$$= 35.53\text{kN}$$

Eurocode:

$$e_i = \frac{H}{400}$$
$$= \frac{1400}{400}$$
$$= 3.5$$

$$e_{tot} = e_o + e_i$$
$$= 2.5 + 3.5$$
$$= 6\text{mm}$$

$$\varphi = 1.14\left(\frac{1 - 2e_{tot}}{h}\right) - 0.02\left(\frac{l_o}{h}\right) \leq \left(\frac{1 - 2e_{tot}}{h}\right)$$
$$= 1.14\left(\frac{1 - 2 \times 6}{62}\right) - 0.02\left(\frac{1400}{62}\right) \leq \left(\frac{1 - 2 \times 6}{62}\right)$$
$$= 0.464 \leq 0.805$$

$$N_{rd} = \varphi\left(f'_c bh\right)$$
$$= 0.464 * 13.7 * 16120 \times 10^{-3}$$
$$= 101.975\text{kN}$$

C.3. Previous researches

Oberlender (1975):

$$P_u = 0.6f'_u A_c \left[1 - \left(\frac{H}{30t}\right)^2\right]$$

$$= 0.6 \times 13.7 \times 16120 \left[1 - \left(\frac{1400}{30 \times 62}\right)^2\right] \times 10^{-3}$$

$$= 56.35\text{kN}$$

Pillai and Parthasarathy (1977):

$$P_u = \varphi 0.57 f'_c A_c \left[1 - \left(\frac{H}{50t}\right)^2\right]$$

$$= 0.57 \times 13.7 \times 16120 \left[1 - \left(\frac{1400}{50 \times 62}\right)^2\right] \times 10^{-3}$$

$$= 99.4\text{kN}$$

Kripanarayanan (1977):

F_1=0.55

$$F_2 = \left[1 - \left(\frac{kH}{40t}\right)^2\right]$$

$$= \left[1 - \left(\frac{0.8 \times 1400}{40 \times 62}\right)^2\right]$$

$$= 0.796$$

$$P_u = F_1 f'_c A_g F_2$$

$$= 0.55 \times 13.7 \times 16120 \times 0.796 \times 10^{-3}$$

$$= 95.916\text{kN}$$

Zielinski et al. (1983):

$$P_u = 0.55f'_cA_c\left[1-\left(\frac{H}{40t}\right)^2\right][1+\rho_m(m-1)]$$

$$= 0.55\times 13.7\times 16120\left[1-\left(\frac{1400}{40\times 62}\right)^2\right]\left[1+0.0058\left(\frac{13.7}{297}-1\right)\right]\times 10^{-3}$$

$$= 95.38\text{kN}$$

Saheb and Desayi (1989):

$$P_u = 0.55\left[f'_cA_c+\left(f_y-f'_c\right)A_s\right]\left[1-\left(\frac{kH}{32t}\right)^2\right]$$

$$= 0.55\times[13.7\times 16120+(297-13.7)\times 94.489]\left[1-\left(\frac{1400}{32\times 62}\right)^2\right]\times 10^{-3}$$

$$= 67.35\text{kN}$$

Fragomeni and Mendis (1996):

$N_u = (t_w - 1.2e - 2e_a)0.6f_c'$

The calculation steps are same as AS3600.

Doh and Fragomeni (2005):

$$H_{we} = \beta\text{H} = 1\times 1400 = 1400$$

$$e_a = \frac{H_{we}^2}{2500t_w}$$

$$= \frac{1400^2}{2500\times 62}$$

$$= 12.71$$

$$N_u = 2f_c'^{0.7}(t_w - 1.2e - 2e_a)\text{b}$$

$$= 2\times 13.7^{0.7}\times(62-1.2\times 2.5-2\times 12.71)\times 260\times 10^{-3}$$

$$= 108.02\text{kN}$$

Ganesan et al. (2012):

$$P_u = 0.56\left[f'_c A_g + (f_y - f'_c)A_s\right]\left[1 + \left(\frac{h}{29t}\right) - \left(\frac{H}{26t}\right)^2\right]\left[1 - \left(\frac{h}{11L}\right)\right]$$

$$= 0.56 \times [13.7 \times 16120 + (297 - 13.7) \times 94.489] \times \left[1 + \left(\frac{1400}{29 \times 62}\right) - \left(\frac{1400}{26 \times 62}\right)^2\right]\left[1 - \left(\frac{1400}{11 \times 260}\right)\right] \times 10^{-3}$$

$$= 71.91\text{kN}$$

Ganesan et al. (2013):

$$P_u = 0.59\left[f'_c A_g + (f_y - f'_c)A_s\right]\left[1 + \left(\frac{h}{40t}\right) - \left(\frac{H}{30t}\right)^2\right]\left[1 - \left(\frac{h}{18L}\right)\right]$$

$$= 0.56 \times [13.7 \times 16120 + (297 - 13.7) \times 94.489] \times \left[1 + \left(\frac{1400}{40 \times 62}\right) - \left(\frac{1400}{30 \times 62}\right)^2\right]\left[1 - \left(\frac{1400}{18 \times 260}\right)\right] \times 10^{-3}$$

$$= 100.54\text{kN}$$

Robinson et al. (2013):

$$P_u = \frac{1}{2}\left[\frac{10}{e} - \frac{\lambda}{100e} - 4 \times 10^{-4}\lambda^2\right] f'_c A_g$$

$$= \frac{1}{2}\left[\frac{10}{2.5} - \frac{23}{100 \times 2.5} - 4 \times 10^{-4} \times 23^2\right] \times 13.7 \times 16120$$

$$= 405.97\text{kN}$$

C.4. Proposed design equation

Eq. 6-5:

Calculation of eccentricity parameter:

$$e_L = -7.77e + 2.51$$
$$= -7.77 \times \frac{2.5}{62} + 2.51$$
$$= 2.197$$

$$exp(-0.038 \times 23) \times 2.197 = 0.917 \leq 1$$

Calculation of elastic modulus parameter:

$$E_{2400} = 2400^{1.5}\left(0.043\sqrt{13.7}\right)$$
$$= 18713\text{MPa}$$

$$E = \frac{E_c}{E_{2400}}$$
$$= \frac{12047}{18713}$$
$$= 0.65$$

Calculation of ultimate axial capacity:

$$\alpha_2 = 0.85 - 0.0015\text{f}'_\text{c} = 0.85 - 0.0015 \times 13.7 = 0.829$$

$$\lambda = 0.97 - 0.0025\text{f}'_\text{c} = 0.97 - 0.0025 \times 13.7 = 0.936$$

$$P_u = 2.73\alpha_2\gamma {f'_c}^{0.68} A_g exp(-0.038\lambda) e_L E^{0.48}$$
$$= 2.73 \times 0.829 \times 0.936 \times 13.7^{0.68} \times 16120 \times 0.917 \times 0.65^{0.48} \times 10^{-3}$$
$$= 150.26\text{kN}$$

Eq. 6-8:

$$C = \frac{13.7}{10} = 1.37$$

$$e_L = \frac{e}{t} = \frac{2.5}{62} = 0.04$$

$$\begin{aligned} P_u/f'_c A_g &= (1.58203 - 0.0495916\lambda - 3.35892e_L - 0.128903\ C + 0.678011E \\ &\quad + 0.0579191\lambda e_L + \ 0.000685507\lambda\ C - 0.00286346\ \lambda E \\ &\quad + 0.104136e_L C + \ -0.790131e_L E + 0.00287261CE \\ &\quad + 0.000425184\lambda^2 - 0.478367e^2 + 0.00629655C^2 - 0.186515E^2) \\ &= (1.58203 - 0.0495916 \times 23 - 3.35892 \times 0.04 - 0.128903\ \times 1.37 \\ &\quad + 0.678011 \times 0.65 + 0.0579191 \times 23 \times 0.04 + \ 0.000685507 \\ &\quad \times 23 \times 1.37 - 0.00286346 \times 23 \times 0.65 + 0.104136 \times 0.04 \times 1.37 \\ &\quad - 0.790131 \times 0.04 \times 0.65 + 0.00287261 \times 1.37 \times 0.65 \\ &\quad + 0.000425184 \times 23^2 - 0.478367 \times 0.04^2 + 0.00629655 \times 1.37^2 \\ &\quad - 0.186515 \times 0.65^2) \\ &= 0.7579 \end{aligned}$$

$$\begin{aligned} P_u &= 13.7 \times 16120 \times 0.7579 \times 10^{-3} \\ &= 164.3\text{kN} \end{aligned}$$

D. Results of Parametric Studies

The results obtained from FEA parametric studies are summarized in Table D.1.

Table D.1: Details of published results

SR	AR	Height (mm)	Length (mm)	Thickness (mm)	Ag (mm^2)	Eccentricity	f'_c (MPa)	Density	f_t/f'_c ratio	E (MPa)	Steel ratio	f_{sy} (MPa)	Failure Load (kN)	Axial strength ratio
15	0.5	900	1800	60	108000	t/600	13.7	1800	0.08	12155	0.0058933	297	1791.99	1.211
20	0.5	1200	2400	60	144000	t/600	13.7	1800	0.08	12155	0.0058933	297	2123.11	1.076
25	0.5	1500	3000	60	180000	t/600	13.7	1800	0.08	12155	0.0058933	297	2271.56	0.921
30	0.5	1800	3600	60	216000	t/600	13.7	1800	0.08	12155	0.0058933	297	2392.76	0.809
35	0.5	2100	4200	60	252000	t/600	13.7	1800	0.08	12155	0.0058933	297	2213.22	0.641
40	0.5	2400	4800	60	288000	t/600	13.7	1800	0.08	12155	0.0058933	297	2073.99	0.526
45	0.5	2700	5400	60	324000	t/600	13.7	1800	0.08	12155	0.0058933	297	1985.79	0.447
50	0.5	3000	6000	60	360000	t/600	13.7	1800	0.08	12155	0.0058933	297	1955.50	0.396
15	0.5	900	1800	60	108000	t/12	13.7	1800	0.08	12155	0.0058933	297	1309.12	0.885
20	0.5	1200	2400	60	144000	t/12	13.7	1800	0.08	12155	0.0058933	297	1474.76	0.748
25	0.5	1500	3000	60	180000	t/12	13.7	1800	0.08	12155	0.0058933	297	1500.48	0.608
30	0.5	1800	3600	60	216000	t/12	13.7	1800	0.08	12155	0.0058933	297	1436.49	0.485
35	0.5	2100	4200	60	252000	t/12	13.7	1800	0.08	12155	0.0058933	297	1351.50	0.391
40	0.5	2400	4800	60	288000	t/12	13.7	1800	0.08	12155	0.0058933	297	1235.08	0.313
45	0.5	2700	5400	60	324000	t/12	13.7	1800	0.08	12155	0.0058933	297	1112.84	0.251
50	0.5	3000	6000	60	360000	t/12	13.7	1800	0.08	12155	0.0058933	297	994.17	0.202
15	0.5	900	1800	60	108000	t/6	13.7	1800	0.08	12155	0.0058933	297	958.69	0.648
20	0.5	1200	2400	60	144000	t/6	13.7	1800	0.08	12155	0.0058933	297	982.40	0.498
25	0.5	1500	3000	60	180000	t/6	13.7	1800	0.08	12155	0.0058933	297	952.95	0.386
30	0.5	1800	3600	60	216000	t/6	13.7	1800	0.08	12155	0.0058933	297	913.44	0.309
35	0.5	2100	4200	60	252000	t/6	13.7	1800	0.08	12155	0.0058933	297	847.46	0.245

(contd.)

SR	AR	Height (mm)	Length (mm)	Thickness (mm)	Ag (mm^2)	Eccentricity	f'_c (MPa)	Density	f_t/f'_c ratio	E (MPa)	Steel ratio	f_{sy} (MPa)	Failure Load (kN)	Axial strength ratio
40	0.5	2400	4800	60	288000	t/6	13.7	1800	0.08	12155	0.0058933	297	789.72	0.200
45	0.5	2700	5400	60	324000	t/6	13.7	1800	0.08	12155	0.0058933	297	746.33	0.168
50	0.5	3000	6000	60	360000	t/6	13.7	1800	0.08	12155	0.0058933	297	714.30	0.145
15	1	900	900	60	54000	t/600	13.7	1800	0.08	12155	0.0058933	297	868.01	1.173
20	1	1200	1200	60	72000	t/600	13.7	1800	0.08	12155	0.0058933	297	1029.07	1.043
25	1	1500	1500	60	90000	t/600	13.7	1800	0.08	12155	0.0058933	297	1107.22	0.898
30	1	1800	1800	60	108000	t/600	13.7	1800	0.08	12155	0.0058933	297	1176.97	0.795
35	1	2100	2100	60	126000	t/600	13.7	1800	0.08	12155	0.0058933	297	1108.51	0.642
40	1	2400	2400	60	144000	t/600	13.7	1800	0.08	12155	0.0058933	297	1041.54	0.528
45	1	2700	2700	60	162000	t/600	13.7	1800	0.08	12155	0.0058933	297	999.09	0.450
50	1	3000	3000	60	180000	t/600	13.7	1800	0.08	12155	0.0058933	297	974.81	0.395
15	1	900	900	60	54000	t/12	13.7	1800	0.08	12155	0.0058933	297	633.14	0.856
20	1	1200	1200	60	72000	t/12	13.7	1800	0.08	12155	0.0058933	297	714.47	0.724
25	1	1500	1500	60	90000	t/12	13.7	1800	0.08	12155	0.0058933	297	737.75	0.598
30	1	1800	1800	60	108000	t/12	13.7	1800	0.08	12155	0.0058933	297	717.46	0.485
35	1	2100	2100	60	126000	t/12	13.7	1800	0.08	12155	0.0058933	297	680.57	0.394
40	1	2400	2400	60	144000	t/12	13.7	1800	0.08	12155	0.0058933	297	615.82	0.312
45	1	2700	2700	60	162000	t/12	13.7	1800	0.08	12155	0.0058933	297	564.38	0.254
50	1	3000	3000	60	180000	t/12	13.7	1800	0.08	12155	0.0058933	297	524.31	0.213
15	1	900	900	60	54000	t/6	13.7	1800	0.08	12155	0.0058933	297	461.40	0.624
20	1	1200	1200	60	72000	t/6	13.7	1800	0.08	12155	0.0058933	297	490.45	0.497
25	1	1500	1500	60	90000	t/6	13.7	1800	0.08	12155	0.0058933	297	482.74	0.392
30	1	1800	1800	60	108000	t/6	13.7	1800	0.08	12155	0.0058933	297	444.29	0.300
35	1	2100	2100	60	126000	t/6	13.7	1800	0.08	12155	0.0058933	297	420.96	0.244
40	1	2400	2400	60	144000	t/6	13.7	1800	0.08	12155	0.0058933	297	398.49	0.202

(contd.)

SR	AR	Height (mm)	Length (mm)	Thickness (mm)	Ag (mm^2)	Eccentricity	f'_c (MPa)	Density	f_t/f'_c ratio	E (MPa)	Steel ratio	f_{sy} (MPa)	Failure Load (kN)	Axial strength ratio
45	1	2700	2700	60	162000	t/6	13.7	1800	0.08	12155	0.0058933	297	392.09	0.177
50	1	3000	3000	60	180000	t/6	13.7	1800	0.08	12155	0.0058933	297	377.71	0.153
23	5.4	1400	260	62	16120	t/600	13.7	1800	0.08	12155	0.0058933	297	199.63	0.904
27	5.4	1675	315	62	19530	t/600	13.7	1800	0.08	12155	0.0058933	297	227.73	0.851
30	5.4	1860	350	62	21700	t/600	13.7	1800	0.08	12155	0.0058933	297	239.95	0.807
35	5.4	2170	410	62	25420	t/600	13.7	1800	0.08	12155	0.0058933	297	232.44	0.667
40	5.4	2480	470	62	29140	t/600	13.7	1800	0.08	12155	0.0058933	297	219.29	0.549
45	5.4	2790	520	62	32240	t/600	13.7	1800	0.08	12155	0.0058933	297	204.44	0.463
50	5.4	3100	580	62	35960	t/600	13.7	1800	0.08	12155	0.0058933	297	200.23	0.406
23	5.4	1400	260	62	16120	t/20	13.7	1800	0.08	12155	0.0058933	297	153.35	0.694
27	5.4	1675	315	62	19530	t/20	13.7	1800	0.08	12155	0.0058933	297	161.69	0.604
30	5.4	1860	350	62	21700	t/20	13.7	1800	0.08	12155	0.0058933	297	162.26	0.546
35	5.4	2170	410	62	25420	t/20	13.7	1800	0.08	12155	0.0058933	297	157.62	0.453
40	5.4	2480	470	62	29140	t/20	13.7	1800	0.08	12155	0.0058933	297	147.73	0.370
45	5.4	2790	520	62	32240	t/20	13.7	1800	0.08	12155	0.0058933	297	131.19	0.297
50	5.4	3100	580	62	35960	t/20	13.7	1800	0.08	12155	0.0058933	297	119.88	0.243
23	5.4	1400	260	62	16120	t/12	13.7	1800	0.08	12155	0.0058933	297	135.49	0.614
27	5.4	1675	315	62	19530	t/12	13.7	1800	0.08	12155	0.0058933	297	141.52	0.529
30	5.4	1860	350	62	21700	t/12	13.7	1800	0.08	12155	0.0058933	297	140.62	0.473
35	5.4	2170	410	62	25420	t/12	13.7	1800	0.08	12155	0.0058933	297	134.89	0.387
40	5.4	2480	470	62	29140	t/12	13.7	1800	0.08	12155	0.0058933	297	124.41	0.312
45	5.4	2790	520	62	32240	t/12	13.7	1800	0.08	12155	0.0058933	297	112.71	0.255
50	5.4	3100	580	62	35960	t/12	13.7	1800	0.08	12155	0.0058933	297	104.99	0.213
23	5.4	1400	260	62	16120	t/6	13.7	1800	0.08	12155	0.0058933	297	92.61	0.419
27	5.4	1675	315	62	19530	t/6	13.7	1800	0.08	12155	0.0058933	297	92.48	0.346

(contd.)

SR	AR	Height (mm)	Length (mm)	Thickness (mm)	Ag (mm^2)	Eccentricity	f'_c (MPa)	Density	f_t/f'_c ratio	E (MPa)	Steel ratio	f_{sy} (MPa)	Failure Load (kN)	Axial strength ratio
30	5.4	1860	350	62	21700	t/6	13.7	1800	0.08	12155	0.0058933	297	89.63	0.302
35	5.4	2170	410	62	25420	t/6	13.7	1800	0.08	12155	0.0058933	297	83.34	0.239
40	5.4	2480	470	62	29140	t/6	13.7	1800	0.08	12155	0.0058933	297	79.90	0.200
45	5.4	2790	520	62	32240	t/6	13.7	1800	0.08	12155	0.0058933	297	75.55	0.171
50	5.4	3100	580	62	35960	t/6	13.7	1800	0.08	12155	0.0058933	297	73.50	0.149
23	5.4	1400	260	62	16120	t/20	25	1800	0.08	16419	0.0058933	297	249.12	0.618
27	5.4	1675	315	62	19530	t/20	25	1800	0.08	16419	0.0058933	297	252.48	0.517
30	5.4	1860	350	62	21700	t/20	25	1800	0.08	16419	0.0058933	297	243.99	0.450
35	5.4	2170	410	62	25420	t/20	25	1800	0.08	16419	0.0058933	297	220.87	0.348
40	5.4	2480	470	62	29140	t/20	25	1800	0.08	16419	0.0058933	297	198.26	0.272
45	5.4	2790	520	62	32240	t/20	25	1800	0.08	16419	0.0058933	297	175.94	0.218
50	5.4	3100	580	62	35960	t/20	25	1800	0.08	16419	0.0058933	297	160.63	0.179
23	5.4	1400	260	62	16120	t/12	25	1800	0.08	16419	0.0058933	297	216.01	0.536
27	5.4	1675	315	62	19530	t/12	25	1800	0.08	16419	0.0058933	297	214.76	0.440
30	5.4	1860	350	62	21700	t/12	25	1800	0.08	16419	0.0058933	297	203.80	0.376
35	5.4	2170	410	62	25420	t/12	25	1800	0.08	16419	0.0058933	297	183.88	0.289
40	5.4	2480	470	62	29140	t/12	25	1800	0.08	16419	0.0058933	297	167.96	0.231
45	5.4	2790	520	62	32240	t/12	25	1800	0.08	16419	0.0058933	297	152.10	0.189
50	5.4	3100	580	62	35960	t/12	25	1800	0.08	16419	0.0058933	297	141.87	0.158
23	5.4	1400	260	62	16120	t/6	25	1800	0.08	16419	0.0058933	297	141.78	0.352
27	5.4	1675	315	62	19530	t/6	25	1800	0.08	16419	0.0058933	297	131.41	0.269
30	5.4	1860	350	62	21700	t/6	25	1800	0.08	16419	0.0058933	297	125.50	0.231
35	5.4	2170	410	62	25420	t/6	25	1800	0.08	16419	0.0058933	297	116.34	0.183
40	5.4	2480	470	62	29140	t/6	25	1800	0.08	16419	0.0058933	297	111.26	0.153
45	5.4	2790	520	62	32240	t/6	25	1800	0.08	16419	0.0058933	297	105.89	0.131

(contd.)

SR	AR	Height (mm)	Length (mm)	Thickness (mm)	Ag (mm^2)	Eccentricity	f'_c (MPa)	Density	f_t/f'_c ratio	E (MPa)	Steel ratio	f_{sy} (MPa)	Failure Load (kN)	Axial strength ratio
50	5.4	3100	580	62	35960	t/6	25	1800	0.08	16419	0.0058933	297	102.44	0.114
23	5.4	1400	260	62	16120	t/20	40	1800	0.08	20769	0.0058933	297	355.15	0.551
27	5.4	1675	315	62	19530	t/20	40	1800	0.08	20769	0.0058933	297	341.15	0.437
30	5.4	1860	350	62	21700	t/20	40	1800	0.08	20769	0.0058933	297	317.12	0.365
35	5.4	2170	410	62	25420	t/20	40	1800	0.08	20769	0.0058933	297	279.21	0.275
40	5.4	2480	470	62	29140	t/20	40	1800	0.08	20769	0.0058933	297	250.64	0.215
45	5.4	2790	520	62	32240	t/20	40	1800	0.08	20769	0.0058933	297	223.39	0.173
50	5.4	3100	580	62	35960	t/20	40	1800	0.08	20769	0.0058933	297	205.25	0.143
23	5.4	1400	260	62	16120	t/12	40	1800	0.08	20769	0.0058933	297	304.48	0.472
27	5.4	1675	315	62	19530	t/12	40	1800	0.08	20769	0.0058933	297	281.53	0.360
30	5.4	1860	350	62	21700	t/12	40	1800	0.08	20769	0.0058933	297	260.81	0.300
35	5.4	2170	410	62	25420	t/12	40	1800	0.08	20769	0.0058933	297	234.88	0.231
40	5.4	2480	470	62	29140	t/12	40	1800	0.08	20769	0.0058933	297	214.48	0.184
45	5.4	2790	520	62	32240	t/12	40	1800	0.08	20769	0.0058933	297	194.25	0.151
50	5.4	3100	580	62	35960	t/12	40	1800	0.08	20769	0.0058933	297	181.13	0.126
23	5.4	1400	260	62	16120	t/6	40	1800	0.08	20769	0.0058933	297	188.37	0.292
27	5.4	1675	315	62	19530	t/6	40	1800	0.08	20769	0.0058933	297	172.67	0.221
30	5.4	1860	350	62	21700	t/6	40	1800	0.08	20769	0.0058933	297	163.94	0.189
35	5.4	2170	410	62	25420	t/6	40	1800	0.08	20769	0.0058933	297	152.73	0.150
40	5.4	2480	470	62	29140	t/6	40	1800	0.08	20769	0.0058933	297	146.36	0.126
45	5.4	2790	520	62	32240	t/6	40	1800	0.08	20769	0.0058933	297	139.26	0.108
50	5.4	3100	580	62	35960	t/6	40	1800	0.08	20769	0.0058933	297	134.22	0.093
23	5.4	1400	260	62	16120	t/20	60	1800	0.08	23361	0.0058933	297	444.83	0.460
27	5.4	1675	315	62	19530	t/20	60	1800	0.08	23361	0.0058933	297	393.71	0.336
30	5.4	1860	350	62	21700	t/20	60	1800	0.08	23361	0.0058933	297	360.54	0.277

(contd.)

SR	AR	Height (mm)	Length (mm)	Thickness (mm)	Ag (mm^2)	Eccentricity	f'_c (MPa)	Density	f_t/f'_c ratio	E (MPa)	Steel ratio	f_{sy} (MPa)	Failure Load (kN)	Axial strength ratio
35	5.4	2170	410	62	25420	t/20	60	1800	0.08	23361	0.0058933	297	317.72	0.208
40	5.4	2480	470	62	29140	t/20	60	1800	0.08	23361	0.0058933	297	285.33	0.163
45	5.4	2790	520	62	32240	t/20	60	1800	0.08	23361	0.0058933	297	253.49	0.131
50	5.4	3100	580	62	35960	t/20	60	1800	0.08	23361	0.0058933	297	234.07	0.108
23	5.4	1400	260	62	16120	t/12	60	1800	0.08	23361	0.0058933	297	368.80	0.381
27	5.4	1675	315	62	19530	t/12	60	1800	0.08	23361	0.0058933	297	324.09	0.277
30	5.4	1860	350	62	21700	t/12	60	1800	0.08	23361	0.0058933	297	300.59	0.231
35	5.4	2170	410	62	25420	t/12	60	1800	0.08	23361	0.0058933	297	271.01	0.178
40	5.4	2480	470	62	29140	t/12	60	1800	0.08	23361	0.0058933	297	247.39	0.141
45	5.4	2790	520	62	32240	t/12	60	1800	0.08	23361	0.0058933	297	223.79	0.116
50	5.4	3100	580	62	35960	t/12	60	1800	0.08	23361	0.0058933	297	208.47	0.097
23	5.4	1400	260	62	16120	t/6	60	1800	0.08	23361	0.0058933	297	220.62	0.228
27	5.4	1675	315	62	19530	t/6	60	1800	0.08	23361	0.0058933	297	206.73	0.176
30	5.4	1860	350	62	21700	t/6	60	1800	0.08	23361	0.0058933	297	196.46	0.151
35	5.4	2170	410	62	25420	t/6	60	1800	0.08	23361	0.0058933	297	184.50	0.121
40	5.4	2480	470	62	29140	t/6	60	1800	0.08	23361	0.0058933	297	176.36	0.101
45	5.4	2790	520	62	32240	t/6	60	1800	0.08	23361	0.0058933	297	166.79	0.086
50	5.4	3100	580	62	35960	t/6	60	1800	0.08	23361	0.0058933	297	160.07	0.074
23	5.4	1400	260	62	16120	t/20	80	1800	0.08	25557	0.0058933	297	508.62	0.394
27	5.4	1675	315	62	19530	t/20	80	1800	0.08	25557	0.0058933	297	432.87	0.277
30	5.4	1860	350	62	21700	t/20	80	1800	0.08	25557	0.0058933	297	397.27	0.229
35	5.4	2170	410	62	25420	t/20	80	1800	0.08	25557	0.0058933	297	350.59	0.172
40	5.4	2480	470	62	29140	t/20	80	1800	0.08	25557	0.0058933	297	314.93	0.135
45	5.4	2790	520	62	32240	t/20	80	1800	0.08	25557	0.0058933	297	279.55	0.108
50	5.4	3100	580	62	35960	t/20	80	1800	0.08	25557	0.0058933	297	256.64	0.089

(contd.)

SR	AR	Height (mm)	Length (mm)	Thickness (mm)	Ag (mm^2)	Eccentricity	f'_c (MPa)	Density	f_t/f'_c ratio	E (MPa)	Steel ratio	f_{sy} (MPa)	Failure Load (kN)	Axial strength ratio
23	5.4	1400	260	62	16120	t/12	80	1800	0.08	25557	0.0058933	297	426.93	0.331
27	5.4	1675	315	62	19530	t/12	80	1800	0.08	25557	0.0058933	297	360.52	0.231
30	5.4	1860	350	62	21700	t/12	80	1800	0.08	25557	0.0058933	297	335.13	0.193
35	5.4	2170	410	62	25420	t/12	80	1800	0.08	25557	0.0058933	297	302.30	0.149
40	5.4	2480	470	62	29140	t/12	80	1800	0.08	25557	0.0058933	297	275.88	0.118
45	5.4	2790	520	62	32240	t/12	80	1800	0.08	25557	0.0058933	297	249.40	0.097
50	5.4	3100	580	62	35960	t/12	80	1800	0.08	25557	0.0058933	297	232.11	0.081
23	5.4	1400	260	62	16120	t/6	80	1800	0.08	25557	0.0058933	297	251.89	0.195
27	5.4	1675	315	62	19530	t/6	80	1800	0.08	25557	0.0058933	297	236.16	0.151
30	5.4	1860	350	62	21700	t/6	80	1800	0.08	25557	0.0058933	297	225.27	0.130
35	5.4	2170	410	62	25420	t/6	80	1800	0.08	25557	0.0058933	297	212.08	0.104
40	5.4	2480	470	62	29140	t/6	80	1800	0.08	25557	0.0058933	297	203.50	0.087
45	5.4	2790	520	62	32240	t/6	80	1800	0.08	25557	0.0058933	297	190.58	0.074
50	5.4	3100	580	62	35960	t/6	80	1800	0.08	25557	0.0058933	297	182.42	0.063
23	5.4	1400	260	62	16120	t/20	13.7	1600	0.08	10186	0.0058933	297	149.39	0.676
27	5.4	1675	315	62	19530	t/20	13.7	1600	0.08	10186	0.0058933	297	154.53	0.578
30	5.4	1860	350	62	21700	t/20	13.7	1600	0.08	10186	0.0058933	297	151.51	0.510
35	5.4	2170	410	62	25420	t/20	13.7	1600	0.08	10186	0.0058933	297	140.61	0.404
40	5.4	2480	470	62	29140	t/20	13.7	1600	0.08	10186	0.0058933	297	126.30	0.316
45	5.4	2790	520	62	32240	t/20	13.7	1600	0.08	10186	0.0058933	297	111.66	0.253
50	5.4	3100	580	62	35960	t/20	13.7	1600	0.08	10186	0.0058933	297	101.74	0.207
23	5.4	1400	260	62	16120	t/12	13.7	1600	0.08	10186	0.0058933	297	131.24	0.594
27	5.4	1675	315	62	19530	t/12	13.7	1600	0.08	10186	0.0058933	297	132.96	0.497
30	5.4	1860	350	62	21700	t/12	13.7	1600	0.08	10186	0.0058933	297	128.49	0.432
35	5.4	2170	410	62	25420	t/12	13.7	1600	0.08	10186	0.0058933	297	116.74	0.335

(contd.)

SR	AR	Height (mm)	Length (mm)	Thickness (mm)	Ag (mm^2)	Eccentricity	f'_c (MPa)	Density	f_t/f'_c ratio	E (MPa)	Steel ratio	f_{sy} (MPa)	Failure Load (kN)	Axial strength ratio
40	5.4	2480	470	62	29140	t/12	13.7	1600	0.08	10186	0.0058933	297	106.70	0.267
45	5.4	2790	520	62	32240	t/12	13.7	1600	0.08	10186	0.0058933	297	96.70	0.219
50	5.4	3100	580	62	35960	t/12	13.7	1600	0.08	10186	0.0058933	297	90.03	0.183
23	5.4	1400	260	62	16120	t/6	13.7	1600	0.08	10186	0.0058933	297	87.46	0.396
27	5.4	1675	315	62	19530	t/6	13.7	1600	0.08	10186	0.0058933	297	83.27	0.311
30	5.4	1860	350	62	21700	t/6	13.7	1600	0.08	10186	0.0058933	297	78.38	0.264
35	5.4	2170	410	62	25420	t/6	13.7	1600	0.08	10186	0.0058933	297	73.13	0.210
40	5.4	2480	470	62	29140	t/6	13.7	1600	0.08	10186	0.0058933	297	70.11	0.176
45	5.4	2790	520	62	32240	t/6	13.7	1600	0.08	10186	0.0058933	297	66.45	0.150
50	5.4	3100	580	62	35960	t/6	13.7	1600	0.08	10186	0.0058933	297	64.45	0.131
23	5.4	1400	260	62	16120	t/20	13.7	2000	0.08	14236	0.0058933	297	156.07	0.707
27	5.4	1675	315	62	19530	t/20	13.7	2000	0.08	14236	0.0058933	297	166.56	0.623
30	5.4	1860	350	62	21700	t/20	13.7	2000	0.08	14236	0.0058933	297	168.50	0.567
35	5.4	2170	410	62	25420	t/20	13.7	2000	0.08	14236	0.0058933	297	166.98	0.479
40	5.4	2480	470	62	29140	t/20	13.7	2000	0.08	14236	0.0058933	297	161.96	0.406
45	5.4	2790	520	62	32240	t/20	13.7	2000	0.08	14236	0.0058933	297	149.17	0.338
50	5.4	3100	580	62	35960	t/20	13.7	2000	0.08	14236	0.0058933	297	138.05	0.280
23	5.4	1400	260	62	16120	t/12	13.7	2000	0.08	14236	0.0058933	297	138.45	0.627
27	5.4	1675	315	62	19530	t/12	13.7	2000	0.08	14236	0.0058933	297	146.56	0.548
30	5.4	1860	350	62	21700	t/12	13.7	2000	0.08	14236	0.0058933	297	147.29	0.495
35	5.4	2170	410	62	25420	t/12	13.7	2000	0.08	14236	0.0058933	297	145.21	0.417
40	5.4	2480	470	62	29140	t/12	13.7	2000	0.08	14236	0.0058933	297	139.58	0.350
45	5.4	2790	520	62	32240	t/12	13.7	2000	0.08	14236	0.0058933	297	128.55	0.291
50	5.4	3100	580	62	35960	t/12	13.7	2000	0.08	14236	0.0058933	297	120.17	0.244
23	5.4	1400	260	62	16120	t/6	13.7	2000	0.08	14236	0.0058933	297	95.87	0.434

(contd.)

SR	AR	Height (mm)	Length (mm)	Thickness (mm)	Ag (mm^2)	Eccentricity	f'_c (MPa)	Density	f_t/f'_c ratio	E (MPa)	Steel ratio	f_{sy} (MPa)	Failure Load (kN)	Axial strength ratio
27	5.4	1675	315	62	19530	t/6	13.7	2000	0.08	14236	0.0058933	297	98.07	0.367
30	5.4	1860	350	62	21700	t/6	13.7	2000	0.08	14236	0.0058933	297	96.89	0.326
35	5.4	2170	410	62	25420	t/6	13.7	2000	0.08	14236	0.0058933	297	93.04	0.267
40	5.4	2480	470	62	29140	t/6	13.7	2000	0.08	14236	0.0058933	297	89.57	0.224
45	5.4	2790	520	62	32240	t/6	13.7	2000	0.08	14236	0.0058933	297	85.14	0.193
50	5.4	3100	580	62	35960	t/6	13.7	2000	0.08	14236	0.0058933	297	82.36	0.167
23	5.4	1400	260	62	16120	t/20	13.7	2200	0.08	16423	0.0058933	297	158.32	0.717
27	5.4	1675	315	62	19530	t/20	13.7	2200	0.08	16423	0.0058933	297	170.34	0.637
30	5.4	1860	350	62	21700	t/20	13.7	2200	0.08	16423	0.0058933	297	173.30	0.583
35	5.4	2170	410	62	25420	t/20	13.7	2200	0.08	16423	0.0058933	297	174.00	0.500
40	5.4	2480	470	62	29140	t/20	13.7	2200	0.08	16423	0.0058933	297	171.07	0.429
45	5.4	2790	520	62	32240	t/20	13.7	2200	0.08	16423	0.0058933	297	161.16	0.365
50	5.4	3100	580	62	35960	t/20	13.7	2200	0.08	16423	0.0058933	297	153.83	0.312
23	5.4	1400	260	62	16120	t/12	13.7	2200	0.08	16423	0.0058933	297	140.87	0.638
27	5.4	1675	315	62	19530	t/12	13.7	2200	0.08	16423	0.0058933	297	150.27	0.562
30	5.4	1860	350	62	21700	t/12	13.7	2200	0.08	16423	0.0058933	297	152.09	0.512
35	5.4	2170	410	62	25420	t/12	13.7	2200	0.08	16423	0.0058933	297	152.36	0.438
40	5.4	2480	470	62	29140	t/12	13.7	2200	0.08	16423	0.0058933	297	149.54	0.375
45	5.4	2790	520	62	32240	t/12	13.7	2200	0.08	16423	0.0058933	297	140.26	0.318
50	5.4	3100	580	62	35960	t/12	13.7	2200	0.08	16423	0.0058933	297	134.37	0.273
23	5.4	1400	260	62	16120	t/6	13.7	2200	0.08	16423	0.0058933	297	98.01	0.444
27	5.4	1675	315	62	19530	t/6	13.7	2200	0.08	16423	0.0058933	297	101.78	0.380
30	5.4	1860	350	62	21700	t/6	13.7	2200	0.08	16423	0.0058933	297	101.68	0.342
35	5.4	2170	410	62	25420	t/6	13.7	2200	0.08	16423	0.0058933	297	99.20	0.285
40	5.4	2480	470	62	29140	t/6	13.7	2200	0.08	16423	0.0058933	297	98.34	0.246

(contd.)

SR	AR	Height (mm)	Length (mm)	Thickness (mm)	Ag (mm^2)	Eccentricity	f'_c (MPa)	Density	f_t/f'_c ratio	E (MPa)	Steel ratio	f_{sy} (MPa)	Failure Load (kN)	Axial strength ratio
45	5.4	2790	520	62	32240	t/6	13.7	2200	0.08	16423	0.0058933	297	93.76	0.212
50	5.4	3100	580	62	35960	t/6	13.7	2200	0.08	16423	0.0058933	297	91.88	0.186
23	5.4	1400	260	62	16120	t/20	13.7	2400	0.08	18713	0.0058933	297	160.34	0.726
27	5.4	1675	315	62	19530	t/20	13.7	2400	0.08	18713	0.0058933	297	173.37	0.648
30	5.4	1860	350	62	21700	t/20	13.7	2400	0.08	18713	0.0058933	297	177.01	0.595
35	5.4	2170	410	62	25420	t/20	13.7	2400	0.08	18713	0.0058933	297	179.77	0.516
40	5.4	2480	470	62	29140	t/20	13.7	2400	0.08	18713	0.0058933	297	176.79	0.443
45	5.4	2790	520	62	32240	t/20	13.7	2400	0.08	18713	0.0058933	297	168.94	0.382
50	5.4	3100	580	62	35960	t/20	13.7	2400	0.08	18713	0.0058933	297	166.06	0.337
23	5.4	1400	260	62	16120	t/12	13.7	2400	0.08	18713	0.0058933	297	142.96	0.647
27	5.4	1675	315	62	19530	t/12	13.7	2400	0.08	18713	0.0058933	297	153.25	0.573
30	5.4	1860	350	62	21700	t/12	13.7	2400	0.08	18713	0.0058933	297	155.19	0.522
35	5.4	2170	410	62	25420	t/12	13.7	2400	0.08	18713	0.0058933	297	157.61	0.453
40	5.4	2480	470	62	29140	t/12	13.7	2400	0.08	18713	0.0058933	297	155.59	0.390
45	5.4	2790	520	62	32240	t/12	13.7	2400	0.08	18713	0.0058933	297	148.22	0.336
50	5.4	3100	580	62	35960	t/12	13.7	2400	0.08	18713	0.0058933	297	144.65	0.294
23	5.4	1400	260	62	16120	t/6	13.7	2400	0.08	18713	0.0058933	297	100.25	0.454
27	5.4	1675	315	62	19530	t/6	13.7	2400	0.08	18713	0.0058933	297	104.15	0.389
30	5.4	1860	350	62	21700	t/6	13.7	2400	0.08	18713	0.0058933	297	104.93	0.353
35	5.4	2170	410	62	25420	t/6	13.7	2400	0.08	18713	0.0058933	297	103.90	0.298
40	5.4	2480	470	62	29140	t/6	13.7	2400	0.08	18713	0.0058933	297	105.40	0.264
45	5.4	2790	520	62	32240	t/6	13.7	2400	0.08	18713	0.0058933	297	101.27	0.229
50	5.4	3100	580	62	35960	t/6	13.7	2400	0.08	18713	0.0058933	297	101.11	0.205

(contd.)

SR	AR	Height (mm)	Length (mm)	Thickness (mm)	Ag (mm^2)	Eccentricity	f'_c (MPa)	Density	f_t/f'_c ratio	E (MPa)	Steel ratio	f_{sy} (MPa)	Failure Load (kN)	Axial strength ratio
23	5.4	1400	260	62	16120	t/20	25	1600	0.08	13760	0.0058933	297	237.19	0.589
30	5.4	1860	350	62	21700	t/20	25	1600	0.08	13760	0.0058933	297	213.88	0.394
40	5.4	2480	470	62	29140	t/20	25	1600	0.08	13760	0.0058933	297	169.29	0.232
50	5.4	3100	580	62	35960	t/20	25	1600	0.08	13760	0.0058933	297	137.32	0.153
23	5.4	1400	260	62	16120	t/12	25	1600	0.08	13760	0.0058933	297	203.60	0.505
30	5.4	1860	350	62	21700	t/12	25	1600	0.08	13760	0.0058933	297	175.55	0.324
40	5.4	2480	470	62	29140	t/12	25	1600	0.08	13760	0.0058933	297	144.51	0.198
50	5.4	3100	580	62	35960	t/12	25	1600	0.08	13760	0.0058933	297	122.08	0.136
23	5.4	1400	260	62	16120	t/6	25	1600	0.08	13760	0.0058933	297	127.10	0.315
30	5.4	1860	350	62	21700	t/6	25	1600	0.08	13760	0.0058933	297	109.97	0.203
40	5.4	2480	470	62	29140	t/6	25	1600	0.08	13760	0.0058933	297	97.98	0.134
50	5.4	3100	580	62	35960	t/6	25	1600	0.08	13760	0.0058933	297	90.08	0.100
23	5.4	1400	260	62	16120	t/20	25	2000	0.08	19230	0.0058933	297	259.95	0.645
30	5.4	1860	350	62	21700	t/20	25	2000	0.08	19230	0.0058933	297	264.11	0.487
40	5.4	2480	470	62	29140	t/20	25	2000	0.08	19230	0.0058933	297	228.76	0.314
50	5.4	3100	580	62	35960	t/20	25	2000	0.08	19230	0.0058933	297	185.43	0.206
23	5.4	1400	260	62	16120	t/12	25	2000	0.08	19230	0.0058933	297	226.76	0.563
30	5.4	1860	350	62	21700	t/12	25	2000	0.08	19230	0.0058933	297	226.06	0.417
40	5.4	2480	470	62	29140	t/12	25	2000	0.08	19230	0.0058933	297	192.63	0.264
50	5.4	3100	580	62	35960	t/12	25	2000	0.08	19230	0.0058933	297	162.56	0.181
23	5.4	1400	260	62	16120	t/6	25	2000	0.08	19230	0.0058933	297	151.03	0.375
30	5.4	1860	350	62	21700	t/6	25	2000	0.08	19230	0.0058933	297	140.94	0.260
40	5.4	2480	470	62	29140	t/6	25	2000	0.08	19230	0.0058933	297	125.36	0.172
50	5.4	3100	580	62	35960	t/6	25	2000	0.08	19230	0.0058933	297	115.08	0.128
23	5.4	1400	260	62	16120	t/20	25	2200	0.08	22186	0.0058933	297	266.38	0.661

(contd.)

SR	AR	Height (mm)	Length (mm)	Thickness (mm)	Ag (mm^2)	Eccentricity	f'_c (MPa)	Density	f_t/f'_c ratio	E (MPa)	Steel ratio	f_{sy} (MPa)	Failure Load (kN)	Axial strength ratio
30	5.4	1860	350	62	21700	t/20	25	2200	0.08	22186	0.0058933	297	277.85	0.512
40	5.4	2480	470	62	29140	t/20	25	2200	0.08	22186	0.0058933	297	254.72	0.350
50	5.4	3100	580	62	35960	t/20	25	2200	0.08	22186	0.0058933	297	212.60	0.236
23	5.4	1400	260	62	16120	t/12	25	2200	0.08	22186	0.0058933	297	233.13	0.578
30	5.4	1860	350	62	21700	t/12	25	2200	0.08	22186	0.0058933	297	240.42	0.443
40	5.4	2480	470	62	29140	t/12	25	2200	0.08	22186	0.0058933	297	216.64	0.297
50	5.4	3100	580	62	35960	t/12	25	2200	0.08	22186	0.0058933	297	184.27	0.205
23	5.4	1400	260	62	16120	t/6	25	2200	0.08	22186	0.0058933	297	158.27	0.393
30	5.4	1860	350	62	21700	t/6	25	2200	0.08	22186	0.0058933	297	154.51	0.285
40	5.4	2480	470	62	29140	t/6	25	2200	0.08	22186	0.0058933	297	138.91	0.191
50	5.4	3100	580	62	35960	t/6	25	2200	0.08	22186	0.0058933	297	127.81	0.142
23	5.4	1400	260	62	16120	t/20	25	2400	0.08	25279	0.0058933	297	271.61	0.674
30	5.4	1860	350	62	21700	t/20	25	2400	0.08	25279	0.0058933	297	287.85	0.531
40	5.4	2480	470	62	29140	t/20	25	2400	0.08	25279	0.0058933	297	273.93	0.376
50	5.4	3100	580	62	35960	t/20	25	2400	0.08	25279	0.0058933	297	238.36	0.265
23	5.4	1400	260	62	16120	t/12	25	2400	0.08	25279	0.0058933	297	238.21	0.591
30	5.4	1860	350	62	21700	t/12	25	2400	0.08	25279	0.0058933	297	250.46	0.462
40	5.4	2480	470	62	29140	t/12	25	2400	0.08	25279	0.0058933	297	237.70	0.326
50	5.4	3100	580	62	35960	t/12	25	2400	0.08	25279	0.0058933	297	203.34	0.226
23	5.4	1400	260	62	16120	t/6	25	2400	0.08	25279	0.0058933	297	163.53	0.406
30	5.4	1860	350	62	21700	t/6	25	2400	0.08	25279	0.0058933	297	164.69	0.304
40	5.4	2480	470	62	29140	t/6	25	2400	0.08	25279	0.0058933	297	152.89	0.210
50	5.4	3100	580	62	35960	t/6	25	2400	0.08	25279	0.0058933	297	140.88	0.157

(contd.)

SR	AR	Height (mm)	Length (mm)	Thickness (mm)	Ag (mm^2)	Eccentricity	f'_c (MPa)	Density	f_t/f'_c ratio	E (MPa)	Steel ratio	f_{sy} (MPa)	Failure Load (kN)	Axial strength ratio
23	5.4	1400	260	62	16120	t/20	40	1600	0.08	17405	0.0058933	297	328.01	0.509
30	5.4	1860	350	62	21700	t/20	40	1600	0.08	17405	0.0058933	297	270.01	0.311
40	5.4	2480	470	62	29140	t/20	40	1600	0.08	17405	0.0058933	297	212.79	0.183
50	5.4	3100	580	62	35960	t/20	40	1600	0.08	17405	0.0058933	297	175.81	0.122
23	5.4	1400	260	62	16120	t/12	40	1600	0.08	17405	0.0058933	297	272.62	0.423
30	5.4	1860	350	62	21700	t/12	40	1600	0.08	17405	0.0058933	297	223.94	0.258
40	5.4	2480	470	62	29140	t/12	40	1600	0.08	17405	0.0058933	297	184.41	0.158
50	5.4	3100	580	62	35960	t/12	40	1600	0.08	17405	0.0058933	297	155.57	0.108
23	5.4	1400	260	62	16120	t/6	40	1600	0.08	17405	0.0058933	297	163.29	0.253
30	5.4	1860	350	62	21700	t/6	40	1600	0.08	17405	0.0058933	297	144.29	0.166
40	5.4	2480	470	62	29140	t/6	40	1600	0.08	17405	0.0058933	297	129.31	0.111
50	5.4	3100	580	62	35960	t/6	40	1600	0.08	17405	0.0058933	297	118.04	0.082
23	5.4	1400	260	62	16120	t/20	40	2000	0.08	24324	0.0058933	297	377.43	0.585
30	5.4	1860	350	62	21700	t/20	40	2000	0.08	24324	0.0058933	297	357.87	0.412
40	5.4	2480	470	62	29140	t/20	40	2000	0.08	24324	0.0058933	297	289.44	0.248
50	5.4	3100	580	62	35960	t/20	40	2000	0.08	24324	0.0058933	297	236.10	0.164
23	5.4	1400	260	62	16120	t/12	40	2000	0.08	24324	0.0058933	297	325.81	0.505
30	5.4	1860	350	62	21700	t/12	40	2000	0.08	24324	0.0058933	297	298.42	0.344
40	5.4	2480	470	62	29140	t/12	40	2000	0.08	24324	0.0058933	297	245.55	0.211
50	5.4	3100	580	62	35960	t/12	40	2000	0.08	24324	0.0058933	297	207.40	0.144
23	5.4	1400	260	62	16120	t/6	40	2000	0.08	24324	0.0058933	297	207.10	0.321
30	5.4	1860	350	62	21700	t/6	40	2000	0.08	24324	0.0058933	297	185.40	0.214
40	5.4	2480	470	62	29140	t/6	40	2000	0.08	24324	0.0058933	297	165.29	0.142
50	5.4	3100	580	62	35960	t/6	40	2000	0.08	24324	0.0058933	297	150.61	0.105
23	5.4	1400	260	62	16120	t/20	40	2200	0.08	28063	0.0058933	297	392.07	0.608

(contd.)

SR	AR	Height (mm)	Length (mm)	Thickness (mm)	Ag (mm^2)	Eccentricity	f'_c (MPa)	Density	f_t/f'_c ratio	E (MPa)	Steel ratio	f_{sy} (MPa)	Failure Load (kN)	Axial strength ratio
30	5.4	1860	350	62	21700	t/20	40	2200	0.08	28063	0.0058933	297	387.08	0.446
40	5.4	2480	470	62	29140	t/20	40	2200	0.08	28063	0.0058933	297	329.73	0.283
50	5.4	3100	580	62	35960	t/20	40	2200	0.08	28063	0.0058933	297	268.79	0.187
23	5.4	1400	260	62	16120	t/12	40	2200	0.08	28063	0.0058933	297	340.40	0.528
30	5.4	1860	350	62	21700	t/12	40	2200	0.08	28063	0.0058933	297	328.06	0.378
40	5.4	2480	470	62	29140	t/12	40	2200	0.08	28063	0.0058933	297	278.21	0.239
50	5.4	3100	580	62	35960	t/12	40	2200	0.08	28063	0.0058933	297	234.90	0.163
23	5.4	1400	260	62	16120	t/6	40	2200	0.08	28063	0.0058933	297	222.73	0.345
30	5.4	1860	350	62	21700	t/6	40	2200	0.08	28063	0.0058933	297	206.59	0.238
40	5.4	2480	470	62	29140	t/6	40	2200	0.08	28063	0.0058933	297	183.20	0.157
50	5.4	3100	580	62	35960	t/6	40	2200	0.08	28063	0.0058933	297	167.44	0.116
23	5.4	1400	260	62	16120	t/20	40	2400	0.08	31975	0.0058933	297	403.36	0.626
30	5.4	1860	350	62	21700	t/20	40	2400	0.08	31975	0.0058933	297	410.30	0.473
40	5.4	2480	470	62	29140	t/20	40	2400	0.08	31975	0.0058933	297	370.12	0.318
50	5.4	3100	580	62	35960	t/20	40	2400	0.08	31975	0.0058933	297	302.96	0.211
23	5.4	1400	260	62	16120	t/12	40	2400	0.08	31975	0.0058933	297	351.83	0.546
30	5.4	1860	350	62	21700	t/12	40	2400	0.08	31975	0.0058933	297	352.69	0.406
40	5.4	2480	470	62	29140	t/12	40	2400	0.08	31975	0.0058933	297	312.14	0.268
50	5.4	3100	580	62	35960	t/12	40	2400	0.08	31975	0.0058933	297	263.46	0.183
23	5.4	1400	260	62	16120	t/6	40	2400	0.08	31975	0.0058933	297	234.84	0.364
30	5.4	1860	350	62	21700	t/6	40	2400	0.08	31975	0.0058933	297	227.77	0.262
40	5.4	2480	470	62	29140	t/6	40	2400	0.08	31975	0.0058933	297	201.28	0.173
50	5.4	3100	580	62	35960	t/6	40	2400	0.08	31975	0.0058933	297	184.37	0.128

(contd.)

SR	AR	Height (mm)	Length (mm)	Thickness (mm)	Ag (mm^2)	Eccentricity	f'_c (MPa)	Density	f_t/f'_c ratio	E (MPa)	Steel ratio	f_{sy} (MPa)	Failure Load (kN)	Axial strength ratio
23	5.4	1400	260	62	16120	t/20	60	1600	0.08	19578	0.0058933	297	385.46	0.399
30	5.4	1860	350	62	21700	t/20	60	1600	0.08	19578	0.0058933	297	307.30	0.236
40	5.4	2480	470	62	29140	t/20	60	1600	0.08	19578	0.0058933	297	243.52	0.139
50	5.4	3100	580	62	35960	t/20	60	1600	0.08	19578	0.0058933	297	198.88	0.092
23	5.4	1400	260	62	16120	t/12	60	1600	0.08	19578	0.0058933	297	315.39	0.326
30	5.4	1860	350	62	21700	t/12	60	1600	0.08	19578	0.0058933	297	258.26	0.198
40	5.4	2480	470	62	29140	t/12	60	1600	0.08	19578	0.0058933	297	213.18	0.122
50	5.4	3100	580	62	35960	t/12	60	1600	0.08	19578	0.0058933	297	179.71	0.083
23	5.4	1400	260	62	16120	t/6	60	1600	0.08	19578	0.0058933	297	193.89	0.200
30	5.4	1860	350	62	21700	t/6	60	1600	0.08	19578	0.0058933	297	173.41	0.133
40	5.4	2480	470	62	29140	t/6	60	1600	0.08	19578	0.0058933	297	155.80	0.089
50	5.4	3100	580	62	35960	t/6	60	1600	0.08	19578	0.0058933	297	140.63	0.065
23	5.4	1400	260	62	16120	t/20	60	2000	0.08	27361	0.0058933	297	495.52	0.512
30	5.4	1860	350	62	21700	t/20	60	2000	0.08	27361	0.0058933	297	416.50	0.320
40	5.4	2480	470	62	29140	t/20	60	2000	0.08	27361	0.0058933	297	329.26	0.188
50	5.4	3100	580	62	35960	t/20	60	2000	0.08	27361	0.0058933	297	270.21	0.125
23	5.4	1400	260	62	16120	t/12	60	2000	0.08	27361	0.0058933	297	414.14	0.428
30	5.4	1860	350	62	21700	t/12	60	2000	0.08	27361	0.0058933	297	344.55	0.265
40	5.4	2480	470	62	29140	t/12	60	2000	0.08	27361	0.0058933	297	283.30	0.162
50	5.4	3100	580	62	35960	t/12	60	2000	0.08	27361	0.0058933	297	238.79	0.111
23	5.4	1400	260	62	16120	t/6	60	2000	0.08	27361	0.0058933	297	249.62	0.258
30	5.4	1860	350	62	21700	t/6	60	2000	0.08	27361	0.0058933	297	220.55	0.169
40	5.4	2480	470	62	29140	t/6	60	2000	0.08	27361	0.0058933	297	198.82	0.114
50	5.4	3100	580	62	35960	t/6	60	2000	0.08	27361	0.0058933	297	179.81	0.083
23	5.4	1400	260	62	16120	t/20	60	2200	0.08	31566	0.0058933	297	528.04	0.546

(contd.)

SR	AR	Height (mm)	Length (mm)	Thickness (mm)	Ag (mm^2)	Eccentricity	f'_c (MPa)	Density	f_t/f'_c ratio	E (MPa)	Steel ratio	f_{sy} (MPa)	Failure Load (kN)	Axial strength ratio
30	5.4	1860	350	62	21700	t/20	60	2200	0.08	31566	0.0058933	297	472.53	0.363
40	5.4	2480	470	62	29140	t/20	60	2200	0.08	31566	0.0058933	297	375.11	0.215
50	5.4	3100	580	62	35960	t/20	60	2200	0.08	31566	0.0058933	297	307.32	0.142
23	5.4	1400	260	62	16120	t/12	60	2200	0.08	31566	0.0058933	297	448.94	0.464
30	5.4	1860	350	62	21700	t/12	60	2200	0.08	31566	0.0058933	297	390.18	0.300
40	5.4	2480	470	62	29140	t/12	60	2200	0.08	31566	0.0058933	297	320.50	0.183
50	5.4	3100	580	62	35960	t/12	60	2200	0.08	31566	0.0058933	297	270.36	0.125
23	5.4	1400	260	62	16120	t/6	60	2200	0.08	31566	0.0058933	297	277.80	0.287
30	5.4	1860	350	62	21700	t/6	60	2200	0.08	31566	0.0058933	297	246.20	0.189
40	5.4	2480	470	62	29140	t/6	60	2200	0.08	31566	0.0058933	297	220.24	0.126
50	5.4	3100	580	62	35960	t/6	60	2200	0.08	31566	0.0058933	297	199.77	0.093
23	5.4	1400	260	62	16120	t/20	60	2400	0.08	35967	0.0058933	297	552.01	0.571
30	5.4	1860	350	62	21700	t/20	60	2400	0.08	35967	0.0058933	297	519.33	0.399
40	5.4	2480	470	62	29140	t/20	60	2400	0.08	35967	0.0058933	297	423.11	0.242
50	5.4	3100	580	62	35960	t/20	60	2400	0.08	35967	0.0058933	297	345.99	0.160
23	5.4	1400	260	62	16120	t/12	60	2400	0.08	35967	0.0058933	297	474.66	0.491
30	5.4	1860	350	62	21700	t/12	60	2400	0.08	35967	0.0058933	297	433.44	0.333
40	5.4	2480	470	62	29140	t/12	60	2400	0.08	35967	0.0058933	297	359.15	0.205
50	5.4	3100	580	62	35960	t/12	60	2400	0.08	35967	0.0058933	297	302.87	0.140
23	5.4	1400	260	62	16120	t/6	60	2400	0.08	35967	0.0058933	297	301.05	0.311
30	5.4	1860	350	62	21700	t/6	60	2400	0.08	35967	0.0058933	297	271.83	0.209
40	5.4	2480	470	62	29140	t/6	60	2400	0.08	35967	0.0058933	297	241.71	0.138
50	5.4	3100	580	62	35960	t/6	60	2400	0.08	35967	0.0058933	297	220.17	0.102

(contd.)

SR	AR	Height (mm)	Length (mm)	Thickness (mm)	Ag (mm^2)	Eccentricity	f'_c (MPa)	Density	f_t/f'_c ratio	E (MPa)	Steel ratio	f_{sy} (MPa)	Failure Load (kN)	Axial strength ratio
23	5.4	1400	260	62	16120	t/20	80	1600	0.08	21418	0.0058933	297	424.81	0.329
30	5.4	1860	350	62	21700	t/20	80	1600	0.08	21418	0.0058933	297	339.11	0.195
40	5.4	2480	470	62	29140	t/20	80	1600	0.08	21418	0.0058933	297	268.97	0.115
50	5.4	3100	580	62	35960	t/20	80	1600	0.08	21418	0.0058933	297	219.03	0.076
23	5.4	1400	260	62	16120	t/12	80	1600	0.08	21418	0.0058933	297	349.73	0.271
30	5.4	1860	350	62	21700	t/12	80	1600	0.08	21418	0.0058933	297	288.76	0.166
40	5.4	2480	470	62	29140	t/12	80	1600	0.08	21418	0.0058933	297	237.88	0.102
50	5.4	3100	580	62	35960	t/12	80	1600	0.08	21418	0.0058933	297	199.17	0.069
23	5.4	1400	260	62	16120	t/6	80	1600	0.08	21418	0.0058933	297	222.34	0.172
30	5.4	1860	350	62	21700	t/6	80	1600	0.08	21418	0.0058933	297	198.48	0.114
40	5.4	2480	470	62	29140	t/6	80	1600	0.08	21418	0.0058933	297	178.63	0.077
50	5.4	3100	580	62	35960	t/6	80	1600	0.08	21418	0.0058933	297	160.03	0.056
23	5.4	1400	260	62	16120	t/20	80	2000	0.08	29933	0.0058933	297	574.40	0.445
30	5.4	1860	350	62	21700	t/20	80	2000	0.08	29933	0.0058933	297	459.42	0.265
40	5.4	2480	470	62	29140	t/20	80	2000	0.08	29933	0.0058933	297	363.42	0.156
50	5.4	3100	580	62	35960	t/20	80	2000	0.08	29933	0.0058933	297	297.24	0.103
23	5.4	1400	260	62	16120	t/12	80	2000	0.08	29933	0.0058933	297	470.15	0.365
30	5.4	1860	350	62	21700	t/12	80	2000	0.08	29933	0.0058933	297	383.85	0.221
40	5.4	2480	470	62	29140	t/12	80	2000	0.08	29933	0.0058933	297	315.80	0.135
50	5.4	3100	580	62	35960	t/12	80	2000	0.08	29933	0.0058933	297	265.82	0.092
23	5.4	1400	260	62	16120	t/6	80	2000	0.08	29933	0.0058933	297	282.49	0.219
30	5.4	1860	350	62	21700	t/6	80	2000	0.08	29933	0.0058933	297	252.18	0.145
40	5.4	2480	470	62	29140	t/6	80	2000	0.08	29933	0.0058933	297	227.97	0.098
50	5.4	3100	580	62	35960	t/6	80	2000	0.08	29933	0.0058933	297	205.05	0.071
23	5.4	1400	260	62	16120	t/20	80	2200	0.08	34534	0.0058933	297	632.76	0.491

(contd.)

SR	AR	Height (mm)	Length (mm)	Thickness (mm)	Ag (mm^2)	Eccentricity	f'_c (MPa)	Density	f_t/f'_c ratio	E (MPa)	Steel ratio	f_{sy} (MPa)	Failure Load (kN)	Axial strength ratio
30	5.4	1860	350	62	21700	t/20	80	2200	0.08	34534	0.0058933	297	523.87	0.302
40	5.4	2480	470	62	29140	t/20	80	2200	0.08	34534	0.0058933	297	413.92	0.178
50	5.4	3100	580	62	35960	t/20	80	2200	0.08	34534	0.0058933	297	339.16	0.118
23	5.4	1400	260	62	16120	t/12	80	2200	0.08	34534	0.0058933	297	525.14	0.407
30	5.4	1860	350	62	21700	t/12	80	2200	0.08	34534	0.0058933	297	434.44	0.250
40	5.4	2480	470	62	29140	t/12	80	2200	0.08	34534	0.0058933	297	357.03	0.153
50	5.4	3100	580	62	35960	t/12	80	2200	0.08	34534	0.0058933	297	300.74	0.105
23	5.4	1400	260	62	16120	t/6	80	2200	0.08	34534	0.0058933	297	316.37	0.245
30	5.4	1860	350	62	21700	t/6	80	2200	0.08	34534	0.0058933	297	280.07	0.161
40	5.4	2480	470	62	29140	t/6	80	2200	0.08	34534	0.0058933	297	252.47	0.108
50	5.4	3100	580	62	35960	t/6	80	2200	0.08	34534	0.0058933	297	228.11	0.079
23	5.4	1400	260	62	16120	t/20	80	2400	0.08	39348	0.0058933	297	675.53	0.524
30	5.4	1860	350	62	21700	t/20	80	2400	0.08	39348	0.0058933	297	587.92	0.339
40	5.4	2480	470	62	29140	t/20	80	2400	0.08	39348	0.0058933	297	466.66	0.200
50	5.4	3100	580	62	35960	t/20	80	2400	0.08	39348	0.0058933	297	382.16	0.133
23	5.4	1400	260	62	16120	t/12	80	2400	0.08	39348	0.0058933	297	568.66	0.441
30	5.4	1860	350	62	21700	t/12	80	2400	0.08	39348	0.0058933	297	486.89	0.280
40	5.4	2480	470	62	29140	t/12	80	2400	0.08	39348	0.0058933	297	399.78	0.171
50	5.4	3100	580	62	35960	t/12	80	2400	0.08	39348	0.0058933	297	337.06	0.117
23	5.4	1400	260	62	16120	t/6	80	2400	0.08	39348	0.0058933	297	349.41	0.271
30	5.4	1860	350	62	21700	t/6	80	2400	0.08	39348	0.0058933	297	308.89	0.178
40	5.4	2480	470	62	29140	t/6	80	2400	0.08	39348	0.0058933	297	277.16	0.119
50	5.4	3100	580	62	35960	t/6	80	2400	0.08	39348	0.0058933	297	251.19	0.087

(contd.)

SR	AR	Height (mm)	Length (mm)	Thickness (mm)	Ag (mm^2)	Eccentricity	f'_c (MPa)	Density	f_t/f'_c ratio	E (MPa)	Steel ratio	f_{sy} (MPa)	Failure Load (kN)	Axial strength ratio
23	5.4	1400	260	62	16120	t/12	13.7	1800	0.05	12155	0.0058933	297	134.00	0.607
27	5.4	1675	315	62	19530	t/12	13.7	1800	0.05	12155	0.0058933	297	140.22	0.524
30	5.4	1860	350	62	21700	t/12	13.7	1800	0.05	12155	0.0058933	297	138.75	0.467
35	5.4	2170	410	62	25420	t/12	13.7	1800	0.05	12155	0.0058933	297	131.68	0.378
40	5.4	2480	470	62	29140	t/12	13.7	1800	0.05	12155	0.0058933	297	120.75	0.302
45	5.4	2790	520	62	32240	t/12	13.7	1800	0.05	12155	0.0058933	297	109.44	0.248
50	5.4	3100	580	62	35960	t/12	13.7	1800	0.05	12155	0.0058933	297	102.22	0.207
23	5.4	1400	260	62	16120	t/6	13.7	1800	0.05	12155	0.0058933	297	90.96	0.412
27	5.4	1675	315	62	19530	t/6	13.7	1800	0.05	12155	0.0058933	297	89.46	0.334
30	5.4	1860	350	62	21700	t/6	13.7	1800	0.05	12155	0.0058933	297	84.82	0.285
35	5.4	2170	410	62	25420	t/6	13.7	1800	0.05	12155	0.0058933	297	77.02	0.221
40	5.4	2480	470	62	29140	t/6	13.7	1800	0.05	12155	0.0058933	297	73.33	0.184
45	5.4	2790	520	62	32240	t/6	13.7	1800	0.05	12155	0.0058933	297	69.36	0.157
50	5.4	3100	580	62	35960	t/6	13.7	1800	0.05	12155	0.0058933	297	67.83	0.138

(contd.)

SR	AR	Height (mm)	Length (mm)	Thickness (mm)	Ag (mm^2)	Eccentricity	f'_c (MPa)	Density	f_t/f'_c ratio	E (MPa)	Steel ratio	f_{sy} (MPa)	Failure Load (kN)	Axial strength ratio
23	5.4	1400	260	62	16120	t/12	13.7	1800	0.15	12155	0.0058933	297	137.69	0.623
27	5.4	1675	315	62	19530	t/12	13.7	1800	0.15	12155	0.0058933	297	144.09	0.539
30	5.4	1860	350	62	21700	t/12	13.7	1800	0.15	12155	0.0058933	297	143.78	0.484
35	5.4	2170	410	62	25420	t/12	13.7	1800	0.15	12155	0.0058933	297	138.84	0.399
40	5.4	2480	470	62	29140	t/12	13.7	1800	0.15	12155	0.0058933	297	131.00	0.328
45	5.4	2790	520	62	32240	t/12	13.7	1800	0.15	12155	0.0058933	297	119.02	0.269
50	5.4	3100	580	62	35960	t/12	13.7	1800	0.15	12155	0.0058933	297	111.04	0.225
23	5.4	1400	260	62	16120	t/6	13.7	1800	0.15	12155	0.0058933	297	99.26	0.449
27	5.4	1675	315	62	19530	t/6	13.7	1800	0.15	12155	0.0058933	297	101.28	0.379
30	5.4	1860	350	62	21700	t/6	13.7	1800	0.15	12155	0.0058933	297	99.23	0.334
35	5.4	2170	410	62	25420	t/6	13.7	1800	0.15	12155	0.0058933	297	95.16	0.273
40	5.4	2480	470	62	29140	t/6	13.7	1800	0.15	12155	0.0058933	297	91.28	0.229
45	5.4	2790	520	62	32240	t/6	13.7	1800	0.15	12155	0.0058933	297	86.67	0.196
50	5.4	3100	580	62	35960	t/6	13.7	1800	0.15	12155	0.0058933	297	83.52	0.170

E. RSM Data

The input data for response surface methodology (RSM) are summarized in Table E.1.

Table E.1: Data for RSM

Run	λ	e_L	T	C	E	Failure Load P_{fea} (kN)	Axial strength ratio $P_{fea}/f'cAg$
1	15	t/20	0.05	1	0.446	518.13	0.96
2	50	t/20	0.05	1	0.446	365.42	0.20
3	15	t/6	0.05	1	0.446	334.39	0.62
4	50	t/6	0.05	1	0.446	219.37	0.12
5	15	t/20	0.05	8	0.446	2263.02	0.52
6	50	t/20	0.05	8	0.446	860.31	0.06
7	15	t/6	0.05	8	0.446	1122.15	0.26
8	50	t/6	0.05	8	0.446	619.78	0.04
9	15	t/20	0.05	1	1	577.00	1.07
10	50	t/20	0.05	1	1	746.68	0.41
11	15	t/6	0.05	1	1	379.16	0.70
12	50	t/6	0.05	1	1	410.57	0.23
13	15	t/20	0.05	8	1	3330.15	0.77
14	50	t/20	0.05	8	1	1818.75	0.13
15	15	t/6	0.05	8	1	2004.88	0.46
16	50	t/6	0.05	8	1	1147.05	0.08
17	15	13t/120	0.1	4.5	0.723	1529.68	0.63
18	50	13t/120	0.1	4.5	0.723	822.94	0.10
19	32.5	t/20	0.1	4.5	0.723	1648.53	0.31
20	32.5	t/6	0.1	4.5	0.723	812.40	0.15
21	32.5	13t/120	0.1	1	0.723	550.19	0.47
22	32.5	13t/120	0.1	8	0.723	1447.86	0.15
23	32.5	13t/120	0.1	4.5	0.446	782.18	0.15
24	32.5	13t/120	0.1	4.5	1	1545.20	0.29
25	32.5	13t/120	0.05	4.5	0.723	1168.81	0.22
26	32.5	13t/120	0.1	4.5	0.723	1285.69	0.24
27	32.5	13t/120	0.1	4.5	0.723	1285.69	0.24
28	32.5	13t/120	0.1	4.5	0.723	1285.69	0.24
29	32.5	13t/120	0.1	4.5	0.723	1285.69	0.24
30	32.5	13t/120	0.1	4.5	0.723	1285.69	0.24
31	32.5	13t/120	0.1	4.5	0.723	1285.69	0.24

F. Details of Published Concrete Wall Test Results

The details of test results from the published literatures are summarized in Table F.1.

Table F.1: Details of published test results

Authors	Specimen	Height (mm)	Length (mm)	Thickness (mm)	SR	AR	Ag (mm^2)	f'c (MPa)	Steel ratio	fsy (MPa)	Eccentricity	Failure Load P_{exp} (kN)	Axial strength ratio $P_{exp}/f'cAg$
Saheb and Desayi (1989)	WAR1	600	900	50	12	0.67	45000	17.864	0.00173	297	t/6	484.27	0.602
	WAR2	600	600	50	12	1	30000	17.86	0.00	297.00	t/6	315.8	0.589
	WAR3	600	400	50	12	1.5	20000	17.86	0.00	297.00	t/6	198.29	0.555
	WSR1	450	300	50	9	1.5	15000	17.34	0.00	297.00	t/6	214.18	0.824
	WSR2	600	400	50	12	1.5	20000	17.34	0.00	297.00	t/6	254.1	0.733
	WSR3	900	600	50	18	1.5	30000	17.34	0.00	297.00	t/6	298.92	0.575
	WSTV2	600	900	50	12	0.67	45000	20.14	0.00	286.00	t/6	535.07	0.591
	WSTV3	600	900	50	12	0.67	45000	20.14	0.01	581.00	t/6	583.52	0.644
	WSTH2	600	900	50	12	0.67	45000	19.6	0.00173	297	t/6	538.01	0.610
Doh and Fragomeni (2005)	OWNS3	1400	1400	40	35	1	56000	52	0.0031	610	t/6	426.7	0.147
	OWNS4	1600	1600	40	40	1	64000	51	0.0031	610	t/6	441.5	0.135
	OWHS3	1400	1400	40	35	1	56000	63	0.0031	610	t/6	441.5	0.125
	OWHS4	1600	1600	40	40	1	64000	75.9	0.0031	610	t/6	455.8	0.094
Ganesan et al. (2013)	OPCAR1	600	320	40	15	1.88	12800	33.832	0.0088	415	t/6	230.53	0.532
	GPCSR1	480	320	40	12	1.5	12800	33.072	0.0088	415	t/6	256.18	0.605
	GPCAR1	600	320	40	15	1.88	12800	33.072	0.0088	415	t/6	211.89	0.501

(contd.)

Authors	Specimen	Height (mm)	Length (mm)	Thickness (mm)	SR	AR	Ag (mm^2)	f'c (MPa)	Steel ratio	fsy (MPa)	Eccentricity	Failure Load P_{exp} (kN)	Axial strength ratio $P_{exp}/f'cAg$
Sam Fragomeni and Mendis (1996)	2a	1000	300	50	20	3.33	15000	42.4	0.0025	450	t/6	231.8	0.364
	2b	1000	300	50	20	3.33	15000	65.4	0.0025	450	t/6	263.5	0.269
	5a	1000	500	40	25	2	20000	35.7	0.0025	450	t/6	201.2	0.282
	5b	1000	500	40	25	2	20000	59.7	0.0025	450	t/6	269.2	0.225
	6b	600	200	40	15	3	8000	67.4	0.0031	450	t/6	178	0.330
Kripanarayanan (1977)	A6	400	700	80	5	0.57	56000	15.59	-	-	t/6	657.63	0.753
	C4	1200	700	80	15	1.71	56000	24.03	-	-	t/6	802.10	0.596
	C5	800	700	80	10	1.14	56000	22.46	-	-	t/6	797.12	0.634
	C6	400	700	80	5	0.57	56000	16.87	-	-	t/6	747.30	0.791
Robinson et al. (2013)	5	3000	500	100	30	6	50000	49.1	0.0094	518	t/6	595	0.242
	6	3000	500	100	30	6	50000	49.1	0.0094	518	t/6	557	0.227
	11	3000	500	100	30	6	50000	51.6	-	-	t/6	582	0.226
	12	3000	500	100	30	6	50000	51.6	-	-	t/6	597	0.231
	13	3000	500	100	30	6	50000	51.6	-	-	t/6	572	0.222
	14	3000	500	100	30	6	50000	51.6	-	-	t/6	568	0.220